Exploring $b \longrightarrow s$ electroweak penguin decays at LHCb

Alexander Shires

High Energy Physics
Blackett Laboratory
Imperial College London

A thesis submitted to Imperial College London
for the degree of Doctor of Philosophy

1st October, 2013

Declaration

The work presented in this thesis was carried out between October 2009 and October 2013. It is the result of my own studies, with the support of members of the Imperial College HEP group and the broader LHCb collaboration. The work of others is explicitly referenced.

The following specific contributions were made by myself.

1. In Chapter 4 describing the LHCb experiment, Section 4.5 on the development of the trigger at LHCb for electroweak penguin and semi-leptonic decays.

2. In Chapter 5, describing the angular analysis of $B^0 \to K^{*0}\mu^+\mu^-$ at LHCb, Section 5.4 detailing the acceptance correction and Section 5.6, giving the methods to assess the data-simulation corrections and the acceptance correction for possible sources of systematic uncertainty.

3. In Chapter 6, the analysis of the effect of a $K\pi$ S-wave in $B^0 \to K^{*0}\ell^+\ell^-$.

4. In Chapter 7, the measurement of a $K\pi$ S-wave in $B^0 \to K^{*0}\mu^+\mu^-$.

This thesis has not been submitted for any other qualification. The measurements presented in Chapter 5 appear in Refs [1] and [2]. The results of the $K\pi$ S-wave theoretical work appear in [3]. The measurements of the $K\pi$ S-wave in $B^0 \to K^{*0}\mu^+\mu^-$ have not been published but will be used in future analyses of electroweak penguin decays at LHCb.

Alex Shires, 1 October 2013

Abstract

The angular distribution of $B^0 \to K^{*0}\mu^+\mu^-$ was studied using $1.0\,\text{fb}^{-1}$ of pp collisions recorded at the LHCb detector at the LHC. Angular observables are measured in five independent bins of the di-muon invariant mass squared, q^2, and the theoretically interesting region from $1 < q^2 < 6\,\text{GeV}^2/c^4$. The results are in good agreement with Standard Model predictions.

The contribution from a $K\pi$ S-wave is included in the angular distribution of $B^0 \to K^+\pi^-\ell^+\ell^-$. The $K\pi$ S-wave is shown to have an overall dilution effect on measurements of the $B^0 \to K^+\pi^-\ell^+\ell^-$ angular observables. For an S-wave contribution of 7% between a $K\pi$ invariant mass squared of $0.64 < p^2 < 1.0\,\text{GeV}^2/c^4$, there is a significant bias on the angular observables for dataset of over 500 events. It is possible to remove this bias by incorporating the S-wave into the angular distribution and by fitting the $K\pi$ mass spectrum.

The fraction of the S-wave in $B^0 \to K^{*0}\mu^+\mu^-$, F_S, was analysed in seven bins of q^2 using $1.0\,\text{fb}^{-1}$ of data from LHCb. The value of F_S in the region from $1 < q^2 < 6\,\text{GeV}^2/c^4$ and from $0.64 < p^2 < 1.0\,\text{GeV}^2/c^4$ was found to be

$$F_\text{S} = 0.083^{+0.057}_{-0.048}(\text{stat.})^{+0.018}_{-0.050}(\text{syst.}).$$

In the regions where no S-wave is found, 95% confidence limits are given. These measurements show that the $K\pi$ S-wave will be a vital consideration for future measurements of $B^0 \to K^{*0}\ell^+\ell^-$.

Acknowledgements

I would like to express my gratitude to the Science and Technologies Facilities Council and to the European Organisation for Nuclear Research (CERN) for giving me the opportunity to pursue this PhD, both in London and in Geneva. Special thanks to Imperial College London for allowing me to do both my undergraduate and postgraduate studies at such an illustrious institution.

I would not have been able to do any of this work without the hundreds of scientists and engineers who develop and run the LHC and participate in CERN. It was an honour to work within the LHCb collaboration and be part of the the Rare Decays working group. I have enjoyed working with the $B^0 \to K^{*0}\mu^+\mu^-$ 'task-force' of Ulrik Egede, Mitesh Patel, Thomas Blake, Nicola Serra, Michel de Cian and Chris Parkinson. Special thanks to Tom for going beyond the call of duty to work with us.

Thank you to the Imperial College HEP group and especially to my supervisor Ulrik Egede, for his support over the years and for giving me the chance to work in HEP, both as an undergraduate and as a postgraduate.

Cheers to Bryn, Martyn, Nick, Rosie, Sam R, Sandra and Wren for life in Geneva, to Sam I for cake and sanity-restoring chat in London, to the Orchestra Saint-Pierre Fusterie for a year of music in French and to the Battersea Badgers for keeping the cricket alive. Thanks to Carla for her love and support at the critical time. I can never thank you enough and look forward to being able to repay you in kind. Thanks to Chris Parkinson for being an excellent colleague and friend; it just wouldn't have been the same without you.

Contents

List of Figures

List of Tables

Chapter 1

Introduction

Particle physics is the study of the fundamental constituents of matter and the behaviour of these components in terms of the forces between them. The aim of particle physics is to determine the rules underlying the universe in terms of the world today and to provide an explanation for the history of the universe. The development of modern day particle physics began around the turn of the 20^{th} century with the discovery of the internal structure in the atom and the exploration of the electromagnetic spectrum. The experimental discovery of the fundamental particles comes from studying particle interactions and collisions, the products of which provide information about the underlying reaction that occurred. At the time of writing, just after the turn of the the 21^{st} century, most of the fundamental particles and forces discovered so far can be placed within the framework called the Standard Model.

The Standard Model (SM) of particle physics is a combination of quantum field theories for the electromagnetic force, the weak force and the strong force, unified by electroweak symmetry breaking and the Higgs mechanism with particle masses introduced through the Yukawa couplings. The SM contains sixteen particles: twelve matter particles and four force particles [13]. However, everyday behaviour is based on only four of these particles, the up and down quarks, the electron and the photon. The great success of the SM of particle physics is that it both explains the behaviour of everyday interactions and also the behaviour of very high energy interactions, at least up to energies of order of one TeV. However, there are two sources of problems with the SM, the first of which

arises from the exact formalism used to describe it and the second is from cosmological observations. The problems from within the SM come from the number of arbitrary and finely tuned parameters in the model. The exact mass of the Higgs, the exact nature of each of the electromagnetic, strong and weak couplings and the arbitrary mass hierarchy are all empirically determined. Also, the incorporation of neutrino masses and the inclusion of quantum theories of gravity both introduce particles beyond the Standard Model. The consistent predictive power of the SM despite these problems drives significant parts of research in particle physics.

Outside of particle physics, observations from cosmology and astrophysics present additional problems. It has been observed that the universe is cooling and that, from measurements of the cosmic microwave background, the universe is flat, homogeneous and isotropic on large scales [14]. These observations can be reconciled by the inflationary model, which proposes that the universe underwent a period of rapid expansion after formation, caused by the negative energy density of a yet undiscovered high energy scalar field [15]. Another problem is that that the observed dynamics of of matter within galaxies does not correspond to the dynamics expected from bodies of such masses [16]. This can be reconciled by assuming either that there is some unknown matter which does not interact electromagnetically or that modifications are required to general relativity on large scales [17,18]. The last problem from cosmology is the observation that the expansion of the universe is taking place at an increasing rate. There is even less basis for a solution to this than for the previous problems, but the negative energy density needed to explain this acceleration is larger than for the inflationary field [19].

The motivation for continued research into particle physics lies in both the unsatisfactory nature of arbitrary parameters and also in the reconciliation of the problems from observational cosmology. Searching for physics beyond the SM takes place in two different ways. The direct approach aims to produce new particles from high energy collisions, whereas indirect searches look at the influence that unknown particles can have on SM processes. The flavour sector of particle physics is concerned with the quarks and their interactions in the bound states they form. The coupling of the quarks to the other forces

and particles is an essential part of the SM and hence is an obvious place to search for deviations from expected behaviour that may indicate effects of new physics. Indirect searches in the flavour sector look for the effects of massive particles which can have subtle higher-order effects on flavour physics observables. Hadrons composed of b quarks are a good test for these effects due to the difference in mass (and therefore the available energy) in transitions from b quarks to lighter quarks.

Measurements of the $B^0 \to K^+\pi^-\mu^+\mu^-$ system using data collected at LHCb during 2011 are presented. An overview of the formalism of the SM is given in Chapter 2. The theoretical description of the $B^0 \to K^+\pi^-\ell^+\ell^-$ decay is presented along with the status of contemporary measurements in Chapter 3. The LHCb detector is described in Chapter 4 along with the work done to develop the trigger for $B^0 \to K^{*0}\mu^+\mu^-$ decays. The first and second angular analyses of $B^0 \to K^{*0}\mu^+\mu^-$ at LHCb are detailed in Chapter 5. The effect of S-wave interference in the $B^0 \to K^+\pi^-\ell^+\ell^-$ system is presented in Chapter 6 and the first measurements of the $K\pi$ S-wave in $B^0 \to K^+\pi^-\mu^+\mu^-$ using data from LHCb are presented in Chapter 7.

Chapter 2

The formalism of particle physics

The Standard Model (SM) of particle physics [20–28] describes the behaviour and the interactions of each of the elementary particles known at the time of writing. In the SM there are twelve matter particles of which there are six quarks and six leptons. The fermions interact via three different forces, the electromagnetic, the weak and the strong force. The particles which mediate the fundamental forces (bosons) are the photon, the $W^{\pm}$ and the Z^0, and the gluon respectively [13]. The mass of each particle, both fermions and bosons, is determined through the interaction with the Higgs field.

This chapter describes the basics on which the Standard Model is based. The flavour sector is described in detail along with a description of possible methods to incorporate physical effects beyond the scope of the Standard Model. The $b \to s$ penguin decay is introduced as a model-independent test for contributions from new physical effects and the current experimental status of $B^0 \to K^{*0}\mu^+\mu^-$ is presented.

2.1 The Standard Model

The Standard Model is a quantum field theory for the fermion fields described by the gauge group $\mathrm{SU(3)_C} \otimes \mathrm{SU(2)_L} \otimes \mathrm{U(1)_Y}$ [29]. The subgroup $\mathrm{SU(3)_C}$ describes the quarks and the strong interactions, and the subgroup $\mathrm{SU(2)_L} \otimes \mathrm{U(1)_Y}$ unifies the electromagnetic and weak interactions. These groups are required to be locally gauge invariant which leads to the addition of fields representing the bosons. The requirement of local gauge invariance

Table 2.1: Table of particles in the SM

Generation	1	2	3
Quarks	u	c	t
	d	s	b
Leptons	e	μ	τ
	ν_e	ν_μ	ν_τ

Bosons
γ
H^0
$W^\pm$
Z^0

implies massless fermion fields but the Higgs mechanism provides a solution by spontaneously breaking the electroweak gauge group to distinguish the weak and electromagnetic interactions and provides locally gauge invariant mass terms to each particle.

In the SM, the fermions are divided up into three generations with two quarks and two leptons per generation. The quarks and charged leptons in each generation are more massive than the previous generation but are otherwise identical. The structure of the particles in the SM is shown in Table 2.1.

The dynamics of the Standard Model particles can be described by a Lagrangian,

$$\mathcal{L}_{\mathrm{SM}} = \mathcal{L}_{\mathrm{EW}} + \mathcal{L}_{\mathrm{QCD}} + \mathcal{L}_{Higgs}\,, \tag{2.1}$$

where the first component describes the electroweak sector, the second the flavour sector and the last is the additional Higgs term. The fermion and boson dynamics and their respective interaction with the Higgs field can be separated out to give an alternative form of the Lagrangian,

$$\mathcal{L}_{\mathrm{SM}} = \mathcal{L}_{Kinetic} + \mathcal{L}_{Higgs} + \mathcal{L}_{Yukawa}\,, \tag{2.2}$$

where the final Yukawa term describes the coupling of the Higgs field to the matter particles. Where not explicitly referenced, the material in this chapter can be found in any good particle physics text and has been drawn primarily from Refs [30–33].

2.1.1 Electromagnetism

The formalism of the fermion and boson fields under a locally gauge invariant group can be demonstrated by consideration of the electromagnetic field. The kinetic part of the

Lagrangian is given as

$$\mathcal{L} = i\bar{\psi}\gamma^{\mu}\partial_{\mu}\psi - \mu\psi\bar{\psi} \tag{2.3}$$

for particle (ψ) and anti-particle ($\bar{\psi}$) fields. It is trivially invariant under gauge transformations of the first kind, or global gauge invariance. A simple example is the group U(1), $\psi \rightarrow \psi^{'} = e^{i\alpha}$. The electromagnetic field is also invariant under transformations which vary in time and space. These are gauge transformations of the second kind, known as local gauge invariance. The group of transformations are defined as

$$\psi \rightarrow \psi^{'} = e^{i\alpha(x)}\psi \tag{2.4}$$

$$\bar{\psi} \rightarrow \bar{\psi}^{'} = e^{-i\alpha(x)}\bar{\psi} \tag{2.5}$$

The kinetic energy Lagrangian is now no longer invariant because the derivative gains an extra term of $i\alpha(x)\psi(x)$. Therefore, the kinetic energy term is kept invariant by introducing a vector field, A_{μ}, along with a covariant derivative

$$D_{\mu} = (\partial_{\mu} - ieA_{\mu}) \ . \tag{2.6}$$

The covariant derivative describes interactions between the particle and the gauge boson through a $\bar{\psi}\gamma^{\mu}\psi A_{\mu}$ term. The coefficient of this term gives the strength of the coupling between particles and the photon, e, and the modified Lagrangian is locally gauge invariant,

$$\mathcal{L} = i\bar{\psi}\gamma^{\mu}D_{\mu}\psi - \psi\bar{\psi}\,, \tag{2.7}$$

where the vector field, also known as the gauge boson, transforms as

$$A_{\mu}^{'} = -\frac{1}{e}\partial_{\mu}\psi + A_{\mu}\,. \tag{2.8}$$

The dynamics of this electromagnetic gauge boson, the photon, are given by the Lagrangian

$$\mathcal{L} = -\frac{1}{2} F_{\mu\nu} F^{\mu\nu} \tag{2.9}$$

where the Faraday tensor is defined as

$$F_{\mu\nu} = \partial_\mu A_\nu - \partial_\nu A_\mu \,. \tag{2.10}$$

The complete electromagnetic Lagrangian is

$$\mathcal{L}_{\mathrm{EM}} = i\bar{\psi}\gamma^\mu D_\mu \psi - \mu\psi\bar{\psi} - \frac{1}{2} F_{\mu\nu} F^{\mu\nu} \tag{2.11}$$

and it can be seen that any additional mass term of the form $m^2 A_\mu A^\mu$ breaks the local gauge invariance. This implies that the photon and the fermions must be massless here.

2.1.2 Electroweak sector

The theory of electroweak interactions was developed in the 1960s and provides both the weak interaction and the electromagnetic interaction with a mathematical basis. The unification of these two fundamental forces resulted in a Nobel prize for Glashow, Salam and Weinberg in 1979 [20–22]. The weak force also interacts with all known particles and the charge associated with the weak force is called the "weak hypercharge‘. The weak force is unique among the fundamental forces in that it is party violating. The electroweak Lagrangian is constructed in a similar manner to the electromagnetic Lagrangian,

$$\mathcal{L} = \mathcal{L}_{Bosons} + \mathcal{L}_{Fermions} + \mathcal{L}_{Higgs} \,. \tag{2.12}$$

The terms for the gauge boson and terms for the fermion couplings are supplemented by the Higgs Lagrangian which introduces mass terms for all particles whilst remaining locally gauge invariant. The symmetry group of the electroweak Lagrangian is $\mathrm{SU}(2)_L \otimes \mathrm{U}(1)_Y$

where the first group provides the parity dependence and Y is the weak hypercharge.

The fermion fields are a combination of two chiral components ($f = f_L + f_R$) where each component can be projected out using the chiral operator,

$$f_{\frac{R}{L}} = (1 \pm \gamma_5)\, f\,, \tag{2.13}$$

that for massless particles selects each state. The left-handed fermions are represented in SU(2) as doublets

$$l_L = \begin{pmatrix} e_L \\ \nu_{e,L} \end{pmatrix}, \begin{pmatrix} \mu_L \\ \nu_{\mu,L} \end{pmatrix}, \begin{pmatrix} \tau_L \\ \nu_{\tau,L} \end{pmatrix}, \tag{2.14}$$

$$q_L = \begin{pmatrix} u_L \\ d_L \end{pmatrix}, \begin{pmatrix} c_L \\ s_L \end{pmatrix}, \begin{pmatrix} t_L \\ b_L \end{pmatrix} \tag{2.15}$$

and the right-handed fermions are represented by SU(2) singlets

$$l_R = e_R, \mu_R, \tau_R, \tag{2.16}$$

$$q_R = u_R, d_R, c_R, d_R, t_R, b_R\,. \tag{2.17}$$

This incorporates the parity violating nature of the weak interactions.

There are three gauge field for SU(2), $W_\mu^{a=1,2,3}$ and one gauge field for U(1), B_μ. The covariant derivative required to keep the Lagrangian locally invariant is

$$D_\mu = \partial_\mu \mathbf{I} + i g_W \mathbf{T}^a W_\mu^a + i g_Y Y B_\mu \mathbf{I}\,, \tag{2.18}$$

where $\mathbf{T}^a$ are the generators of SU(2) which are linear combinations of the Pauli matrices,

$$\mathbf{T}^{1,2} = \frac{1}{2}\left(\sigma^1 \pm i\sigma^2\right) \text{ and } \quad \mathbf{T}^3 = \sigma^3\,. \tag{2.19}$$

In order to require that only left-handed particles participate in the weak interaction, the

covariant derivative must be split into

$$D_{L,\mu} = \partial_\mu \mathbf{I} + i g_W \mathbf{T}^a W_\mu^a + i g_Y Y B_\mu \mathbf{I} \tag{2.20}$$

$$\text{and} \quad D_{R,\mu} = \partial_\mu \mathbf{I} + i g_Y Y B_\mu \mathbf{I} \,. \tag{2.21}$$

The massless fermion Lagrangian is given as

$$\mathcal{L} = \bar{f}_L \left(i\gamma^\mu D_{L,\mu}\right) f + \bar{f}_R \left(i\gamma^\mu D_{R,\mu}\right) f_R \tag{2.22}$$

for $f = l, q$. The Lagrangian for the dynamics of the gauge fields can be written in a similar manner, to the electromagnetic Lagrangian with two tensors for each symmetry group:

$$\mathcal{L} = -\frac{1}{4}\left(W_{\mu\nu}^a W^{a,\mu\nu} + B_{\mu\nu} B^{\mu\nu}\right) \,, \tag{2.23}$$

where each tensor is given through the

$$W_{\mu\nu}^a = \partial_\mu W_\nu^a - \partial_\nu W_\mu^a + g_W \epsilon^{a,b,c} W_\mu^b W_\nu^c \,, \tag{2.24}$$

$$B_{\mu\nu} = \partial_\mu B_\nu - \partial_\nu B_\mu \,, \tag{2.25}$$

where $\epsilon^{a,b,c}$ are the structure constants of SU(2) that define the relation

$$\tau^a = i\epsilon^{a,b,c}\left[\tau^b, \tau^c\right] \,. \tag{2.26}$$

Symmetry breaking

A solution to the problem of breaking local gauge invariance by adding mass terms to the SM Lagrangian was proposed in Ref [23] (among others). This involves adding a scalar field, the Higgs field (Φ), to the Lagrangian of the form

$$\mathcal{L}_{Higgs} = (D_\mu \Phi)^\dagger D^\mu \Phi + \left(\mu^2 |\Phi|^2 + \lambda |\Phi|^4\right) \,, \tag{2.27}$$

where the first term is the kinetic term and the second is a potential term constructed with a non-zero minimum in Φ at $v = \mu/\sqrt{\lambda}$. If the field is a scalar doublet, the minimum of the scalar field is

$$\Phi_0 = \frac{1}{\sqrt{2}} \begin{pmatrix} 0 \\ v \end{pmatrix} , \tag{2.28}$$

which breaks the symmetry by choosing a particular minimum and separates the scalar field up into distinct massive and massless Goldstone bosons. The non-zero expectation value of the scalar field leads mass terms to arise from mixtures of the gauge fields. These mixtures are the real electroweak gauge bosons,

$$\begin{pmatrix} W_\mu^+ \\ W_\mu^- \end{pmatrix} = \frac{1}{\sqrt{2}} \begin{pmatrix} 1 & i \\ 1 & -i \end{pmatrix} \begin{pmatrix} W_\mu^1 \\ W_\mu^2 \end{pmatrix} , \quad \begin{pmatrix} Z_\mu^0 \\ A_\mu \end{pmatrix} = \frac{1}{\sqrt{2}} \begin{pmatrix} \cos\theta_\mathrm{W} & -\sin\theta_\mathrm{W} \\ \sin\theta_\mathrm{W} & \cos\theta_\mathrm{W} \end{pmatrix} \begin{pmatrix} W_\mu^3 \\ B_\mu \end{pmatrix} , \tag{2.29}$$

where the angle θ_W is the Weinberg angle and parametrises the mixing between the neutral bosons. The masses of the $W^\pm$ and the Z^0 along with the mass term for the Higgs field can be written as

$$m_W = \frac{g_W \mu}{2\sqrt{\lambda}}, \quad m_{Z^0} = \frac{m_W}{\sqrt{2}\cos\theta_\mathrm{W}} \quad \text{and} \quad m_H = \sqrt{2}\mu \,. \tag{2.30}$$

The $W^\pm$ and Z^0 bosons were first discovered at CERN by the UA1 experiment [34, 35] and a new particle compatible with the Higgs boson with a mass of around 125 GeV was observed at the LHC [36, 37].

2.1.3 The flavour sector

The Lagrangian for the flavour sector is given by

$$\mathcal{L} = \mathcal{L}_{Quarks} + \mathcal{L}_{Gluons} + \mathcal{L}_{Yukawa} \,, \tag{2.31}$$

where the first term describes the kinetics of the quarks and the second describes the gauge bosons for the strong force along with their interactions with the quarks. The last term describes the interactions of the quarks and gluons with the Higgs field via Yukawa couplings which determine the mass eigenstates of the quarks.

The structure of the flavour sector is given by the SU(3) gauge group and each of the quarks form colour triplets,

$$q_C = \begin{pmatrix} q_R \\ q_G \\ q_B \end{pmatrix} , \tag{2.32}$$

where there are three colour indices, R, G and B. Applying local gauge invariance to the SU(3) group requires a gauge field (G^a_μ) of the strong force. The covariant derivative is constructed as

$$D_\mu = \partial_\mu \mathbf{I} + i g_S \mathbf{T}^a G^a_\mu \, , \tag{2.33}$$

where g_S is the strong coupling constant and $\mathbf{T}^{a=1-8}$ are the SU(3) generators which obey the commutation relation,

$$\mathbf{T}^a = i f^{a,b,c} \left[\mathbf{T}^b, \mathbf{T}^c \right] , \tag{2.34}$$

where $f^{a,b,c}$ are the structure constants of SU(3). The dynamics of the gluon field are given by the tensors

$$G^a_{\mu\nu} = \partial_\mu G^a_\nu - \partial_\nu G^a_\mu + g_S f^{a,b,c} G^b_\mu G^c_\nu \, , \tag{2.35}$$

The massless part of the Lagrangian for the flavour sector is given by

$$\mathcal{L} = \bar{q}^C \left(i \gamma^\mu D_\mu \right) q^C + -\frac{1}{4} G^a_{\mu\nu} G^{a,\mu\nu} \, , \tag{2.36}$$

where the last term shows a self-coupling between the gluons.

2.1.4 Fermion masses: $\mathcal{L}_{Yukawa}$

The fermion masses can be introduced through the Higgs mechanism whilst retaining local gauge invariance. The Lagrangian for the coupling of the fermion and Higgs fields is given by

$$\mathcal{L} = m_u^i \bar{u}_R^i u_L^i + m_d^i \bar{d}_R^i d_L^i + m_e^i \bar{\ell}_R^i \ell_L^i \tag{2.37}$$

where u, d are the 'up' and 'down' type quarks, ℓ represents the leptons and the index i runs over the three generations of fermions. The mass term $m_{u,d,\ell}^i = \frac{v}{\sqrt{2}} Y_{u,d,\ell}^i$ is a combination of the vacuum expectation value for the Higgs field and a unique Yukawa coupling [26] to parametrise the mass. In the SM there are no right-handed neutrinos, therefore the Lagrangian for neutrino mass eigenstates cannot be defined using this mechanism.

Each of the Yukawa terms, Y_j^i, can be written as a 3x3 dimensional matrix for the quarks and leptons. In order to remove terms which couple between the fermion generation each of these Yukawa matrices must be diagonal. The Yukawa matrices can by diagonalised by unitary matrices, $\mathcal{U}$, which acts on each fermion field through

$$f_H = \mathcal{U}(f, H) f_H^{'}\,, \tag{2.38}$$

for a given fermion f of handedness H leading to

$$\mathcal{U}(u,R)^\dagger Y_u \mathcal{U}(u,L) = \begin{pmatrix} m_u & 0 & 0 \\ 0 & m_c & 0 \\ 0 & 0 & m_t \end{pmatrix}, \tag{2.39a}$$

$$\mathcal{U}(d,R)^\dagger Y_d \mathcal{U}(d,L) = \begin{pmatrix} m_d & 0 & 0 \\ 0 & m_s & 0 \\ 0 & 0 & m_b \end{pmatrix}, \tag{2.39b}$$

$$\mathcal{U}(\ell,R)^\dagger Y_\ell \mathcal{U}(\ell,L) = \begin{pmatrix} m_e & 0 & 0 \\ 0 & m_\mu & 0 \\ 0 & 0 & m_\tau \end{pmatrix}, \tag{2.39c}$$

where the mass eigenstates are given on the right side of the equations.

The left-handed fermion fields are SU(2) doublets so these transformations act independently on each part of the doublet, i.e.

$$\begin{pmatrix} u_L \\ d_L \end{pmatrix} = \begin{pmatrix} \mathcal{U}(u,L) u'_L \\ \mathcal{U}(d,L) d'_L \end{pmatrix} = \mathcal{U}(u,L) \begin{pmatrix} u'_L \\ V\, d'_L \end{pmatrix}, \tag{2.40}$$

where the matrix $V = \mathcal{U}(u,L)^\dagger \mathcal{U}(d,L)$ describes the transformations between the left-handed up and down quarks. The SU(2) singlet representation of the right-handed fermions allows mass terms without mixing matrices.

The mixing matrix V is the Cabbibo-Kobayashi-Maskawa (CKM) matrix [27,28] which is a 3x3 unitary matrix and completely specified by three mixing angles and a complex phase. The CKM matrix can be written both in terms of the 9 matrix elements V_{ij} and also in terms of the Wolfenstein parametrisation [13],

$$V_{\text{CKM}} = \begin{pmatrix} V_{ud} & V_{us} & V_{ub} \\ V_{cd} & V_{cs} & V_{cb} \\ V_{td} & V_{ts} & V_{tb} \end{pmatrix} = \begin{pmatrix} 1-\lambda^2/2 & \lambda & A\lambda^3(\rho - i\eta) \\ -\lambda & 1-\lambda^2/2 & A\lambda^2 \\ A\lambda^2(1-\rho-i\eta) & -A\lambda^2 & 1 \end{pmatrix} \tag{2.41}$$

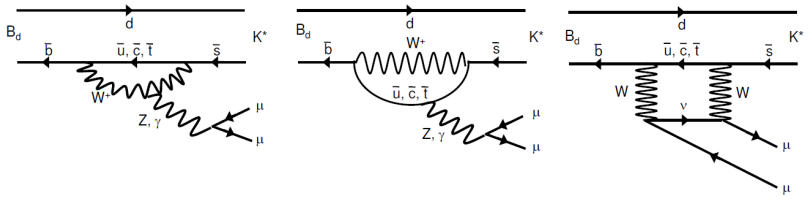

Figure 2.1: Three different Feynman diagrams showing the SM process that allow a $b \to s\ell^+\ell^-$ transition, two penguin diagrams and a W box diagram.

where the parameters ρ, η, λ and A are chosen such that the matrix is unitary of $\mathcal{O}(\lambda^4)$.

The unitary transformation allows the electroweak couplings with the quarks and the $W^\pm$ bosons but does not affect the coupling between the neutral bosons,

$$\bar{u}\, U_u^\dagger\, U_d\, d\, W^\pm\,, \quad \bar{d}\, U_d^\dagger\, U_d\, d\, Z^0\,, \tag{2.42}$$

where the charged current allows transitions between mass eigenstates for up and down type quarks but, due to the unitary nature of the mixing matrix, the neutral current does not mix with the mass eigenstates. This gives flavour-changing charged currents at tree level but not flavour-changing neutral currents. In order to construct flavour changing neutral currents, higher order diagrams with a loop containing a charged current are required. Flavour violating effects from particles beyond the SM can come from particles in these loop processes.

2.2 Flavour changing neutral currents

Flavour-changing neutral currents (FCNCs) are quark transitions which change the generation of the quark without any total change in electric charge. FCNC processes are forbidden at tree level in the SM as shown above but can occur in loop processes where the mediating $W^\pm$ boson is entirely virtual such as a $b \to s$ transition. The $b \to s$ loop can radiate a photon ($b \to s\gamma$) and or dilepton ($b \to s\ell^+\ell^-$) with either a penguin or box internal structure. Examples of different $b \to s\ell^+\ell^-$ transitions in the SM are shown in Fig. 2.1. Processes which contain a $b \to s$ transition are popular FCNC decays for tests of contributions from new physics [38]. Measurements of FCNCs are model-independent

tests of any new physics model that contribute to change the overall properties of the decay.

The formalism of b-hadron decays can be expressed in terms of an effective theory, which separates different contributions to the decay by a particular mass scale. The effective theory of B decays, Heavy Quark Effective Theory [32, 33] , separates out particles with masses much greater than that of a b quark, such as the electroweak gauge bosons, the Higgs, the t quark and any new massive particles. The operator product expansion separates these high and low energy contributions into a set of coefficients and operators [39],

$$\langle f|\mathcal{H}|i\rangle = \sum_k \mathcal{C}_{k(\mu)} \langle f|\mathcal{O}_k(\mu)|i\rangle \,, \tag{2.43}$$

where the Wilson coefficients (C) and the operators (O) are normalised to a mass scale (μ).

The operators encode the low energy contributions from the quarks in the decay and the Wilson coefficients encode the contributions from higher mass particles above the mass scale μ. For this reason the Wilson coefficients are said to encode the 'short' distance physics whilst the operators encode the 'long' distance physics. The short distance physics covers everything above the mass scale of the effective Hamiltonian, such weak interactions and any contribution from physics beyond the SM. The long distance physics covers everything below the mass scale of the Hamiltonian, *i.e.* the K^* physics and the interactions with the light spectator quark. The benefit of this formalism is that the Wilson coefficients can include arbitrary contributions from new physical models and provide a model-independent formalism through which to measure these contributions.

The effective Hamiltonian for the $b \to s\ell^+\ell^-$ transition [40] is

$$H = \frac{4G_F}{\sqrt{2}} V_{tb}^* V_{ts} \sum_{i=1}^{10} C_i(\mu) O_i(\mu) \,. \tag{2.44}$$

The electroweak penguin operators are

$$\mathcal{O}_7 = \frac{e}{g^2} m_b \left(\bar{s} \sigma_{\mu\nu} \frac{1}{2} (1 \pm \gamma^5) b \right) F^{\mu\nu} \,, \tag{2.45a}$$

$$\mathcal{O}_8 = \frac{1}{g} m_b \left(\bar{s} \sigma_{\mu\nu} T^a \frac{1}{2} (1 \pm \gamma^5) b \right) G^{a,\mu\nu} \,, \tag{2.45b}$$

$$\mathcal{O}_9 = \frac{e^2}{g^2} m_b \left(\bar{s} \gamma_\mu \frac{1}{2} (1 \mp \gamma^5) b \right) (\bar{\ell} \gamma^\mu \ell) \,, \tag{2.45c}$$

$$\mathcal{O}_{10} = \frac{e^2}{g^2} m_b \left(\bar{s} \gamma_\mu \frac{1}{2} (1 \mp \gamma^5) b \right) (\bar{\ell} \gamma^\mu \gamma^5 \ell) \,, \tag{2.45d}$$

where g is the strong coupling constant and m_b is the b mass dependent on the chosen renormalisation scheme. The operator $\mathcal{O}_7$ describes the electroweak penguin decay with a photon propagator, $\mathcal{O}_8$ describes the diagram with a gluon propagator and the operators $\mathcal{O}_9$ and $\mathcal{O}_{10}$ describe the diagrams with electroweak bosons, either $W^\pm$ or Z^0. The respective Wilson coefficients for these quark transitions are $\mathcal{C}_7$, $\mathcal{C}_8$, $\mathcal{C}_9$ and $\mathcal{C}_{10}$ [41]. The Wilson coefficients at the b mass are evolved down from the weak mass scale, giving effective Wilson coefficients which also include contributions from the four-quark and gluonic operators $\mathcal{C}_{1\to6,}$

$$\mathcal{C}_7^{(\text{eff})} = \frac{4\pi}{\alpha_S} \mathcal{C}_7 - \frac{1}{3} \mathcal{C}_3 - \frac{4}{9} \mathcal{C}_4 - \frac{20}{3} \mathcal{C}_5 - \frac{80}{9} \mathcal{C}_6, \tag{2.46}$$

$$\mathcal{C}_8^{(\text{eff})} = \frac{4\pi}{\alpha_S} \mathcal{C}_8 + \mathcal{C}_3 - \frac{1}{6} \mathcal{C}_4 + 20 \mathcal{C}_5 - \frac{10}{3} \mathcal{C}_6, \tag{2.47}$$

$$\mathcal{C}_9^{(\text{eff})} = \frac{4\pi}{\alpha_S} \mathcal{C}_9 + Y(q^2) \tag{2.48}$$

$$\mathcal{C}_{10}^{(\text{eff})} = \frac{4\pi}{\alpha_S} \mathcal{C}_{10} \tag{2.49}$$

$$\mathcal{C}_{7,8,9,10}^{(\text{eff})} = \frac{4\pi}{\alpha_S} \mathcal{C}_{7,8,9,10}^{\prime(\text{eff})} \,. \tag{2.50}$$

where $\mathrm{Y}(q^2)$, along with more detail about the effective coefficients can be found in Ref [40]. Contributions from physics beyond the SM can also be parameterised in terms of the Wilson coefficients. Right handed currents for each operator can be introduced as primed counterparts to the SM Wilson coefficients ($\mathcal{C}_{7,}^{\prime}$ $\mathcal{C}_{8,}^{\prime}$ $\mathcal{C}_9^{\prime}$ and $\mathcal{C}_{10}^{\prime}$) and contributions from new scalars and pseudoscalar particles can be incorporated in the form of additional Wilson coefficients $\mathcal{C}_S$ and $\mathcal{C}_P$.

Constraints on the Wilson coefficients can be obtained from measurements of different FCNCs [12]. Measurements of $b \to s\gamma$ transitions are proportional to the magnitude of $\mathcal{C}_7$ and measurements of $b \to s\ell^+\ell^-$ transitions in the form of $B_s^0 \to \mu^+\mu^-$ are proportional the value of $\mathcal{C}_{10}$ and could incorporate contributions from $\mathcal{C}_S$ and $\mathcal{C}_P$. The $b \to s\ell^+\ell^-$ electroweak penguin decay is mainly parameterised by $\mathcal{C}_{7,}$ $\mathcal{C}_9$ and $\mathcal{C}_{10}$, allowing measurements of the $b \to s\ell^+\ell^-$ decays to constrain a wide range of models of physics beyond the SM.

2.3 Experimental results

The first measurement of a $b \to s$ FCNC was the $b \to s\gamma$ transition observed in the measurement of the branching fraction of $B \to K^*\gamma$ at CLEO in 1993 [42]. $B^0 \to K^{*0}\gamma$ is a radiative electroweak penguin decay described by the photon operator $\mathcal{O}_7$ and hence is sensitive to $\mathcal{C}_7$. Subsequent precision measurements of $B^0 \to K^{*0}\gamma$ and the similar decay $B_s^0 \to \phi\gamma$ have been performed by the B factories, BaBar [43] and Belle [44] along with LHCb [45–47]. These measurements of the differential branching fraction of $B^0 \to K^{*0}\gamma$, $B_s^0 \to \phi\gamma$ and measurements of the *CP* asymmetry $\mathcal{A}^{CP}$ $(B^0 \to K^{*0}\gamma)$ [13] agree well with the predictions from the SM [48, 49].

The FCNC decay $B^0 \to K^{*0}\ell^+\ell^-$ was proposed as a further test for contribution from physics beyond the SM in Ref [50]. However, the differential branching fraction of the inclusive decay $B^0 \to K^{*0}\ell^+\ell^-$ and the exclusive decay $B^0 \to K^{*0}\mu^+\mu^-$ have been measured [48] to be

$$\Gamma(B^0 \to K^{*0}\ell^+\ell^-) = 9.9^{+1.2}_{-1.1} \times 10^{-7} \tag{2.51}$$

$$\Gamma(B^0 \to K^{*0}\mu^+\mu^-) = 1.06 \pm 0.10 \times 10^{-6} \tag{2.52}$$

and are compatible with SM prediction [51, 52].

Further measurements of $B^0 \to K^{*0}\ell^+\ell^-$ are based on evaluating the angular distribution of the daughter particles to understand the K^{*0} polarisation amplitudes. How to determine the maximal amount of information from the decay while keeping uncertainties from QCD minimal has recently attracted much interest [40, 53–57].

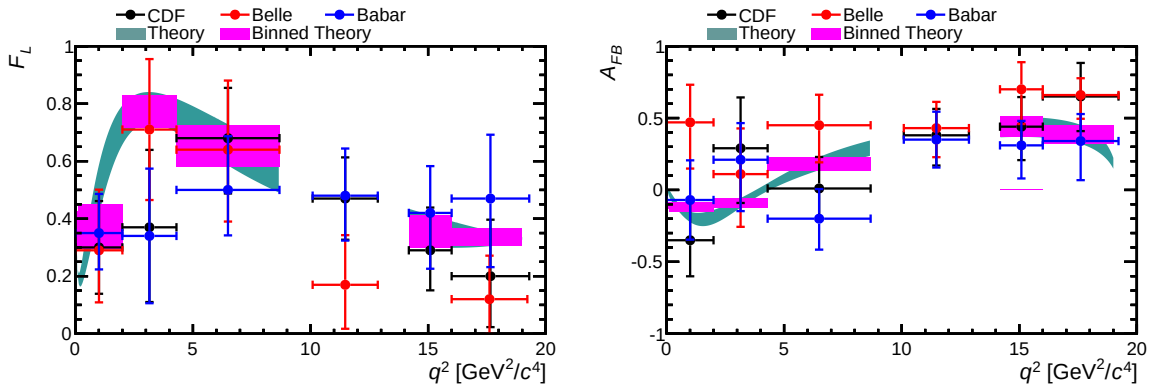

(a) F_{L} (b) A_{FB}

Figure 2.2: The fraction of longitudinal polarisation of the K^{*0} (F_{L}) and the forward-backward asymmetry of the dimuon system (A_{FB}) as measured by CDF [9, 10], Belle [8] and BaBar [6, 7] along with the theoretical prediction from Ref. [11].

The results from the experimental analyses of $B^0 \to K^{*0}\ell^+\ell^-$ [7–9, 58] have focused on the forward-backward asymmetry of the dimuon system (A_{FB}) and the fraction of longitudinal polarisation of the K^{*0} (F_{L}) as a function of the dimuon invariant mass. The latest measurements from BaBar, Belle and CDF for F_{L} and A_{FB} are shown in Fig. 2.2. It is possible to see that there is some tension between these measurements of both F_{L} and A_{FB} at low dimuon invariant masses. Contributions from physics beyond the SM have been predicted to change the q^2 spectrum of A_{FB} [55] which are not excluded by these measurements. New measurements of F_{L} and A_{FB} are needed to understand the exact shape of A_{FB} and clarify the discrepancy in the regions of low and high q^2.

Chapter 3

The $B^0 \to K^{*0}\ell^+\ell^-$ decay

3.1 Angular basis

The differential angular distribution for $B^0 \to K^{*0}\ell^+\ell^-$ is expressed as a function of five kinematic variables: three angles ($\cos\theta_l$, $\cos\theta_K$, ϕ) and two invariant masses; the mass squared of the $K\pi$ system is denoted p^2 and the mass squared of the dilepton pair (q^2), the angle θ_K is defined as the angle between the K^+ and the B momentum vector in the rest frame of the B^0. The angle θ_ℓ is defined as the one between the ℓ^+ in the rest frame of the dilepton pair and the momentum vector of the B^0. The angle ϕ is defined as the signed angle between the planes formed by the dilepton pair and the $K\pi$ pair respectively, in the rest frame of the B^0.[1]

For the *CP*-conjugate decay $\overline{B}^0 \to \overline{K}^{*0}\ell^+\ell^-$, θ_ℓ is defined with respect to the ℓ^- instead of the ℓ^+ and θ_K is defined with respect to the K^- instead of the K^+. There are two possible definitions of ϕ, a *CP* symmetric definition which changes through a minus sign and a *CP* anti-symmetric definition, $\phi_{\rm ACP}$, which is unchanged between the B^0 and $\overline{B}^0$ decay. An illustration of the angles for $\overline{B}^0 \to \overline{K}^{*0}\ell^+\ell^-$ is shown in Fig 3.1.

The angles $\cos\theta_l$ and $\cos\theta_K$ are given explicitly as

$$\cos\theta_l = \left(\frac{\vec{p}_{\ell^+}\cdot\vec{p}_{\ell^+\ell^-}}{|\vec{p}_{\ell^+}||\vec{p}_{\ell^+\ell^-}|}\right), \quad \cos\theta_K = \left(\frac{\vec{p}_{K^+}\cdot\vec{p}_{K\pi}}{|\vec{p}_{K^+}||\vec{p}_{K\pi}|}\right), \tag{3.1}$$

[1] This is the same sign convention for $\cos\theta_l$ as used in all previous experiments and the same ϕ convention as used in LHCb [2].

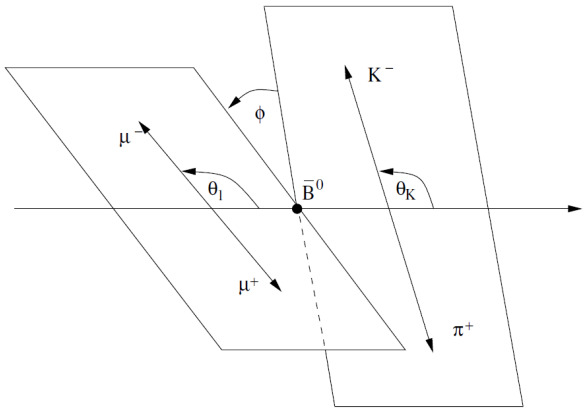

Figure 3.1: An illustration of the angles used to describe the $\overline{B}^0 \to \overline{K}^{*0}\ell^+\ell^-$ decay. The angle θ_l is defined between the ℓ^- and the $\overline{B}^0$ in the dilepton rest frame. The angle θ_K is defined between the K^- and the $\overline{B}^0$ in the $K\pi$ rest frame. The angle ϕ is the signed angle between ℓ^- and K^- in the rest frame of the $\overline{B}^0$.

where each momentum vector $\vec{p}$ is defined in the rest frame of the parent particle, i.e. the lepton momentum, $\vec{p}_{\ell^+}$, is in the dilepton rest frame and dilepton momentum, $\vec{p}_{\ell^+\ell^-}$, is in B^0 rest frame. The angle ϕ is calculated as

$$\cos\phi = \left(\frac{\vec{p}_{\ell^+} \times \vec{p}_{\ell^-}}{|\vec{p}_{\ell^+} \times \vec{p}_{\ell^-}|}\right) \cdot \left(\frac{\vec{p}_{K^+} \times \vec{p}_{\pi^-}}{|\vec{p}_{K^+} \times \vec{p}_{\pi^-}|}\right). \tag{3.2}$$

For the CP-conjugate $\overline{B}^0 \to \overline{K}^{*0}\ell^+\ell^-$ decay, the angles $\cos\theta_l$ and $\cos\theta_K$ are given explicitly as

$$\cos\theta_{\bar{\ell}} = \left(\frac{\vec{p}_{\ell^-} \cdot \vec{p}_{\ell^+\ell^-}}{|\vec{p}_{\ell^-}||\vec{p}_{\ell^+\ell^-}|}\right), \quad \cos\theta_{\bar{K}} = \left(\frac{\vec{p}_{K^-} \cdot \vec{p}_{K\pi}}{|\vec{p}_{K^-}||\vec{p}_{K\pi}|}\right), \tag{3.3}$$

and applying the *CP* operator to the definition of ϕ gives the relation,

$$\cos\phi = \left(\frac{\vec{p}_{\ell^-} \times \vec{p}_{\ell^+}}{|\vec{p}_{\ell^-} \times \vec{p}_{\ell^+}|}\right) \cdot \left(\frac{\vec{p}_{K^-} \times \vec{p}_{\pi^+}}{|\vec{p}_{K^-} \times \vec{p}_{\pi^+}|}\right). \tag{3.4}$$

The *CP* anti-symmetric definition of ϕ is given by only applying the *CP* operator to the $K\pi$ state,

$$\cos\phi_{\mathrm{ACP}} = \left(\frac{\vec{p}_{\ell^+} \times \vec{p}_{\ell^-}}{|\vec{p}_{\ell^+} \times \vec{p}_{\ell^-}|}\right) \cdot \left(\frac{\vec{p}_{K^-} \times \vec{p}_{\pi^+}}{|\vec{p}_{K^-} \times \vec{p}_{\pi^+}|}\right). \tag{3.5}$$

Each of the angles are defined over the intervals

$$0 \leq \theta_l < \pi, \quad 0 \leq \theta_K < \pi, \quad -\pi \leq \phi < \pi, \tag{3.6}$$

such that the angular distribution is defined over the range

$$-1 \leq \cos\theta_l < 1, \quad -1 \leq \cos\theta_K < 1, \quad -\pi < \phi < \pi\,. \tag{3.7}$$

3.2 Angular distribution

Following Ref [50], the angular distribution of $B^0 \to K^{*0}\ell^+\ell^-$ can be written as an explicit function of $\cos\theta_l$ and ϕ,

$$\begin{aligned}\frac{\mathrm{d}^5\Gamma}{\mathrm{d}q^2\mathrm{d}p^2\mathrm{d}\cos\theta_K\mathrm{d}\cos\theta_l\mathrm{d}\phi} =& \frac{3}{8}\Big(I_1^c + 2I_1^s + (I_2^c + 2I_2^s)\cos 2\theta_l + 2I_3\sin^2\theta_l\cos 2\phi \\ &+ 2\sqrt{2}I_4\sin 2\theta_l\cos\phi + 2\sqrt{2}I_5\sin\theta_l\cos\phi + 2I_6\cos\theta_l \\ &+ 2\sqrt{2}I_7\sin\theta_l\sin\phi + 2\sqrt{2}I_8\sin 2\theta_l\sin\phi + 2\sqrt{2}I_9\sin^2\theta_l\sin 2\phi\Big)\,,\end{aligned} \tag{3.8}$$

where each of the angular coefficients (I_i) are combinations of the helicity amplitudes and contain an implicit dependence on $\cos\theta_K$ and the invariant masses, p^2 and q^2.

The nine angular coefficients are expressed as

$$I_1^c = |\mathcal{A}_{0L}|^2 + |\mathcal{A}_{0R}|^2 + 8\frac{m_l^2}{q^2}\Re(\mathcal{A}_{L0}\mathcal{A}_{R0}^*) + 4\frac{m_l^2}{q^2}|\mathcal{A}_t|^2 \tag{3.9a}$$

$$I_1^s = \frac{3}{4}(|\mathcal{A}_{L||}|^2 + |\mathcal{A}_{L\perp}|^2 + (L \to R))(1 - \frac{4m_l^2}{q^2}) + \frac{4m_l^2}{q^2}\Re(\mathcal{A}_{L\perp}\mathcal{A}_{R\perp} + \mathcal{A}_{R||}\mathcal{A}_{R||})) \tag{3.9b}$$

$$I_2^c = -\beta_l^2\left(|\mathcal{A}_{L0}|^2 + |\mathcal{A}_{R0}|^2\right) \tag{3.9c}$$

$$I_2^s = \frac{1}{4}\beta_l^2\left(|\mathcal{A}_{L||}|^2 + |\mathcal{A}_{L\perp}|^2 + |\mathcal{A}_{R||}|^2 + |\mathcal{A}_{R\perp}|^2\right) \tag{3.9d}$$

$$I_3 = \frac{1}{2}\beta_l^2\left(|\mathcal{A}_{1L\perp}|^2 - |\mathcal{A}_{1L||}|^2 + |\mathcal{A}_{R\perp}|^2 - |\mathcal{A}_{R||}|^2\right) \tag{3.9e}$$

$$I_4 = \frac{1}{\sqrt{2}}\beta_l^2\left(\Re(\mathcal{A}_{L0}\mathcal{A}_{L||}^*) + (L \to R)\right) \tag{3.9f}$$

$$I_5 = \sqrt{2}\beta_l\left(\Re(\mathcal{A}_{L0}\mathcal{A}_{L\perp}^*) - (L \to R)\right) \tag{3.9g}$$

$$I_6 = 2\beta_l\left(\Re(\mathcal{A}_{L||}\mathcal{A}_{L\perp}^*) - (L \to R)\right) \tag{3.9h}$$

$$I_7 = \sqrt{2}\beta_l\left(\Im(\mathcal{A}_{L0}\mathcal{A}_{L||}^*) - (L \to R)\right) \tag{3.9i}$$

$$I_8 = \frac{1}{\sqrt{2}}\beta_l^2\left(\Im(\mathcal{A}_{L0}\mathcal{A}_{L\perp}^*) + (L \to R)\right) \tag{3.9j}$$

$$I_9 = \beta_l^2\left(\Im(\mathcal{A}_{L||}\mathcal{A}_{L\perp}^*) + (L \to R)\right), \tag{3.9k}$$

where $\mathcal{A}_{H(0,||,\perp,t)}$ are the K^{*0} spin amplitudes for a given handedness, m_l is the lepton mass and $\beta_l = \sqrt{1 - 4m_l^2/q^2}$ [50]. The lepton mass is assumed to be insignificant, such that $I_{1,2}$ have no m_l dependence, $\beta_l = 1$ and $\mathcal{A}_t$ disappears from the angular distribution.

Neglecting any *CP* asymmetry, as measured in Ref. [59], the B^0 and $\overline{B}^0$ decays can be combined to give

$$\frac{\mathrm{d}^5\left[\Gamma_{B^0} + \Gamma_{\overline{B}^0}\right]}{\mathrm{d}q^2\mathrm{d}p^2\mathrm{d}\cos\theta_K\mathrm{d}\cos\theta_l\mathrm{d}\phi} = \sum_{i=1}^{9} I_i(\cos\theta_l, \cos\theta_K, \phi) + \bar{I}_i(\cos\theta_l, \cos\theta_K, \phi)\ . \tag{3.10}$$

The *CP* anti-symmetric angular distribution is given by

$$\frac{\mathrm{d}^5\left[\Gamma_{B^0} - \Gamma_{\bar{B}^0}\right]}{\mathrm{d}q^2\mathrm{d}p^2\mathrm{d}\cos\theta_K\mathrm{d}\cos\theta_l\mathrm{d}\phi} = \sum_{i=1}^{9} I_i(\cos\theta_l, \cos\theta_K, \phi) - \bar{I}_i(\cos\theta_l, \cos\theta_K, \phi_{\mathrm{ACP}})\ . \tag{3.11}$$

Simplification of the angular distribution can be achieved by applying a transformation in ϕ such that $\phi' = \phi - \pi$ for $\phi < 0$ [60]. The $I_{4,5,7,8}$ angular terms which are dependent

on $\cos\phi$ or $\sin\phi$ cancel, leaving $I_{1,2,3,6,9}$ in the angular distribution.

For a $K\pi$ state which is a combination of different resonances, the amplitudes for a given handedness ($H = L, R$) can be expressed as a sum over the resonances (J) [61],

$$\begin{aligned}\mathcal{A}^{L,R}_{H,0/t}(p^2,q^2) &= \sum_J \sqrt{N_J}\ A^{L,R}_{J,H,0}(q^2)\ P_J(p^2)\ Y^0_J(\theta_K,0)\\ \mathcal{A}^{L,R}_{H,\|/\perp}(p^2,q^2) &= \sum_J \sqrt{N_J}\ A^{L,R}_{J,H,\|/\perp}(q^2)\ P_J(p^2)\ Y^{-1}_J(\theta_K,0),\end{aligned} \tag{3.12}$$

where $Y^m_J(\theta_K,0)$ are the spherical harmonics, $\mathcal{M}$ is the matrix element encompassing the q^2 dependence and $P_J(p^2)$ is the propagator of the resonant K^{*0} state.

3.3 Amplitudes

The amplitudes of $B^0 \to K^+\pi^-\ell^+\ell^-$ parametrise the decay and are different for each polarisation of the $K\pi$ state and of the dilepton system. The dilepton is a vector state and the $K\pi$ system is considered to be in a scalar (S-wave) or a vector (P-wave) state. The matrix element for $B^0 \to K^+\pi^-\ell^+\ell^-$ takes the same form for both $K\pi$ states and can be written [40] as

$$\begin{aligned}\mathcal{M} =& \frac{G_F\alpha_s}{2\pi}|V_{tb}||V_{ts}|\Bigg(\Bigg[\langle K\pi|\bar{s}\gamma_\mu\left(\mathcal{C}_9^{(\text{eff})}P_L + \mathcal{C}_9^{\prime(\text{eff})}P_R\right)b|\bar{B}\rangle\\ &- \frac{2m_b}{q^2}\langle K\pi|\bar{s}i\sigma^{\mu\nu}q_\nu\left(\mathcal{C}_7^{(\text{eff})}P_R + \mathcal{C}_7^{\prime(\text{eff})}P_L\right)b|\bar{B}\rangle\Bigg]\left(\bar{\ell}\gamma_\mu\ell\right)\\ &+ \langle K\pi|\bar{s}\gamma^\mu\left(\mathcal{C}_{10}^{(\text{eff})}P_L + \mathcal{C}_{10}^{\prime(\text{eff})}P_R\right)b|\bar{B}\rangle\left(\bar{\ell}\gamma_\mu\gamma_5\ell\right)\Bigg)\end{aligned} \tag{3.13}$$

where contributions from scalar and pseudoscalar operators have been ignored.

3.3.1 $B^0 \to K^{*0}\ell^+\ell^-$

The $K\pi$ P-wave has three polarisation states: The total amplitude for the decay of a pseudo-scalar to two vector particles, $P \to V_1V_2$, can be written as a combination of the

polarisation tensors and the matrix element,

$$M(P \to V_1 V_2) = \epsilon^{*\mu}_{V_1} M_{\mu\nu} \epsilon^{*\nu}_{V_2} \,. \tag{3.14}$$

Each of the polarisation states for a vector state described by the momentum vector $p^\mu = (p_0, 0, 0, p_z)$ can be written as

$$\epsilon^\mu_V(\pm) = (0, 1, \pm i, 0)\,/\sqrt{2} \tag{3.15a}$$

$$\epsilon^\mu_V(0) = (p_z, 0, 0, -p_0)\,/\sqrt{p^2} \tag{3.15b}$$

$$\epsilon^\mu_V(t) = (p_0, 0, 0, p_z)\,/\sqrt{p^2}\ . \tag{3.15c}$$

In the context of the decay $B^0 \to K^{*0}\ell^+\ell^-$ there is a virtual gauge boson and a real K^{*0}. The gauge boson can exist in all four possible polarisation states $(0, \pm, t)$ but the K^{*0} is on shell and only has three states $(0, \pm)$. The helicity amplitudes can be obtained by contracting the polarisation states for each of the particles in Eq 3.14 to give

$$H_i = M_{i,i}\,, \tag{3.16}$$

with an implicit sum over $i = 0, ||$ and $\perp$, and additionally $H_t = M_{0,t}$. The transversity amplitudes are combinations of the helicity amplitudes

$$A_{||,\perp} = (H_+ \mp H_-)\sqrt{2}, \quad A_0 = H_0, \quad \text{and}\, A_t = H_t \tag{3.17}$$

The subsequent decay of the vector boson to dilepton system allows for both left and right-handed currents in the longitudinal, parallel and perpendicular polarisations so there are in total seven transversity amplitudes. The transversity amplitudes for the P-wave K^{*0}_1

state can be written to leading order [40] as

$$
\begin{aligned}
A_{1,L/R,0}(q^2) = &- \frac{N}{2m_{K_1^{*0}}\sqrt{q^2}}\Bigg(\Big((\mathcal{C}_9^{(\mathrm{eff})} - \mathcal{C}_9^{\prime(\mathrm{eff})}) \mp (\mathcal{C}_{10}^{(\mathrm{eff})} - \mathcal{C}_{10}^{\prime(\mathrm{eff})})\Big) \\
&\left[\left(m_{B^0}^2 - m_{K_1^{*0}}^2 - q^2\right)\left(m_{B^0} + m_{K_1^{*0}}\right) A_1(q^2) - \lambda \frac{A_2(q^2)}{m_{B^0} + \mathrm{m}_{\mathrm{K}_1^{*0}}}\right] \qquad (3.18a) \\
&+ 2m_b\left(\mathcal{C}_7^{(\mathrm{eff})} - \mathcal{C}_7^{\prime(\mathrm{eff})}\right)\left[\left(m_{B^0}^2 + 3m_{K_1^{*0}}^2 + q^2\right) T_2(q^2) - \frac{\lambda(m_{B^0}, K_1^{*0}, q^2)}{m_{B^0}^2 - m_{K_1^{*0}}^2} T_3(q^2)\right]\Bigg) \\
A_{1,L/R,\|}(q^2) = &- N\sqrt{2}\left(m_{B^0}^2 - m_{K_1^{*0}}^2\right)\left[\Big((\mathcal{C}_9^{(\mathrm{eff})} - \mathcal{C}_9^{\prime(\mathrm{eff})}) \mp (\mathcal{C}_{10}^{(\mathrm{eff})} - \mathcal{C}_{10}^{\prime(\mathrm{eff})})\Big) \frac{A_1(q^2)}{m_{B^0} + m_{K_1^{*0}}}\right. \\
&\left. + 2\frac{m_b}{q^2}\left(\mathcal{C}_7^{(\mathrm{eff})} - \mathcal{C}_7^{\prime(\mathrm{eff})}\right) T_2(q^2)\right] \qquad (3.18b) \\
A_{1,L/R,\perp}(q^2) = &N\sqrt{2}\lambda(m_{B^0}, K_1^{*0}, q^2)^{1/2}\left[\Big((\mathcal{C}_9^{(\mathrm{eff})} - \mathcal{C}_9^{\prime(\mathrm{eff})}) \mp (\mathcal{C}_{10}^{(\mathrm{eff})} - \mathcal{C}_{10}^{\prime(\mathrm{eff})})\Big) \frac{V(q^2)}{m_{B^0} + m_{K_1^{*0}}}\right. \\
&\left. + 2\frac{m_b}{q^2}\left(\mathcal{C}_7^{(\mathrm{eff})} + \mathcal{C}_7^{\prime(\mathrm{eff})}\right) T_1(q^2)\right] \qquad (3.18c)
\end{aligned}
$$

with $\lambda(m_{B^0}, p^2, q^2) = \left(m_{B^0}^2 - p^2 - q^2\right)^2 - 4p^2q^2$. This expression uses the narrow width assumption for the K^{*0} (892) which assumes the K^{*0} decays on shell to $K\pi$, allowing the relativistic Breit-Wigner to be approximated as

$$
P_1^2(p^2) = \frac{1}{\left(p^2 + m_{K^{*0}}^2\right)^2 + m_{K^{*0}}^2 \Gamma_{m_{K^{*0}}}^2} \frac{m_{K^{*0}}\Gamma_{m_{K^{*0}}}}{\pi} \quad \rightarrow \quad \delta\left(p^2 - m_{K^{*0}}^2\right) \ . \qquad (3.19)
$$

The transversity amplitudes can then be expressed in terms of seven $B \rightarrow K_1^{*0}$ form factors $(A_i(q^2), T_i(q^2), V(q^2))$. For large K^* energies, of order $m_{B^0}/2$, it is possible to reduce the seven different form factors to two *heavy-to-light* form factors as in Ref [53]. This allows

the amplitudes to take a simple form neglecting corrections of order $1/m_b$ and α_S,

$$\begin{aligned} A_{1,L/R,0}(q^2) =& -\frac{N}{2m_{K_1^{*0}}\sqrt{q^2}}(1-q^2)^2\Bigg[\left((\mathcal{C}_9^{(\text{eff})}-\mathcal{C}_9^{\prime(\text{eff})})\mp(\mathcal{C}_{10}^{(\text{eff})}-\mathcal{C}_{10}^{\prime(\text{eff})})\right) \\ &+2m_b\left(\mathcal{C}_7^{(\text{eff})}-\mathcal{C}_7^{\prime(\text{eff})}\right)\Bigg]\xi_{||}\left(E_{K^{*0}}\right) \qquad (3.20a) \\ A_{1,L/R,||}(q^2) =& -N\sqrt{2}m_{B^0}(1-q^2)\Bigg[\left((\mathcal{C}_9^{(\text{eff})}-\mathcal{C}_9^{\prime(\text{eff})})\mp(\mathcal{C}_{10}^{(\text{eff})}-\mathcal{C}_{10}^{\prime(\text{eff})})\right) \\ &+2\frac{m_b}{q^2}\left(\mathcal{C}_7^{(\text{eff})}-\mathcal{C}_7^{\prime(\text{eff})}\right)\Bigg]\xi_{\perp}\left(E_{K^{*0}}\right) \qquad (3.20b) \\ A_{1,L/R,\perp}(q^2) =& +N\sqrt{2}m_{B^0}(1-q^2)\Bigg[\left((\mathcal{C}_9^{(\text{eff})}-\mathcal{C}_9^{\prime(\text{eff})})\mp(\mathcal{C}_{10}^{(\text{eff})}-\mathcal{C}_{10}^{\prime(\text{eff})})\right) \\ &+2\frac{m_b}{q^2}\left(\mathcal{C}_7^{(\text{eff})}+\mathcal{C}_7^{\prime(\text{eff})}\right)\Bigg]\xi_{\perp}\left(E_{K^{*0}}\right)\ . \qquad (3.20c) \end{aligned}$$

3.3.2 $B^0 \to K^+\pi^-\ell^+\ell^-$ amplitudes

Non-resonant $K\pi$ effects in have been explored in Ref [62] and the combination of multiple K^* resonances have been explored in Ref [61]. A combination of several resonant $K\pi$ states can be achieved though the dependence of the matrix elements on the resonant mass, $m_{K_J^{*0}}$ and adding coefficients derived from the polarisation tensor [61]. The effect of a $K\pi$ S-wave has been explored in Refs [63, 64] and also in more detail later in Chapter 6. The single K_0^{*0} S-wave amplitude [61] is given by

$$\begin{aligned} A_{0,L/R,0} =& N\frac{\lambda\left(m_{B^0},K_0^{*0}q^2\right)^{1/2}}{\sqrt{q^2}}\Bigg[\left((\mathcal{C}_9^{(\text{eff})}-\mathcal{C}_9^{\prime(\text{eff})})\mp(\mathcal{C}_{10}^{(\text{eff})}-\mathcal{C}_{10}^{\prime(\text{eff})})\right)F_1(q^2) \\ &+2m_b\left(\mathcal{C}_7^{(\text{eff})}+\mathcal{C}_7^{\prime(\text{eff})}\right)\frac{F_T(q^2)}{m_{B^0}+m_{K_0^{*0}}}\Bigg] \qquad (3.21) \end{aligned}$$

where $F_1(q^2)$ and $F_T(q^2)$ are the $B^0 \to K_0^{*0}$ form factors.

3.4 Angular observables

The contributions from the Wilson coefficients defined above can be measured by measuring the transversity amplitudes through an angular analysis of the $B^0 \to K^{*0}\ell^+\ell^-$ angular distribution. Direct measurements of the transversity amplitudes are dependent

on the values of the form factors which have a significant theoretical uncertainty. To mitigate these uncertainties and allow measurements of the Wilson coefficients, angular observables can be constructed from the transversity amplitudes that are independent of the two heavy-to-light form factors. Many angular observables have been proposed for the decay $B^0 \to K^{*0}\ell^+\ell^-$ [40, 53, 54, 56, 57]. These observables are combinations of the amplitudes which both minimise the uncertainty from the form factors and maximise the contribution from new physics models. So far the forward-backward asymmetry ($A_{\rm FB}$), the fraction of the K^{*0} longitudinal polarisation ($F_{\rm L}$) and two combinations of the transverse amplitudes ($A_{\rm T}^2$ and $A_{\rm Im}$) have been measured [6–10].

3.4.1 P-wave observables

These observables are constructed from combinations of amplitudes and are normalised to the sum of amplitudes for the P-wave state, given as

$$|A_{10}|^2 + |A_{1||}|^2 + |A_{1\perp}|^2\,, \tag{3.22}$$

where the generic combination of amplitudes $A_{Ji}A^*_{Ji}$ is defined for a spin J and a polarisation (0,||,$\perp$) as

$$A_{Ji}A^*_{Ji} = A_{JiL}A^*_{JiL} + A_{JiR}A^*_{JiR}\,. \tag{3.23}$$

The forward-backward asymmetry of the dilepton system, $A_{\rm FB}$, enters in the angular coefficient I_6 and is defined in terms of the amplitudes as

$$A_{\rm FB}(q^2) = \frac{3}{2}\frac{\Re(A_{1L||}A^*_{1L\perp}) - \Re(A_{1R||}A^*_{1R\perp})}{|A_{10}|^2 + |A_{1||}|^2 + |A_{1\perp}|^2}\,. \tag{3.24}$$

In a similar way, $F_{\rm L}$, S_3 and S_9 are defined as

$$\begin{aligned} F_{\rm L}(q^2) &= \frac{|A_{10}|^2}{|A_{10}|^2 + |A_{1||}|^2 + |A_{1\perp}|^2} \\ S_3(q^2) &= \frac{|A_{1\perp}|^2 - |A_{1||}|^2}{|A_{10}|^2 + |A_{1||}|^2 + |A_{1\perp}|^2} \\ S_9(q^2) &= \frac{\Im(A_{1L||}A^*_{1L\perp}) - \Im(A_{1R||}A^*_{1R\perp})}{|A_{10}|^2 + |A_{1||}|^2 + |A_{1\perp}|^2} \end{aligned} \tag{3.25}$$

where S_3 and S_9 are related to the angular coefficients I_3 and I_9 respectively. These theoretical observables are normalised to the sum of the P-wave amplitudes and the factorisation of the amplitudes into matrix elements and the propagators removes the p^2 dependence from these theoretical observables.

In terms of the angular distribution, $A_{\rm FB}$ can also be expressed as the difference between the number of 'forward-going' μ^+ and the number of 'backward-going' μ^+ in the rest frame of the B^0,

$$\left[\int_0^1 - \int_{-1}^0\right] \mathrm{d}\cos\theta_l \frac{\mathrm{d}\Gamma}{\mathrm{d}q^2 \mathrm{d}\cos\theta_l} / \frac{\mathrm{d}\Gamma}{\mathrm{d}q^2}\,, \tag{3.26}$$

which explains the name of the observable.

3.4.2 Transverse observables

Angular observables which are normalised to only the transverse helicity amplitudes have been studied with the additional aim of reducing the theoretical uncertainties [38, 53]. This is achieved by separating out the dependence on the longitudinal amplitudes and their form factors from the calculation. The main transverse observable is $A_{\rm T}^2$ which comes from the angular coefficient I_3,

$$A_{\rm T}^2(q^2) = \frac{|A_{1\perp}|^2 - |A_{1||}|^2}{|A_{1\perp}|^2 + |A_{1||}|^2}\,. \tag{3.27}$$

The observables associated with I_6 and I_9 can be similarly reparameterised [65] to give

$$\begin{aligned} A_{\mathrm{T}}^{\mathrm{Re}}(q^2) &= \frac{|A_{1\perp}|^2 - |A_{1\parallel}|^2}{|A_{1\parallel}|^2 + |A_{1\perp}|^2} \\ A_{\mathrm{T}}^{\mathrm{Im}}(q^2) &= \frac{\Im(A_{1L\parallel}A_{1L\perp}^*)\Im(A_{1R\parallel}A_{1R\perp}^*)}{|A_{1\parallel}|^2 + |A_{1\perp}|^2}\,. \end{aligned} \tag{3.28}$$

These observables are correlated to $(1 - F_{\mathrm{L}})$ when the the angular distribution is normalised to the sum of the P-wave amplitudes.

3.4.3 *CP* asymmetric angular observables

Angular observables equivalent to S_3 and S_9 for the *CP* antisymmetric angular distribution can by constructed from the definition of $I_i - \bar{I}_i$. Two *CP* antisymmetric angular observables, A_3 and A_9 for the angular coefficients I_3 and I_9, which can be compared to the S_i angular observables

$$A_3 = \frac{1}{2}\frac{\left(I_3 - \bar{I}_3\right)}{|A_{10}|^2 + |A_{1\parallel}|^2 + |A_{1\perp}|^2}\,, \tag{3.29}$$

$$A_9 = \frac{1}{2}\frac{\left(I_9 - \bar{I}_9\right)}{|A_{10}|^2 + |A_{1\parallel}|^2 + |A_{1\perp}|^2}\,. \tag{3.30}$$

3.4.4 Relation to the Wilson coefficients

Each of the observables is related to the Wilson coefficients through bi-linear combinations of the transversity amplitudes. This means that there are terms proportional to the combinations $|\mathcal{C}_{9,10}^{(\mathrm{eff})} \pm \mathcal{C}_{9,10}^{\prime(\mathrm{eff})}|^2$ and $|\mathcal{C}_7^{(\mathrm{eff})} - \mathcal{C}_7^{\prime(\mathrm{eff})}|^2$. Each of these terms is multiplied by the relevant K^{*0} form factors giving the q^2 dependence. This can be seen in the SM predictions for A_{FB} and F_{L} in Fig. 2.2.

3.5 The angular distribution with observables

The angular distribution of $B^0 \to K^{*0}\mu^+\mu^-$ including the angular observables as a function of $\cos\theta_l$, $\cos\theta_K$ and $\phi^{'}$ is given by

$$\begin{aligned}\frac{1}{\Gamma}\frac{\mathrm{d}^4\Gamma}{\mathrm{d}q^2\mathrm{dcos}\theta_K\mathrm{dcos}\theta_l\mathrm{d}\phi^{'}} = \frac{9}{16\pi}\Bigg(&2F_{\mathrm{L}}\cos^2\theta_K(1-\cos^2\theta_l) \\ &+\frac{1}{2}(1-F_{\mathrm{L}})(1-\cos^2\theta_K)(1+\cos^2\theta_l) \\ &+\frac{1}{2}(1-F_{\mathrm{L}})A_{\mathrm{T}}^2(1-\cos^2\theta_K)(1-\cos^2\theta_l)\cos 2\phi^{'} \\ &+\frac{4}{3}A_{\mathrm{FB}}(1-\cos^2\theta_K)\cos\theta_l \\ &+S_3(1-\cos^2\theta_K)(1-\cos^2\theta_l)\sin 2\phi^{'}\Bigg). \end{aligned} \tag{3.31}$$

The two-dimensional angular distribution as a function of $\cos\theta_l$ and $\cos\theta_K$ is given by integrating over ϕ in Eq. 3.31

$$\begin{aligned}\frac{1}{\Gamma}\frac{\mathrm{d}^3\Gamma}{\mathrm{d}q^2\mathrm{d}\cos\theta_K\mathrm{d}\cos\theta_l} = \frac{9}{16}\Bigg(&2F_{\mathrm{L}}\cos^2\theta_K(1-\cos^2\theta_l)+\frac{1}{2}(1-F_{\mathrm{L}})(1-\cos^2\theta_K)(1+\cos^2\theta_l) \\ &+\frac{4}{3}A_{\mathrm{FB}}(1-\cos^2\theta_K)\cos\theta_l\Bigg)\end{aligned} \tag{3.32}$$

and further integration from Equation 3.31 yields the angular distribution for each of the angles,

$$\begin{aligned}\frac{1}{\Gamma}\frac{\mathrm{d}^2\Gamma}{\mathrm{d}q^2\mathrm{dcos}\theta_l} &= \frac{3}{4}F_{\mathrm{L}}(1-\cos^2\theta_l)+\frac{3}{8}(1-F_{\mathrm{L}})(1+\cos^2\theta_l)+A_{\mathrm{FB}}\cos\theta_l, \\ \frac{1}{\Gamma}\frac{\mathrm{d}^2\Gamma}{\mathrm{d}q^2\mathrm{dcos}\theta_K} &= \frac{3}{2}F_{\mathrm{L}}\cos^2\theta_K+\frac{3}{4}(1-F_{\mathrm{L}})(1-\cos^2\theta_K), \\ \frac{1}{\Gamma}\frac{\mathrm{d}^2\Gamma}{\mathrm{d}q^2\mathrm{d}\phi^{'}} &= F_{\mathrm{L}}+\frac{1}{2}(1-F_{\mathrm{L}})A_{\mathrm{T}}^2\cos 2\phi^{'}+S_3\sin 2\phi^{'}.\end{aligned} \tag{3.33}$$

There is a physical limit on the size of A_{FB} and F_{L} given by $A_{\mathrm{FB}} \leq \frac{3}{4}(1-F_{\mathrm{L}})$, where if $F_{\mathrm{L}} \to 1$, then the parallel and perpendicular amplitudes must tend to zero, implying $A_{\mathrm{FB}} \to 0$.

3.6 Summary

In this chapter the angular distribution of $B^0 \to K^{*0}\ell^+\ell^-$ was presented. The helicity amplitudes for $B^0 \to K_1^{*0}\ell^+\ell^-$ and $B^0 \to K_0^{*0}\ell^+\ell^-$ are detailed showing the structure arising from a Hamiltonian written in terms of Wilson coefficients. Several experimental observables are set out which are favoured theoretically for the ability to calculate predictions cleanly.

Chapter 4

The LHCb experiment

This chapter was the work of the LHCb collaboration. The author contributed to the development of the trigger in Section 4.5.

4.1 Introduction

The LHCb detector is a single-arm forward spectrometer designed for precision measurements of particles containing b quarks [5]. It is one of the four main experiments at the Large Hadron Collider (LHC) at the European Organisation for Nuclear Research (CERN) in Geneva, Switzerland. In this chapter the LHCb detector, its performance and its use to select $B^0 \to K^{*0}\mu^+\mu^-$ events is shown. The LHCb detector is described in Section 4.2 detailing the sub-detector components required for measurements of $b \to s\ell^+\ell^-$ decays. The trigger system used in the LHCb detector is described in Section 4.3 and an overview of the software used in LHCb is given in Section 4.4. The development of the trigger system used to select $B^0 \to K^{*0}\mu^+\mu^-$ decays for the 2011 data-taking is presented in Section 4.5 along with the final configuration of the LHCb trigger system used throughout 2011.

4.1.1 CERN

CERN is an international organisation founded in 1954 in order to provide a politically neutral place to carry out research in nuclear and particle physics. At the time of writing, CERN has 20 full member states and there are around ten thousand people associated

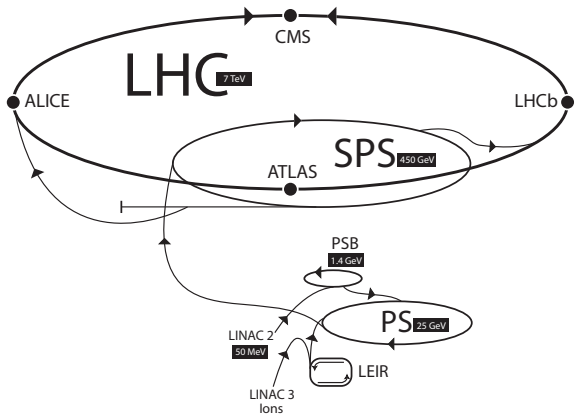

Figure 4.1: A illustration of the the LHC accelerator complex showing each of the stages in the injection chain for the LHC ring along with the four main experiments on the LHC ring [67].

with science at CERN. Over the years that CERN has operated, it has contributed to the discovery of neutral currents [66], the electroweak gauge bosons [34, 35] and recently the Higgs boson [36, 37]. CERN is primarily home to the LHC accelerator complex, which is a proton-proton (pp) collider with a circumference of 27 km at a depth of 100 m under the the French-Swiss border just outside Geneva. The LHC accelerator is built in the tunnel originally used for the LEP accelerator and ran at an energy of $\sqrt{s}$ =7 TeV in 2011. The injection chain for the LHC consists of one linear accelerator and three synchrotrons as shown in Fig. 4.1. It starts with a linear accelerator which accelerates the protons from rest to 50 MeV. The synchrotrons increase the beam energy and refine the proton bunches to a configuration suitable for the LHC. Firstly the Proton Synchrotron Booster (PSB) takes the beam from 50 MeV to 1.5 GeV at which point the beam enters the Proton Synchrotron (PS) where the beam energy is increased to 25 GeV. The beam is then transferred to the Super Proton Synchrotron (SPS) which increases the energy to 450 GeV before injecting the protons into the LHC. The LHC accelerates the proton bunches from injection energy at 450 GeV to the final collision energy, which was 3.5 TeV per beam in 2011 and 4 TeV per beam in 2012. Consolidation upgrades of the LHC to take place in 2013 and 2014 are expected to increase this collision energy to the design energy of 7 TeV per beam. During operation in 2011-12 there were 1380 proton bunches per beam with a bunch spacing of 50 ns. There are four main experiments on the LHC ring, two general purpose detectors (ATLAS and CMS), along with a heavy-ion experiment (ALICE) and a dedicated B-

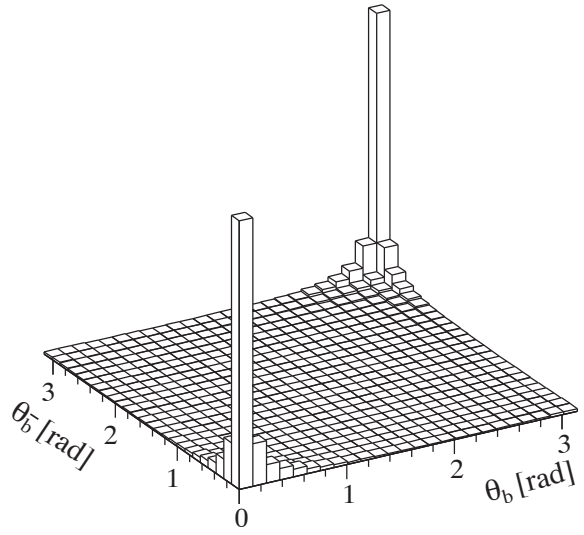

Figure 4.2: The angular distribution of $b\bar{b}$ pairs in terms of the polar angle from the beam axis. The $b\bar{b}$ pairs are largely produced within a very small opening angle hence the development of LHCb as a forward spectrometer [5].

physics experiment (LHCb).

At the LHCb interaction point the instantaneous luminosity of the colliding proton bunches is constant at around $\mathcal{L} \approx 3 \times 10^{32}\,\mathrm{cm}^2\,\mathrm{s}^{-1}$. This is significantly below the LHC luminosity, which in 2011 reached over $\mathcal{L} \approx 1 \times 10^{33}\,\mathrm{cm}^2\mathrm{s}^{-1}$. This luminosity was chosen so that the number of interactions per proton bunch crossing (μ) stayed uniform throughout the period of proton collisions for each 'fill' of the LHC. This ensures that the environment is consistent and has a low multiplicity for reconstruction of B mesons but that there is still a sufficient number of B meson decays of interest for a given number of collisions.

The production of $b\bar{b}$ pairs in pp interactions is governed predominantly by gluon fusion, $gg \rightarrow b\bar{b}$. The collision of partons of unequal energy and a momentum boost along the direction of the collision results in $b\bar{b}$ pairs that are produced at small angles to the beam axis. The angular distribution of $b\bar{b}$ production is shown in Fig. 4.2. The $b\bar{b}$ cross section at $\sqrt{s}$ =7 TeV is 75 µb within the LHCb acceptance [68]. In total the experiment recorded an integrated luminosity of $1.0\,\mathrm{fb}^{-1}$ in 2011 that could be used for further analysis. The increase in integrated luminosity throughout the year can be seen in Fig. 4.3 along with the technical stops and periods of machine development.

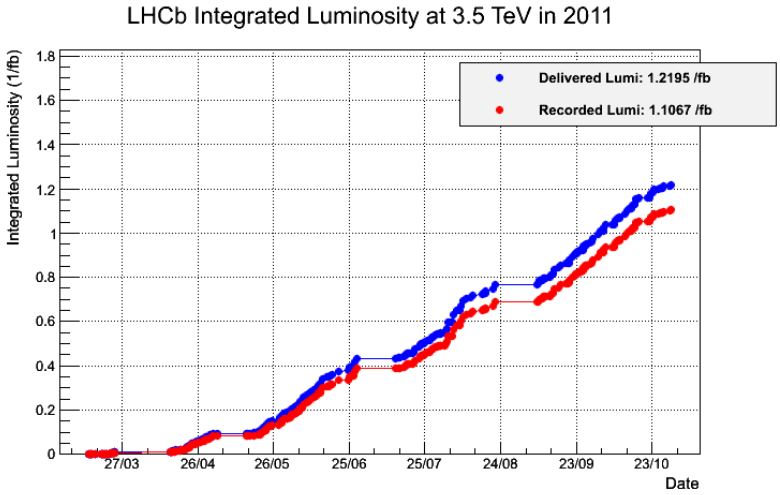

Figure 4.3: The integrated luminosity recorded by LHCb during 2011 [4].

4.2 The LHCb detector

The LHCb detector at the LHC is a 25 m long forward spectrometer covering the pseudorapidity range $2 < \eta < 5$ and the angular range above and below the horizontal beam pipe from 15 mrad to 350 mrad [5]. The experiment is situated at point 8 of the LHC ring on the French-Swiss border close to Geneva Airport and Ferney-Voltaire. The LHCb detector and its sub-detector components are illustrated in Fig. 4.4 and Fig. 4.5.

The LHCb detector consists of a tracking system, detectors for identification of charged hadrons and muons and calorimeters to provide energy measurements of charged and neutral particles. The high precision tracking system consists of a silicon-strip vertex detector surrounding the pp interaction region, a large-area silicon-strip detector located upstream of a dipole magnet with a bending power of about 4 Tm, and three stations of silicon-strip detectors and straw drift tubes placed downstream of the magnet. The combined tracking system has a momentum resolution ($\Delta p/p$) that varies from 0.4% at 5 GeV/c to 0.6% at 100 GeV/c, and an impact parameter resolution of 20 µm for tracks with high transverse momentum. Charged hadrons are identified using two ring-imaging Cherenkov detectors [69]. Photon, electron and hadron candidates are identified by a calorimeter system consisting of scintillating-pad and pre-shower detectors, an electromagnetic calorimeter and a hadronic calorimeter. Muons are identified by a system composed of alternating layers of iron and multi-wire proportional chambers. The trigger consists of a hardware

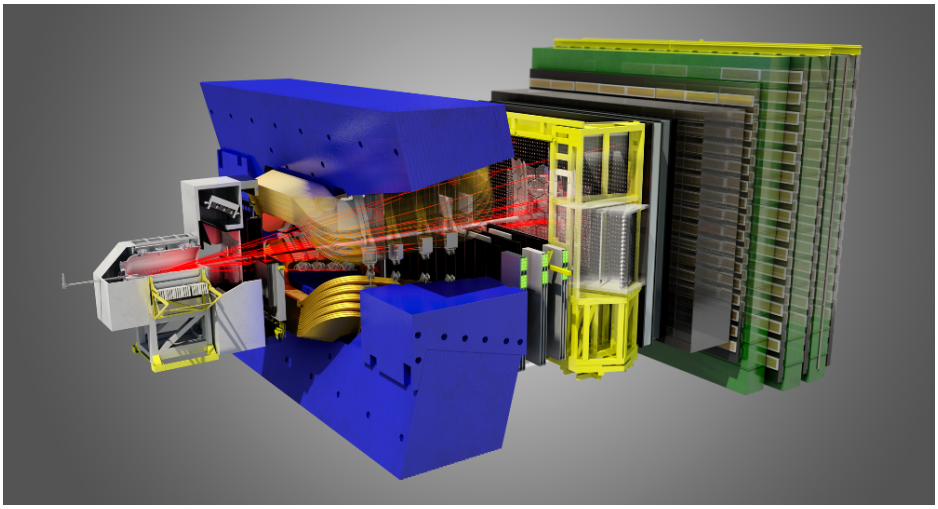

Figure 4.4: The LHCb detector shown in from a three dimensional perspective.

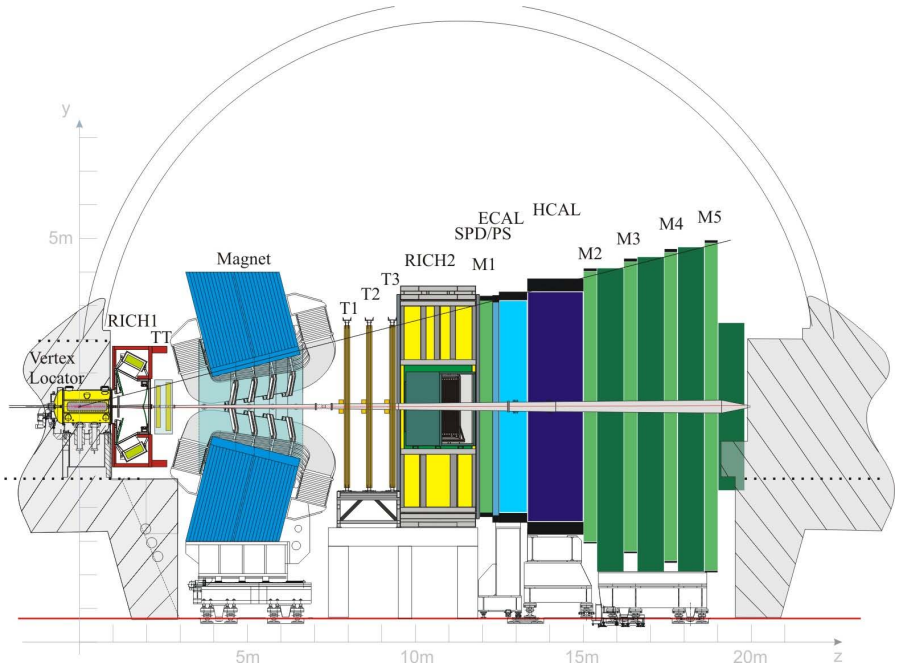

Figure 4.5: The LHCb detector shown side-on. The VELO and the interaction point is to the left followed by the first RICH detector. The magnet is surrounded by the tracking stations with the second RICH detector to the right of the magnet. The calorimeters and the muon stations are towards the rear of the detector [5].

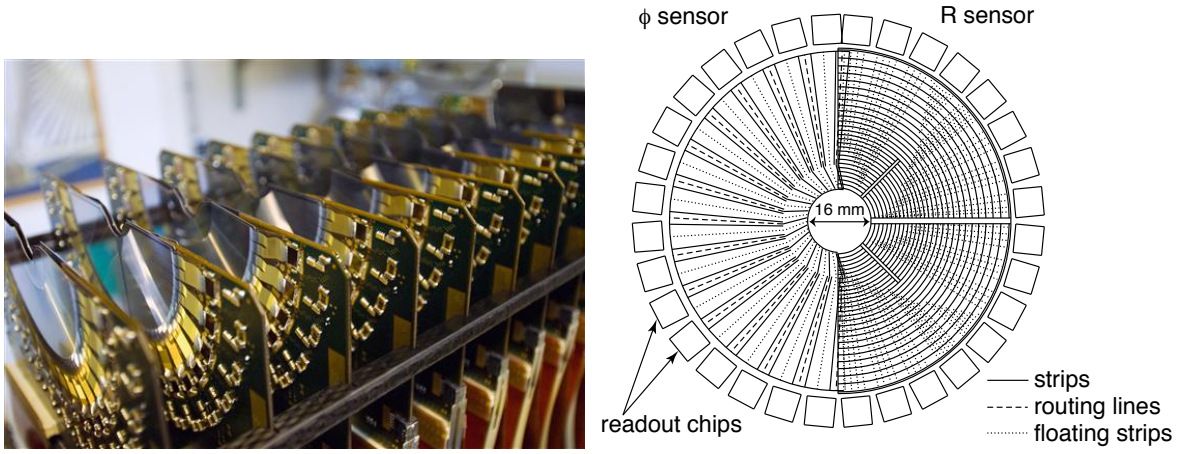

(a) (b)

Figure 4.6: (a) One half of the VELO showing the hemispherical silicon detectors [71] (b) The geometry of the VELO illustrating the $r - \phi$ arrangement of the silicon sensors.

stage, based on information from the calorimeter and muon systems, followed by a software stage which applies a full event reconstruction [70].

4.2.1 Tracking system

The tracking system of LHCb consists of a VErtex LOcator(VELO), four tracking stations and a warm dipole magnet. The VELO is positioned around the interaction points, and there is one tracking station after the VELO and before the magnet, the Tracker Turenscis (TT). Downstream of the magnet, there are three tracking stations, made from an Inner Tracker (IT) and an Outer Tracker (OT).

The VELO provides precise measurements of tracks that originate close to the vertices of the proton-proton interactions. This allows the primary vertices, where the pp interaction takes place, to be distinguished from the secondary and tertiary vertices which are distinct properties of B decays. The VELO is a silicon tracker with modules that provide radial (r) and polar (ϕ) information for tracks. The VELO has a geometrical acceptance from $1.6 < \eta < 4.9$. The arrangement of the sensors into the $r - \phi$ geometry was chosen in order to permit fast reconstruction of the tracks in the trigger, as described in Section 4.3. The geometry of the VELO sensors is illustrated in Fig. 4.6. The VELO was constructed in two halves so that the detector can be moved closer to the interaction point from each

side once the beams are in a stable configuration.

The TT is a 150 cm by 130 cm silicon strip detector which covers the full acceptance of the detector. The IT is placed in the region close to the beam pipe which has a very high occupancy of tracks, as measured in [72], and is made from the same silicon strips as the TT, covering a total area of 120 by 40 cm. The OT encompasses the regions with lower particle density out to 250 cm in the vertical place and 300 cm in the horizontal plane. Each of the OT detectors is made out of straw tubes containing a mixture of argon and CO_2, which were chosen to give a fast read-out time of less than 50 ns and to have a drift co-ordinate resolution of 200 μm.

The LHCb magnet is a warm dipole magnet with an integrated field strength of 4 Tm. The magnet covers the full LHCb acceptance with an area of 250 cm by 300 cm. The magnet was designed to minimise the magnetic field in the RICH detectors and to also maximise the field strength between the tracking stations. This is because the photon detectors used to detect Cherenkov radiation in the RICH detectors are highly sensitive to stray magnetic fields. The bending plane of the magnet is in the horizontal plane and data is taken with both magnet polarities in roughly equal amounts.

The performance of the track reconstruction in LHCb can be evaluated by measuring the tracking efficiency using the 'tag-and-probe' method [73] . The 'tag-and-probe' method takes a fully reconstructed two-body decay, such as $Z^0 \to \mu^+\mu^-$ or $J/\psi \to \mu^+\mu^-$, and looks for the probability that one of the daughters is found (the 'probe') given the reconstruction of the other daughter (the 'tag'). The tracking efficiency overall is around 96% for the data taken in 2011 and is flat in η and in the momentum range from 10 to 200 GeV.

4.2.2 Particle identification

Charged hadron identification

The identification of charged hadrons is provided by two Ring Imaging Cherenkov (RICH) detectors which provide particle identification over a large momentum range from 2 to 100 GeV/c. The RICH detectors distinguish pions, kaons and protons through measurements of the Cherenkov angle of particles which pass through the detector. These particles are

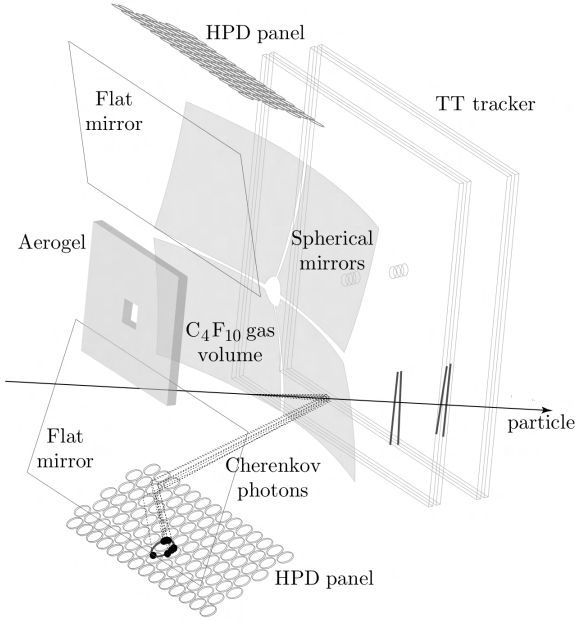

Figure 4.7: An illustration of the geometry of RICH1 showing the path taken by Cherenkov light from the track to the photodiode [74].

travelling faster than the phase velocity of light in the detector gas and therefore emit Cherenkov radiation in a cone around the track. The opening angle of this cone (θ_c) is related to the velocity of the particle through $\theta_c = (n\beta)^{-1}$ where n is the refractive index of the material. A measurement of θ_c combined with momentum information from the tracking system provides a measurement of the mass of the particle. This differentiation of charged particles allows dramatic reductions in the the level of combinatorial background for B decays which have several hadrons in the final state. For $B^0 \to K^{*0}\ell^+\ell^-$, this is of critical importance in the separation of pions and kaons.

The optical system of the RICH detectors consists of two components, a tilted spherical mirror to focus the Cherenkov light and a second flat mirror to guide the light onto two arrays of hybrid photon detectors (HPDs). The geometry of the first RICH detector (RICH1) is shown in Fig. 4.7. RICH1 provides information for particles at high polar angles and at low momentum, from 2 GeV/c to 40 GeV/c. It is placed before the magnet in order to limit the overall volume of gas since the detector covers the full angular acceptance and rotated such that the light is reflected out in the vertical plane. The second RICH detector (RICH2) is placed after the magnet and the downstream tracking detectors. Both RICH detectors use the full information from the tracking system, for RICH1 the

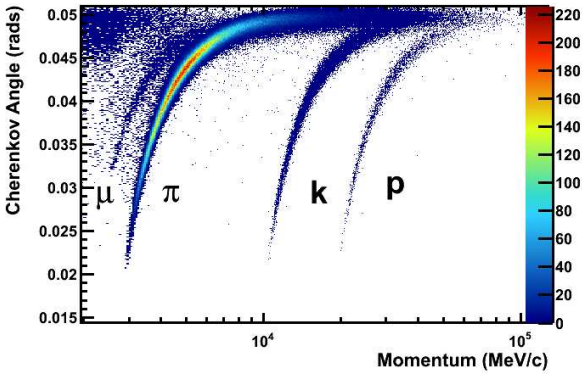

Figure 4.8: The Cherenkov angle for different particles as a function of momentum [69]. It is possible to see the separation for kaons, pions and protons at high momenta along with the separation between muon and pions at low momenta.

tracks are interpolated and for RICH2 the tracks are extrapolated. RICH2 covers the high momentum region ($15-100\,\mathrm{GeV}/c$) and the low polar angular region ($15-120\,\mathrm{mrad}$) and the light is reflected in the horizontal plane. Two different fluorocarbon gases are used as the Cherenkov radiators, C_4F_{10} for RICH1 and CF_4 for RICH2.

The reconstruction of the Cherenkov angle for a photon ring comes from a full analytical solution for the RICH optics based on the mirror alignment and the position of the HPDs. The measured Cherenkov angle can be calculated with respect to the reconstructed track position and the overall resolution on the Cherenkov angles for RICH1 and RICH2 is $1.618 \pm 0.002\,\mathrm{mrad}$ and $0.68 \pm 0.01\,\mathrm{mrad}$ respectively [69]. The Cherenkov angle for different particles from data taken in 2011 can be seen in Fig. 4.8. The RICH detector system not only provides clear separation between kaons and pion, but also between muons with low momenta and high momentum protons.

The particle identification was obtained by calculating the degree to which the track matches the ring for a given mass when compared to the assumption that the track was a pion. This is due to the abundance of charged pions in pp collisions. The likelihood ($\mathcal{L}$) that the Cherenkov angle came from a pion for all the tracks and rings is calculated for a given event. This calculation is changed on a track-by-track basis by testing different mass hypothesis. The measure of particle identification is then the difference between the optimal calculation, i.e. the best set of mass hypotheses for all tracks in the event, compared to the assumption that all tracks are pions. This results in a $\Delta(\log\mathcal{L})$ value

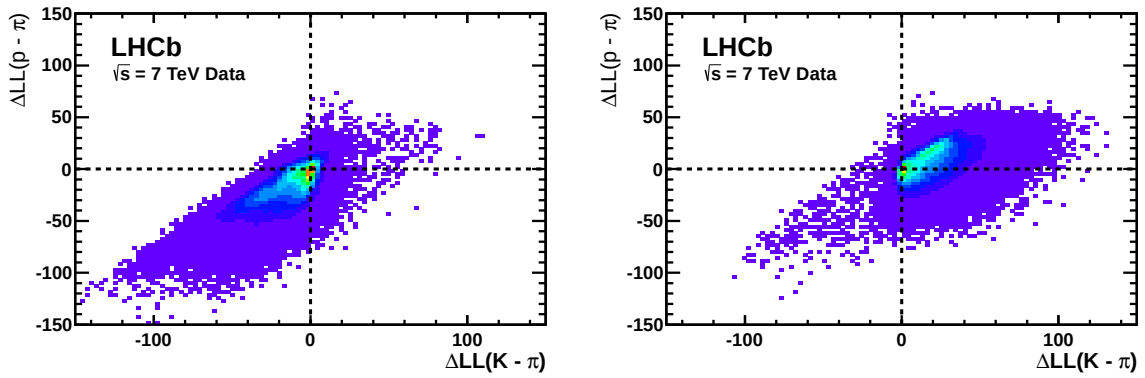

(a) (b)

Figure 4.9: Distributions of (a) pions and (b) kaons showing the separation available when using the $\Delta(\log\mathcal{L})_{K\pi}$ and the $\Delta(\log\mathcal{L})_{p\pi}$ variables. Separation between pions and kaons can be achieved be selecting tracks with a $\Delta(\log\mathcal{L})_{K\pi}$ greater or less than zero [69].

between all tracks in the event. The distribution of $\Delta(\log\mathcal{L})_{K\pi}$ for pions and kaons is given in Fig. 4.9. The resolution on the Cherenkov angle is close to what is expected from simulations of the RICH detectors and is it possible to achieve excellent kaon and pion separation when using the $\Delta(\log\mathcal{L})$ measures.

Muon identification

There are five muon detectors in LHCb which are situated over 15m away from the interaction point. The first muon station is situated before the calorimeters and the remaining four stations are the last elements of LHCb downstream of the interaction point. Each of the rectangular muon stations has projective geometry, meaning that the angular acceptance is equivalent for each station. In the horizontal, bending plane, the muon stations cover from 20 to 306 mrad and in the vertical, non-bending plane cover from 16 to 258 mrad. Each station consists of multi-wire proportional chambers (MWPCs) interleaved with iron absorbers except for the inner part of M1 which is made from gas-electron multiplier (GEM) detectors. Each chamber is filled with a mixture of Argon, CO_2 and CF_4 chosen to maximise charge collection efficiency. The chamber size increases with distance from the beam pipe to ensure there is enough precision in the polar region with high occupancy. Diagrams and a detailed description of the muon detector can be in found in Ref [5].

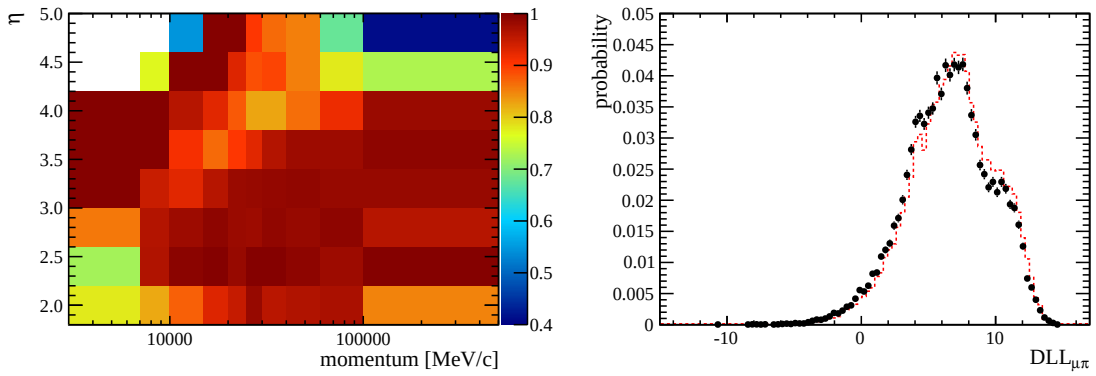

(a) (b)

Figure 4.10: The efficiency of the muon identification in LHCb [77]. In (a) the efficiency of the IsMuon flag as a function of muon momentum and pseudorapidity and in (b) the distribution of the $\Delta(\log\mathcal{L})_\mu$ measure for $B^+ \to J/\psi\ K^+$ for data (points) and simulation (dotted histogram).

Muon identification is provided by matching track hits in the M2-5 stations [75] with tracks projected from the tracking system. This results in a Boolean decision depending on whether the muons satisfy sufficient criteria based on the track momentum. A further measure of muon identification is provided by a $\Delta(\log\mathcal{L})$ variable from the muon system similar to the RICH $\Delta(\log\mathcal{L})$ variables. This $\Delta(\log\mathcal{L})_\mu$ variable tests whether a given track is compatible with the hypothesis of being a muon using clearly identified sources of muons and non-muons to build a discriminant. Information from the muon detectors is used in the trigger to inform a decision at both the hardware and software stages. In the hardware trigger, the presence of hits in M2 and M3 stations are used to look for a hit in M1 to identify a muon candidate to trigger on. The performance of the muon identification has been tested on both 2010 [76] and 2011 data using the 'tag-and-prob' method. The efficiency of the Boolean muon decision (IsMuon) is shown in Fig. 4.10. It is possible to see that there is excellent muon identification efficiency for muons with momenta above 10 GeV and that the $\Delta(\log\mathcal{L})_\mu$ measure has excellent agreement between the data and the LHCb simulation.

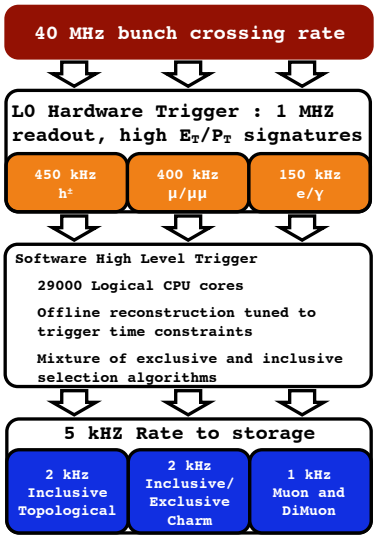

Figure 4.11: An illustration of the LHCb trigger system showing the two distinct stages with the rate of data input and output and the three main trigger line categories [70].

4.3 The LHCb trigger

The trigger in LHCb selects events which contain common signatures of heavy flavour hadron decays which are suitable for subsequent reconstruction. The trigger design is motivated by the infrequency of $b\bar{b}$ production and also the small branching fraction of decays such as $B^0 \to K^{*0}\mu^+\mu^-$, which is of order 10^{-6}. At the LHC collision energy of 7 TeV, the total cross-section of pp interactions when single diffractive processes are included is 50 mb but the $b\bar{b}$ cross-section in the LHCb acceptance is around 75 µb [78]. The trigger is required to reduce the event rate from about 10 MHz to an output rate of around 4 kHz. The LHCb trigger and its performance in 2011 is documented in Ref. [70] and an illustration of the stages of the LHCb trigger can be seen in Fig. 4.11. The LHCb trigger consists of two stages, a hardware stage called Level 0 (L0) and a software stage, the high level trigger (HLT). This separation and the further separation of the HLT into two sub-stages is due to the different timing required to process the information and the amount of information available within the time limit for the trigger stage.

4.3.1 The hardware trigger

The L0 trigger is a hardware trigger because it is required to accept or reject events faster than the time that the sub-detectors can buffer the data. The L0 trigger reduces the incoming rate from 10 MHz to 1 MHz by selecting events with basic characteristics of b-hadron events. These characteristics are either the presence of muons with high transverse momentum (p_{T}), L0Muon, or the presence of large energy deposits in the calorimeters, L0Calo. The L0Muon channel triggers on high p_{T} muons by assigning each quadrant of the muon stations to a different processor. The p_{T} of the muon is calculated through the information from the the M1 and M2 stations and an event is triggered if there is one high p_{T} muon passing through the same quadrant of all five muon stations.

4.3.2 The software trigger

Once events are selected by the L0 trigger, they pass from the detector electronics to a batch system of processors called the Event Filter Farm (EFF). There are 29,000 instances of the HLT running as software processes on the EFF, where they are processed by the HLT algorithms to decide whether the event contains enough interesting information and should be written to tape. Event-by-event, the HLT is required to make a decision in under 30 ms.

The first stage of the HLT (HLT1) performs basic particle track reconstruction. The HLT1Track trigger line triggers on events which pass any L0 decision that contain one prominent track with a high momentum and a high impact parameter. The impact parameter (IP) is defined as the distance between the vector of the reconstructed track and the point of the primary vertex. Alternatively, if the event fired the L0Muon trigger the muon candidate is reconstructed. The HLT1TrackMuon trigger selects the event if the muon candidate had a momentum above 6 GeV/c.

The second software trigger (HLT2) performs further reconstruction of tracks in order to filter events down to a final output rate of around 4 kHz. For the processing of data in 2011, the HLT2 was re-written in order to cope with conditions different to the design requirements. The main trigger in HLT2 is a ‘topological trigger‘ which is designed to select

partially reconstructed b-hadron decays from combinations of 2, 3, or 4 tracks and select on properties of the n-body combination. There are two other triggers which are exclusive muon triggers that select good quality high momentum muons with a significant impact parameter and a large p_{T}, similar to the HLT1TrackMuon trigger. The development of the HLT2 is described in Section 4.5.

4.4 The LHCb software

4.4.1 The LHCb software

The processing of the data from the detector in LHCb is controlled by custom software applications [79]. Each of these software applications is based on the Gaudi framework [80] which provides libraries and a custom API written in C++ and Python to integrate the common requirements and features needed in particle physics software. The organisation of the LHCb software for data analyses can be separated into three different components. First, the trigger software (Moore) runs the HLT and processes the detector output. Then, the reconstruction software (Brunel) performs a complete event reconstruction of events that pass the trigger. This takes into account the understanding of the detector and the conditions under which the detector was run. Finally, the analysis software (DaVinci) runs algorithms that process the fully reconstructed event.

4.4.2 Simulation of the LHCb data

Simulated data is a large part of data analysis due to the rarity of many b-hadron decays of interest. There are two applications that are unique to the simulation of events in LHCb, one to simulate the physics and one to simulate the detector hardware [81]. The physics simulation application, Gauss, contains several different stand-alone programs. The underlying event from the pp collision is simulated using Pythia [82, 83]. Signal decays, for example $B^0 \to K^{*0}\mu^+\mu^-$, are generated specifically using EvtGen [84]. The simulated particles coming from Pythia are also processed with EvtGen to determine at what state they enter the detector. The interactions of the particles with the detector

are simulated using GEANT4 [85,86]. The response of the LHCb detector hardware to the simulated particles is simulated using BOOLE, which both digitises the simulated event data and writes the simulation into a format equivalent to the output of the detector hardware.

There are three different simulations of the LHCb detector used in Chapters 5 and 7. Each of them corresponds to the best simulation conditions known in 2009, 2010 and 2011 and are called MC09, MC10 and MC11 respectively. The first of these, MC09 corresponds to the best estimate of the detector performance before the running of the LHC and the start of data-taking. This was only used in Section 4.5 for work performed at the end of 2010. The second of these simulation configurations, MC10, contains significant improvements applied as a result of information from the 2010 period of data-taking. These come from adjustments made to the trigger, the reconstruction and the analysis software along with improvements to the underlying simulation. The final simulation configuration, MC11, was defined after the end of data-taking in 2011 and uses the best information available at that point in time. The analyses of $B^0 \to K^{*0}\mu^+\mu^-$ presented in Chapter 5 use both MC10 and MC11 simulation based on what was available at the time.

4.4.3 Data-simulation agreement

The agreement between the data and the LHCb simulation is generally very good but there are several significant differences which are the IP resolution, the particle identification for hadrons and the occupancy of the detector. There are also minor effects for which the disagreement is smaller, including the relative tracking efficiency and the particle identification for muons. These known differences are corrected for using a variety of methods depending on the type of correction. The IP resolution is corrected within the simulation itself, whereas the particle identification for hadrons is corrected after the events are simulated. The difference in event occupancy, tracking efficiency, trigger efficiency and the muon identification are corrected for by applying weights to each simulated event.

The IP resolution for pions from data and from MC10 simulation as a function of

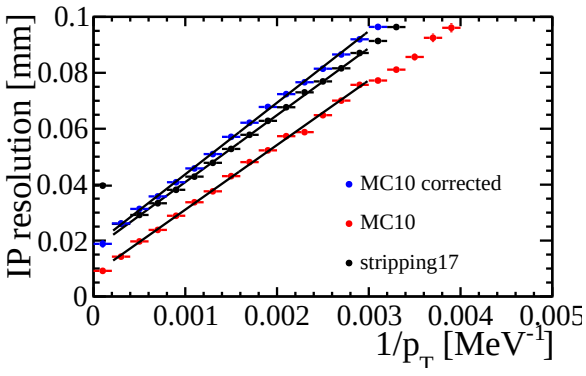

Figure 4.12: The resolution of the IP in x as a function of inverse p_{T} for pions from data and simulation. The data, labelled 'stripping17', is processed with two reconstruction versions used in 2011 and the two simulation versions are MC10 and MC11.

inverse p_{T} are shown in Fig. 4.12. It is possible to see that the IP resolution is consistently different for both versions of the simulation. This effect comes from the way the scattering of particles within the material, both in the RF foils and the gas inside the VELO, is simulated. Contributing factors include the exact description of the amount of material in the VELO in terms of the shape of the RF foils, the alignment of the VELO and the position of the simulated primary vertex.

The IP resolution as a function of x or y for tracks from the primary vertex can be parametrised using a linear function

$$f_{(x/y)\mathrm{data}}(1/p_{\mathrm{T}}) = a_{(x/y)}\ (1/p_{\mathrm{T}}) + b_{(x/y)}\,, \tag{4.1}$$

where a and b are coefficients found for the IP resolution in x and y. The tracks in the simulation can be corrected by smearing the reconstructed track. The smearing function is a Gaussian with a zero mean and with the width defined by the difference of the IP resolution for the data and the simulation,

$$\sigma_{diff}^{(x/y)} = \sqrt{f^2_{(x/y),\mathrm{data}}(1/p_{\mathrm{T}}) \ - \ f^2_{(x/y),\mathrm{sim}}(1/p_{\mathrm{T}})}\,. \tag{4.2}$$

The smeared track is subsequently processed by the reconstruction software which recalculates the new momentum vector for the track.

Another significant difference between the data and the simulation is the $\Delta(\log\mathcal{L})$

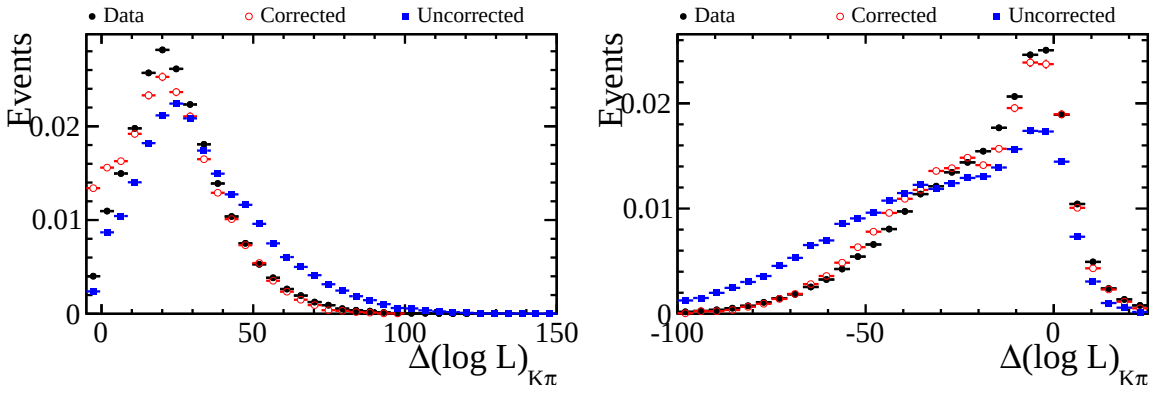

Figure 4.13: The $\Delta(\log\mathcal{L})_{K\pi}$ distributions for (a) kaons and (b) pions to illustrate the difference between data and simulation. The $B^0 \to J/\psi\, K^{*0}$ data is shown in black, the uncorrected $B^0 \to J/\psi\, K^{*0}$ simulation in blue and the corrected simulation in red.

value returned from the pattern recognition in the RICH detectors. The difference here is an artifact of the lower average occupancy of each simulated event than an average data event. This is because the higher number of tracks produces more Cherenkov radiation which is related to the overall saturation of the HPDs and subsequently the ability for the reconstruction software to match Cherenkov rings to tracks. The $\Delta(\log\mathcal{L})$ value for each simulated track was obtained from a sample of high purity $D^{*+} \to D^0\ \pi^+$ (and charge conjugate) decays, where the D^0 can be tagged using the π^+ from the D^{*+}. This allows a clean sample of kaons and pions to be selected. The distribution of the $\Delta(\log\mathcal{L})_{K\pi}$ for kaons and pions from $B^0 \to J/\psi\, K^{*0}$ events before and after the correction was applied is shown in Fig. 4.13. It can be seen that there is a significant difference between the $\Delta(\log\mathcal{L})$ distributions for data and uncorrected simulation but that there is significantly better agreement after correction.

The third major difference between the data and the simulation is in the overall event occupancy, defined by the number of tracks passing through the detector per event. This comes from both the generators used to simulate the proton interaction and also from the description of the material in the detector in the simulation. The simulation is corrected by re-weighting the simulation by the relative difference between data and simulation in terms of the number of tracks per event. The ratio between data and simulation is given in Fig. 4.14. The data/simulation ratio is binned per 25 tracks below 400 tracks and in one single bin above 400 tracks. This is because there is not enough simulation with an

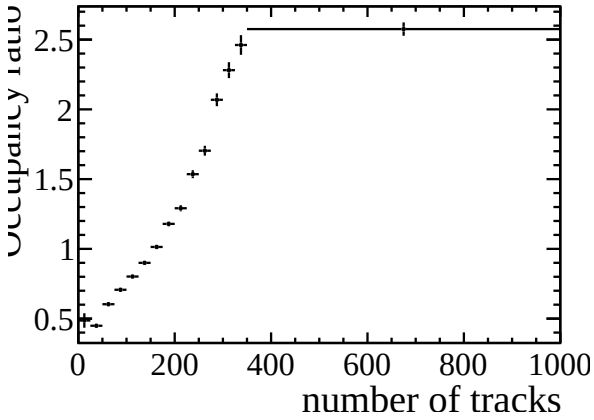

Figure 4.14: The relative event occupancy measured by the number of tracks per event for selected $B^0 \to J/\psi K^{*0}$ events from data and simulation. The data is from the $1.0\,\mathrm{fb}^{-1}$ sample and the simulation is from MC11.

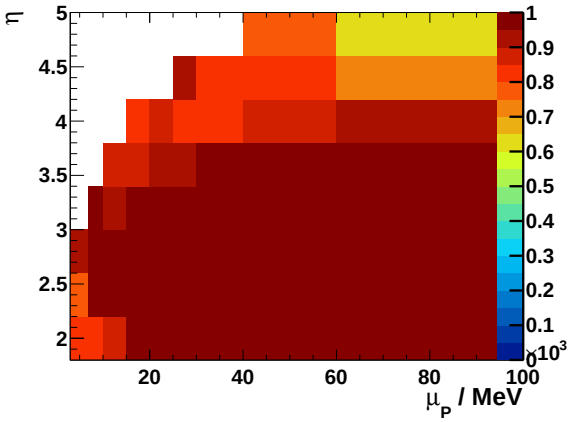

Figure 4.15: The relative muon identification efficiency between data and simulation for muons from $J/\psi \to \mu^+\mu^-$ events identified using the 'tag-and probe' method [76]. The data is from the $1.0\,\mathrm{fb}^{-1}$ sample and the simulation is MC11.

occupancy of above 400 tracks to accurately correct the simulation on a finer level.

The efficiency of muon identification in the data and the simulation is determined by selecting a good sample of muons from $J/\psi \to \mu^+\mu^-$ events using the 'tag-and-probe' method. There are two muon identification parameters considered. Firstly `IsMuon`, which comes from the muon stations and the relative efficiency for the muon identification flag is shown in Fig. 4.15. It can be seen that there is good agreement between the data and simulation for the muon identification flag. The relatively uniform values for the relative efficiency allows each data event to be weighted based on the relative efficiency as a function of the momentum of both muons. The $\Delta(\log \mathcal{L})$ value for muons is obtained from the data in a similar way to the hadron particle identification but using selected muons

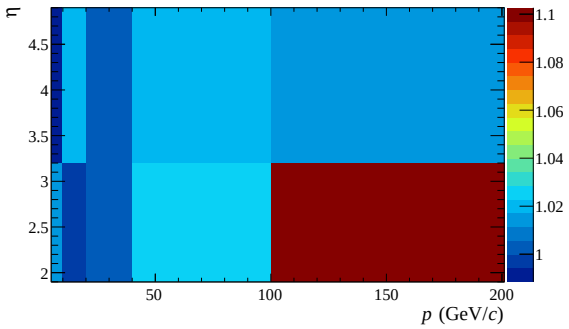

Figure 4.16: The ratio of tracking efficiency between data and simulation for pions from $K^0_S \to \pi^+\pi^-$ decays selected from the $1.0\,\text{fb}^{-1}$ data and MC11 simulated events [87].

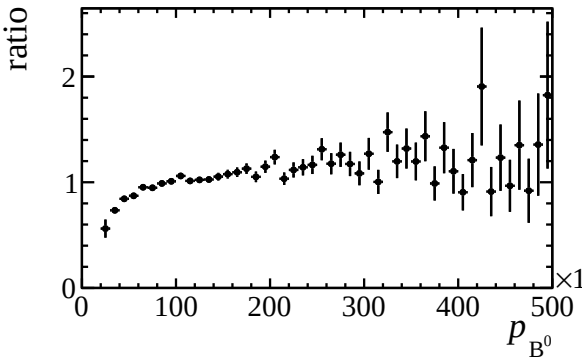

Figure 4.17: The ratio of the B^0 momentum distribution for selected $B^0 \to J/\psi\, K^{*0}$ events from the $1.0\,\text{fb}^{-1}$ data sample and from MC11 simulated events. It is possible to see that the ratio diverges from unity at both low and high momenta.

from the $J/\psi \to \mu^+\mu^-$ sample.

The relative tracking efficiency for all tracks in the LHCb detector can be determined using the 'tag-and-probe' method on pions from a high purity sample of reconstructed $K^0_S \to \pi^+\pi^-$ candidates. The relative efficiency between data and simulation can be seen in Fig. 4.16. The simulated events are weighted by the relative efficiency for each of the four tracks in the decay.

After all of the above corrections and weights have been applied, there are residual differences between data and simulation in the momentum spectrum of the B^0. The ratio of B^0 momentum between data and simulation for $B^0 \to J/\psi\, K^{*0}$ events from data and simulation is shown in Fig 4.17. The B^0 momentum spectra is corrected by weighting the simulated events by the ratio of data when compared to simulation. The total weight

given to a $B^0 \to K^{*0}\mu^+\mu^-$ simulated event, for example, is

$$\begin{aligned}\omega(P_{\mu^-}, P_{\mu^+}, P_\pi, P_K, P_{B^0}) = \omega^{\mu^-}_{\text{IsMuon}}(P_{\mu^-}) \times \omega^{\mu^+}_{\text{IsMuon}}(P_{\mu^+}) \\ \times \omega^{\pi}_{trackeff}(P_\pi) \times \omega^{K}_{trackeff}(P_K) \\ \times \omega^{\mu^-}_{trackeff}(P_{\mu^-}) \times \omega^{\mu^+}_{trackeff}(P_{\mu^+}) \\ \times \omega_P(P_{B^0})\,. \end{aligned} \tag{4.3}$$

4.5 Development of the trigger for $B^0 \to K^{*0}\mu^+\mu^-$

4.5.1 Introduction

The development of a new LHCb trigger for 2011 was motivated by the significant change in the operating conditions of both the LHC and LHCb between the 2010 and 2011 running periods. With the successful operation of the detector at the design luminosity in 2010, the decision was taken to go beyond this to counteract the reduced beam energy and number of proton bunches. This was in order to acquire enough integrated luminosity for the LHCb measurements of key channels, such as $B^0_s \to \mu^+\mu^-$ and $B^0 \to K^{*0}\mu^+\mu^-$ [88], to remain competitive with CMS in 2011. This increase in the luminosity required the redevelopment of the trigger in order to keep a high efficiency for the main signal channels, chosen to represent the physics programme of LHCb, whilst keeping the rate of background events taken at a reasonable level.

The design of the LHCb trigger in 2010 contained an inclusive topological trigger [5] which was designed to select hadronic B decays, as well as several exclusive trigger algorithms to select particular decays such as $B^0 \to K^{*0}\mu^+\mu^-$. The exclusive trigger algorithms were unworkable for the expected conditions for 2011 running due to the time taken to process an event in the trigger and the rate at which the exclusive trigger lines accepted background events.The development of a muonic inclusive trigger was proposed since this was advantageous for both electroweak penguin decays such as $B^0 \to K^{*0}\mu^+\mu^-$ and semi-leptonic decays such as $B \to D\mu\nu$.

The requirements for a new inclusive trigger in LHCb were defined so that the new

trigger should reject sufficient background events, keep a good enough signal efficiency when compared to the previous exclusive triggers and minimise the acceptance effect for the distribution of the signal decays. The rejection rate is correlated to the bandwidth in the trigger allowed for the trigger line. The new inclusive trigger would be allocated 200 Hz of bandwidth out of a total of 500 Hz available for the topological triggers, corresponding to a background rate of around 0.2% when running at an average number of interactions per bunch crossing of $\mu = 2.5$.

The hadronic topological trigger is an inclusive trigger which selects a 2, 3 or 4-track potential 'B' candidate by requiring candidates to have kinematic properties common to B decays. They include the invariant mass, momentum, transverse momentum and the daughter track impact parameter. The electroweak penguin decays, such as $B^0 \to K^{*0}\mu^+\mu^-$ and $B_s^0 \to \phi\mu^+\mu^-$, have two muons and two hadrons in their final state. The high momentum requirements of muons to pass the LHCb reconstruction mean that, on average, in the final state there are higher momentum muons then hadrons. The semi-leptonic B decays such as $B^0 \to D^{(*)}\mu\nu$ have similar kinematics but the hadrons which come from a intermediate D meson have a longer lifetime. This allows the trigger to have stricter requirements on the muon but needs looser requirements on the quality of the B vertex and on the invariant mass of the n-body candidate as at least one of the daughter particles is missing.

Simultaneously, a multi-variate topological trigger (HLT2Topological) was also developed [89, 90] using a Boosted Decision Tree (BDT) [91–93]. In order to allow a BDT to select generic b-hadron events in the trigger, the input variables were discretised to reduce the dependence of the trigger efficiency on the data used to train the BDT. A muon-specific version of the BDT trigger was developed in parallel to the HLT2MuNTrack lines, called the HLT2MuTopo trigger lines. This ran a similarly trained BDT but with the added benefit of including information about the muon candidate in the n-body combination.

In order to develop a trigger line for analysis of general B decays, consideration must be given to the distribution of events which pass the trigger. The angular analysis of $B^0 \to K^{*0}\mu^+\mu^-$ is sensitive to the acceptance effect caused by event reconstruction and

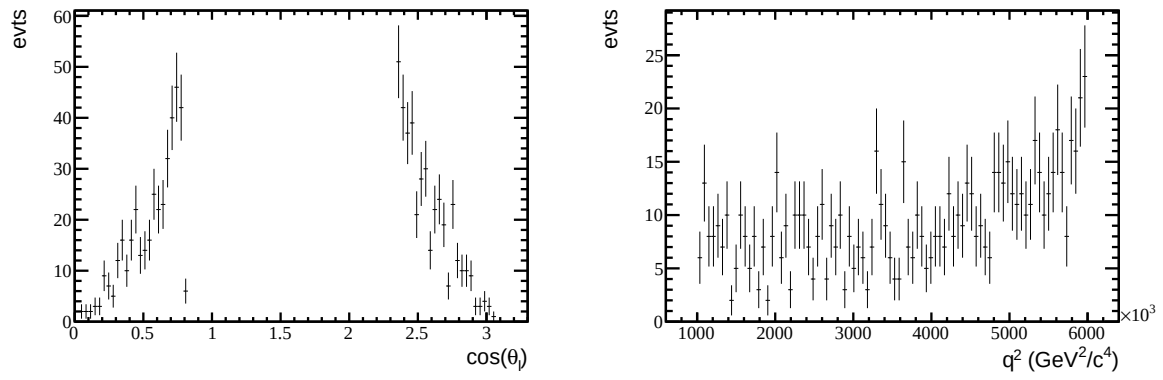

(a) (b)

Figure 4.18: The (a) $\cos\theta_l$ and (b) q^2 distribution of the selected $B^0 \to K^{*0}\mu^+\mu^-$ simulated events used to optimise the trigger efficiency. These events are the most sensitive to acceptance effects and hence provided a ideal sample to optimise against.

selection [94, 95]. Measurements of the semi-leptonic decays requires a relatively unbiased lifetime and are hindered by cuts which have a non-trivial lifetime acceptance for the D mesons. The data used to develop the trigger for muonic B decays are detailed in Section 4.5.2 and the resultant trigger configuration is given in Section 4.5.3. The results on testing the trigger on simulation and background data are shown in Section 4.5.4.

4.5.2 Datasets

The datasets used in the optimisation of the trigger consist of samples of simulated data to represent the signal decays and a sample of data events recorded to represent the expected background events. The signal sample for $B^0 \to K^{*0}\mu^+\mu^-$ consists of two sets of simulated events which have passed the LHCb reconstruction. The first set has the expected offline selection applied and the second set contains events with extreme values of $\cos\theta_l$. These the events are particularly difficult to select since the extreme value of $\cos\theta_l$ implies one low-momentum (soft) muon. These extreme $\cos\theta_l$ events also give maximum sensitivity to a measurement of $A_{\rm FB}$. The conditions of the simulation used are the configuration available at the end of 2010 (MC10). The $\cos\theta_l$ and q^2 distributions of this sample are shown in Fig. 4.18.

Two signal samples were used to evaluate the efficiency of the trigger on semi-leptonic B decays. These were one sample of $B \to D\mu\nu$ simulated events and one sample of $B \to$

$D_s^+\mu\nu$ simulated events. These samples were generated using the latest conditions known before the start of data-taking, in the configuration MC09. Other samples of selected simulated events for $B_s^0 \to \phi\mu^+\mu^-$ and $B_s^0 \to J/\psi\,\phi$ were provided to test and ensure that the trigger was suitably inclusive.

The background data consisted of data events from a preparatory run of the LHC in 2010 which was expected to be representative of the conditions for the 2011 data-taking period. This run has an average number of 2 interactions per bunch crossing and all the events in the data pass the L0 trigger and the HLT1 trigger, giving data which is representative of the type of events expected to be input to HLT2.

4.5.3 Trigger configuration

The trigger lines were written to minimise the time taken to process the event and the time taken to make a decision. The first algorithmic optimisation was to compare all of the tracks used in HLT2 with the track(s) that passed the HLT1 trigger lines. Tracks in HLT2 are filtered based on whether both the tracks match, i.e they were created from the same hits in the tracking system. This ensures consistency between the trigger lines and excludes mis-matched tracks. The second stage is to make up-front cuts on the properties of the tracks to reduce the combinatorics to make the candidates. A last algorithmic choice was to only form $(n+1)$-body candidates from candidates that pass the n-body criteria. This means that 3(4)-body candidates are made from permissible 2(3) track combinations with an extra track added ensuring that the number of candidates tested is minimised.

The number of different requirements and different priorities along with the time constraints of the trigger development lead to manual optimisation of the kinematic cuts in the HLT2MuNTrack trigger. Firstly, a basic set of cuts was identified that reduced the background rate to a sufficiently small level. Secondly, additional cuts were introduced to maximise the signal efficiency on electroweak penguin and semi-leptonic decays. Lastly, the full range of cuts were adjusted to minimise the acceptance effect on the $B^0 \to K^{*0}\mu^+\mu^-$ signal decay. Each of the kinematic quantities used to optimise the trigger selection are discussed below.

- The minimum p_{T} of the tracks was required to be over 600 MeV and the minimum p_{T} of the muons was required to be above 800 MeV. The higher p_{T} requirement for the muons was based on the average kinematics for the the signal decays. This was minimised to reduce any angular acceptance effect on $B^0 \to K^{*0}\mu^+\mu^-$ tracks.

- The sum of the p_{T} of all of the particles is a measure which allows for a more flexible combination where one high p_{T} track can compensate for several low p_{T} tracks. This is advantageous in both electroweak penguin and semi-leptonic B decays where there is a distinct separation between the muon kinematics and the hadronic kinematics.

- The invariant mass of each track combination was required to be above the mass of the D mesons in order to ensure decays with a b quark are selected.

- The track χ^2 parametrises the quality of the track fit to the hits in the tracking stations. For the reconstruction software used in 2011, a maximum track χ^2 of 4 per degree of freedom was sufficient to remove the majority of ghosts and clone tracks.

- The flight distance χ^2 is defined by the difference in χ^2 value of the primary vertex fit when the tracks of the candidate are added to it. This is a good measure for discriminating between combinations consisting of prompt and non-prompt tracks.

- The direction angle, (δ_{PV}), is defined by the angle between the track direction and the related primary vertex, is a good measure to determine whether the tracks of interest originate from the expected primary vertex. The tracks from signal decays was found to mostly be below 10(15) mrad for tracks with (without) muon identification. This is because of the harder kinematics of muons as opposed to the hadrons.

- The distance of closest approach (DOCA) between the direction vector of the track and the primary vertex is another good measure to separate signal and background events and is highly correlated with the direction angle. A limit of a maximum distance of closest approach of 12 mm was set for all tracks to pass the trigger.

- The IP χ^2 is a similar quantity to the distance of closest approach and also encompasses the error information from the resolution on the primary vertex.

Table 4.1: The kinematic and topological cuts used in the HLT2MuNTrack trigger lines.

Kinematic quantity	2-body	3-body	4-body
M_{corr}^{max}(GeV)	7	7	7
M_{corr}^{min}(GeV)	0	4	4
$\sum p_{\mathrm{T}}$ (GeV)	2	2	2.6
max p_{T} (GeV)	1.5	1.5	1.5
track p_{T} (MeV)	600	600	600
muon p_{T} (MeV)	800	800	800
momentum (GeV)	5	5	5
$m_{\mu+(1,2,3)tracks}$(GeV)	2	3	4
IP χ^2	16	16	16
track χ^2	4	4	4
flight distance χ^2	36	36	36
$\cos\delta_{\mathrm{PV}}$ (track) (rad)	15	15	15
$\cos\delta_{\mathrm{PV}}$ (μ) (rad)	10	10	10
DOCA(mm)	0.12	0.12	0.12

- The corrected mass is a quantity which attempts to balance the p_{T} of the particles in the n-body candidate with the p_{T} measured between the primary and secondary vertex [96]. This correction to the n-body mass is needed as the n-body combination is predominately a subset of the daughters from the B decay.

A list of the cuts used in the each of the three HLT2MuNTrack trigger lines are given in Table 4.1.

4.5.4 Results and Discussion

There were three performance measures used to test the quality of the new trigger lines. These are the signal efficiency, the expected rate of background rejection and the time taken to run the trigger lines. The order within which each of the cuts were applied was also adjusted to minimise the time spent on the quantities which require the calculation of both a primary vertex and a secondary vertex compared to simple kinematic cuts. The HLT2 forward tracking was timed to take a total of 44 ms. On top of this, the HLT2Mu1Track line took 15 ms, the HLT2Mu2Track line took 0.12 ms and the HLT2Mu3Track line took a further 0.07 ms. These timings are well within the limit of 20 ms limit for these lines.

A break down of the results for the different HLT2MuNTrack lines is given in Ta-

Table 4.2: The trigger efficiency of selected simulated signal samples and of background data for the final configuration of the HLT2Mu1Track and HLT2Mu2Track lines along with the HLT2MuTopo lines and full HLT2 trigger.

Sample	HLT2Topological	HLT2MuNTrack	HLT2MuTopo	HLT2
Selected K*$\mu^+\mu^-$	79.8 %	79.6 %	79.3 %	92.9 %
Reconstructible K*$\mu^+\mu^-$	55.9 %	57.3 %	54.3 %	85.5 %
$D\mu\nu$	65.9 %	64.3 %	67.6 %	84.3 %
$\phi\mu^+\mu^-$	76.1 %	80.0 %	75.9 %	95.1 %
Background (train)	0.9 %	0.47 %	0.27 %	5.2 %
Background (test)	0.8 %	0.57 %	0.27 %	5.1 %

Table 4.3: The breakdown of trigger efficiency by line on $B^0 \to K^{*0}\mu^+\mu^-$, semi-leptonic and the background rejection rate.

Line	$B^0 \to K^{*0}\mu^+\mu^-$	$B \to D\mu\nu$	Background Rate
HLT2MuTopo 2 Body	71 %	52 %	0.3 %
HLT2MuTopo 3 Body	69%	56 %	0.1 %
HLT2MuTopo 4 Body	42%	21 %	0.1 %
HLT2MuNTrack 1	73 %	47 %	0.3 %
HLT2MuNTrack 2	64 %	62 %	0.3 %
All HLT2MuTopo	79.3 %	67.6 %	0.27 %
All HLT2MuNTrack	79.6 %	67.3 %	0.47 %

ble 4.2. The efficiency of each of the trigger lines in development per line on the two main signal samples along with the background rate is given in Table 4.3. The efficiency of the HLT2MuNTrack lines is comparable to the HLT2MuTopo for the main decay $B^0 \to K^{*0}\mu^+\mu^-$ but the HLT2Mu2Track line is the most efficient trigger on the semi-leptonic signal sample. However, the HLT2MuNTrack lines select more background than the equivalent HLT2MuTopo lines.

The efficiency of each of the n-body combinations for the HLT2MuNTrack trigger lines as a function of $\cos\theta_l$ and q^2 for offline selected $B^0 \to K^{*0}\mu^+\mu^-$ simulation are given in Fig 4.19. It is possible to see that there is no dramatic acceptance effect in q^2 but a slight bias in the lower region of $\cos\theta_l$. The total efficiency of the HLT2MuNTrack and the HLT2Topological lines is shown in Fig 4.20. The HLT2Topological containing the muon-specific HLT2MuTopo has a comparable efficiency on simulated $B^0 \to K^{*0}\mu^+\mu^-$ with a better acceptance effect in $\cos\theta_l$. The improved performance of the HLT2Topological when compared to the HLT2MuNTrack lines comes from the gain in performance when using a multi-variate algorithm. This allows advantage to be taken of correlations between

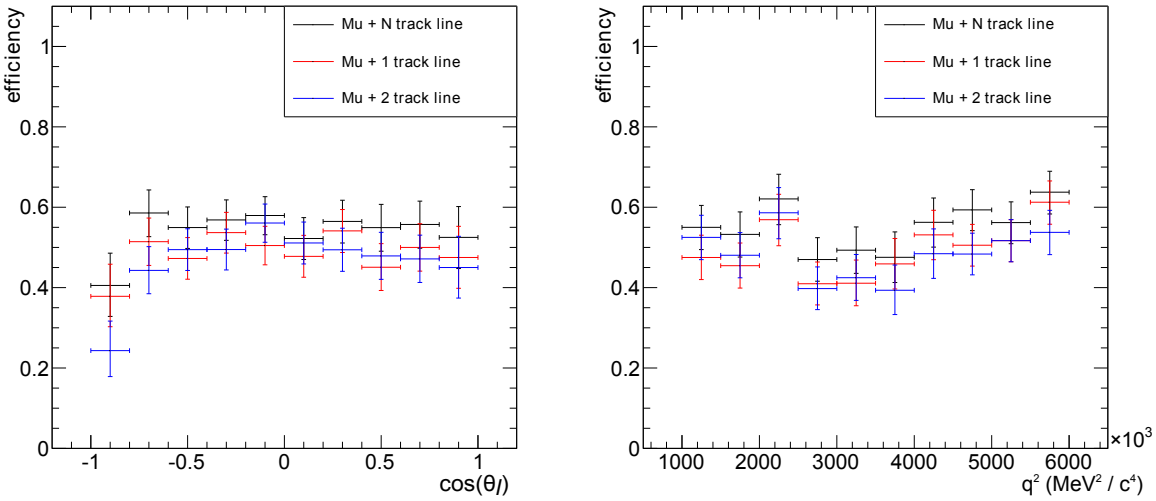

Figure 4.19: The $\cos\theta_l$ and q^2 efficiency of the each individual HLT2MuNTrack line. There is a slight bias in $\cos\theta_l$ but not significant effects in q^2. The drop in efficiency at low $\cos\theta_l$ is also due to the low numbers of simulated statistics in that region.

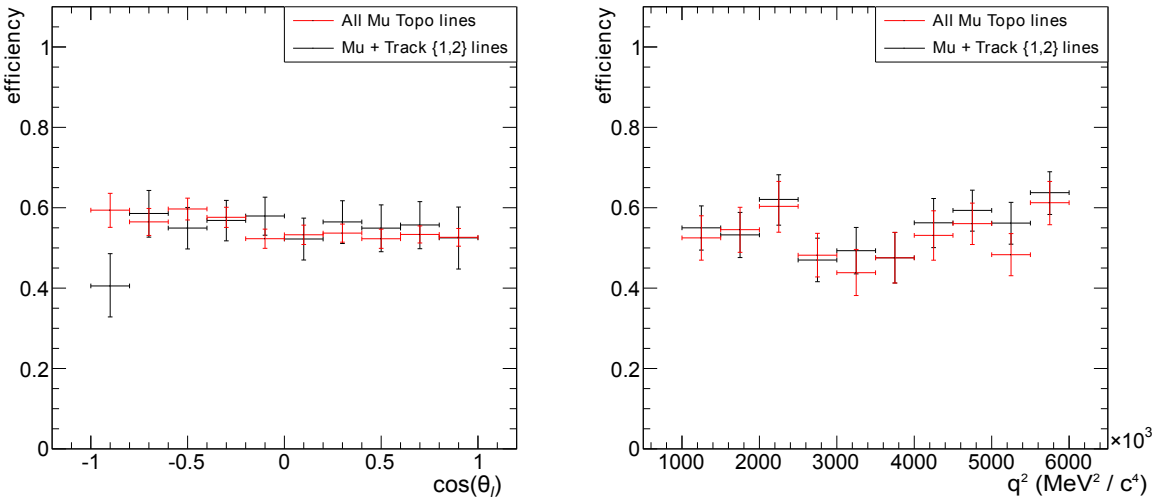

Figure 4.20: A comparison of the efficiency as a function of $\cos\theta_l$ and q^2 efficiency of the HLT2MuNTrack and the HLT2Topological lines.

the kinematic variables for each of the daughters and of the n-body track combinations.

4.6 Conclusions

The LHCb detector is a dedicated B-physics experiment at the LHC designed to reconstruct rare b quark decays. The LHCb detector was designed to be able to clearly separate primary and secondary vertices, reconstruct the tracks from $p-p$ collisions with high resolution and to clearly identify charged hadrons and muons using dedicated detectors. The sub-detectors comprising LHCb and their excellent performance are presented, the result of which has enabled an integrated luminosity of $1.0\,\mathrm{fb}^{-1}$ to be collected throught 2011.

Simulation of b quark decays within the LHCb detector is an important part of understanding the detector. This allows the ability of the detector to select of rare B decays to be evaluated and the effect such a selection has on the resulting data. The organisation of the LHCb software and the simulation is described along with the main differences between LHCb data and simulation. Different methods to correct the IP resolution, the particle identification, the detector occupancy and the tracking efficiency are shown. These methods allow the simulation to be corrected to accurately represent the $B^0 \to K^{*0}\mu^+\mu^-$ candidates in the data.

The change in data-taking conditions between 2010 and 2011 required a redevelopment of the trigger used to select b quark decays in LHCb. Two options were explored, a cut-based algorithm and a multi-variate algorithm that combine 2,3 and 4 body combinations of track to form a potential B candidate. These triggers use general features of the B decays and basic reconstruction to selects n-body combinations of basic tracks.The performance of the multi-variate trigger was shown of be better than the cut-based trigger. This is due to the ability of the multi-variate trigger to use more correlations between the variables provided than the cut-based selection and this was the trigger selected for use in the 2011 data-taking period.

Chapter 5

The angular analysis of $B^0 \to K^{*0}\mu^+\mu^-$

This chapter contains the work of the LHCb collaboration. The author contributed to Section 5.4 and Section 5.6. The results in this chapter were published in Refs [1] and [2]. The first analysis is presented as the author contributed to the acceptance correction and the results were the first measurements of electroweak penguins at LHCb.

5.1 Introduction

The angular analyses presented in this chapter are the first and second angular analyses of $B^0 \to K^{*0}\mu^+\mu^-$ performed at LHCb. The first angular analysis concentrates on measuring the values of $A_{\rm FB}$, $F_{\rm L}$ and the differential branching fraction in seven bins of dimuon mass. This was performed on the first $0.38\,{\rm fb}^{-1}$ of data recorded at LHCb in 2011. The second angular analysis is an extension of the first to encompass the angular observables dependent on ϕ. This allowed the measurement of $S_{3,}$ S_9 and A_9 as well as the transverse angular observables, $A_{\rm T}^{\rm Re}$, $A_{\rm T}^{\rm Im}$ and $A_{\rm T}^{2}$. This analysis uses the complete dataset of $1.0\,{\rm fb}^{-1}$ recorded in 2011 at LHCb.

Both analyses followed three main steps to obtain the values of the angular observables and the differential branching fraction in bins of q^2. A cut-based selection and a multivariate discriminant are used to select signal $B^0 \to K^{*0}\mu^+\mu^-$ candidates from the data.

Subsequently, the selected $B^0 \to K^{*0}\mu^+\mu^-$ candidates were corrected for the acceptance effect introduced from their reconstruction and selection. Finally, the weighted data was simultaneously fitted with a PDF describing the B^0 invariant mass distribution and the angular distribution to determine the results.

This chapter follows the structure of the analysis in a similar manner. The data for each analysis and the simulation used in this analysis are described in Sec. 5.2. The selection of the $K\pi\mu^+\mu^-$ candidates for both analyses is described in Sec. 5.3. The two different methods used for the acceptance correction are detailed in Sec. 5.4. The PDF used to determine the angular observables for each analysis and the method of determining the errors is described in Sec. 5.5. The estimates of the contribution from systematic effects are detailed in Sec 5.6. The results for the angular observables and for the differential branching fraction from both angular analyses are presented in Sec. 5.7.

5.2 Data samples

This section describes the data and simulation samples used in the angular analysis of $B^0 \to K^{*0}\mu^+\mu^-$. The second set of data is a superset of the first but processed with a later version of the reconstruction and event selection software. There are two distinct versions of simulated events, one representing the data-taking conditions and detector knowledge at the end of 2010 (MC10) and the second representing the equivalent conditions for the 2011 data-taking period (MC11). The MC11 samples were only used in the second angular analysis.

5.2.1 Data

Sample 1 - 0.38 $\mathbf{fb^{-1}}$

The dataset used in the first analysis of $B^0 \to K^{*0}\mu^+\mu^-$ at LHCb was collected between March and June 2011. The data was taken at a centre-of-mass energy of $\sqrt{s} = 7\,\text{TeV}$ using both polarities of the LHCb magnet. The data sample corresponds to an integrated luminosity of $0.38\,\text{pb}^{-1}$. The vast majority of data was taken in the trigger configuration

using the multi-variate topological trigger with smaller samples being taken in almost identical conditions throughout the year. The data are reconstructed with reconstruction version `Reco10`, as described in Section 4.4, and stripped with version `Stripping13b`, described in detail below.

Sample 2 - 1.0 fb^{-1}

The dataset used in the second angular analysis of $B^0 \to K^{*0}\mu^+\mu^-$ at LHCb was the full dataset from the 2011 run of the LHC. This corresponds to an integrated luminosity of $1.0\,\mathrm{fb}^{-1}$ of data at a centre-of-mass energy of $\sqrt{s} = 7\,\mathrm{TeV}$. The trigger configuration was consistent throughout 2011 for the trigger lines used to select events in the angular analysis. The reconstruction and the event selection are consistent for the whole dataset. The particular versions of the reconstruction and event selection software used are `Reco12` and `Stripping17` respectively.

5.2.2 Simulation

The samples of simulation used in the angular analysis were generated as outlined in Sec. 4.4. The generation and reconstruction conditions of each sample are described in detail below. To ensure that the correct efficiency is calculated from the simulation, the properties of the simulation are compared with large data control samples. In order to update the simulations to agree with the best knowledge of the detector in 2011, the set of corrections derived in Section 4.4.3 was checked using $B^0 \to J/\psi\, K^{*0}$ data and simulation.

MC10

The samples of MC10 that were used for both angular analyses were simulated to be a close approximation of the data-taking conditions in 2010. In order to use this simulation with the 2011 data, an updated version of the trigger and event selection software was re-run over the simulated events. The sample of simulated events generated in the MC10 configuration was of $B^0 \to K^{*0}\mu^+\mu^-$ events. This sample was generated using a decay model such that the events are flat in phase space and therefore have a uniform distribution

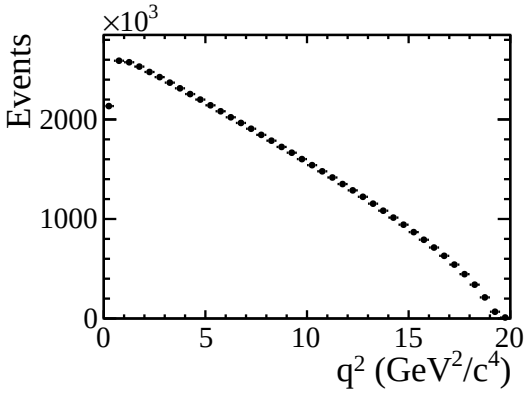

Figure 5.1: The q^2 distribution of simulated $B^0 \to K^{*0}\mu^+\mu^-$ events generated using a phase space model. The phase space available for the decay decreases towards high q^2. The distribution of events is uniform in $\cos\theta_l$, $\cos\theta_K$ and ϕ.

in $\cos\theta_l$, $\cos\theta_K$ and ϕ. The distribution of phase space events in q^2 decreases as the size of the phase space available for the decay at higher q^2 values gets smaller. The generator level distribution for q^2 is shown in Fig. 5.1. This sample of simulated events was used to calculate the efficiency to correct for the acceptance effects, as described in Sec. 5.4.

MC11

The samples of MC11 that were used in the second angular analysis of $B^0 \to K^{*0}\mu^+\mu^-$ consist of several signal decay modes, including $B^0 \to K^{*0}\mu^+\mu^-$, $B^0 \to J/\psi\, K^{*0}$, $B^+ \to K^+\mu^+\mu^-$, $B^+ \to K^{*+}\mu^+\mu^-$, $B_s^0 \to \phi\mu^+\mu^-$ and $\Lambda_b^0 \to \Lambda^*(1520)\mu^+\mu^-$. The B decays were generated using the `BTOSLLBALL` [97] model from EvtGen [84] to model the $b \to s$ FCNC decay. This model calculates the helicity amplitudes for the $B^0 \to K^{*0}$ transition using the form factors calculated with the QCD sum rule using Standard Model parameters. For the generation of the non-B^0 modes decays, the same model is used based on the assumption that the masses and kinematic distributions of the parent and daughter particles are approximately equal. The Λ_b^0 decay was generated uniformly in phase space. The $B^0 \to J/\psi\, K^{*0}$ simulation was also used to test the corrections applied to the phase space $B^0 \to K^{*0}\mu^+\mu^-$ sample to make the data match the simulation and determine the accuracy of any corrections applied. All of the samples were used to determine the level of irreducible 'peaking' background decays that satisfy all the selection criteria and may introduce a systematic bias.

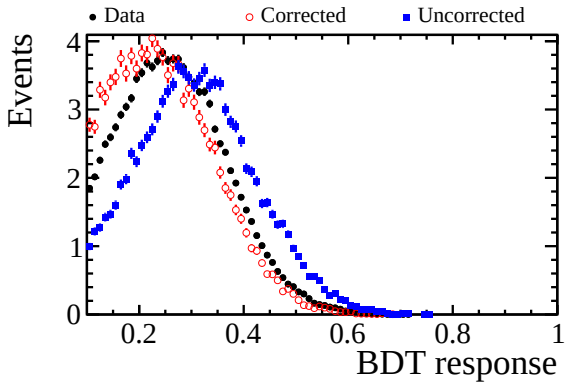

(a) BDT distribution

Figure 5.2: The distribution of MVA classification values for $B^0 \to J/\psi\ K^{*0}$ candidates from data and simulation. The MVA is described in Sec 5.3. The data (black) is from the $1.0\,\text{fb}^{-1}$ sample. The corrected (red) and uncorrected (blue) $B^0 \to J/\psi\, K^{*0}$ candidates are from the same MC11 simulation sample.

Data-simulation validation

The complete set of data-simulation corrections described previously were verified by applying the procedure to simulated $B^0 \to J/\psi\, K^{*0}$ candidates. The distribution of the BDT response of the $B^0 \to J/\psi\, K^{*0}$ candidates in data and simulation is given in Fig 5.2. There is good agreement between the data and the corrected-simulated candidates, giving confidence that the set of corrections replicates the BDT selection efficiency correctly.

5.3 Selection

The aim of the $B^0 \to K^{*0}\mu^+\mu^-$ event selection is to select complete $B^0 \to K^{*0}\mu^+\mu^-$ candidates from the triggered data. As mentioned in Section 4.5, biases in the selection of $B^0 \to K^{*0}\mu^+\mu^-$ candidates have the effect of removing events which contribute the most to measurements of A_{FB}. The trigger lines, the pre-selection and the multivariate selection have been designed to minimise the bias from the acceptance effect.

The trigger lines used to select $B^0 \to K^{*0}\mu^+\mu^-$ events are the same for both angular analyses. The trigger selects events by using the properties of the final state particles but use the topological n-body properties available in the software trigger. In the hardware trigger, events are selected which have at least one high p_{T} muon. In the software trigger,

Table 5.1: The cut based selection used in the event selection software `Stripping17` to identify $B^0 \to J/\psi K^{*0}$ and $B^0 \to K^{*0}\mu^+\mu^-$ candidates. The four body candidate is constructed by combining a kaon and a pion track to form a K^{*0} candidate and two opposite sign muons to form the dimuon candidate. The two body candidates are then combined to make the four body $K\pi\mu^+\mu^-$ candidate.

Particle	Selection Requirement
B^0	$4850 < m_{K\pi\mu^+\mu^-} < 5780\,\text{MeV}/c^2$
B^0	$\cos\theta_{\text{PV}} > 0.9999$
B^0	Vertex χ^2/d.o.f < 6
B^0	$IP\chi^2 < 16$
B^0	flight distance $\chi^2 > 121$
K^{*0}	$600 < m_{K\pi} < 2000\,\text{MeV}/c^2$
K^{*0}	Vertex χ^2/d.o.f < 12
K^{*0}	flight distance $\chi^2 > 9$
$\mu^+\mu^-$	flight distance $\chi^2 > 9$
$\mu^+\mu^-$	Vertex χ^2/d.o.f < 12
Track	fit χ^2/d.o.f < 5
Track	$IP\chi^2 > 9$
Track	$p_{\text{T}} > 250\,\text{MeV}$
$\mu^\pm$	`IsMuon` True

events are first selected with one high momentum and large IP track, with or without MuonID. In the second software trigger, the multi-variate topological trigger lines are used to select 2, 3 or 4 body track combinations satisfying general properties of B mesons as described in Section 4.5. Additional $B^0 \to K^{*0}\mu^+\mu^-$ candidates pass the topological trigger lines, where the n-body combinations have one or more tracks with associated muon identification. An additional line which triggers on a muon candidate with high p and high p_{T} is also used.

The selection for the data taken in 2011 is the same for both angular analyses. This selection contains kinematic cuts as well as cuts on the quality of the four-body and two-body vertices, the quality of the individual tracks and their displacement from the vertex. The event selection selection requirements are set out in Table 5.1.

The pre-selection requirements were chosen to remove pathological events such as events where the kaon track is a duplicate of the pion track. The lower bound of the B^0 mass window was chosen to be at 5150 MeV/c^2 to lie above most of the partially reconstructed background. $B^0 \to K^{*0}\mu^+\mu^-$ candidates are rejected based on a measure of the track similarity called the Kullback-Lieber (KL) distance [98]. In the case of B

Table 5.2: Pre-selection cuts applied to $B^0 \to J/\psi K^{*0}$ or $B^0 \to K^{*0}\mu^+\mu^-$ candidates to remove pathological events such as partially reconstructed backgrounds and peaking backgrounds within the B^0 mass window.

Particle	Selection Requirement
Per Track	$0 < \theta < 400\,\text{mrad}$
Per Track	KL distance > 5000
Each pair of tracks	$\delta\theta > 1\,\text{mrad}$
$\mu^+\mu^-$ candidate	`IsMuon`
K	$\Delta(\log\mathcal{L})_{K\pi} > -5$
π	$\Delta(\log\mathcal{L})_{K\pi} < 25$
Primary vertex location	$\lvert X - < X > \rvert < 5\,\text{mm}$
Primary vertex location	$\lvert Y - < Y > \rvert < 5\,\text{mm}$
Primary vertex location	$\lvert Z - < Z > \rvert < 200\,\text{mm}$

candidates for which the final state particles have similar momenta, one is randomly removed. Candidates which contain final state particles that have a very small opening angle ($< 1\,\text{mrad}$) between them are removed. This removes tracks which are made up of a particle and an incorrectly matched track. The summary of pre-selection requirements in the analysis is given in Table 5.2.

Specific background vetoes

A second set of pre-selection requirements were chosen using simulation to veto the effect of partially reconstructed backgrounds and peaking backgrounds within the B^0 mass window. This removes candidates with incorrect PID that may form peaking backgrounds.

In both angular analyses, the charmonium modes $B^0 \to J/\psi K^{*0}$ and $B^0 \to K^{*0}\psi(2S)$ are vetoed due to their different underlying physics. Events with a dimuon mass between $2946 < m_{\mu^+\mu^-} < 3176\,\text{MeV}/c^2$ and $3586 < m_{\mu^+\mu^-} < 3766\,\text{MeV}/c^2$ are removed. In addition, events with $m_{K\pi\mu^+\mu^-} < 5230\,\text{MeV}/c^2$ but with a dimuon mass of $2796 < m_{\mu^+\mu^-} < 3176\,\text{MeV}/c^2$ and $3466 < m_{\mu^+\mu^-} < 3766\,\text{MeV}/c^2$ are also removed to account for the radiative tail from the J/ψ and the $\psi(2S)$. A final veto of $3176 < \text{m}_{\mu^+\mu^-} < 3210\,\text{MeV/c}^2$ removes mis reconstructed J/ψ decays. Combinatorial background is also removed using these vetoes so the remaining candidates in the vetoed q^2 bin are re-weighted by the proportion of the bin vetoed. The selected $B^0 \to J/\psi K^{*0}$ events used in the analysis are those removed by the vetoes for the J/ψ. The $K\pi$ mass window used to select $B^0 \to K^{*0}\mu^+\mu^-$

and $B^0 \to J/\psi K^{*0}$ candidates was $|m_{K\pi} - m_{K^{*0}}| < 100\,\text{MeV}/c^2$.

In both angular analyses, a number of specific combinations of background may introduce bias in the angular analysis and vetoes are therefore applied to remove them. The $\Lambda_b^0 \to \Lambda^*(1520)\mu^+\mu^-$ vetoes were only implemented in the second angular analysis because the contribution was significant in this dataset.

- $B^0 \to K^{*0}\mu^+\mu^-$ events where a kaon has been misidentified as a pion. This is dealt with by applying a strict $\Delta(\log\mathcal{L})_{K\pi}$ values on candidates which have a mass within the range $|m_{K\pi} - m_{K^{*0}}| < 100\,\text{MeV}/c^2$ when the kaon and pion masses are exchanged.

- $B^0 \to J/\psi K^{*0}$ or $B^0 \to K^{*0}\psi(2S)$ events where the muon is misidentified as a kaon or pion. Possible events of this type are vetoed if the mass of the hadron-muon pair lies within the $|m_{\mu^+\mu^-} - m_{J/\psi}| < 40\,\text{MeV}$ window or $|m_{\mu^+\mu^-} - m_{\psi(2S)}| < 40\,\text{MeV}/c^2$.

- $B_s^0 \to \phi\mu^+\mu^-$ events where one of the kaons from the ϕ-meson has been misidentified as a pion. These events are vetoed with stringent particle identification cuts if the $K\pi$ mass lies close to the mass of the ϕ when calculated using the kaon mass for the pion.

- $B^+ \to K^+\mu^+\mu^-$ events where an additional pion has been added from elsewhere in the event. This is removed by vetoing the $K\ \mu^+\mu^-$ invariant mass from $5220 < m_{K\mu^+\mu^-} < 5340\,\text{MeV}/c^2$.

- Candidates from $\Lambda_b^0 \to \Lambda^*(1520)\mu^+\mu^-$ decays where the proton is misidentified as a kaon and the kaon is misidentified as a pion. Events of this type are removed by applying stringent particle identification criteria on $K\pi$ pairs that fall within the correct mass window to come from a Λ_b^0 decay.

Other peaking backgrounds are studied using simulation and the contribution was found to be negligible. Partially reconstructed $B^0 \to K^+\pi^-\mu^+\mu^- + X$ decays are vetoed by requiring a $K\pi\mu^+\mu^-$ invariant mass of greater than $5150\,\text{MeV}/c^2$. Cascade decays of two semi-leptonic decays from a B^0 and from a D^0 meson also sit in the lower mass sideband and are removed by the previous cut.

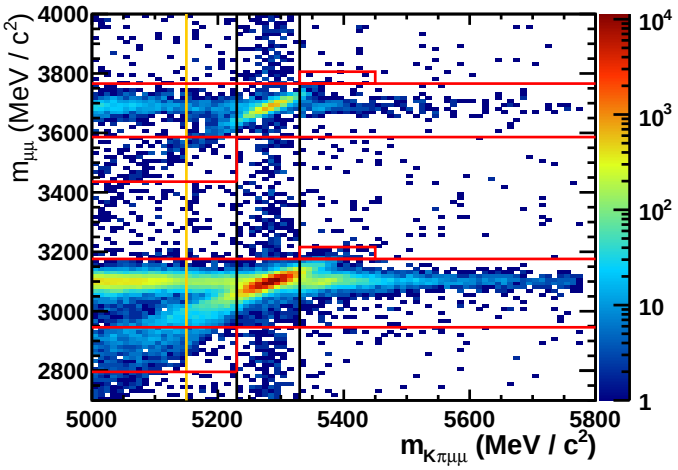

Figure 5.3: The $K\pi\mu^+\mu^-$ versus $\mu^+\mu^-$ invariant mass distribution of $B^0 \to K^{*0}\mu^+\mu^-$ candidates. The charmonium veto regions are indicated by the red lines. The yellow line indicates the extent of the lower mass sideband used for the angular analysis.

The mass distribution of selected candidates is shown in Fig 5.3. It is possible to see both the charmonium resonances along with the $B^0 \to K^{*0}\mu^+\mu^-$ events in the B^0 mass window. The large low invariant mass tail from radiative and mis-reconstructed J/ψ and $\psi(2S)$ decays is also evident.

MVA selection

In order to select a clean sample of good quality $B^0 \to K^{*0}\mu^+\mu^-$ candidate decays, a BDT was used to take advantage of correlations between the kinematic, particle identification and topological properties of the candidates. The BDT was trained using $B^0 \to J/\psi\, K^{*0}$ events as signal and upper mass sideband $B^0 \to K^{*0}\mu^+\mu^-$ events, i.e. events above $5400\,\mathrm{MeV}/c^2$, that pass the pre-selection as background. The events used for training were selected from an independent data sample taken at LHCb at $\sqrt{s}$ =7 TeV in 2010. Half these events were used for training and half were used to test the performance of the BDT.

The BDT makes use of the following information: The properties of the B^0 are the B^0 pointing to the primary vertex, the B^0 flight-distance and the B^0 impact parameter χ^2 with respect to the primary vertex, the B^0 p_{T} and it's vertex quality (χ^2) ; The properties of the K^{*0} and the di-muon pair are the flight-distance and the impact parameter χ^2 with respect to the primary vertex (associated to the B^0), the K^* and di-muon p_{T} and

it's vertex quality (χ^2); For each of the final state particles, the impact parameter χ^2, the $\Delta(\log\mathcal{L})_{K\pi}$ and $\Delta(\log\mathcal{L})_{\mu}$ were used. The value of the BDT output was chosen to optimise the sensitivity to $A_{\rm FB}$.

5.4 Acceptance correction

The angular distribution of fully reconstructed and offline selected $B^0 \to K^{*0}\mu^+\mu^-$ candidates is not representative of the angular distribution of $B^0 \to K^{*0}\mu^+\mu^-$ events which come from a proton-proton interaction. This is because the process of reconstruction and selection introduces an acceptance effect, both from the geometry of the LHCb detector and from the reconstruction and selection software. In order to perform an angular analysis, this acceptance effect must be corrected for. There are two main approaches to including the acceptance in an angular analysis. The acceptance can be parametrised and included in the signal PDF and fitted to the data, along with various external inputs to help constrain the parameters. This approach has several benefits but it also introduces additional parameters into the fit. Angular analyses that have used this approach include the LHCb and CDF measurements of $B^0 \to J/\psi\,\phi$ [99, 100]. As an alternative, the efficiency can be calculated in different regions of phase space to give each candidate a weight proportional to the inverse of the efficiency,

$$\omega(\cos\theta_l, \cos\theta_K, \phi)_i = \frac{1}{\epsilon(\cos\theta_l, \cos\theta_K, \phi)_i}\,. \tag{5.1}$$

This method has the benefit of being separate from the result extraction, keeping the angular PDF purely to describe the data. This is the method presented in this thesis and was the method used in the first two angular analyses of $B^0 \to K^{*0}\mu^+\mu^-$ at LHCb.

5.4.1 Total acceptance effect on simulation

Simulation was used to calculate the selection efficiency for $B^0 \to K^{*0}\mu^+\mu^-$ candidates in different regions of phase space by comparing the distribution of $B^0 \to K^{*0}\mu^+\mu^-$ candidates as a function of the angular variables and q^2 before and after the complete selection

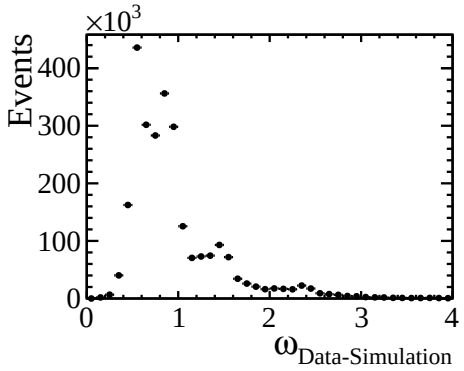

Figure 5.4: The distribution of weights to correct the simulated phase space $B^0 \to K^{*0}\mu^+\mu^-$ candidates for known differences between the data and the simulation.

has been applied. The simulated events were generated as described in Section 4.4 and corrected as described in Section 4.4.3. The IP resolution and the particle identification corrections were applied before the selection. The distribution of the weights given to each of the simulated $B^0 \to K^{*0}\mu^+\mu^-$ candidates from the remaining data-simulation corrections is shown in Fig 5.4. The structure of four distinct peaks comes from the re-weighting for the event occupancy.

The angular distribution of fully reconstructed and selected phase space $B^0 \to K^{*0}\mu^+\mu^-$ candidates is given in Fig. 5.5. Is is possible to see the symmetric acceptance at high $\cos\theta_l$, due to 'backward-going' muons in the rest frame of the B^0 that have a very low momenta in the lab frame. There is an asymmetric acceptance for $\cos\theta_K$ from the same effect but the asymmetry is due to the difference in masses of the K and the π. The different momentum spectra for the kaon and the pion is also affected by both the tracking efficiency and by the particle identification efficiency. This is where most of the data/simulation corrections have a significant effect.

The total acceptance effect for a four-body decay is a function of the kinematic angles and invariant masses of the di-muon pair and the $K\pi$ pair. The p^2 window is assumed to be sufficiently small that there is no varying acceptance effect within it. The angular analysis is performed in bins of q^2 requiring that the acceptance effect is corrected for on a finer level than the q^2 binning.

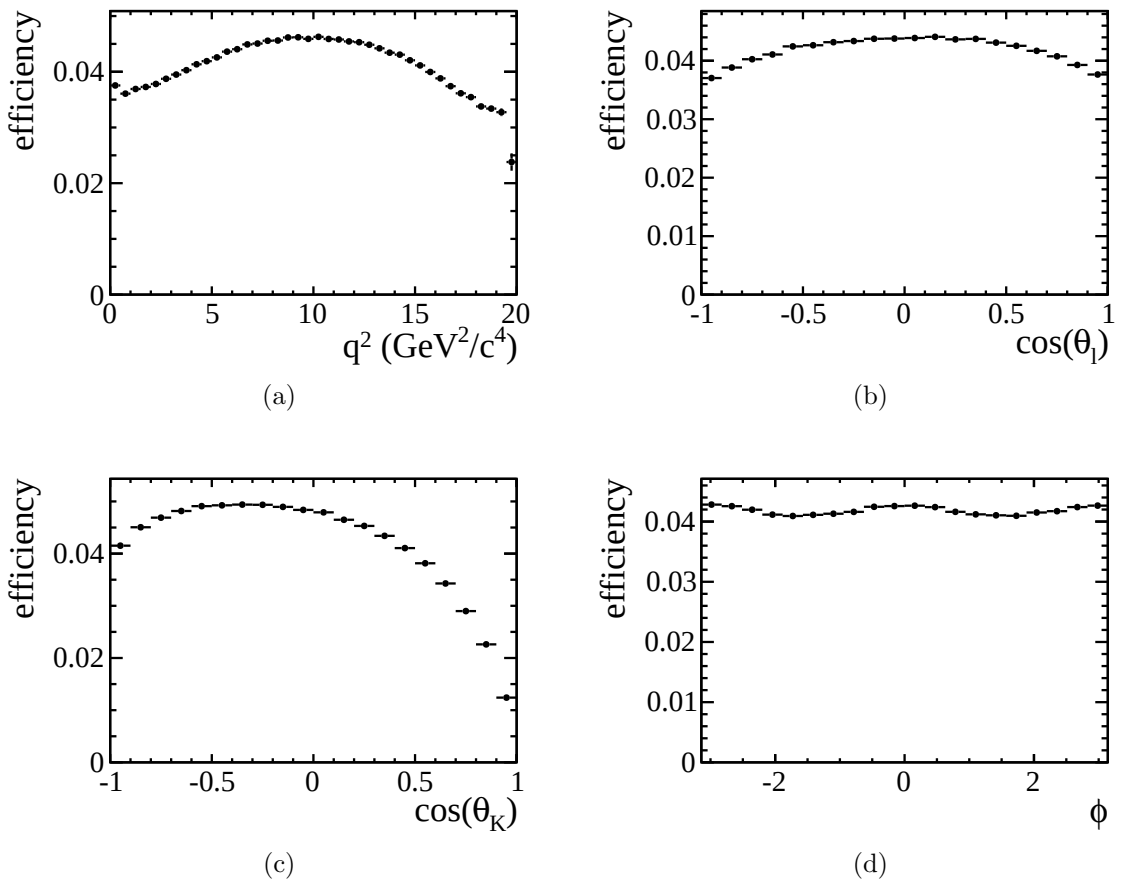

Figure 5.5: The efficiency for selected phase space simulated $B^0 \to K^{*0}\mu^+\mu^-$ candidates as a function of (a) q^2, (b) $\cos\theta_l$, (c) $\cos\theta_K$ and (d) ϕ. There is a reasonably symmetric acceptance in $\cos\theta_l$ and an asymmetric acceptance effect in $\cos\theta_K$. The acceptance in q^2 varies across the full range and there is a very small acceptance effect in ϕ.

5.4.2 A full 3D acceptance correction algorithm

One method of evaluating the efficiency as a function of phase space is to count events before and after the selection in fine bins of phase space. This method was used in the first angular analysis of $0.38\,\mathrm{fb}^{-1}$ of data. For an event at a particular point, the efficiency can be calculated by comparing the number of offline selected events with the number of generator level events 'close' to that point :

$$\epsilon(\cos\theta_l, \cos\theta_K, q^2)_{r<R} = \frac{\text{Offline selected events } (\delta d < R)}{\text{Generator level events } (\delta d < R)} = \frac{n}{m} \tag{5.2}$$

where n is the number of weighted offline selected simulated events and m is the number of generator level simulated events. The distance d is defined over the metric of the phase space and R is the maximum distance within which events are chosen to contribute to the efficiency calculation. The condition $\delta d < R$ defines a hyper-spheroid over the phase space. The distance between event i and event j, δd_{ij}, is given by

$$\delta d_{ij} = \frac{1}{N_{\cos\theta_l}}(\cos\theta_{li} - \cos\theta_{lj})^2 + \frac{1}{N_{\cos\theta_K}}(\cos\theta_{Ki} - \cos\theta_{Kj})^2 + \frac{1}{N_{q^2}}(q_i^2 - q_j^2)^2 \tag{5.3}$$

where the normalisation factors, $(N_{\cos\theta_l}, N_{\cos\theta_K}, N_{q^2})$, are chosen such that the dimensions are each scaled between $[0, 1]$. In order to collect events efficiently, a k-nearest neighbour algorithm was used to collect events in a small region of phase space.

The error on the efficiency for a given bin is defined by the combination of the Poisson errors from n and m, i.e.

$$\sigma_\epsilon = \epsilon \times \sqrt{\frac{\sigma_n^2}{n^2} + \frac{1}{m}}, \tag{5.4}$$

since the offline selection simulation is not a subset of the generation simulation. The maximum radius R is chosen such that the statistical error from the number of events within the hyper-spheroid is sufficiently small when compared to the size of the phase space. The average error and the average fractional error as a function of the radius of the hyper-spheroid is shown in Fig. 5.6. The average error follows the expected Poisson

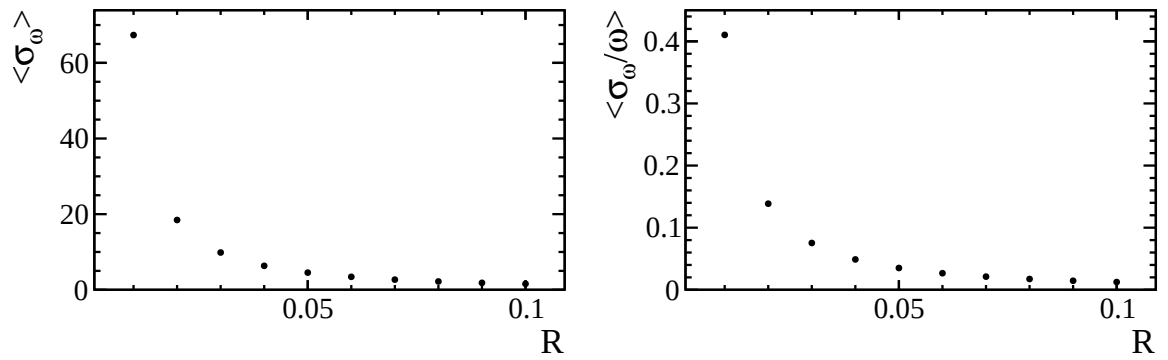

(a) (b)

Figure 5.6: The average error (a) and the fractional error (b) on 150 weights for $B^0 \to K^{*0}\mu^+\mu^-$ phase space simulated events for radii between 0.01 and 0.1. It is possible to see the $\sqrt{n^3}$ behaviour in the reduction of the error as more events are used to calculate the efficiency.

behaviour but the fractional error is significant for radii of less than 0.02.

For the first angular analysis of $0.38\,\text{fb}^{-1}$ of data, a radius of $R = 0.02$ was used to calculate an acceptance correction weight on an event-by-event basis. This is chosen as a balance between contributing a large systematic error and retaining the accuracy on the correction. The distribution of acceptance correction weights on data and the correlation between these weights and the angles are shown in Fig. 5.7. It is possible to see that the weight values at extreme ($|\cos\theta_K| > 0.8$) $\cos\theta_K$ are higher than the weights in the centre. The same effect can be seen in $\cos\theta_l$ but to a lesser degree due to the integration over q^2. However, at low and high q^2 it is possible to see a variation of weights to accommodate the change in acceptance.

One limitation of the k-nearest-neighbour algorithm is that the error on the efficiency is entirely dominated by the number of offline selected simulated events at high q^2. If the data sample is binned more finely than the chosen collection radius R, then the 'averaging effect' over the hyper-spheroid can be seen. In Fig. 5.8, an example of this can be seen in the large $B^0 \to J/\psi K^{*0}$ sample. A second limitation of the k-nearest-neighbour algorithm is the computational performance. The algorithm is at worst of order $\mathcal{O}(n)$ per event. This can be simplified by only searching for neighbours in a small region of phase space, sufficient to encompass the subset of events within the radius R. As the number of events

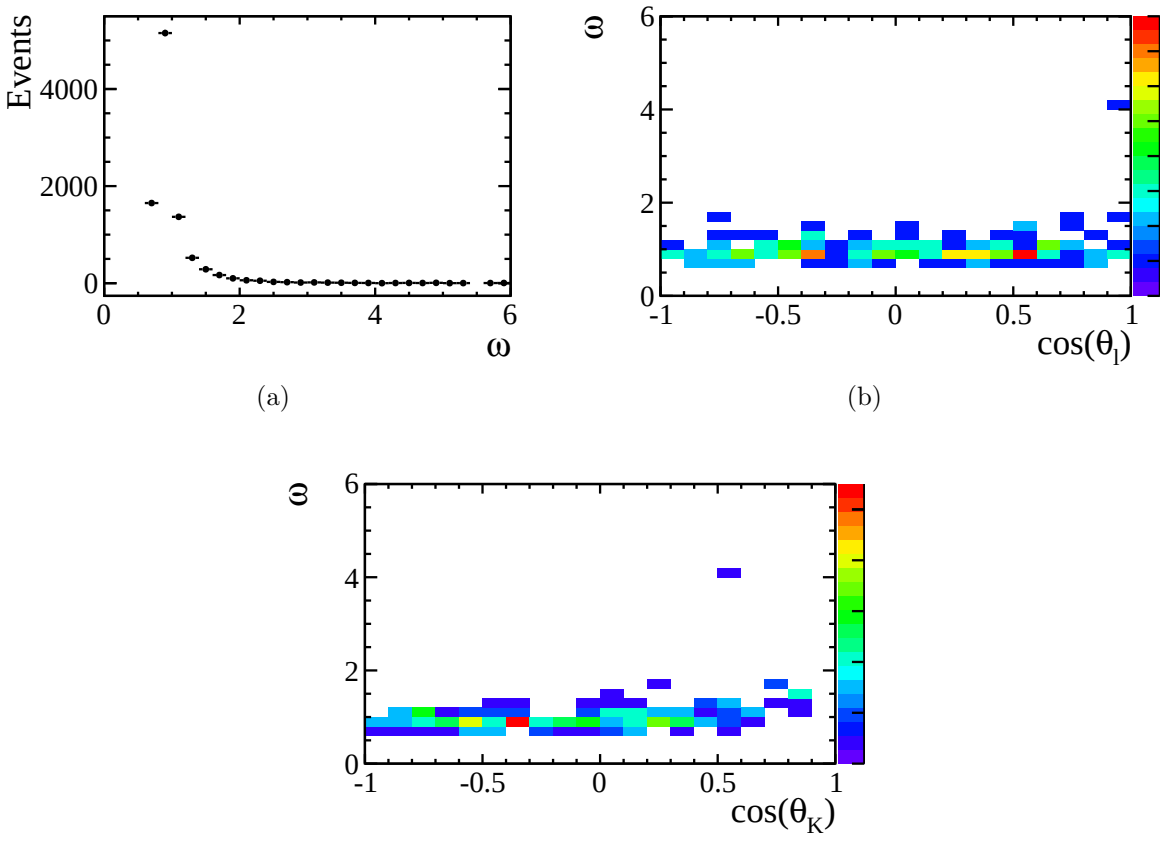

Figure 5.7: The distribution of weights for 150 phase space simulated $B^0 \to K^{*0}\mu^+\mu^-$ events (a) and the correlation between the weights and $\cos\theta_l$ (b) and $\cos\theta_K$ (c). The weights are normalised such that the sum of weights is equal to the number of events. The high weights for extreme $\cos\theta_K$ and $\cos\theta_l$ can be seen.

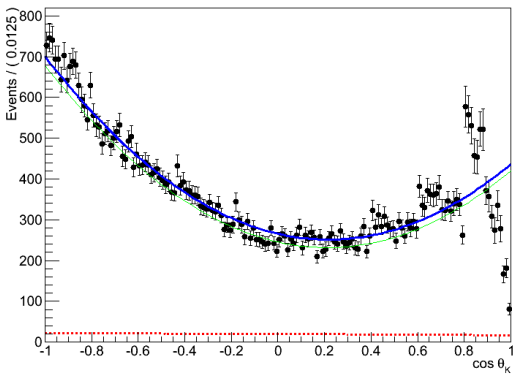

Figure 5.8: Weighted $B^0 \to J/\psi\, K^{*0}$ events using a radius of $R = 0.05$. The total expected number of events is shown in blue, along with the total expected number of signal events in green and the number of background events in red. The effect of integrating over a rapidly varying efficiency is evident at high $\cos\theta_K$ with a large statistics data sample.

in the simulation has to scale with the size of the data, n_{data}, the overall scaling of the algorithm is $\mathcal{O}(n_{data}^2)$. This, along with the required decrease in the systematic uncertainty on the efficiency calculation, necessitated the development of a more efficient acceptance algorithm for the angular analysis on the full 2011 dataset.

5.4.3 A factorised acceptance correction algorithm

In order to reduce the error on the acceptance correction beyond the reduction in statistical error for the full 2011 dataset, a factor of $1/\sqrt{3}$ was required to compensate for the threefold increase in data. One solution to this issue, along with reducing the $\mathcal{O}(m^2)$ scaling of the k-nearest neighbour algorithm, is to model the distribution of events before and after selection using a PDF. The error on the fitted PDFs at a point in phase space is smaller than the error on a bin of k events because the whole dataset is used to evaluate the efficiency.

In general, the efficiency function is not analytical so the choice of PDF to model the efficiency is entirely empirical. The efficiency can be calculated at a particular point in phase space,

$$\epsilon(\cos\theta_l, \cos\theta_K, \phi, q^2) = \frac{n}{m} \times \frac{S(\cos\theta_l, \cos\theta_K, \phi, q^2)}{G(\cos\theta_l, \cos\theta_K, \phi, q^2)}\,, \tag{5.5}$$

where S is the PDF modelling the selected data and G is the PDF modelling the generator level data. The PDFs are normalised by the weighted number of events in the selected sample (n) divided by the number of generator level events (m).

Maximum use of the simulated events to give a large reduction in the error can be made by factorising the efficiency in the form,

$$\epsilon(\cos\theta_l, \cos\theta_K, \phi, q^2) = \epsilon(\cos\theta_l) \times \epsilon(\cos\theta_K) \times \epsilon(\phi) \times \epsilon(q^2)\,. \tag{5.6}$$

This factorisation is in general not possible due to the fact that there is a correlation between the angles and q^2. The efficiency for each of the angles for offline selected simulated phase space $B^0 \to K^{*0}\mu^+\mu^-$ events in a low q^2 bin are given in Fig. 5.9. From this

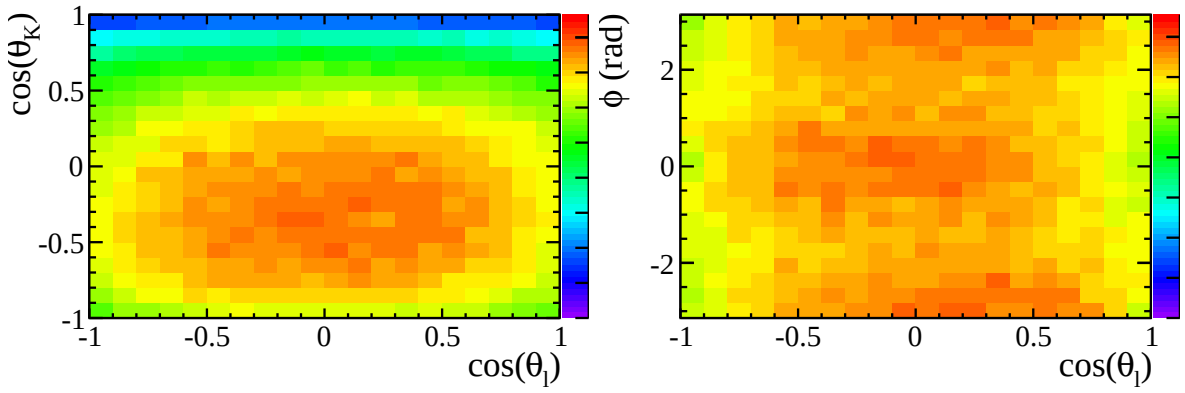

(a) $\cos\theta_l$ v.s. $\cos\theta_K$

(b) $\cos\theta_l$ v.s. ϕ

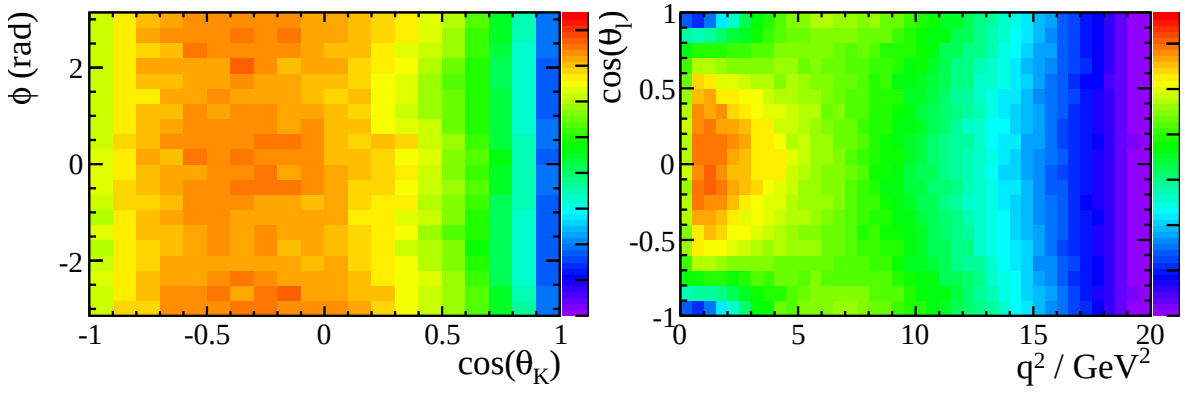

(c) $\cos\theta_K$ v.s. ϕ

(d) $\cos\theta_l$ v.s. q^2

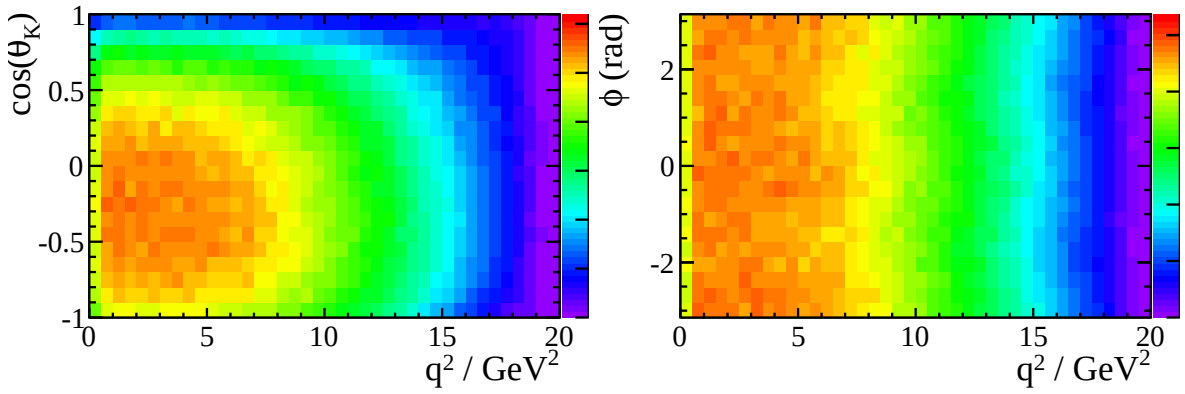

(e) $\cos\theta_K$ v.s. q^2

(f) ϕ v.s. q^2

Figure 5.9: The efficiency for selected phase space simulated $B^0 \to K^{*0}\mu^+\mu^-$ events. In (a), (b), and (c), events are selected in the low q^2 bin ($1 < q^2 < 2\,\mathrm{GeV}^2/c^4$). In (d), (e) and (f), the correlation between the individual angles and the full q^2 range is shown.

it is possible to see that the efficiency function varies as q^2, but there is no significant non-factorisable effect in the angles. This means that the PDFs must be binned in q^2 but can be factorised between the angles. The efficiency function for a bin in q^2 is given by

$$\epsilon(\cos\theta_l, \cos\theta_K, \phi, x < q^2 < y) = \left(\frac{n_{(x<q^2<y)}}{m_{(x<q^2<y)}}\right) \times S_L(\cos\theta_l) \times S_K(\cos\theta_K) \times S_P(\phi) \quad (5.7)$$

where S_i is the PDF describing the distribution of offline selected phase space events for each angle. The generator level PDF (G) is uniform as a function of each of the angles and can be integrated out.

A non-uniform binning scheme was chosen to take advantage of the uneven distribution of the simulated statistics in q^2. At low q^2, where statistics are higher, bins of 0.1 GeV^2/c^4 are used. Bins of 0.2 GeV^2/c^4 are used in the q^2 range from 1 to 6 GeV^2/c^4, and bins of 0.5 GeV^2/c^4 above 6 GeV^2/c^4 to the upper limit of $19\,\mathrm{GeV}^2/c^4$. These bins are chosen such that there are at least fifteen thousand offline selected events in the least populated bin from a total of two million simulated events.

The one-dimensional efficiency is modelled as a 6th order Chebychev polynomial [101] and normalised such that the polynomial integrates to 1,

$$\int S_i(\mathrm{x}; p_0, p_1, p_2, p_3, p_4, p_5)\ \mathrm{dx} = 1\,, \quad (5.8)$$

where p_i are the coefficients of the polynomial. In order to acquire higher statistics in each q^2 bin, further reducing the error on the PDF, the efficiency functions for $\cos\theta_l$ and ϕ are assumed to be symmetric around 0. This symmetry holds to the level of CP-violating detector effects which are assumed to be less than 5%. The total efficiency is given by

$$\begin{aligned}\epsilon(q^2, \cos\theta_l, \cos\theta_K, \phi)_{(x<q^2<y)} = &\left(\frac{n_{(x<q^2<y)}}{m_{(x<q^2<y)}}\right) \\ &\times S_L(\cos\theta_l; 0, a_1, 0, a_3, 0, a_5) \\ &\times S_K(\cos\theta_K; b_0, b_1, b_2, b_3, b_4, b_5) \\ &\times S_P(\phi; 0, c_1, 0, c_3, 0, c_5) \end{aligned} \quad (5.9)$$

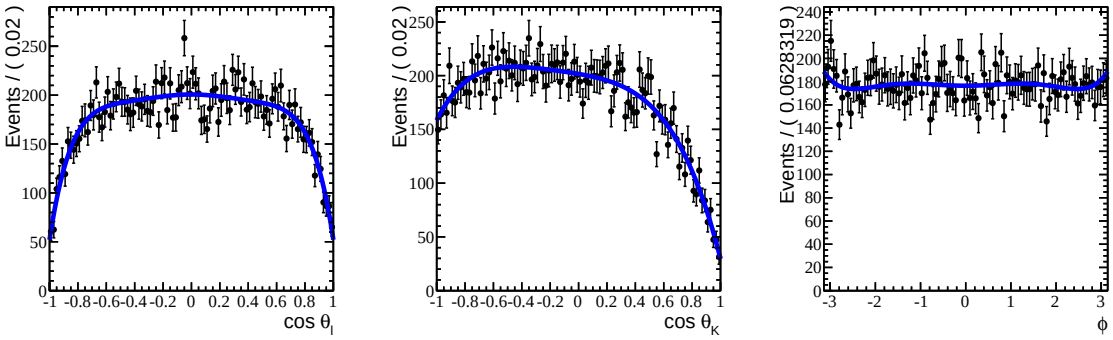

Figure 5.10: The angular efficiency in each of the angles for the q^2 bin from 0.1 to 0.2 GeV^2/c^4. The factorised PDF was fitted to phase space $B^0 \to K^{*0}\mu^+\mu^-$ simulation.

where the even (odd) parameters describe the symmetric (anti-symmetric) components of the polynomial. The efficiency PDFs for $\cos\theta_l$, $\cos\theta_K$ and ϕ for an example low q^2 bin are shown in Fig. 5.10.

The distribution of weights on ten thousand phase space events is given in Fig 5.11. The larger weights for extreme $\cos\theta_l$ and $\cos\theta_K$ regions can be seen.

Testing the factorisation

The assumption that the efficiency can be factorised is tested and the quality of the fit are assessed by using a variation of the binned χ^2 test. This modified test compares the distribution of data events used to fit a PDF to the distribution of toy Monte Carlo events generated from the fitted PDF. The number of toy Monte Carlo events generated from the fitted PDF using an accept/reject method was scaled to one hundred times the number of data events. The phase space of $\cos\theta_l$, $\cos\theta_K$ and ϕ was divided up into one thousand bins. The pull value for each bin is calculated from

$$p^i = n^i_{Data} - \left(\frac{n^i_{Data} - 10^{-2} n^i_{MC}}{\sigma} \right) \tag{5.10}$$

where the error is defined as

$$\sigma = \sqrt{(n^i_{Data} + 10^{-2} n_{MC})}\,. \tag{5.11}$$

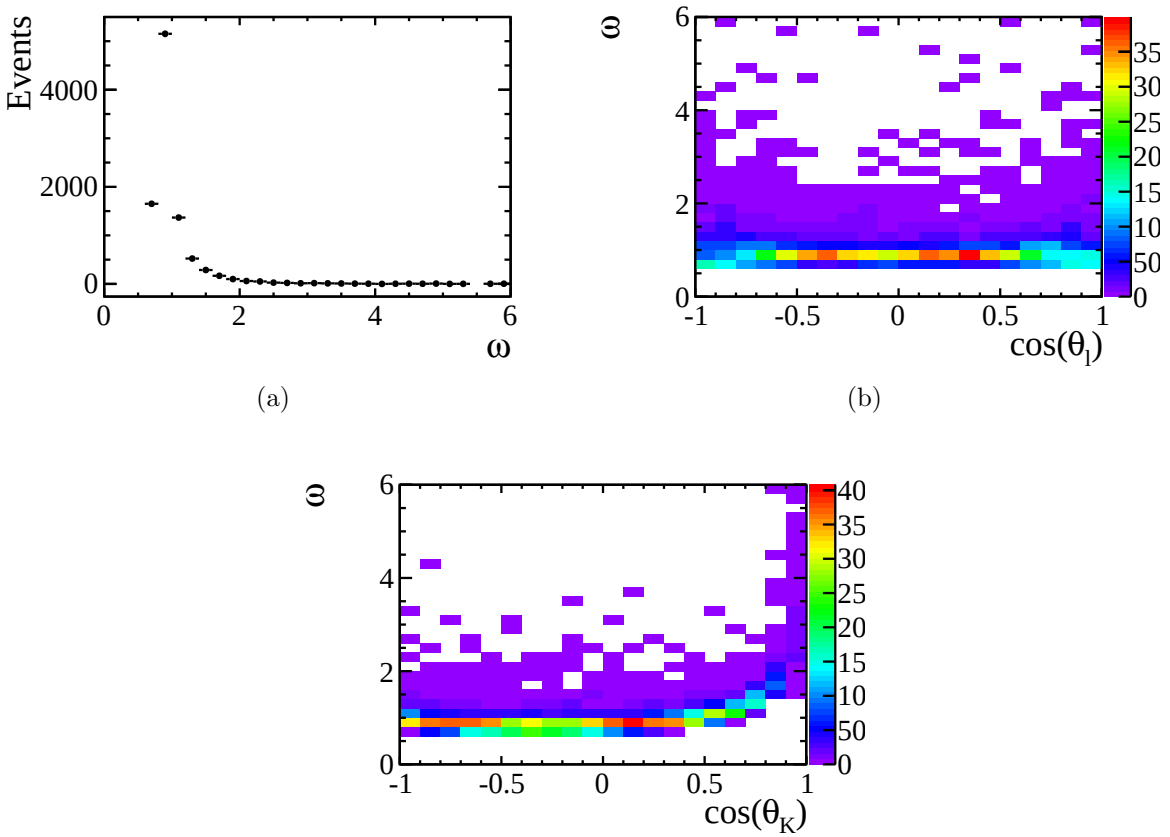

(a) (b)

(c)

Figure 5.11: The distribution of weights for 10000 phase space simulated $B^0 \to K^{*0}\mu^+\mu^-$ events and the correlation between the weights and $\cos\theta_l$ and $\cos\theta_K$. The weights are normalised such that the sum of weights is equal to the number of events. The high weights for extreme $\cos\theta_K$ and $\cos\theta_l$ can be seen.

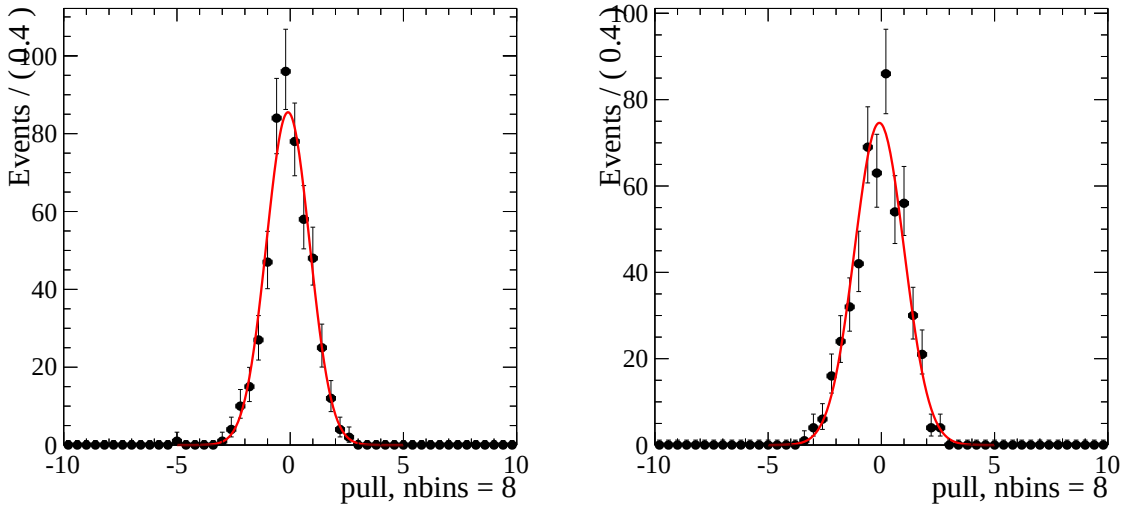

(a) (b)

Figure 5.12: The pull distribution of a toy simulation from the factorised PDFs. A low q^2 bin (a) ($1 < q^2 < 2\,\mathrm{GeV}^2/c^4$) and a high q^2 bin (b) ($15 < q^2 < 15.5\,\mathrm{GeV}^2/c^4$). The fit for both distributions is compatible with a Gaussian of zero mean and unit width.

If the PDF is a good fit to the data then the pull values should be normally distributed. Here the 'data' is the offline selected sample of phase space $B^0 \to K^{*0}\mu^+\mu^-$ simulated events. Pull distributions for one low and one high q^2 bin are shown in Fig. 5.12. Both pull distributions are compatible with a Gaussian with zero mean and unit width. The mean and width of the pull distribution for each bin in q^2 are given in Fig. 5.13. This shows that there are no regions of great discrepancy between the simulation and the factorised PDF in these bins of q^2.

The factorisation of the efficiency allows for a more precise acceptance correction at the cost of incurring a possible source of systematic uncertainty associated with integrating over non-factorisable effects. The factorisation was also tested by comparing the re-weighted phase space simulated events to the generator level distributions in each of the factorised dimensions.

5.4.4 Re-weighted phase space distributions

The most basic test of an acceptance correction is that the original generator level distribution used to create the acceptance correction can be recovered. In this case the phase

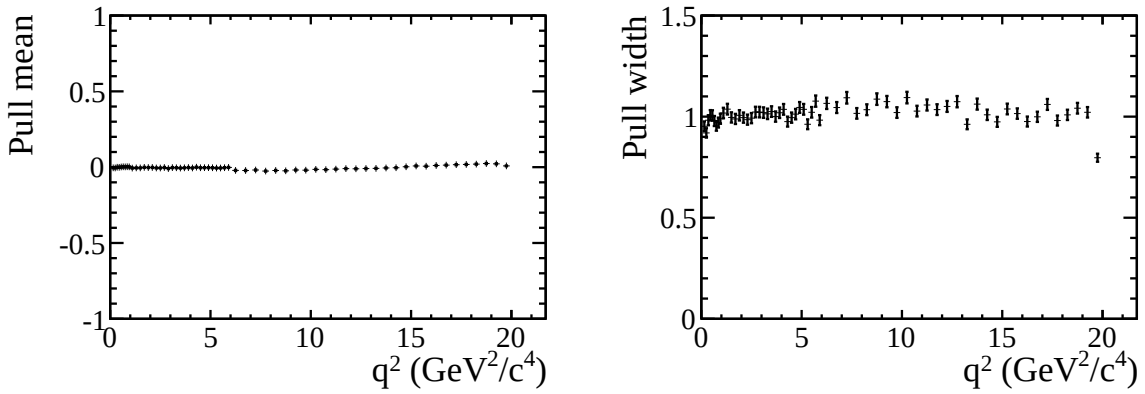

(a) (b)

Figure 5.13: The (a) mean and (b) width of each pull distribution of a toy simulation from the factorised PDFs in bins of q^2. The bins are all compatible with a Gaussian of zero mean and unit width.

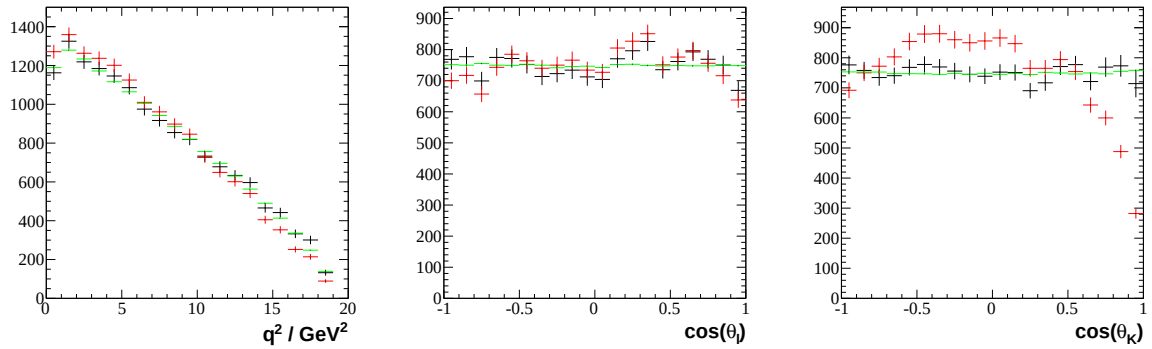

(a) (b) (c)

Figure 5.14: Generated (green), offline selected (red) and re-weighted (black) events for $B^0 \to K^{*0}\mu^+\mu^-$ using the k-nearest-neighbour acceptance correction method.

space distribution should be recovered when the phase space candidates are themselves weighted. The number of re-weighted $B^0 \to K^{*0}\mu^+\mu^-$ candidates per bin in phase space is given by

$$N_{\text{bin}} = \sum_{i=1}^{ncand} \frac{1}{\epsilon(\cos\theta_l, \cos\theta_K, \phi)_i} = \sum_{i=1}^{ncand} \omega_i. \tag{5.12}$$

which can be compared to the expected number of generator level events in that bin.

The weighted distributions for the k-nearest-neighbour acceptance correction method are shown in Fig. 5.14. Is it possible to see that the efficiency at extreme $\cos\theta_K$ and extreme $\cos\theta_l$ is recovered.

The weighted distributions for the factorised acceptance correction method are shown in Fig. 5.15. The compatibility between the re-weighted distribution and the distribution of generator level events is good for both acceptance correction methods.

The k-nearest-neighbour method is by construction the most optimal acceptance correction method as it relies only on the accuracy of the simulation from which to calculate the efficiency. However, the dependence on the simulation statistics in regions of phase space with low efficiency does not allow it to be used with larger datasets. The factorised efficiency correction has for the $1.0\,\mathrm{fb}^{-1}$ analysis a lower total systematic error. The statistical component from the simulation sample size is much smaller but the assumption of factorisation incurs an additional but still small systematic uncertainty.

5.5 Angular analysis

Each of the angular analyses were performed by simultaneously fitting a PDF for the mass and the angular distribution to the data. The simultaneous fit to the B^0 mass spectrum and to the angles ensures that the maximum information available is used to reduce the error on all of the angular observables. It also ensures that the correlations are propagated correctly between the angular observables. The total PDF (F) is a combination of a model for the signal (S) and background (B) , each containing component PDFs to describe the mass distribution and the angular distribution,

$$\begin{aligned} F(m_{B^0}, \cos\theta_l, \cos\theta_K, \phi) =& f_{sig}\left(S_i(m_{B^0}) \times S_i(\cos\theta_l, \cos\theta_K, \phi)\right) \\ &+ (1 - f_{sig})\left(B_i(m_{B^0}) \times B_i(\cos\theta_l, \cos\theta_K, \phi)\right) . \end{aligned} \tag{5.13}$$

where i indicates the model used for the first or second analysis. The different components of the total PDF are described in detail below.

The dataset is divided into seven bins of q^2. There are six separate bins in the full q^2 range, detailed in Table 5.3. The binning is analogous to the binning used in Ref [8] along with the region from $1 < q^2 < 6\,\mathrm{GeV}^2/c^4$, which is a theoretically clean region where the observables are easily calculable. The binning is chosen such that there is a bin below and

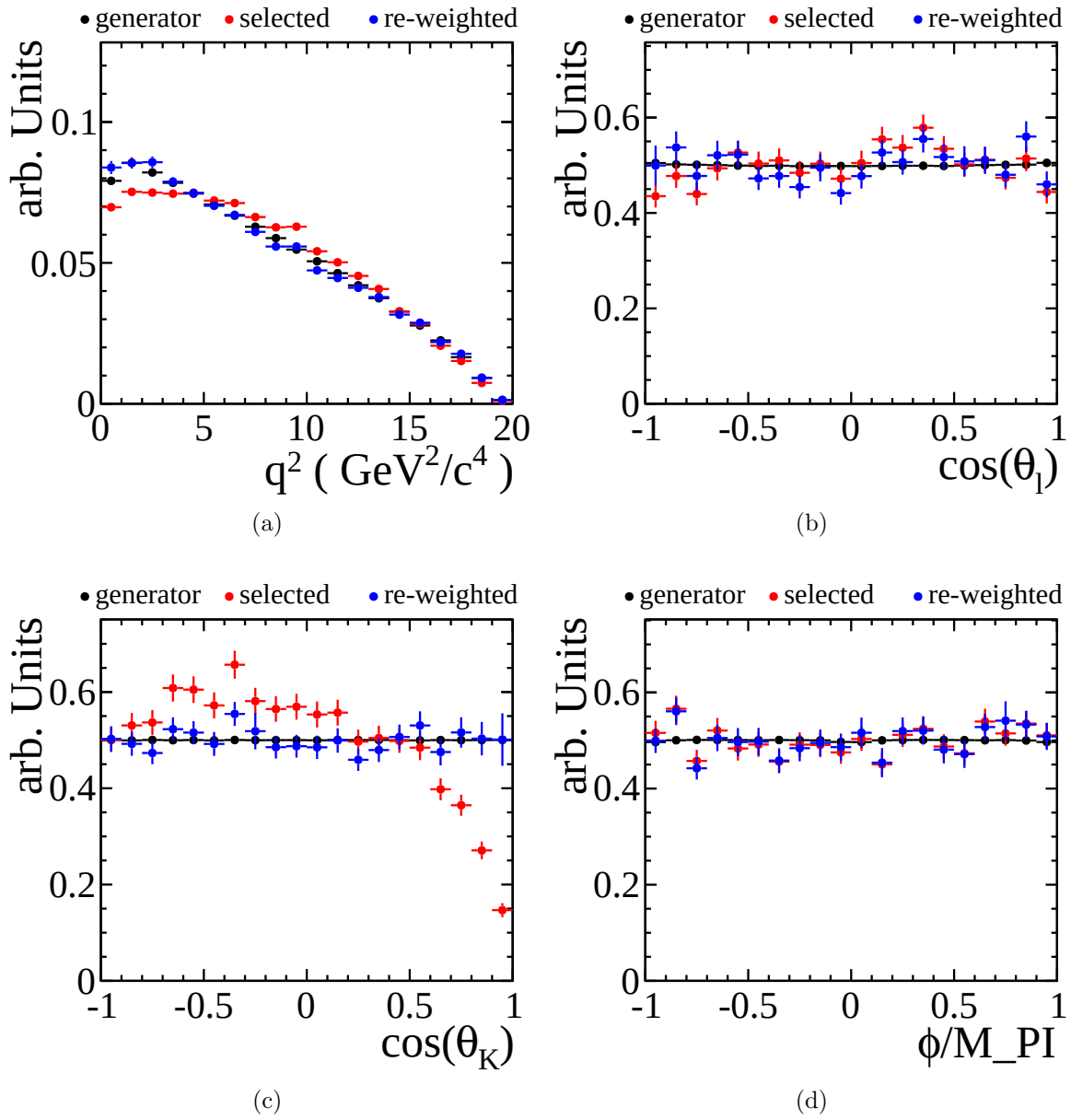

Figure 5.15: Generated (black), offline selected (red) and re-weighted (blue) events for $B^0 \to K^{*0}\mu^+\mu^-$ using the factorised acceptance correction method.

Table 5.3: The q^2 binning scheme used in both angular analyses. The binning is analogous to the binning used in Ref [8] including the q^2 region of 1 to 6 GeV^2/c^4.

lower limit (GeV^2/c^4)	upper limit (GeV^2/c^4)
0.1	2
2	4.3
4.3	8.68
10.09	12.9
14.18	16
16	19
1.0	6.0

above the point where $A_{\rm FB}$ is predicted to change sign in the Standard Model, and also with boundaries to avoid the $c\bar{c}$ resonances.

5.5.1 Mass model

Two different mass models were used to parametrise the B^0 signal invariant mass distribution. The signal invariant mass model used to parametrise the B^0 invariant mass distribution in the first angular analysis was a double Gaussian function,

$$\begin{aligned} S_{(1)}\left(m_{K\pi\mu^+\mu^-};\sigma_1,\sigma_2,\alpha,n\right) = f \times G\left(m_{K\pi\mu^+\mu^-};m_B,\sigma_1\right) \\ + (1-f)\times G\left(m_{K\pi\mu^+\mu^-};m_B,\sigma_2\right)\ , \end{aligned} \tag{5.14}$$

where f is the fraction of signal between each component and $\sigma_{1,2}$ are the different widths of each Gaussian component. The signal mass model for the second angular analysis was an empirical model consisting of two Crystal Ball functions. The Crystal Ball was a function developed to model the radiative tail from the $b\bar{b}$ resonances [102]. It consists of a Gaussian distribution with an exponential tail and is expressed for a given mass ($m_{K\pi\mu^+\mu^-}$) as

$$\mathrm{CB}\left(m_{K\pi\mu^+\mu^-};m_{B^0},\sigma,\alpha,n\right) = N\begin{cases} \exp\left(\frac{-(m_{K\pi\mu^+\mu^-}-m_{B^0})^2}{2\sigma^2}\right) & \text{if } m_{K\pi\mu^+\mu^-} > \alpha \\ \frac{\left(\frac{n}{\alpha^2}\right)^n}{\frac{\left(m_{K\pi\mu^+\mu^-}-m_{B^0}\right)}{\sigma}+\frac{n}{\alpha}-\alpha} & \text{if } m_{K\pi\mu^+\mu^-} \leq \alpha \end{cases} \tag{5.15}$$

where N is the signal normalisation, m_{B^0} is the nominal B mass, σ is the Gaussian width and n and α are the tail parameters. Here the Crystal Ball function is used as an empirical formula to describe tails in the B^0 mass spectrum from resolution effects. The parameters for the B^0 mass signal shape are assumed to be equivalent for both Crystal Ball functions except for the widths,

$$\begin{aligned} S_{(2)}\left(m_{K\pi\mu^+\mu^-};\sigma_1,\sigma_2,\alpha,n\right) = f\,\mathrm{CB}\left(m_{K\pi\mu^+\mu^-};m_B,\sigma_1,\alpha,n\right) \\ + (1-f)\times \mathrm{CB}\left(m_{K\pi\mu^+\mu^-};m_B,\sigma_2,a,n\right)\ . \end{aligned} \tag{5.16}$$

The shape of the signal mass model for both analyses is taken from fits to the $B^0 \to J/\psi K^{*0}$ invariant mass spectrum. Due to the high statistics of $B^0 \to J/\psi K^{*0}$ in the data, it is necessary to include an additional contribution from the suppressed $B_s^0 \to J/\psi K^{*0}$ mode. The decay $B_s^0 \to J/\psi K^{*0}$ is suppressed by a factor of $f_d|V_{td}|/|V_{ts}|\ f_s$compared to $B^0 \to J/\psi K^{*0}$. The model used for the $B_s^0 \to J/\psi K^{*0}$ is identical to the model for the $B^0 \to J/\psi K^{*0}$ except for the central mass value and shares all of it's parameters with the $B^0 \to J/\psi K^{*0}$ model. The only remaining free parameter is the relative normalisation between the two contributions. There is a relative factor

$$\frac{n_{B^0}}{n_{B_s^0}} = 0.007 \pm 0.002\,, \tag{5.17}$$

which is applied as a Gaussian constraint on the overall size of the $B_s^0 \to J/\psi K^{*0}$ contribution.

The model for the background contribution to the $m_{K\pi\mu^+\mu^-}$ spectrum for both analyses is the same. This is an exponential function,

$$B_{(1,2)}\left(m_{K\pi\mu^+\mu^-};\lambda\right) = N_B \exp\left(-\lambda m_{K\pi\mu^+\mu^-}\right), \tag{5.18}$$

where λ is the decay constant for the exponential and N_B is the normalisation of the background PDF.

5.5.2 Angular model

The signal angular model for each of the analyses is a simplification of the full angular distribution for $B^0 \to K^{*0}\ell^+\ell^-$ as described in Sec. 3.2. The angular distribution is integrated over one bin of p^2 and integrated over each of the six bins of q^2. The signal model

used in the $0.38\,\mathrm{fb}^{-1}$ angular analysis to measure A_{FB} and F_{L} is

$$\begin{aligned} S_{(1)}(\cos\theta_l, \cos\theta_K) = & \frac{9}{16}\Bigg(2F_{\mathrm{L}}\cos^2\theta_K(1-\cos^2\theta_l) \\ & + \frac{1}{2}(1-F_{\mathrm{L}})(1-\cos^2\theta_K)(1+\cos^2\theta_l) \\ & + \frac{4}{3}A_{\mathrm{FB}}(1-\cos^2\theta_K)\cos\theta_l \Bigg). \end{aligned} \tag{5.19}$$

The angular distribution for the $1.0\,\mathrm{fb}^{-1}$ angular analysis was extended to include angular observables dependent on ϕ. The distribution was simplified using the transformation described in Sec. 3.2 and [60]. The analysis uses two parameterisations of the angular distribution. The angular distribution for A_{FB}, F_{L}, S_3 and S_9 is given by

$$\begin{aligned} S_{(2a)}(\cos\theta_l, \cos\theta_K, \phi^{'}) = & \frac{9}{16\pi}\Bigg(2F_{\mathrm{L}}\cos^2\theta_K(1-\cos^2\theta_l) \\ & + \frac{1}{2}(1-F_{\mathrm{L}})(1-\cos^2\theta_K)(1+\cos^2\theta_l) \\ & + S_3(1-\cos^2\theta_K)(1-\cos^2\theta_l)\cos 2\phi^{'} \\ & + \frac{4}{3}A_{\mathrm{FB}}(1-\cos^2\theta_K)\cos\theta_l \\ & + S_9(1-\cos^2\theta_K)(1-\cos^2\theta_l)\sin 2\phi^{'} \Bigg). \end{aligned} \tag{5.20}$$

The re-parametrised angular distribution contains the transverse angular observables ($A_{\mathrm{T}}^{\mathrm{Re}}$, $A_{\mathrm{T}}^{2,}$ $A_{\mathrm{T}}^{\mathrm{Im}}$) as described in Sec. 3.4,

$$\begin{aligned} S_{(2b)}(\cos\theta_l, \cos\theta_K, \phi^{'}) = & \frac{9}{16\pi}\Bigg(2F_{\mathrm{L}}\cos^2\theta_K(1-\cos^2\theta_l) \\ & + \frac{1}{2}(1-F_{\mathrm{L}})(1-\cos^2\theta_K)(1+\cos^2\theta_l) \\ & + \frac{1}{2}(1-F_{\mathrm{L}})A_{\mathrm{T}}^{2}(1-\cos^2\theta_K)(1-\cos^2\theta_l)\cos 2\phi^{'} \\ & + \frac{4}{3}(1-F_{\mathrm{L}})A_{\mathrm{T}}^{\mathrm{Re}}(1-\cos^2\theta_K)\cos\theta_l \\ & + (1-F_{\mathrm{L}})A_{\mathrm{T}}^{\mathrm{Im}}(1-\cos^2\theta_K)(1-\cos^2\theta_l)\sin 2\phi^{'} \Bigg). \end{aligned} \tag{5.21}$$

The angular distribution used to measure A_9 uses the CP anti-symmetric definition of ϕ where the sign changes for B^0 and $\overline{B}^0$ decays as given in Sec 3.4. The signal angular distribution is a function of $\phi^{'}_{\mathcal{A}^{CP}}$,

$$\begin{aligned} S_{(2c)}(\cos\theta_l, \cos\theta_K, \phi^{'}_{\mathcal{A}^{CP}}) = \frac{9}{16\pi}\Bigg(& 2F_{\rm L}\cos^2\theta_K(1-\cos^2\theta_l) \\ & + \frac{1}{2}(1-F_{\rm L})(1-\cos^2\theta_K)(1+\cos^2\theta_l) \\ & + A_3(1-\cos^2\theta_K)(1-\cos^2\theta_l)\cos 2\phi^{'}_{\mathcal{A}^{CP}} \\ & + \frac{4}{3}A_{\rm FB}(1-\cos^2\theta_K)\cos\theta_l \\ & + A_9(1-\cos^2\theta_K)(1-\cos^2\theta_l)\sin 2\phi^{'}_{\mathcal{A}^{CP}}\Bigg). \end{aligned} \tag{5.22}$$

The model for the background in each of the angles is equivalent for both angular analyses. The background PDF is an $n^{\rm th}$ order Chebychev polynomial of the first kind for each angle,

$$T_n(x) = \cos\left(n\arccos(x)\right)\ . \tag{5.23}$$

The total background angular PDF is factorised into each of the angles,

$$B(m_{K\pi\mu^+\mu^-}) = P^{'bkg}_n(\cos\theta_l, \cos\theta_K, \phi^{'}) = P^L_n(\cos\theta_l) \times P^K_n(\cos\theta_K) \times P^P_n\phi^{'})\,. \tag{5.24}$$

The assumption that the background angular distribution factorises was tested using the point-to-point dissimilarity test [103]. The probability of the test statistic having a value less than the test statistic of the data was 25%. This value is entirely compatible with the assumption that the background factorises into the three angles.

5.5.3 Result extraction

The signal PDF is fitted to the data by performing an unbinned maximum-log-likelihood fit to the data, minimising

$$-\log\mathcal{L} = \sum_{i}^{N} \omega_i F(m^i_{K\pi\mu^+\mu^-}, \cos\theta_l{}^i, \cos\theta_K{}^i, \phi^i, \vec{p}, \vec{O}), \tag{5.25}$$

where F is the total PDF described in Eq. 5.14. The set of parameters for the signal and background mass models are $\vec{p}$, while $\vec{O}$ is the set of angular observables. Each of the data candidates is weighted for acceptance as described in Section 5.4. These weights distort the shape of the likelihood such that the errors extracted from the standard NLL minimisation are not guaranteed to be the true errors. In each angular analysis, two different techniques were used to extract the likelihood minima and a better estimate of the error from the likelihood function. In the $0.38\,\text{fb}^{-1}$ analysis, the profile likelihood was calculated and the error determined from the two-dimensional 68% confidence interval in both A_{FB} and F_{L}. For the $1.0\,\text{fb}^{-1}$ analysis, the errors were extracted in a Frequentist manner using the Feldman-Cousins (FC) technique [104].

The FC technique maps out the likelihood for an observable, allowing the size of the confidence intervals for a given observable to be calculated. For an observable of interest in a given set of parameters, the ratio between the likelihood calculated with all parameters free ($\mathcal{L}_0$) and the likelihood calculated with the observable fixed is calculated ($\mathcal{L}_1$). The ratio between these likelihood (R_{data}) is obtained for the result obtained from data, and for a large ensemble of toy datasets (R_i). The fraction of $R_i < R_{data}$ (f_R) is proportional to the probability of the data result being the most optimum solution in the phase space of the parameters. This fraction is calculated for a range of values for the observable and the 68% confidence limits on the observable are calculated from the points where the $f_R < 0.68$.

The results of the angular fits along with the calculated confidence limits are shown in Section 5.7.

5.6 Systematic uncertainties

Systematic effects which may affect the angular analysis are considered if there is an effect on the $K\pi\mu^+\mu^-$ invariant mass distribution, the q^2 spectrum or the angular distributions. These include the acceptance correction method and the model for the B^0 mass spectrum. There are three main categories of sources of systematic uncertainty, listed in order of importance

- Any systematic bias originating from the acceptance correction method.
- The uncertainty on the data-simulation corrections used in the acceptance correction.
- The uncertainty on the exact parametrisation of the B^0 mass spectrum and the use of polynomials to model the angular background.

All these effects were considered for both analyses but the exact size and specific systematic effects arising from the data-simulation corrections and acceptance method differ between the two analyses. An additional source of systematic uncertainty was considered for the $1.0\,\text{fb}^{-1}$ analysis from possible peaking backgrounds.

5.6.1 Systematic contributions for the $0.38\,\text{fb}^{-1}$ analysis

The dominant systematic for the $0.38\,\text{fb}^{-1}$ analysis comes from the acceptance correction, with other systematic contributions originating from the data-simulation corrections and a minor contribution from the model used for the B^0 mass distribution.

Acceptance correction

The systematic uncertainty from the acceptance correction method comes from the choice of the radius of the hyperspheroid. The size of the possible bias was tested by using a smaller radius (0.01) and a larger radius (0.03) then the one chosen (0.02) to select events. Apart from the difference in the overall statistical error on the acceptance correction weight, no significant difference was found in the absolute efficiency. The estimates

of the systematic uncertainty arising from the various data-simulation corrections were propagated to give an overall uncertainty for the weight value given to each event.

In order to explore possible extreme systematic variations, two methods of altering the angular analysis were tested. Firstly, the acceptance correction was ignored and the central values of $A_{\rm FB}$ and $F_{\rm L}$ were found to move less than the statistical uncertainty on the observable. Secondly, the background model was assumed to be flat in the $\cos\theta_l$ and $\cos\theta_K$ to similar effect. These extreme changes are not propagated to the final systematic uncertainty.

The systematic error on the observables is around $\approx 30\%$ of the final statistical error. When added in quadrature to the statistical error, this only makes the total error (3-4)% larger. This is with the exception of the highest q^2 bin where the low simulation statistics leads to the total error being 10% larger than the statistical error.

Data-simulation corrections

A conservative estimate of the uncertainty based on smearing the IP of the simulated tracks was tested by using the unsmeared tracks. This can change the efficiency to select the events and the calculated angles. A conservative estimate of the uncertainty associated with applying the correction for the hadron particle identification was evaluated by using the simulated values instead of the data-derived values. This estimate gives a change in the absolute efficiency of around 20% but does not change the angular distributions. This estimate of the systematic uncertainty for the relative efficiency of the muon identification was obtained by changing the relative efficiency by one standard deviation. The weight applied to the simulation is shifted down by 1σ for $p_\mu < 10\,\text{GeV}/c$ and upwards for $p_\mu > 10\,\text{GeV}/c$. A similar procedure is used to gain an estimate of the relative tracking efficiency but changing the weight applied for track momenta above and below 20 GeV. The effect of these changes on the measurement of the differential branching fraction is much smaller as it cancels out in the normalisation to $B^0 \to J/\psi\, K^{*0}$ to first order.

Mass model

The systematic uncertainty associated with the model of the B^0 mass spectrum is evaluated by replacing the double Gaussian function with a double Crystal Ball function. This tests the degree to which the tails of the Gaussian distribution are correctly modelled. The systematic uncertainty associated with the background model is checked by using a linear function instead of an exponential function. This is because the upper mass sideband may contain unknown background which can be incorrectly modelled by using a falling exponential. The systematic uncertainty associated with using a polynomial to model the angular background is checked by using a template function for the background, taken from a fit to the B^0 upper mass sideband, i.e. events with m_{B^0} of greater then $5400\,\mathrm{MeV}^2/c^4$. This ensures that the background model is free of any signal contribution but assumes that the high mass background is entirely combinatorial and the angular distribution is equivalent under the signal peak and in the high mass region.

5.6.2 Systematic contributions in the $1.0\,\mathrm{fb}^{-1}$ analysis

The contributions to the systematic uncertainty on the angular analysis of $1.0\,\mathrm{fb}^{-1}$ come from the the event selection, the model for the B^0 invariant mass and the acceptance correction. The dominant effect comes from both the acceptance correction and the data-simulation corrections. Tables of the size of the contribution from each of the possible sources of systematic uncertainty are given in Appendix A.

Acceptance Correction

The systematic uncertainty on the acceptance correction method was estimated by testing the addition of both factorisable effects, testing the addition of non-factorisable effects and by using a different q^2 binning scheme. The systematic uncertainty associated with factorisable effects was tested by changing the acceptance correction weight by a factorisable function that increases the weight at extreme values of $\cos\theta_l$ and $\cos\theta_K$,

$$\omega_i \rightarrow \omega_i \times (1 + \alpha \cos\theta_l{}^2) \times (1 + \alpha \cos\theta_K{}^2). \tag{5.26}$$

The value of α was chosen to give a 10% increase in the weight values at the extremities of the angular distribution. The estimate includes any mis-modelling of the efficiency in such a way that it will maximally affect the angular distribution. The systematic uncertainty associated with non-factorisable effects was tested as described in Sec. 5.4.3. A non-factorisable effect of 10% is used to provide an estimate of any hidden systematic effect because this is the maximum value that the acceptance correction is insensitive to. The estimates of the systematic uncertainty from the acceptance correction are the dominant contribution to the total systematic error.

Data-simulation corrections

An estimate of the systematic uncertainty of each of the data-simulation corrections was evaluated for each of the different corrections. The systematic uncertainty on the trigger efficiency is estimated by applying a weight of $\pm 3\%$ to events with a muon of momentum less than 10 GeV. This comes from an estimate of the L0 trigger efficiency [70]. The systematic uncertainty on the relative tracking efficiency correction is changed twice. The relative tracking efficiency correction is shifted firstly down by one σ for tracks below 20 GeV and up by one σ for tracks above 20 GeV and secondly in the opposite direction. This correction is chosen to reflect the possibility of a systematic mis-modelling of low momentum tracks and to reflect the relatively easier reconstruction of high momentum tracks. The relative efficiency for the muon identification is systematically shifted using the same method as the relative tracking efficiency, but for muons with momentum above and below 10 GeV/c. A possible source of systematic uncertainty from changing the particle identification for hadrons comes from the binning scheme used to calculate the new $\Delta(\log \mathcal{L})$ values from data. The effect of the binning scheme is tested twice by drawing $\Delta(\log \mathcal{L})$ values from bins higher or lower for events close to the edge of the bin boundary.

In order to introduce a very conservative source of systematic uncertainty all hadrons with a momentum of less than 3 GeV/c were removed from the sample of phase space simulated events. The effect of this cut on the weight distribution as a function of $\cos\theta_K$ and the effect on the re-weighted phase space simulated events is shown in Fig 5.16.

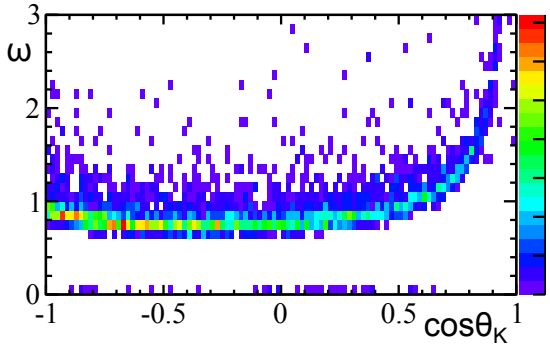

Figure 5.16: The effect of the removal of all hadrons of $p < 3\,\mathrm{GeV}/c$ from the phase space simulation used in the acceptance correction. It is possible to see the artificially higher weights at high values of $\cos\theta_K$.

Mass Model

There is a systematic effect from using the same mass model for the multiple different q^2 bins. The widths of the two Crystal Ball functions used for the signal mass model are checked using corrected simulated $B^0 \to K^{*0}\mu^+\mu^-$ data. The width is found to vary within errors to $\pm 5\%$ and both widths in the signal mass model are varied by this amount to compensate for this.

The systematic uncertainty on the parametrisation of the angular background is estimated by using a constant background as opposed to a 2^{nd} order Chebychev polynomial. This has no significant impact on the values of the angular observables.

Event Selection

The two sources of possible systematic uncertainty from the event selection are from the consideration of peaking backgrounds and from the treatment of multiple candidates. Peaking background decays such as $B_s^0 \to K^{*0}\ \mu^+\mu^-$ and $B_s^0 \to \phi\ \mu^+\mu^-$ are difficult to account for in the angular fit because the angular distribution of the decay products is not well known. A conservative estimate of the contribution from these decays is assumed by assigning a 5% systematic to the events that have $A_{\mathrm{FB}} = \pm 1$, $F_{\mathrm{L}} = 0, 1$. This method gives a total estimate of the systematic uncertainty from peaking backgrounds of approximately 2%.

The treatment of multiple candidates is systematically accounted for by removing

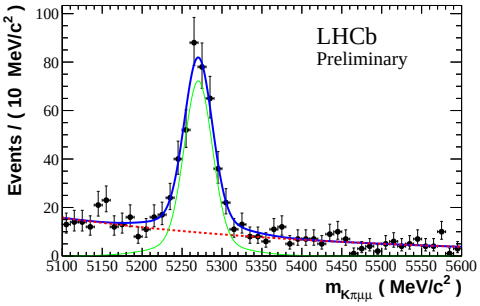

Figure 5.17: The fit to the $m_{K\pi\mu^+\mu^-}$ invariant mass distribution of selected $B^0 \to K^{*0}\mu^+\mu^-$ candidates from $0.37\,\text{fb}^{-1}$. The fit to the mass distribution gives an estimate of 337 ± 21 signal events.

all events with multiple candidates. The fraction of events with multiple candidates is between 1-2% and consists mainly of $K \leftrightarrow \pi$ swapped candidates. This has no impact on the final values for the angular observables.

Tables of systematic uncertainties

5.7 Results

The results for the angular analysis of $B^0 \to K^{*0}\mu^+\mu^-$ for $.38\,\text{fb}^{-1}$ and $1.0\,\text{fb}^{-1}$ of data collected at LHCb are presented below. A measurement of the differential branching fraction of $B^0 \to K^{*0}\mu^+\mu^-$ was obtained by fitting the invariant mass distribution of selected candidates in each q^2 bin and normalising to $B^0 \to J/\psi\, K^{*0}$.

5.7.1 Angular analysis of $0.38\,\text{fb}^{-1}$ of data

The invariant mass distribution of the selected $B^0 \to K^{*0}\mu^+\mu^-$ candidates in the data is shown in Fig. 5.17. The fit gives an estimate of 337 ± 21 signal events with a background of 97 ± 6 events. The measured values of A_{FB}, F_{L} and the differential branching fraction of $B^0 \to K^{*0}\mu^+\mu^-$ are shown in Fig. 5.18. The central values for the angular observables along with the statistical and systematic errors are given in Table 5.4. All of the values for the angular observables lie within the physical limits of A_{FB} and F_{L} (Section 3.4) except for the values for the $14.18 < q^2 < 16\,\text{GeV}^2$ bin. The statistical errors for the physically valid A_{FB} and F_{L} values are given by the Bayesian error estimate with a prior that the points

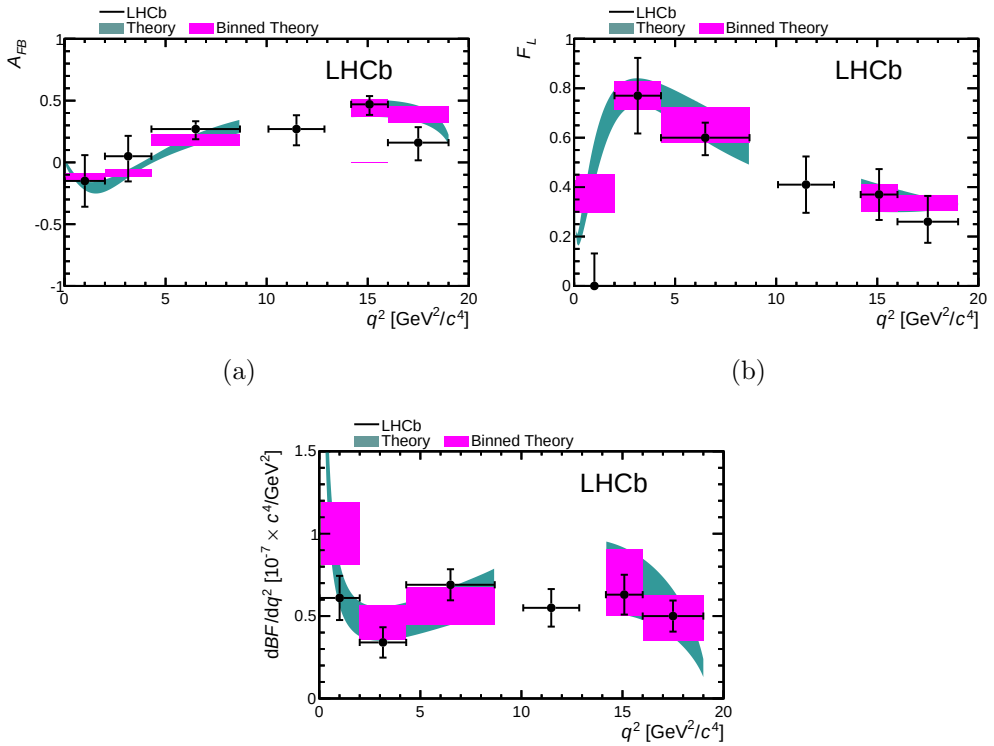

Figure 5.18: The final results from the angular analysis of $B^0 \to K^{*0}\mu^+\mu^-$ at LHCb using $0.38\,\text{pb}^{-1}$ of data collected in 2011 at 7 TeV. Values for A_{FB}, F_{L} and the differential branching fraction are extracted in the six different bins of q^2. The Standard Model prediction is from [11]

Table 5.4: The central values and statistical plus systematic uncertainties for A_{FB}, F_L and $d\mathcal{B}/dq^2$ for the $0.38\,\text{fb}^{-1}$ angular analysis. The first, asymmetric, set of errors is given by the Bayesian error estimate, with a prior that the points sit within the physical region. The second error is the systematic error on A_{FB}, F_L and the branching fraction.

$q^2(\,\text{GeV}^2/c^4)$	A_{FB}	F_{L}	$d\mathcal{B}/dq^2$ $(\times 10^{-7}\,\text{GeV}^{-2}c^4)$
$0.10 < q^2 < 2.00$	$-0.15^{+0.20}_{-0.20} \pm 0.06$	$0.00^{+0.13}_{-0.00} \pm 0.02$	$0.61 \pm 0.12 \pm 0.06$
$2.00 < q^2 < 4.30$	$+0.05^{+0.16}_{-0.20} \pm 0.04$	$0.77^{+0.15}_{-0.15} \pm 0.03$	$0.34 \pm 0.09 \pm 0.02$
$4.30 < q^2 < 8.68$	$+0.27^{+0.06}_{-0.08} \pm 0.02$	$0.60^{+0.06}_{-0.07} \pm 0.01$	$0.69 \pm 0.08 \pm 0.05$
$10.09 < q^2 < 12.86$	$+0.27^{+0.11}_{-0.13} \pm 0.02$	$0.41^{+0.11}_{-0.11} \pm 0.03$	$0.55 \pm 0.09 \pm 0.07$
$14.18 < q^2 < 16.00$	$+0.47^{+0.06}_{-0.08} \pm 0.03$	$0.37^{+0.09}_{-0.09} \pm 0.05$	$0.63 \pm 0.11 \pm 0.05$
$16.00 < q^2 < 19.00$	$+0.16^{+0.11}_{-0.13} \pm 0.06$	$0.26^{+0.10}_{-0.08} \pm 0.03$	$0.50 \pm 0.08 \pm 0.05$
$1.00 < q^2 < 6.00$	$-0.06^{+0.13}_{-0.14} \pm 0.04$	$0.55^{+0.10}_{-0.10} \pm 0.03$	$0.42 \pm 0.06 \pm 0.03$

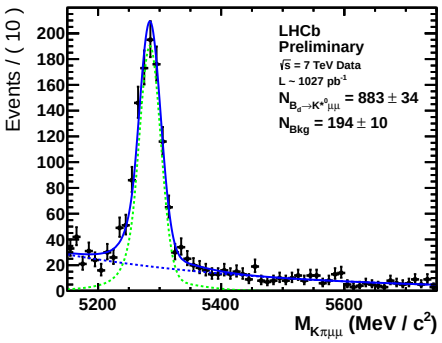

Figure 5.19: The fit to invariant mass distribution of selected $B^0 \to K^{*0}\mu^+\mu^-$ candidates from $1.0\,\text{fb}^{-1}$ of data. The fit gives and estimate of 900 ± 34 candidates.

sit within the physical region. To extract a physical value for the $14.18 < q^2 < 16\,\text{GeV}^2$ bin, the lowest value of the likelihood was taken and the errors obtained by integrating the likelihood to reach one σ coverage. These were the most precise measurements of the angular observables at the time of publication.

5.7.2 Analysis of $1.0\,\text{fb}^{-1}$ of data

The invariant mass distribution of selected $B^0 \to K^{*0}\mu^+\mu^-$ candidates is shown in Fig. 5.19 and there are an estimated 900 ± 34 signal candidates in $1.0\,\text{fb}^{-1}$ of data. The results for seven angular observables are presented in Table 5.5. The values for the differential branching fraction are presented in Table 5.6. The results are also shown in Fig. 5.20, Fig. 5.21, and Fig. 5.22 along with the theoretical prediction from [11] where available.

5.8 Conclusions

The angular analysis of $B^0 \to K^{*0}\mu^+\mu^-$ at LHCb was performed on both $0.38\,\text{fb}^{-1}$ and $1.0\,\text{fb}^{-1}$ of data taken in 2011.

Clean samples of $B^0 \to K^{*0}\mu^+\mu^-$ candidates were selected using both a cut-based selection and a multi-variate algorithm. There were around 340 candidates in $0.38\,\text{fb}^{-1}$ and 900 candidates in $1.0\,\text{fb}^{-1}$ of data. The first dataset is comparable to previous results from the BaBar, Belle and CDF and the second dataset is the largest sample of $B^0 \to K^{*0}\mu^+\mu^-$ candidates at one experiment to date.

Table 5.5: Fraction of longitudinal polarisation of the K^{*0}, $F_{\rm L}$, dimuon system forward backward asymmetry, $A_{\rm FB}$, and the angular observables S_3, S_9 and A_9 from the $B^0 \to K^{*0}\mu^+\mu^-$ decay in six bins of q^2. The lower table includes the transverse observables $A_{\rm T}^{\rm Re}$ and $A_{\rm T}^2$ that are thought to have reduced form factor uncertainties. Results are also presented in the $1 < q^2 < 6\,{\rm GeV}^2/c^4$ range where theoretical uncertainties are best controlled.

q^2 $({\rm GeV}^2/c^4)$	$F_{\rm L}$	$A_{\rm FB}$	S_3	S_9
$0.10 - 2.00$	$0.36\,^{+0.11\,+0.05}_{-0.10\,-0.03}$	$-0.02\,^{+0.13\,+0.03}_{-0.12\,-0.00}$	$-0.05\,^{+0.09\,+0.01}_{-0.10\,-0.01}$	$0.06\,^{+0.10\,+0.01}_{-0.10\,-0.00}$
$2.00 - 4.30$	$0.74\,^{+0.01\,+0.02}_{-0.12\,-0.02}$	$-0.20\,^{+0.08\,+0.02}_{-0.08\,-0.01}$	$-0.04\,^{+0.09\,+0.01}_{-0.08\,-0.01}$	$-0.03\,^{+0.11\,+0.01}_{-0.04\,-0.01}$
$4.30 - 8.68$	$0.55\,^{+0.08\,+0.03}_{-0.07\,-0.03}$	$0.16\,^{+0.05\,+0.01}_{-0.06\,-0.02}$	$0.07\,^{+0.07\,+0.01}_{-0.08\,-0.01}$	$0.01\,^{+0.07\,+0.01}_{-0.08\,-0.00}$
$10.09 - 12.86$	$0.48\,^{+0.09\,+0.02}_{-0.07\,-0.04}$	$0.28\,^{+0.07\,+0.02}_{-0.06\,-0.02}$	$-0.16\,^{+0.11\,+0.01}_{-0.08\,-0.01}$	$-0.02\,^{+0.12\,+0.01}_{-0.11\,-0.01}$
$14.18 - 16.00$	$0.33\,^{+0.08\,+0.02}_{-0.09\,-0.03}$	$0.51\,^{+0.08\,+0.02}_{-0.05\,-0.02}$	$0.03\,^{+0.09\,+0.02}_{-0.11\,-0.01}$	$0.00\,^{+0.10\,+0.01}_{-0.09\,-0.01}$
$16.00 - 19.00$	$0.38\,^{+0.10\,+0.03}_{-0.08\,-0.03}$	$0.30\,^{+0.08\,+0.01}_{-0.08\,-0.02}$	$-0.22\,^{+0.11\,+0.02}_{-0.09\,-0.01}$	$0.06\,^{+0.11\,+0.01}_{-0.11\,-0.02}$
$1.00 - 6.00$	$0.65\,^{+0.08\,+0.03}_{-0.07\,-0.03}$	$-0.15\,^{+0.07\,+0.02}_{-0.07\,-0.01}$	$-0.03\,^{+0.08\,+0.01}_{-0.08\,-0.00}$	$-0.05\,^{+0.08\,+0.01}_{-0.08\,-0.01}$

q^2 $({\rm GeV}^2/c^4)$	A_9	$A_{\rm T}^2$	$A_{\rm T}^{\rm Re}$
$0.10 - 2.00$	$0.12\,^{+0.10\,+0.01}_{-0.09\,-0.01}$	$-0.16\,^{+0.30\,+0.03}_{-0.31\,-0.03}$	$-0.04\,^{+0.25\,+0.03}_{-0.24\,-0.01}$
$2.00 - 4.30$	$0.07\,^{+0.12\,+0.00}_{-0.09\,-0.01}$	$-0.32\,^{+0.65\,+0.05}_{-0.49\,-0.04}$	$-1.00\,^{+0.15\,+0.05}_{-0.00\,-0.01}$
$4.30 - 8.68$	$-0.14\,^{+0.07\,+0.02}_{-0.06\,-0.01}$	$0.33\,^{+0.30\,+0.01}_{-0.31\,-0.05}$	$0.51\,^{+0.15\,+0.00}_{-0.14\,-0.05}$
$10.09 - 12.86$	$0.00\,^{+0.12\,+0.01}_{-0.11\,-0.01}$	$-0.60\,^{+0.41\,+0.06}_{-0.18\,-0.02}$	$0.72\,^{+0.14\,+0.02}_{-0.15\,-0.03}$
$14.18 - 16.00$	$-0.07\,^{+0.11\,+0.02}_{-0.08\,-0.00}$	$0.07\,^{+0.26\,+0.00}_{-0.28\,-0.04}$	$1.00\,^{+0.00\,+0.01}_{-0.05\,-0.02}$
$16.00 - 19.00$	$0.00\,^{+0.11\,+0.01}_{-0.10\,-0.01}$	$-0.71\,^{+0.34\,+0.07}_{-0.25\,-0.04}$	$0.64\,^{+0.14\,+0.01}_{-0.14\,-0.03}$
$1.00 - 6.00$	$0.02\,^{+0.08\,+0.01}_{-0.08\,-0.00}$	$0.15\,^{+0.39\,+0.04}_{-0.42\,-0.02}$	$-0.57\,^{+0.25\,+0.03}_{-0.22\,-0.06}$

Table 5.6: Signal yield ($N_{\rm sig}$) and differential branching fraction ($d\mathcal{B}/dq^2$) of the $B^0 \to K^{*0}\mu^+\mu^-$ decay in the six q^2 bins used in this analysis. Results are also presented in the $1 < q^2 < 6\,{\rm GeV}^2/c^4$ range where theoretical uncertainties are best controlled. The final uncertainty on $d\mathcal{B}/dq^2$ comes from an estimate of the pollution from $B^0 \to K^+\pi^-\mu^+\mu^-$ in the $792 < m_{K^+\pi^-} < 992\,{\rm MeV}/c^2$ mass window.

q^2 $({\rm GeV}^2/c^4)$	$N_{\rm sig}$	$d\mathcal{B}/dq^2$ $(10^{-7}\,{\rm GeV}^{-2}c^4)$
$0.10 - 2.00$	140 ± 13	$0.61 \pm 0.08 \pm 0.05\,^{+0.00}_{-0.05}$
$2.00 - 4.30$	73 ± 11	$0.30 \pm 0.05 \pm 0.03\,^{+0.00}_{-0.02}$
$4.30 - 8.68$	271 ± 19	$0.50 \pm 0.05 \pm 0.04\,^{+0.00}_{-0.04}$
$10.09 - 12.86$	168 ± 15	$0.43 \pm 0.05 \pm 0.04\,^{+0.00}_{-0.03}$
$14.18 - 16.00$	115 ± 12	$0.57 \pm 0.07 \pm 0.04\,^{+0.00}_{-0.05}$
$16.00 - 19.00$	116 ± 13	$0.42 \pm 0.05 \pm 0.04\,^{+0.00}_{-0.03}$
$1.00 - 6.00$	197 ± 17	$0.35 \pm 0.04 \pm 0.04\,^{+0.00}_{-0.03}$

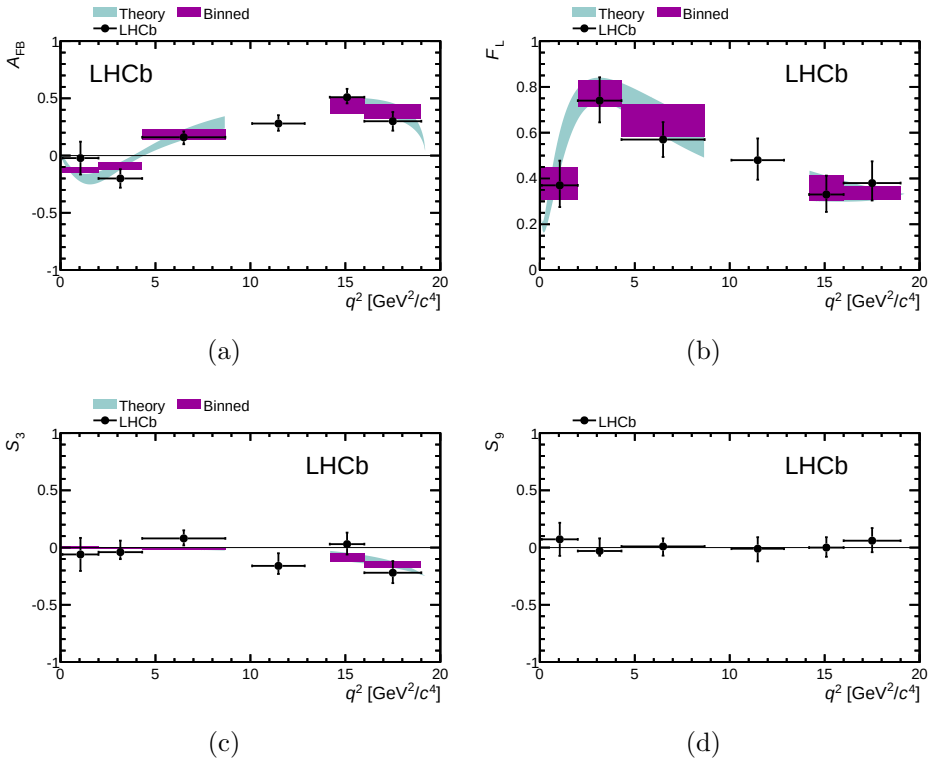

Figure 5.20: The final results from the angular analysis of $B^0 \to K^{*0}\mu^+\mu^-$ at LHCb using $1.0\,\text{fb}^{-1}$ of data collected in 2011 at 7 TeV. Values for the original observables are extracted in the six different bins of q^2. The Standard Model prediction is from [11].

The candidates were corrected for the acceptance effect introduced by the reconstruction and selection by applying a weight to each event. The first analysis used a k-nearest-neighbour method to calculate the efficiency to selected simulated events at a point in $\cos\theta_l$ and $\cos\theta_K$. This was an accurate calculation but the prevision and accuracy was limited by the number of simulated candidates in the regions of phase space with low efficiency. The second analysis calculated the efficiency from a function fitted to each of the $\cos\theta_l$, $\cos\theta_K$ and ϕ distributions independently. This limitation of this method is that it assumes that the efficiency factorises into each dimension, which introduces additional sources of systematic uncertainty. The method of weighting each of the $B^0 \to K^{*0}\mu^+\mu^-$ candidate for their acceptance was chosen over the alternative method, of combining the signal model and a function for the efficiency, in order to minimise the number of free parameters in the final model. This allowed measurement of the angular observables using the multi-dimensional angular distribution which fully incorporated the correlations between the angular observables.

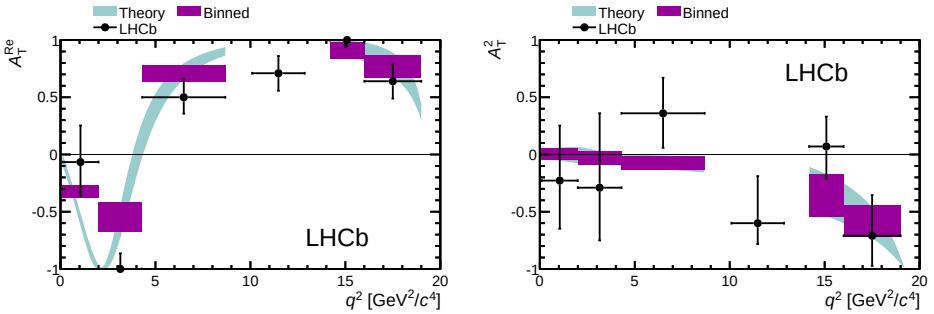

(a)

(b)

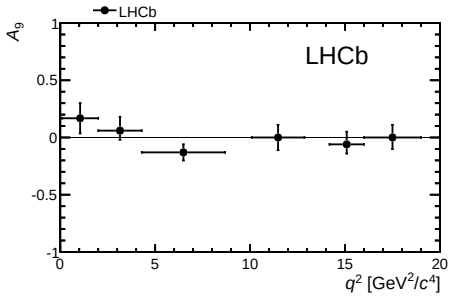

(c)

Figure 5.21: The final results from the angular analysis of $B^0 \to K^{*0}\mu^+\mu^-$ at LHCb using $1.0\,\text{fb}^{-1}$ of data collected in 2011 at 7 TeV. Values for the the reparameterised observables and the CP asymmetric observable A_9 are extracted in the six different bins of q^2. The Standard Model prediction is from [11].

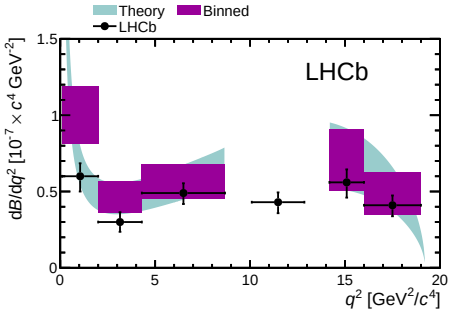

(a)

Figure 5.22: The final results from the angular analysis of $B^0 \to K^{*0}\mu^+\mu^-$ at LHCb using $1.0\,\text{fb}^{-1}$ of data collected in 2011 at 7 TeV. The differential branching fraction is extracted in the six different bins of q^2. The Standard Model prediction is from [11].

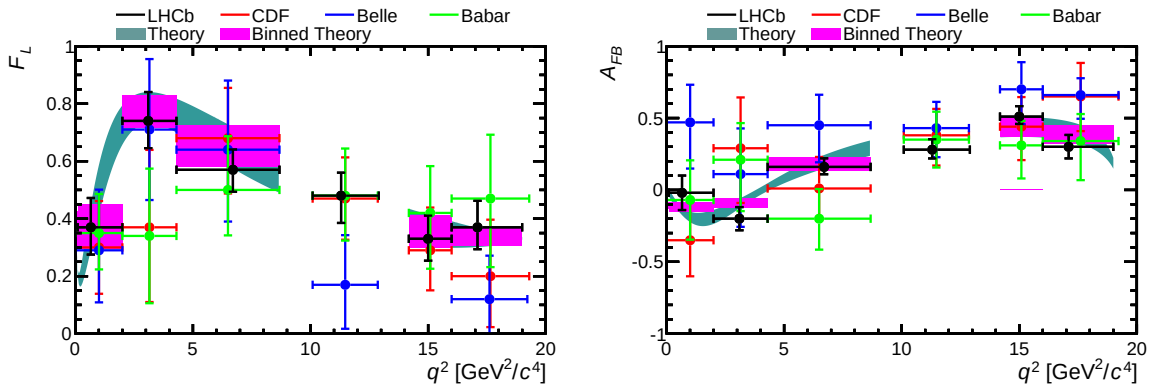

(a) (b)

Figure 5.23: The measurements of the angular observables $F_{\rm L}$ and $A_{\rm FB}$ from LHCb, BaBar [6,7], Belle [8] and CDF [9,10] along with the theoretical prediction from Ref. [11]. It is possible to see that the LHCb results are the most precise and are compatible with the SM prediction.

The acceptance effect and the data-simulation corrections were the dominant sources of systematic uncertainty for both analyses. This is because the events with lowest efficiency, at extreme $\cos\theta_l$ and high $\cos\theta_K$, have a large effect on the central value of $A_{\rm FB}$ and $F_{\rm L}$. This can be improved by a better understanding of the simulation and the efficiency to select $B^0 \to K^{*0}\mu^+\mu^-$ candidates but the understanding of the efficiency in this region of phase space is a limitation on the accuracy of the measurement.

The first angular analysis obtained the worlds most precise measurements of the observables $A_{\rm FB}$ and $F_{\rm L}$ as well as measuring the differential branching fraction. The second angular analysis improved the measurements of $A_{\rm FB}$ and $F_{\rm L}$ as well as measuring several new angular observables for the first time. The measurements of $A_{\rm FB}$ and $F_{\rm L}$ from LHCb along with the measurements from BaBar, Belle and CDF are shown in Figure 5.23.

The combination of these results, along with other radiative, semi-leptonic and purely leptonic decays has enabled stringent limits to be set on the values for the Wilson coefficients $\mathcal{C}_7$, $\mathcal{C}_9$ and $\mathcal{C}_{10}$ along with a high limit on the mass scale of any particle that contributes via electroweak penguin diagrams [12, 105, 106]. These constraints affect any new physics model that contains high mass particles with flavour couplings, providing a model-independent test of the mass scale of contributions from physics beyond the standard model.

Chapter 6

The effect of an S-wave on the angular analysis of $B^0 \to K^+\pi^-\ell^+\ell^-$

This chapter is the work of the author except where referenced. This work was published in Ref [3]. This work was based on Ref. [107] and uses different values for the angular observables than were measured in the previous chapter. This does not affect the conclusions of this chapter since the size of the bias comes from the size of the dilution factor coming from the $K\pi$ S-wave contribution.

6.1 Introduction

With the acquisition of large data sets of $B^0 \to K^{*0}\ell^+\ell^-$ decays, it is possible to study the validity of some of the assumptions that have been made to measure the angular observables in experiments to date. Nearly all theoretical papers to date use the assumption that for the $K\pi$ system the natural width of the $K^{*0}(892)$ can be ignored. This means there is no interference with other $K\pi$ resonances. Existing $B^0 \to K^{*0}\ell^+\ell^-$ analyses consider $B^0 \to K^{*0}\ell^+\ell^-$ signal with $K\pi$ candidates in a narrow mass window around the $K^{*0}(892)$. However, in this region there is evidence of a broad S-wave below the $K^{*0}(892)$ and higher mass states which decay strongly to $K\pi$, such as the S-wave $K_0^{*0}(1430)$ and the D-wave $K_2^{*0}(1430)$ [13]. The best understanding of the low mass S-wave contribution comes from the analysis of $K\pi$ scattering at the LASS experiment [108].

The interference of an S-wave in a predominantly P-wave system has previously been used to disambiguate otherwise equivalent solutions for the value of the *CP*-violating phase in B^0 [109] and B_s^0 [110] oscillations. In the determination of ϕ_s in the $B_s^0 \to J/\psi\,\phi$ decay it was also shown that it is required to take the S-wave contribution into account [111] and this has subsequently been done for the experimental measurements described in [99, 112, 113]. In Chapter 5, the S-wave was included as a systematic error on the analysis. Here, the K^{*0} is used for any neutral kaon state which decays to $K\pi$.

In this Chapter, a generic $K\pi$ S-wave contribution to $B^0 \to K^{*0}\ell^+\ell^-$ is included in the angular analysis. The explicit inclusion of a spin-0 S-wave and a spin-1 P-wave state in the $B^0 \to K^+\pi^-\ell^+\ell^-$ angular distribution is developed in Section 6.2. The consequences of including a $K\pi$ S-wave on the angular observables is shown in Section 6.3. The impact of an S-wave contribution on the determination of the theoretical observables is evaluated in Section 6.4. The minimum sample size in which ignoring a $K\pi$ S-wave contribution contributs a significant bias to measurements of the angular observables is found in Section 6.5 along with the minimum S-wave contribution needed to bias the angular observables. Section 6.6 demonstrates how the S-wave contribution can be correctly taken into account and evaluates the effect of this on the angular observables.

6.2 Theoretical formalism of the p^2 spectrum

The $B^0 \to K^+\pi^-\ell^+\ell^-$ angular distribution can be expressed for multiple S-wave states as described in Section 3.2 and Ref. [61]. For $K\pi$ masses below 1200 MeV, the contribution to the amplitudes from the higher K^{*0} states is small enough that it can be ignored. In order to understand the S-wave contribution to the $B^0 \to K^+\pi^-\ell^+\ell^-$ angular distribution close to the $K^{*0}(892)$ so only the $J = 0, 1$ terms in the sums of Eq. 3.12 were considered.

The S-wave contribution to these amplitudes only enters in the amplitude $\mathcal{A}_0$,

$$\mathcal{A}_{H0} = \sqrt{\frac{1}{4\pi}} A_{0H0} + \sqrt{\frac{3}{4\pi}} A_{1H0} \cos\theta_K \tag{6.1}$$

$$\mathcal{A}_{H||} = \sqrt{\frac{3}{8\pi}} A_{1H||} \sin\theta_K \tag{6.2}$$

$$\mathcal{A}_{H\perp} = \sqrt{\frac{3}{8\pi}} A_{1H\perp} \sin\theta_K \tag{6.3}$$

where the spherical harmonics are expanded, leaving the phase space factor, the propagator and the matrix element as part of the spin-dependent amplitudes

$$\begin{aligned} A_{0,H,0} &\propto \rho(p^2, q^2) \times M_{0,H,0}(q^2) \times P_0(p^2), \\ A_{1,H,0} &\propto \rho(p^2, q^2) \times M_{1,H,0}(q^2) \times P_1(p^2), \\ A_{1,H,\perp} &\propto \rho(p^2, q^2) \times M_{1,H,\perp}(q^2) \times P_1(p^2), \\ A_{1,H,||} &\propto \rho(p^2, q^2) \times M_{1,H,||}(q^2) \times P_1(p^2), \end{aligned} \tag{6.4}$$

where the first index denotes the spin. The normalisation from the three-body phase space factor is described in more detail below.

6.2.1 Phase space factors

The phase space for the four-body decay $B^0 \to K^+\pi^-\ell^+\ell^-$ can be described by three three-body phase space factors

$$\rho(B^0 \to (K\pi)(\ell^+\ell^-)) \times \rho((K\pi) \to K\pi) \times \rho((\ell^+\ell^-) \to \ell^+\ell^-)\,. \tag{6.5}$$

The three-body phase space factor is

$$\rho(a \to bc) = \left(\frac{\sqrt{\lambda(a,b,c)}}{8\pi a^2} \right)^{2J+1} \tag{6.6}$$

where $\lambda(a,b,c) = (a^2 + b^2 + c^2)^2 - 4b^2c^2$ is the triangle function and J is the difference in spin of a and b. The phase space for $B^0 \to K^+\pi^-\ell^+\ell^-$ as a function of p^2 and q^2 is given in Fig. 6.1. The region of S-wave and P-wave interference is mainly at p^2 values below

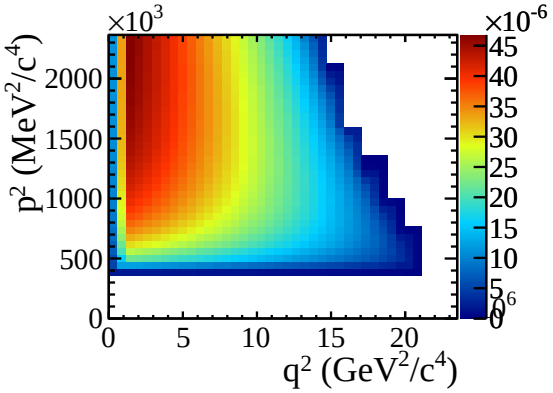

Figure 6.1: The phase space for $B^0 \to K^+\pi^-\ell^+\ell^-$ as a function of p^2 and q^2. The kinematic edge for the high mass K^{*0} states is clearly seen.

$1200^2\,\mathrm{MeV}^2/c^4$ where there is a small reduction in phase space at high q^2.

6.2.2 Propagator functions

The propagator for the P-wave is described by a relativistic Breit-Wigner distribution with the amplitude given by

$$P_1(p^2) = \frac{m_{K_1^{*0}}\Gamma_{K_1^{*0}}(p^2)}{m^2_{K_1^{*0}} - p^2 + i\; m_{K_1^{*0}}\Gamma_{K_1^{*0}}(p^2)} \tag{6.7}$$

where $m_{K_1^{*0}}$ is the resonant mass and

$$\Gamma_{K_1^{*0}}(p^2) = \Gamma^0_{K_1^{*0}} \left(\frac{t}{t_0}\right)^{2J+1} \left(\frac{m_{K_1^{*0}}}{p}\right) \frac{B\,(tR_P)}{B\,(t_0R_P)} \tag{6.8}$$

the running width. Here t is the K^+ momentum in the rest frame of the $K\pi$ system and t_0 is t evaluated at the $K\pi$ pole mass. B is the Blatt-Weisskopf damping factor [114] with a radius R_P. For P-wave the value of R_P is taken to be $3.0\,\mathrm{GeV}^{-1}$ (from Ref [115]). The amplitude can be defined in terms of a phase (δ) through the substitution

$$\cot\delta = \frac{p^2 - m^2_{K_1^{*0}}}{\Gamma_{m_{K_1^{*0}}}(p^2) m_{K_1^{*0}}} \tag{6.9}$$

Table 6.1: Parameters of the $K\pi$ resonances used to generate toy data sets. The K^* masses and widths are taken from Ref. [13] and the K_1^{*0} Blatt-Weisskopf radius and the LASS parameters are taken from Ref. [115]

State.	mass (MeV)	Γ (MeV)	R $(\,\mathrm{GeV})^{-1}$	r $(\,\mathrm{GeV})^{-1}$	a $(\,\mathrm{GeV})^{-1}$	δ_{J}
K_0^{*0}	1425 ± 50	270 ± 80	1.0	1.94	1.73	π
K_1^{*0}	894.94 ± 0.22	48.7 ± 0.8	3.0			0
K_2^{*0}	1432.4 ± 1.3	109 ± 5	1.5			0

to give the polar form of the relativistic Breit-Wigner propagator

$$P_1(p^2) = \frac{1}{\cot\delta - i} \tag{6.10}$$

The LASS parametrisation of the S-wave [108] can be used to describe a generic $K\pi$ S-wave. In this parametrisation, the S-wave propagator is defined as

$$P_0(p^2) = \frac{p}{t}\left(\frac{1}{\cot\delta_B - i} + e^{2i\delta_B}(\frac{1}{\cot\delta_R - i})\right) \tag{6.11}$$

where the first term is an empirical term from inelastic scattering and the second term is the resonant contribution with a phase factor to retain unitarity. The first phase factor is defined as

$$\cot\delta_B = \frac{1}{ta} + \frac{1}{2}rt, \tag{6.12}$$

where r and a are free parameters and t is defined previously, while the second phase factor describes the $K_0^{*0}(1430)$ through

$$\cot\delta_R = \frac{p^2 - m_{\mathrm{S}}^2}{\Gamma_{\mathrm{S}}(p^2)m_{\mathrm{S}}}. \tag{6.13}$$

Here, m_{S} is the S-wave pole mass and Γ_{S} is the running width using the pole mass of the $K_0^{*0}(1430)$. The overall strong phase shift between the results from the LASS scattering experiment and measured values for $B^0 \to J/\psi\ K\pi$ has been found to be consistent with π [109]. The parameters for the p^2 spectrum used are given in Table 6.1.

6.2.3 Angular coefficients

The angular terms modified by the inclusion of the S-wave are $I_{1,2,4,5,7,8}$ and the complete set of angular terms expressed in terms of the spin-dependent amplitudes are

$$
\begin{aligned}
I_1^c &= \frac{1}{4\pi}|A_{0L0}|^2 + \frac{3}{4\pi}|A_{1L0}|^2\cos^2\theta_K + 2\frac{\sqrt{3}}{4\pi}|A_{0L0}||A_{1L0}|\cos\delta^L_{0,0}\cos\theta_K + (L\to R)\\
I_1^s &= \frac{3}{4}\frac{3}{8\pi}\left(|A_{1L||}|^2 + |A_{1L\perp}|^2 + (L\to R)\right)\ \sin^2\theta_K\\
I_2^c &= -I_1^c, \qquad I_2^s = \frac{1}{3}I_1^s\\
I_3 &= \frac{1}{2}\frac{3}{8\pi}\left(|A_{1L\perp}|^2 - |A_{1L||}|^2 + (L\to R)\right)\sin^2\theta_K\\
I_4 &= \frac{1}{\sqrt{2}}\left[\frac{1}{4\pi}\sqrt{\frac{3}{2}}\Re(A_{0L0}A^*_{1L||})\cos\delta^L_{0,||}\sin\theta_K\right.\\
&\quad\left. + \frac{3}{4\pi}\sqrt{\frac{1}{2}}\Re(A_{1L0}A^*_{1L||})\sin\theta_K\cos\theta_K + (L\to R)\right]\\
I_5 &= \frac{1}{\sqrt{2}}\left[\frac{1}{4\pi}\sqrt{\frac{3}{2}}\Re(A_{0L0}A^*_{1L\perp})\cos\delta^L_{0,\perp}\sin\theta_K\right.\\
&\quad\left. + \frac{3}{4\pi}\sqrt{\frac{1}{2}}\Re(A_{1L0}A^*_{1L\perp})\sin\theta_K\cos\theta_K - (L\to R)\right]\\
I_6 &= 2\frac{3}{8\pi}\left(\Re(A_{1L||}A^*_{1L\perp}) - (L\to R)\right)\sin^2\theta_K\\
I_7 &= \frac{1}{\sqrt{2}}\left[\frac{1}{4\pi}\sqrt{\frac{3}{2}}\Im(A_{0L0}A^*_{1L||})\cos\delta^L_{0,||}\sin\theta_K\right.\\
&\quad\left. + \frac{3}{4\pi}\sqrt{\frac{1}{2}}\Im(A_{1L0}A^*_{1L||})\sin\theta_K\cos\theta_K - (L\to R)\right]\\
I_8 &= \frac{1}{\sqrt{2}}\left[\frac{1}{4\pi}\sqrt{\frac{3}{2}}\Im(A_{0L0}A^*_{1L\perp})\cos\delta^L_{0,\perp}\sin\theta_K\right.\\
&\quad\left. + \frac{3}{4\pi}\sqrt{\frac{1}{2}}\Im(A_{1L0}A^*_{1L\perp})\sin\theta_K\cos\theta_K + (L\to R)\right]\\
I_9 &= \frac{3}{8\pi}\left(\Im(A_{1L||}A^*_{1L\perp}) + (L\to R)\right)\sin^2\theta_K
\end{aligned}
\tag{6.14}
$$

The interference term of I_1 shows how this parametrisation includes the strong phase difference between the S- and P-wave state. The left handed part of the interference term

for I_1 can be written as

$$2|A_{0L0}||A_{1L0}|\cos\delta^L_{0,0} \propto 2\,|M_{0,L,0}||P_0(p^2)||M_{1,L,0}||P_1(p^2)|\cos(\delta^L_{0,0}) \tag{6.15}$$

where

$$\delta^L_{0,0} = \delta_{M_{0L0}} + \delta_{P_0} - \delta_{M_{1L0}} - \delta_{P_1}. \tag{6.16}$$

where $\delta_{M_{JL0}}$ is the phase of the longitudinal matrix element and δ_{P_J} is the phase of the propagator. The phases in the interference terms for $I_{4,5,7,8}$ can be similarly defined. For real matrix elements, i.e. nearly true in the Standard Model, the phases are equal for both handed interference terms $\delta^L = \delta^R$. The phase difference between the S-wave and the P-wave propagators can be expressed as a single strong phase, $\delta_{\rm S}$.

6.2.4 The p^2 spectrum for $B^0 \to K^+\pi^-\ell^+\ell^-$

The p^2 spectrum for the $B^0 \to K^+\pi^-\ell^+\ell^-$ angular distribution can be calculated by summing over the S- and P-waves and integrating out the $\cos\theta_l$, $\cos\theta_K$ and ϕ dependence. This is illustrated in Fig. 6.2 where the matrix elements from Refs. [54,55] at a q^2 value of $6\,\text{GeV}^2$ are used. Here the S-wave amplitude is assumed to be equivalent to the longitudinal P-wave amplitude. The S-wave fraction in the $800 < p < 1000\,\text{MeV}$ window around the P-wave is calculated to be 16% when using this approximation. The size of the S-wave fraction, the P-wave fraction and the interference fraction w.r.t the total branching fraction are given in Fig. 6.3. As will be seen later there are no interference terms left in the angular distribution after the integral over $\cos\theta_K$.

6.3 S-wave observables

The angular observables for the P-wave are defined in Section 3.4. The inclusion of the S-wave in the complete angular distribution means that $A_{\rm FB}$ can no longer be determined by experimentally counting the number of events with forward-going and backward-going

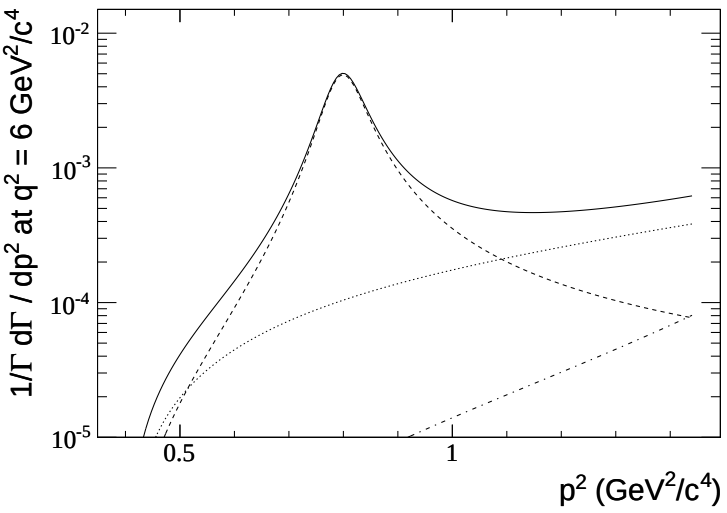

Figure 6.2: An illustration of the p^2 spectrum for the P-wave (dashed) and the S-wave (dotted). The total distribution from both states is the solid line. The values were calculated at $q^2 = 6\,\mathrm{GeV}^2$ by integrating out the angular distribution of $B^0 \to K^+\pi^-\ell^+\ell^-$ using equal matrix elements for each state. The S-wave fraction here is 16% between $800 < p < 1000\,\mathrm{MeV}$

leptons, as Eqs. 3.24 and 3.26 are no longer equivalent. This is because the total normalisation for the angular distribution changes to the sum of S- and P-wave amplitudes,

$$\Gamma'' \equiv \frac{\mathrm{d}^2\Gamma}{\mathrm{d}p^2\mathrm{d}q^2} = |A_{10}|^2 + |A_{1||}|^2 + |A_{1\perp}|^2 + |A_{00}|^2. \tag{6.17}$$

such that there is a factor of

$$\mathcal{F}_{\mathrm{P}}(p^2, q^2) = \left(\frac{|A_{10}|^2 + |A_{1||}|^2 + |A_{1\perp}|^2}{|A_{10}|^2 + |A_{1||}|^2 + |A_{1\perp}|^2 + |A_{00}|^2} \right) \tag{6.18}$$

between the pure P-wave and the admixture of the S- and the P-wave. This is the fraction of the yield coming from the P-wave at a given value of p^2 and q^2. Similarly, the S-wave fraction is defined as

$$\mathcal{F}_{\mathrm{S}}(p^2, q^2) = \left(\frac{|A_{00}|^2}{|A_{10}|^2 + |A_{1||}|^2 + |A_{1\perp}|^2 + |A_{00}|^2} \right) \tag{6.19}$$

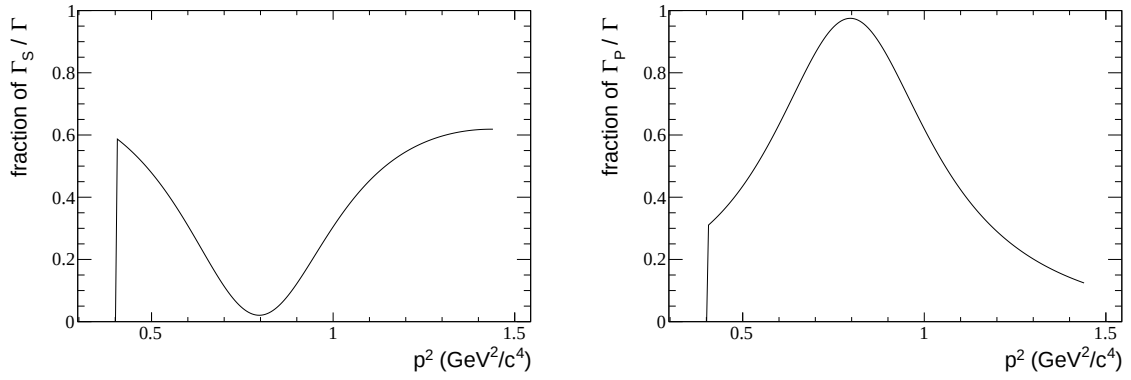

(a)

(b)

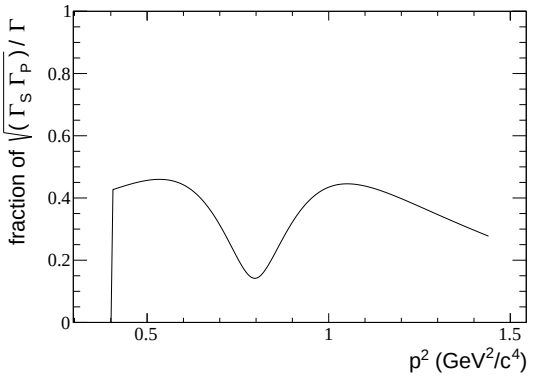

(c)

Figure 6.3: An illustration of the size of the S-wave, P-wave and S↔P-wave interference fractions with respect to the total branching fraction. The values were calculated at $q^2 = 6\,\mathrm{GeV}^2$ by integrating out the angular distribution of $B^0 \to K^+\pi^-\ell^+\ell^-$ using equal matrix elements for each state.

and the interference between the S-wave and the P-wave as

$$\mathcal{A}_{\mathrm{S}}(p^2, q^2) = \frac{\sqrt{3}}{2}\left(\frac{|A_{0L0}||A_{1L0}|\cos\delta_L + (L \to R)}{|A_{10}|^2 + |A_{1||}|^2 + |A_{1\perp}|^2 + |A_{00}|^2}\right) . \tag{6.20}$$

Substituting the above observables into the angular terms gives

$$\begin{aligned}
\frac{I_1^c}{\Gamma''} &= \frac{1}{4\pi}\mathcal{F}_{\rm S} + \frac{3}{4\pi}\mathcal{F}_{\rm P}F_{\rm L}\cos^2\theta_K + \frac{3}{4\pi}\mathcal{A}_{\rm S}\cos\theta_K \\
\frac{I_1^s}{\Gamma''} &= \frac{3}{4}\frac{3}{8\pi}\mathcal{F}_{\rm P}\left(1-F_{\rm L}\right)\left(1-\cos^2\theta_K\right) \\
\frac{I_2^c}{\Gamma''} &= -\left(\frac{1}{4\pi}\,\mathcal{F}_{\rm S} + \frac{3}{4\pi}\mathcal{F}_{\rm P}\left(1-F_{\rm L}\right)\cos^2\theta_K + \frac{3}{4\pi}\mathcal{A}_{\rm S}\cos\theta_K\cos\theta_K\right), \\
\frac{I_2^s}{\Gamma''} &= \frac{1}{4}\frac{3}{8\pi}\mathcal{F}_{\rm P}\left(1-F_{\rm L}\right)\left(1-\cos^2\theta_K\right) \\
\frac{I_3}{\Gamma''} &= \frac{1}{2}\frac{3}{8\pi}\mathcal{F}_{\rm P}A_{\rm T}^2\left(1-\cos^2\theta_K\right) \\
\frac{I_6}{\Gamma''} &= 2\frac{3}{8\pi}\frac{4}{3}\mathcal{F}_{\rm P}A_{\rm FB}\left(1-\cos^2\theta_K\right) \\
\frac{I_9}{\Gamma''} &= \frac{3}{8\pi}\mathcal{F}_{\rm P}A_{\rm Im}\left(1-\cos^2\theta_K\right)\,.
\end{aligned} \tag{6.21}$$

Following what is described in Section 3.2, simplification of the angular distribution can be achieved by folding the distribution in ϕ such that $\phi' = \phi - \pi$ for $\phi < 0$ [60]. The $I_{4,5,7,8}$ angular terms which are dependent on $\cos\phi$ or $\sin\phi$ are cancelled, leaving $I_{1,2,3,6}$, in the angular distribution:

$$\begin{aligned}
\frac{\mathrm{d}^5\Gamma}{\mathrm{d}q^2\mathrm{d}p^2\mathrm{d}\cos\theta_K\mathrm{d}\cos\theta_l\mathrm{d}\phi'} =& \frac{3}{8}\Big(I_1^c + 2I_1^s + \left(I_2^c + 2I_2^s\right)\cos 2\theta_l + 2I_3\sin^2\theta_l\cos 2\phi' \\
&+2I_6\cos\theta_l + 2\sqrt{2}I_9\sin^2\theta_l\sin 2\phi'\Big)\,.
\end{aligned} \tag{6.22}$$

Combining Equation 6.22 with 6.21 gives the differential decay distribution,

$$\begin{aligned}\frac{1}{\Gamma''}\frac{\mathrm{d}^5\Gamma}{\mathrm{d}q^2\mathrm{d}p^2\mathrm{dcos}\theta_K\mathrm{dcos}\theta_l\mathrm{d}\phi'} = \frac{9}{16\pi}\Bigg(&\left(\frac{2}{3}\mathcal{F}_\mathrm{S} + \frac{4}{3}\mathcal{A}_\mathrm{S}\cos\theta_K\right)(1-\cos^2\theta_l) \\ &+ \mathcal{F}_\mathrm{P}\Bigg[2F_\mathrm{L}\cos^2\theta_K(1-\cos^2\theta_l) \\ &+ \frac{1}{2}(1-F_\mathrm{L})(1-\cos^2\theta_K)(1+\cos^2\theta_l) \\ &+ \frac{1}{2}(1-F_\mathrm{L})A_\mathrm{T}^2(1-\cos^2\theta_K)(1-\cos^2\theta_l)\cos 2\phi' \\ &+ \frac{4}{3}A_\mathrm{FB}(1-\cos^2\theta_K)\cos\theta_l \\ &+ A_\mathrm{Im}(1-\cos^2\theta_K)(1-\cos^2\theta_l)\sin 2\phi'\Bigg]\Bigg).\end{aligned} \tag{6.23}$$

which is a combination of the P-wave observables and the transverse angular observables. The angular distribution as a function of $\cos\theta_l$ and $\cos\theta_K$ is given by integrating over ϕ in Eq. 6.23

$$\begin{aligned}\frac{1}{\Gamma''}\frac{\mathrm{d}^4\Gamma}{\mathrm{d}q^2\mathrm{d}p^2\mathrm{d}\cos\theta_K\mathrm{d}\cos\theta_l} = \frac{9}{16}\Bigg(&\left(\frac{2}{3}\mathcal{F}_\mathrm{S} + \frac{4}{3}\mathcal{A}_\mathrm{S}\cos\theta_K\right)(1-\cos^2\theta_l) \\ &+ \mathcal{F}_\mathrm{P}\Bigg[2F_\mathrm{L}\cos^2\theta_K(1-\cos^2\theta_l) \\ &+ \frac{1}{2}(1-F_\mathrm{L})(1-\cos^2\theta_K)(1+\cos^2\theta_l) \\ &+ \frac{4}{3}A_\mathrm{FB}(1-\cos^2\theta_K)\cos\theta_l\Bigg]\Bigg)\end{aligned} \tag{6.24}$$

and further integration from Equation 6.23 yields the angular distribution for each of the

angles,

$$\begin{aligned}
\frac{1}{\Gamma''}\frac{\mathrm{d}^3\Gamma}{\mathrm{d}q^2\mathrm{d}p^2\mathrm{dcos}\theta_l} &= \frac{3}{4}\mathcal{F}_{\mathrm{S}}(1-\cos^2\theta_l) + \mathcal{F}_{\mathrm{P}}\Bigg[\frac{3}{4}F_{\mathrm{L}}(1-\cos^2\theta_l) \\
&\quad + \frac{3}{8}(1-F_{\mathrm{L}})(1+\cos^2\theta_l) + A_{\mathrm{FB}}\cos\theta_l\Bigg], \\
\frac{1}{\Gamma''}\frac{\mathrm{d}^3\Gamma}{\mathrm{d}q^2\mathrm{d}p^2\mathrm{dcos}\theta_K} &= \frac{1}{2}\mathcal{F}_{\mathrm{S}} + \mathcal{A}_{\mathrm{S}}\cos\theta_K \\
&\quad + \mathcal{F}_{\mathrm{P}}\left[\frac{3}{2}F_{\mathrm{L}}\cos^2\theta_K + \frac{3}{4}(1-F_{\mathrm{L}})(1-\cos^2\theta_K)\right], \\
\frac{1}{\Gamma''}\frac{\mathrm{d}^3\Gamma}{\mathrm{d}q^2\mathrm{d}p^2\mathrm{d}\phi'} &= \frac{1}{\pi}\left(1 + \frac{3}{4}\mathcal{F}_{\mathrm{S}} + \mathcal{F}_{\mathrm{P}}\left[F_{\mathrm{L}} + \frac{1}{2}(1-F_{\mathrm{L}})A_{\mathrm{T}}^2\cos 2\phi' + S_3\sin 2\phi'\right]\right).
\end{aligned} \tag{6.25}$$

Angular distribution integrated over p^2

The angular distribution can be integrated over p^2 using the weighted integral

$$O(q^2) = \frac{\int \mathcal{O}(p^2,q^2)\frac{\mathrm{d}^2\Gamma}{\mathrm{d}p^2\mathrm{d}q^2}\mathrm{d}p^2}{\int \frac{\mathrm{d}^2\Gamma}{\mathrm{d}p^2\mathrm{d}q^2}\mathrm{d}p^2} \tag{6.26}$$

for the value of the observables integrated over a given region in p^2. This leads to the integrated observables F_{P}, F_{S} and A_{S} which are solely dependant on q^2. By definition, the fraction of the S-wave and the P-wave sum to one, $F_{\mathrm{S}} + F_{\mathrm{P}} = 1$. The complete angular distribution without any p^2 dependence is given by

$$\begin{aligned}
\frac{1}{\Gamma'}\frac{\mathrm{d}^5\Gamma}{\mathrm{d}q^2\mathrm{dcos}\theta_K\mathrm{dcos}\theta_l\mathrm{d}\phi'} = \frac{9}{16\pi}\Bigg(&\left(\frac{2}{3}F_{\mathrm{S}} + \frac{4}{3}A_{\mathrm{S}}\cos\theta_K\right)(1-\cos^2\theta_l) \\
&+ (1-F_{\mathrm{S}})\Bigg[2F_{\mathrm{L}}\cos^2\theta_K(1-\cos^2\theta_l) \\
&\quad + \frac{1}{2}(1-F_{\mathrm{L}})(1-\cos^2\theta_K)(1+\cos^2\theta_l) \\
&\quad + \frac{1}{2}(1-F_{\mathrm{L}})A_{\mathrm{T}}^2(1-\cos^2\theta_K)(1-\cos^2\theta_l)\cos 2\phi' \\
&\quad + \frac{4}{3}A_{\mathrm{FB}}(1-\cos^2\theta_K)\cos\theta_l \\
&\quad + S_3(1-\cos^2\theta_K)(1-\cos^2\theta_l)\sin 2\phi'\Bigg]\Bigg).
\end{aligned} \tag{6.27}$$

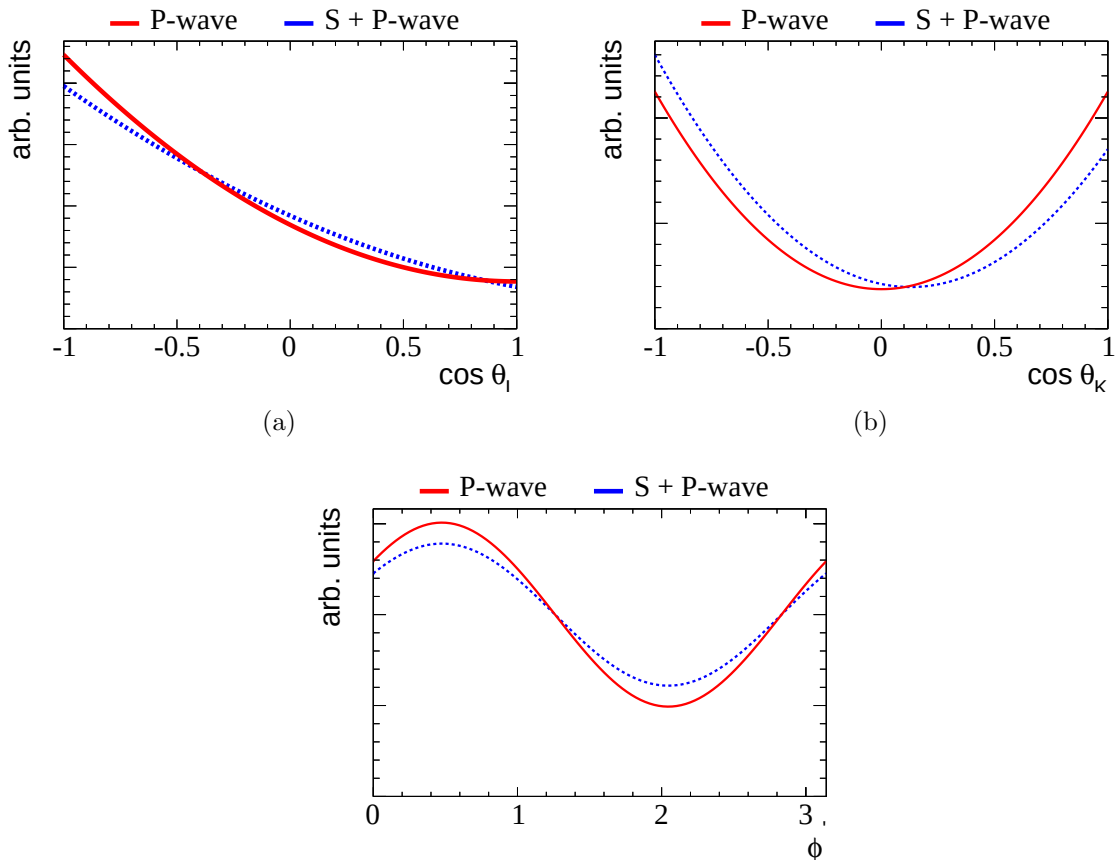

Figure 6.4: One-dimensional projections of (a) $\cos\theta_l$, (b) $\cos\theta_K$, (c) ϕ' for the angular distribution of $B^0 \to K^{*0}\ell^+\ell^-$ with (blue-dashed) and without (red-solid) an S-wave component of 7%. The dilution effect of the S-wave on the asymmetry in $\cos\theta_l$ and the asymmetric effect in $\cos\theta_K$ can be clearly seen.

where the normalisation of the angular distribution is given by

$$\Gamma' = \frac{\mathrm{d}\Gamma}{\mathrm{d}q^2}\,. \tag{6.28}$$

The 'dilution' effect of the S-wave can clearly be seen from the factor of $(1 - F_{\mathrm{S}})$ that appears in front of the observables in Eq. 6.27.

The effect of an S-wave on the angular distribution as a function of $\cos\theta_K$, $\cos\theta_l$ and ϕ' is illustrated in Fig. 6.4. Here it is possible to see that the asymmetry in $\cos\theta_l$, given by A_{FB}, has decreased and that there is an asymmetry in $\cos\theta_K$ introduced by the interference term.

6.4 Testing the effect of a $K\pi$ S-wave

In an angular analysis of $B^0 \to K^+\pi^-\ell^+\ell^-$, the S-wave can be considered to be a systematic effect that could bias the results of the angular observables. The implications of this systematic effect are tested by generating toy Monte Carlo experiments and fitting the angular distribution to them. The results of the fit to the observables are evaluated for multiple toy datasets.

The effect of the S-wave is evaluated for two different cases. Firstly, the effect of S-wave interference is examined as a function of the size of the dataset used. The aim of this study is to explore the possibility of biases in any measurements to date and the possible implications on future measurements of $B^0 \to K^+\pi^-\ell^+\ell^-$. Datasets of sizes between 50 and 1000 events are tested. For comparison, the results from Chapter 5 have between 20 and 200 signal events in the 6 different q^2 bins considered. Second, the effect of different levels of S-wave contribution is examined. At present, the only information about the S-wave fraction is obtained by the measurement of $F_{\rm S}$ of approximately 7% in the decay $B^0 \to J/\psi\, K\pi$ from [109] for the range $800 < p < 1000\,\text{MeV}$. As the value may be different in $B^0 \to K^+\pi^-\ell^+\ell^-$, we consider values of $F_{\rm S}$ in this region ranging from 1% to 60%. The fraction of the S-wave, $F_{\rm S}$, is expected to have some q^2 dependence because of the q^2 dependence of the transverse P-wave amplitudes.

The parameters used to generate the toy datasets are summarised in Tables 6.1 and 6.2. The values of the angular observables used to generate toy Monte Carlo simulations are taken from the analysis of $1.0\,\text{fb}^{-1}$ presented in [107]. Within errors, these measurements are compatible with the Standard Model prediction for $B^0 \to K^{*0}\ell^+\ell^-$ and the central value of the measurement is used. The nominal magnitude and phase difference of the S-wave contribution are taken from the angular analysis of $B^0 \to J/\psi\ K\pi$ [109]. The toy datasets are generated as samples of pure signal in order to test the trend on the bias on the angular observables in the signal distribution that could be incurred from an increasing $K\pi$ S-wave component. As this is a phenomenological study, a background component is not included as this is not expected to affect the trends. The correlation between the S-wave component and any possible background is expected to be small. This

Table 6.2: Parameters used to generate toy datasets. $A_{\rm FB}$, $F_{\rm L}$, $A_{\rm T}^2$ and $A_{\rm Im}$ are taken from [107] in the $1 < q^2 < 6$ ($\rm GeV^2$) bin. The $F_{\rm S}$ value is taken from Ref. [109]

Obs.	$A_{\rm FB}$	$F_{\rm L}$	$A_{\rm T}^2$	$A_{\rm Im}$	$F_{\rm S}$
Value	-0.15	0.65	$0.03/(1-0.65)$	0.05	0.07

.

expectation is based on the results presented in Table X of [116] where the uncertainty in the background on the K^+ K^- S-wave component in the $B_s^0 \to J/\psi$ ϕ final state is evaluated and shown to be small.

The toy datasets are generated as a function of the $\cos\theta_l$, $\cos\theta_K$, ϕ and p^2 using an accept/reject method. The PDF used is the angular distribution given in Eq. 6.23. For each set of input parameters 1000 toy datasets were generated. For each of these toy datasets, an unbinned log likelihood fit is performed that returns the best fit value of the observables and an estimate of their error. The expected experimental resolution is obtained by plotting the best fit values of an observable for the ensemble of toy simulations as illustrated for $A_{\rm FB}$ in Fig. 6.5 (left). The pull value for an observable (O) is defined as

$$p_O^i = \frac{O^i_{\rm fit} - O^i_{\rm gen}}{\sigma^i_O} \tag{6.29}$$

where σ^i_O is the estimated error on the fit to the observable O^i. This distribution is seen in Fig. 6.5 (right). The mean and the width are extracted from a Gaussian fit. For a well performing fit without bias, the pull distribution should have zero mean and unit width. A negative pull value implies that the result is underestimated and a positive pull value implies overestimation of the true observable.

6.5 The impact of ignoring the S-wave in an angular analysis of $B^0 \to K^{*0}\ell^+\ell^-$

The effect of ignoring or including a $K\pi$ S-wave was tested as a function of dataset size in order to find a minimum dataset at which the bias from ignoring the S-wave contribution to the angular distribution when measuring the angular observables becomes significant. Datasets were generated for sample sizes ranging from 50 to 1000 events and analysed

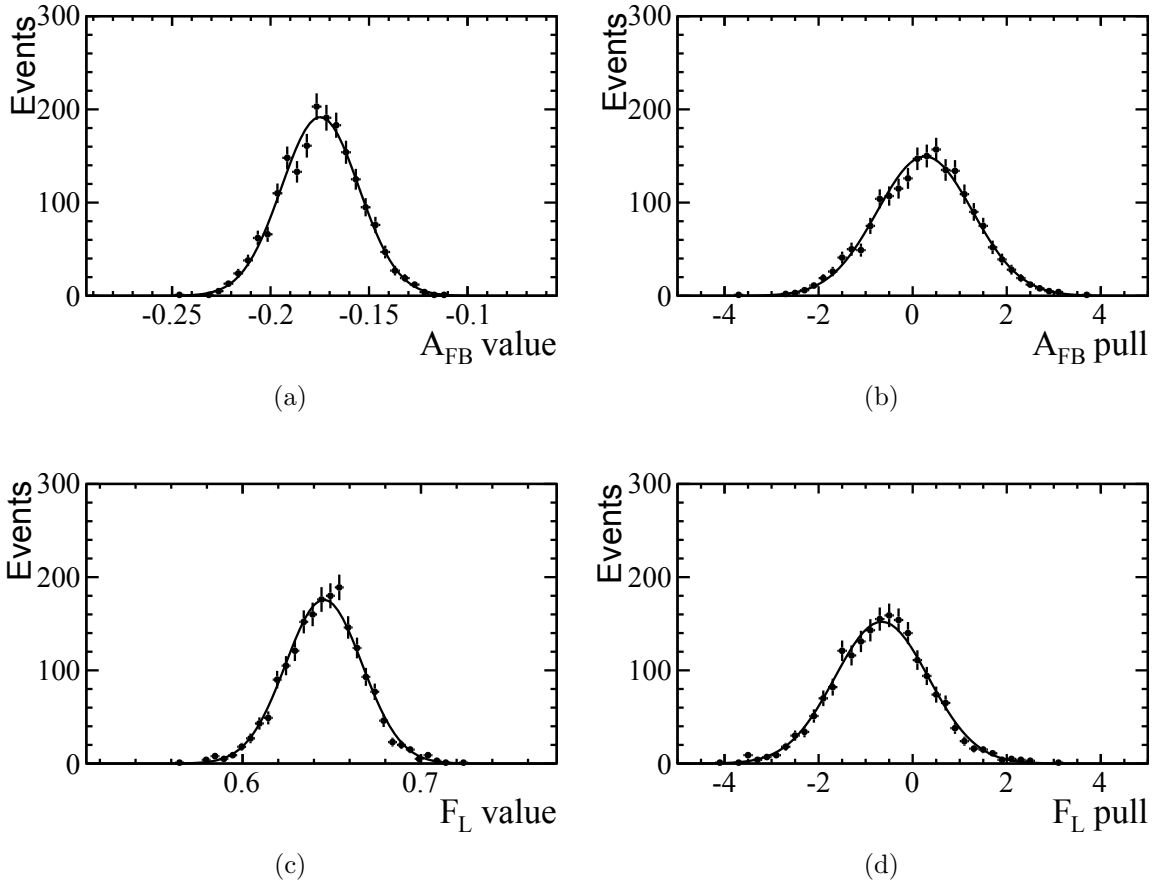

Figure 6.5: Distribution of the results and pull values for $A_{\rm FB}$ (a,b) and $F_{\rm L}$ (c,d) respectively for fits to 1000 toy simulations each containing 1000 events. The S-wave is ignored in these fits. The resolution obtained on $A_{\rm FB}$ is 0.026 ± 0.001. Since the S-wave is ignored there is a non-zero pull mean for both observables at (0.26 ± 0.02) and (-0.65 ± 0.02) respectively. The widths of the pull distribution are consistent with unity at (1.01 ± 0.01) and (0.99 ± 0.01).

assuming a pure P-wave state. The results are shown in Fig. 6.6.

From Eq. 6.24, it can be seen that $A_{\rm T}^2$ has a factor of (1-$F_{\rm L}$) in front of it. The large value of $F_{\rm L}$ used to generated datasets is in turn causing $A_{\rm T}^2$ to have a much worse resolution than $A_{\rm FB}$, $F_{\rm L}$ and S_3. There is significant bias (non-zero mean) of the pull distribution for all observables when the S-wave is ignored in the angular distribution for datasets of more than 200 events. This corresponds to a change of 0.2σ in $F_{\rm L}$ for a dataset of 200 events. The behaviour can be understood in terms of the $(1 - F_{\rm S})$ factor in Eq. 6.24. It gives an offset to the fitted values of the observables which are proportional to the value of $(1 - F_{\rm S})$.

The angular fit was performed on toy datasets with an increasing S-wave contribution.

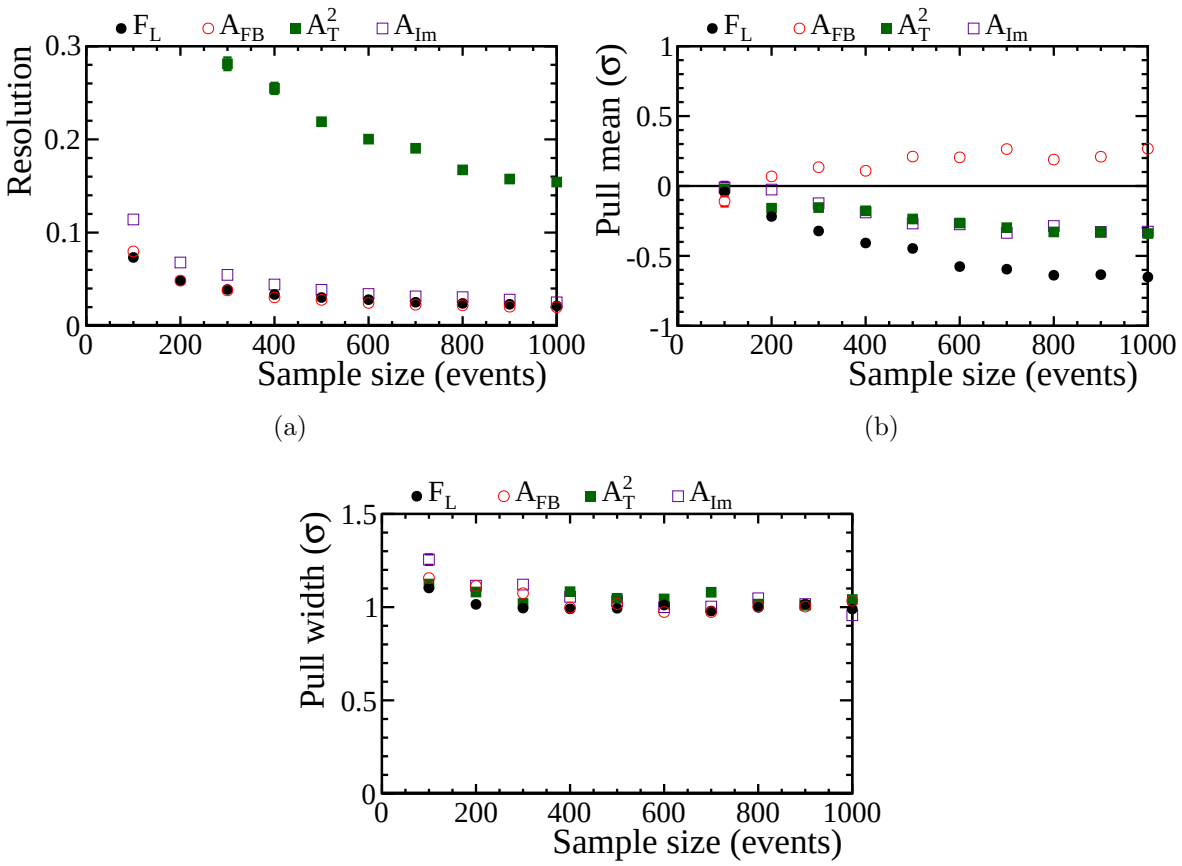

Figure 6.6: Resolution (a), pull mean (b) and pull width (c) of 1000 toy datasets analysed as a pure P-wave state as a function of dataset size. It can be seen that the bias on the observable (non-zero pull mean) increases dramatically as the sample size increases. This is because the statistical error decreases increasing the sensitivity to the ignored S-wave contribution. The bias of $A_{\rm FB}$ is positive because $A_{\rm FB}$ is negative in the q^2 bin chosen.

Datasets of 500 events were generated with a varying S-wave contribution in the narrow p^2 mass window of ($800 < p < 1000\,\text{MeV}$) from no S-wave up to a $F_{\rm S}$ value of 0.4. The resolution and the mean and width of the pull distribution for each of the four observables ($A_{\rm FB}$, $F_{\rm L}$, $A_{\rm T}^2$, S_3) were calculated and the results are shown in Fig. 6.7. Significant bias is seen in the angular observables when the S-wave is ignored for an S-wave magnitude of greater than 5%. The linear increase in the bias is another consequence of the (1-$F_{\rm S}$) factor in the angular distribution.

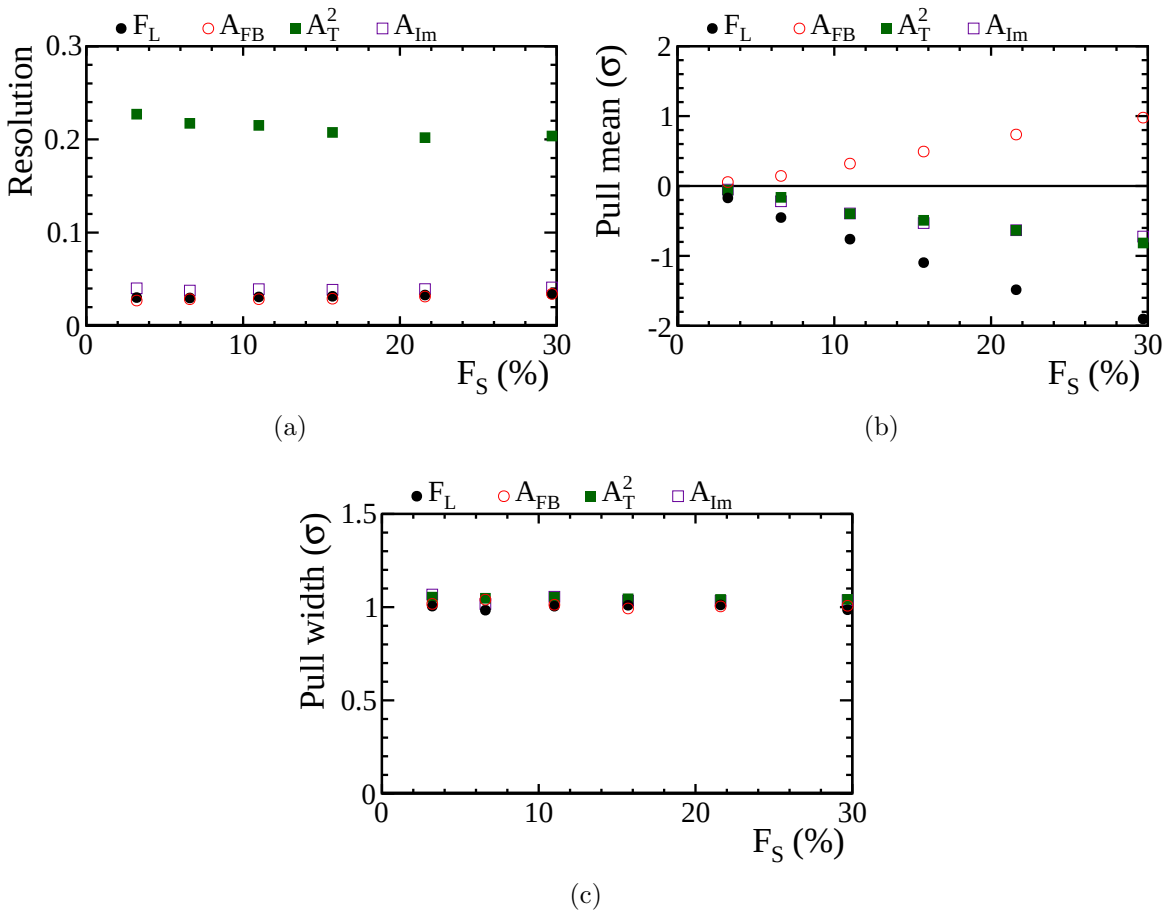

Figure 6.7: The resolution (a) the mean (b) and the width (c) of the pull distribution of 1000 toy datasets analysed as a pure P-wave state as a function of S-wave contribution. The resolution and the bias can be seen to increase with the size of the S-wave contribution in a linear fashion.

6.6 Measuring the S-wave in $B^0 \to K^+\pi^-\ell^+\ell^-$

Obtaining unbiased values for the angular observables beyond the limits shown requires including the S-wave contribution in the angular model. With the formalism developed in Section 6.2, three options are explored for measuring it. The first option is to ignore the p^2 dependence in the measured parameters and simply fit for p^2-averaged values of F_S and A_S. The second option is to fit the p^2 line-shape simultaneously with the angular distribution. This can be done in a small p window between 800 and 1000 MeV or in the region from the lower kinematic threshold to 1200 MeV. In all cases the datasets used to perform the studies are identical to those used in Sect. 5.1 and the dataset and the S-wave sizes refer to the number of events in the smaller p^2 window.

The angular distribution without p^2 dependence is given in Eq. 6.27. For each set of samples, the resolution and the mean and the width of the pull distribution of the angular observables are tested.

The change in the resolution obtained on the angular observables for the three different methods of including the S-wave in the angular distribution (ignoring the p^2 dependence, fitting a narrow p^2 window and fitting a wide p^2 window) is demonstrated by plotting the ratio with respect to the resolution obtained when a single P-wave state is assumed.

The resolution and the mean of the pull distributions for the three different fit methods are shown relative to the resolution and mean obtained using the assumption of a pure P-wave state. The ratio between the fit methods, including the S-wave in the angular distribution and assuming a P-wave state, as a function of dataset size are shown in Fig 6.8. The pull mean for all three fit methods is shown in Fig 6.9. The pull width for all three fit methods is shown in Fig 6.10.

For all observables, it can be seen that the resolution degrades when the S-wave is included and the p^2 dependence is ignored. The resolution degrades by a smaller amount when the p^2 dependence is included in a small bin and the original resolution is recovered to within 10% when using the large p^2 range. There are two effects contributing to the improvement of the resolution. There are more P-wave events in the larger range and the wider mass window allows for the S-wave to be constrained by using the information from above and below the P-wave resonance. This results in the best resolution when the S-wave is included in the angular distribution.

For all the observables, the pull mean approaches zero for datasets of greater than 300 events implying that the bias present in the observables when a pure P-wave state is assumed is removed when an S-wave is included in the angular distribution. This means that the inclusion of the S-wave component will be mandatory for all future experimental analyses.

The ratio of the resolutions for the three different fit methods as a function of increasing S-wave size is given in Fig. 6.11. The pull mean as a function of S-wave contribution for all three fit methods is shown in Fig. 6.12. The pull width as a function of S-wave contribution

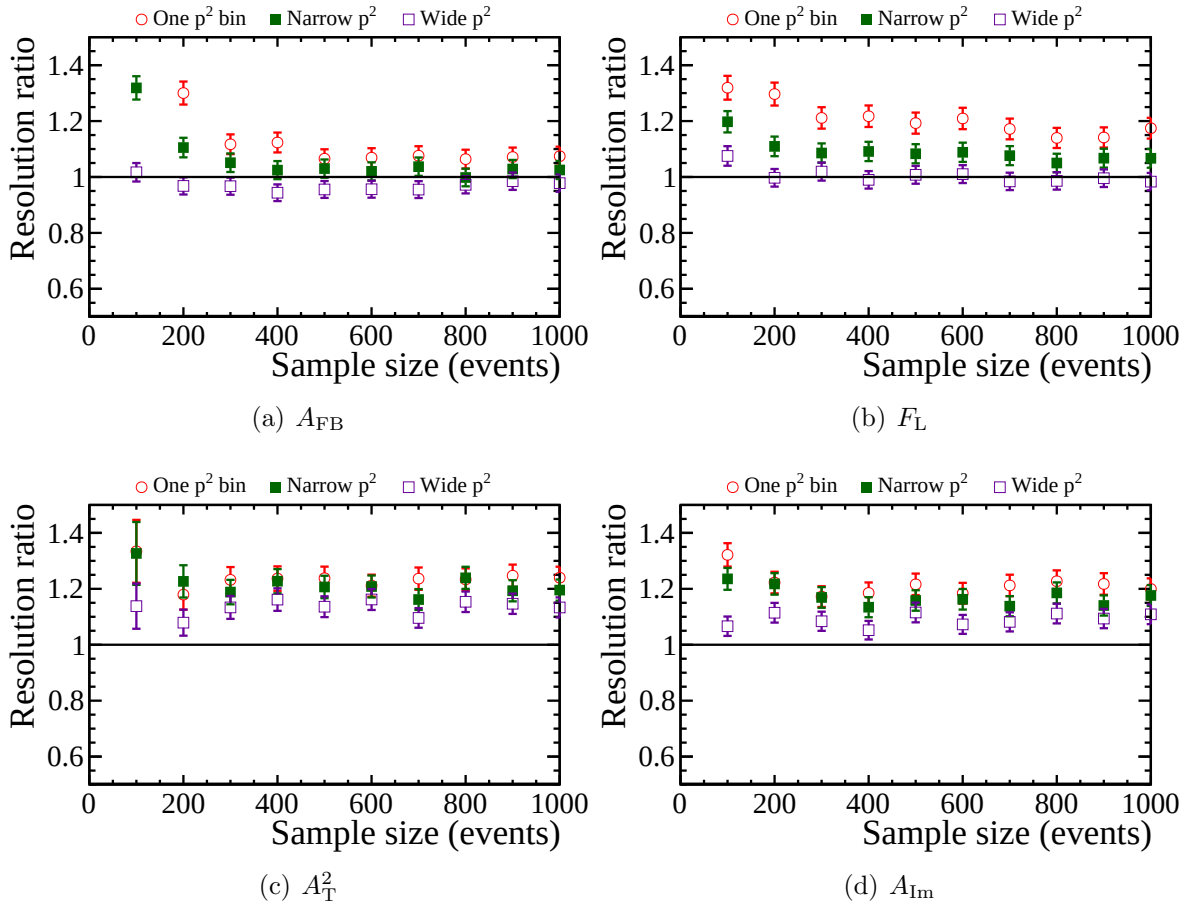

(a) A_{FB} (b) F_{L}

(c) A_{T}^{2} (d) A_{Im}

Figure 6.8: Resolutions for three different methods to incorporate the S-wave relative to the resolution obtained when the S-wave is ignored. It can be seen that the best resolution is obtained when using the largest p^2 window. The original resolution is recovered to within 10%.

for all three fit methods is shown in Fig. 6.13.

6.7 Systematic test

The results shown in Figs. 6.9 and 6.12 could have an implicit model dependence through the use of the LASS parametrisation to model the p^2 spectrum. In order to understand the size of this effect, the measurements were repeated using an isobar model to parametrise the $K\pi$ S-wave as in Ref. [117]. In the isobar model the S-wave is described as a simple sum of functions for the $K_0^{*0}(1430)$ and the $\kappa(800)$ along with a constant non-resonant

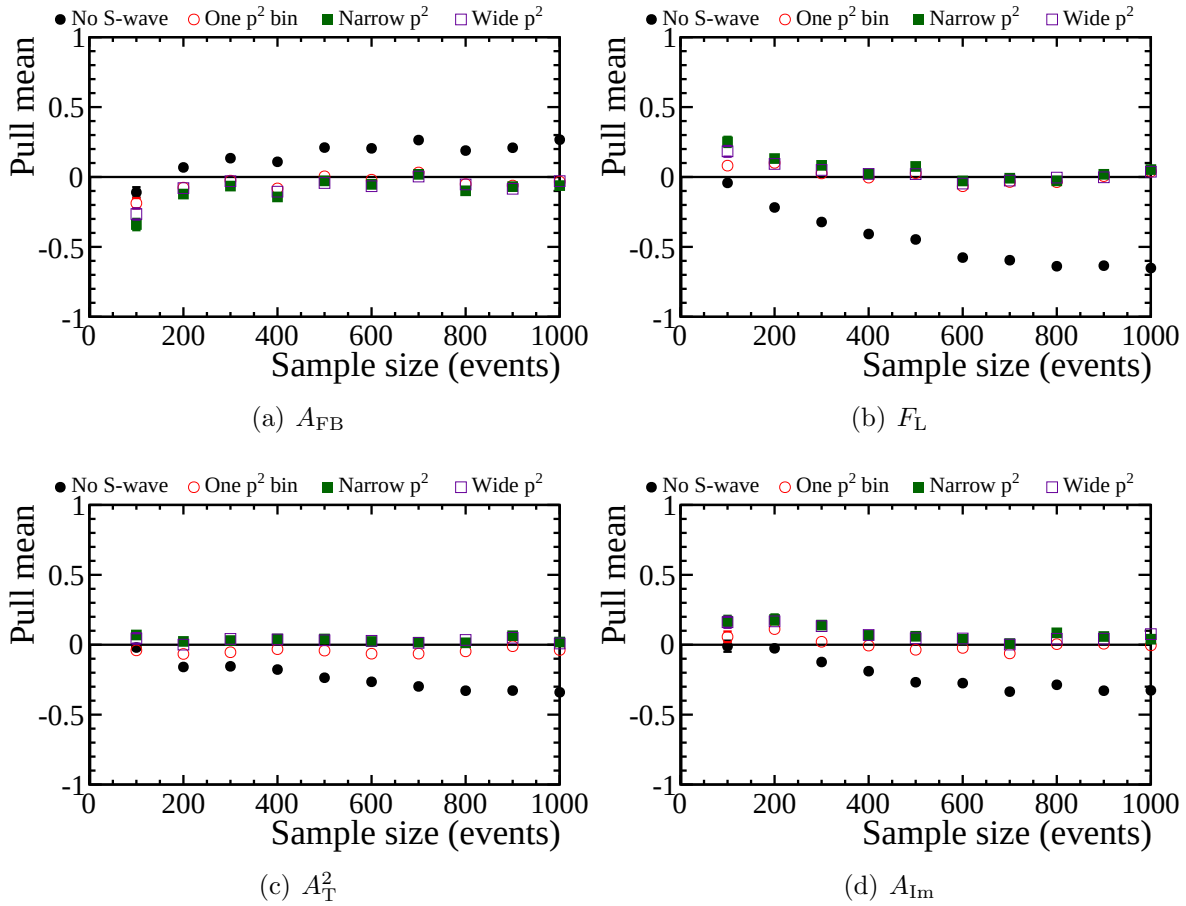

(a) A_{FB} (b) F_{L}

(c) A_{T}^2 (d) A_{Im}

Figure 6.9: Pull mean for the three different methods to incorporate the S-wave and when the S-wave is ignored. There is a slight shift when the S-wave is included for datasets of less than 200 events but this is removed from all the observables when the S-wave is included in the fit for datasets of over 500 events.

term,

$$T_I(p^2) = N_\kappa \mathcal{F}_\kappa(p^2)\exp(\phi_\kappa) + N_S \mathcal{F}_S(p^2)\exp(\phi_S) + NR \tag{6.30}$$

where N_i is the normalisation for each contribution and ϕ_i is the phase of each contribution. The $K_0^{*0}(1430)$ is described by a relativistic Breit-Wigner function as in the LASS parametrisation,

$$\mathcal{F}_S(p^2) = \cot\delta_S = \frac{p^2 - m_{\mathrm{S}}^2}{\Gamma_{\mathrm{S}}(p^2) m_{\mathrm{S}}}. \tag{6.31}$$

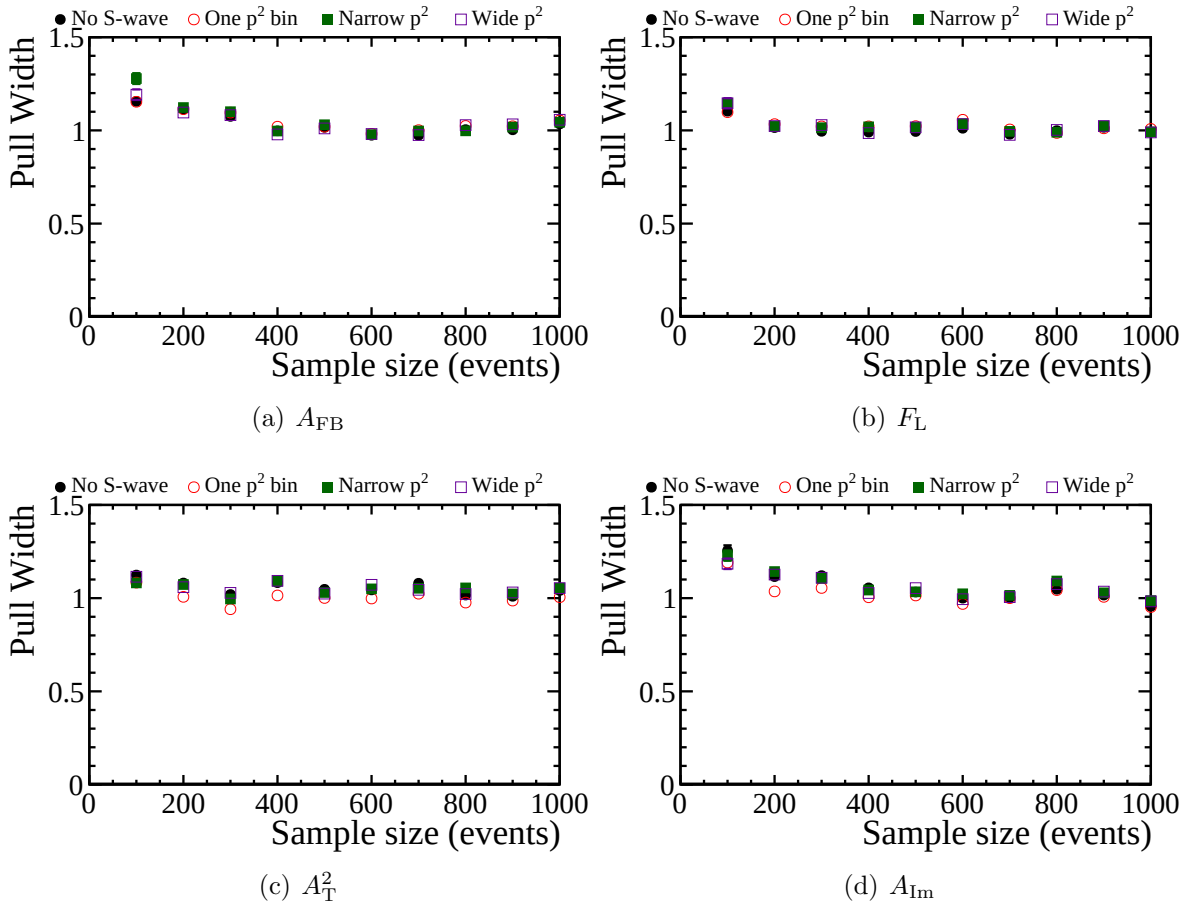

(a) A_{FB} (b) F_{L}

(c) A_{T}^2 (d) A_{Im}

Figure 6.10: Pull width for the three different methods to incorporate the S-wave and when the S-wave is ignored. There is a slight shift when the S-wave is included for datasets of less than 200 events but this is removed from all the observables when the S-wave is included in the fit for datasets of over 500 events.

and the $\kappa(800)$ is described similarly

$$\mathcal{F}_{\kappa}(p^2) = \cot\delta_{\kappa} = \frac{p^2 - m_{\kappa}^2}{\Gamma_{\kappa}(p^2) m_{\kappa}}. \tag{6.32}$$

where the mass and width of the $\kappa(800)$ are taken from Ref. [13]. The existence of the $\kappa(800)$ is under debate with no conclusive evidence. The amplitude T_I is normalised such that it has the same integral as the LASS amplitude (T_S) over the p^2 range from threshold to an upper limit of $2.5\,\mathrm{GeV}^2/c^4$. This limit is chosen to encompass most of resonant $K_0^{*0}(1430)$. The p^2 spectrum of the combined P wave and the two S-wave models is shown in Fig. 6.14.

The model-dependence of the p^2 spectrum was tested by generating events where an

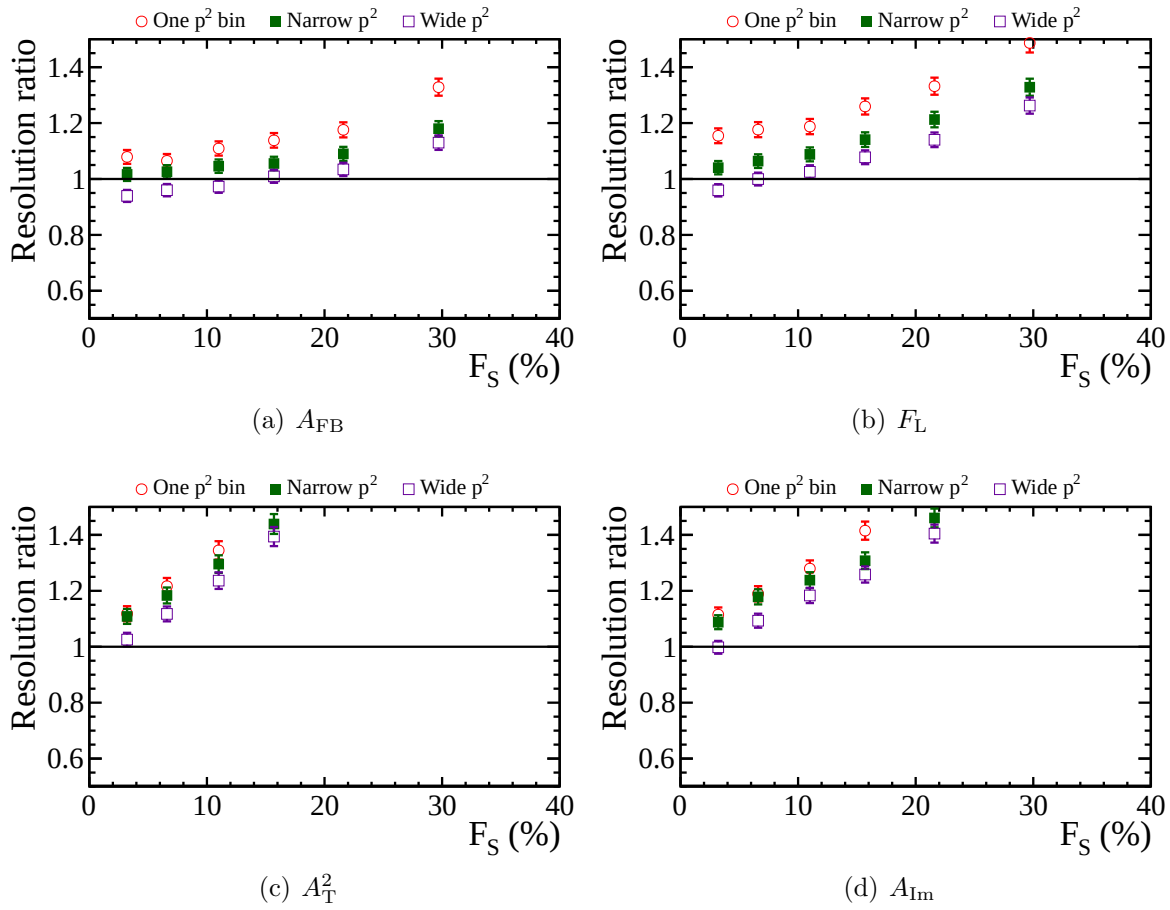

(a) $A_{\rm FB}$ (b) $F_{\rm L}$

(c) $A_{\rm T}^2$ (d) $A_{\rm Im}$

Figure 6.11: Resolutions for three different methods to incorporate the S-wave relative to the resolution obtained when the S-wave is ignored. It can be seen that the best resolution is obtained when using the largest p^2 window. The original resolution is recovered to within 10%.

isobar model was used for the S-wave contribution and fitting the angular distribution using the LASS parametrisation. The relative resolution between the results obtained when generating with the LASS parametrisation and the results obtained when generating with an isobar model are shown in Fig. 6.15. The bias on the central values of the angular observables when the S-wave is ignored as a function of the size of the dataset is shown in Fig. 6.16. From this it is possible to see that the results obtained in Sec. 6.6 are compatible with the results where the events are generated with a different model for the $K\pi$ continuum.

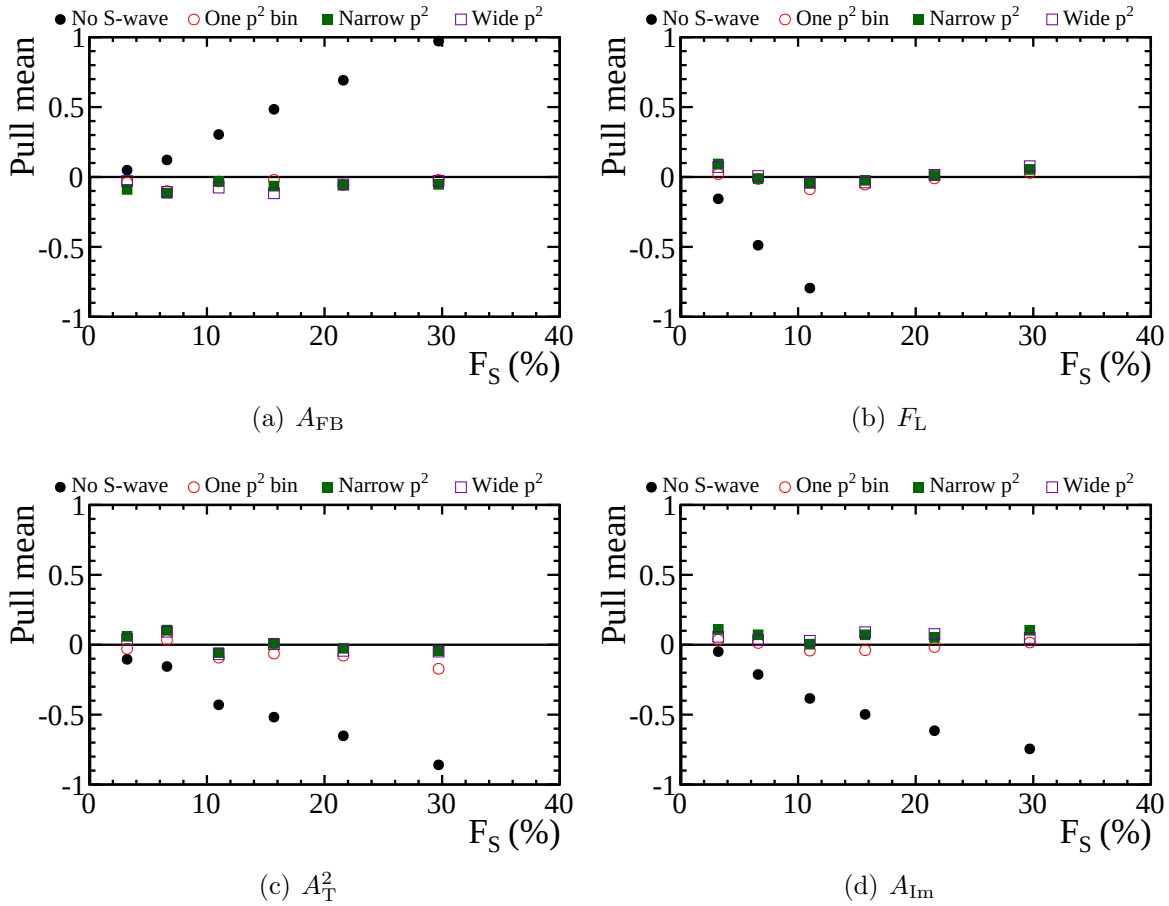

(a) $A_{\rm FB}$ (b) $F_{\rm L}$

(c) $A_{\rm T}^2$ (d) $A_{\rm Im}$

Figure 6.12: Pull mean for the three different methods to incorporate the S-wave and when the S-wave is ignored. There is a slight shift when the S-wave is included for datasets of less than 200 events but this is removed from all the observables when the S-wave is included in the fit for datasets of over 500 events.

6.8 Conclusions

In summary, the inclusion of a resonant $K\pi$ S-wave in the angular analysis of $B^0 \to K^{*0}\ell^+\ell^-$ has been formalised and the complete angular distribution for both an S and P wave state described. The inclusion of an S-wave state has an overall dilution effect on the theoretical observables. The impact of an S-wave on an angular analysis is evaluated using toy Monte Carlo events. The S-wave contribution can only be ignored for datasets of less than 200 events, meaning the angular observables measured in the q^2 bin between 4.3 and 8.68 GeV$^2/c^4$ and between 1 and 6 GeV$^2/c^4$ measured in Chapter 5 may be affected. The bias on the angular observables incurred by assuming a pure P-wave $K\pi$ state can be removed by including the S-wave in the angular distribution. The degradation in resolution

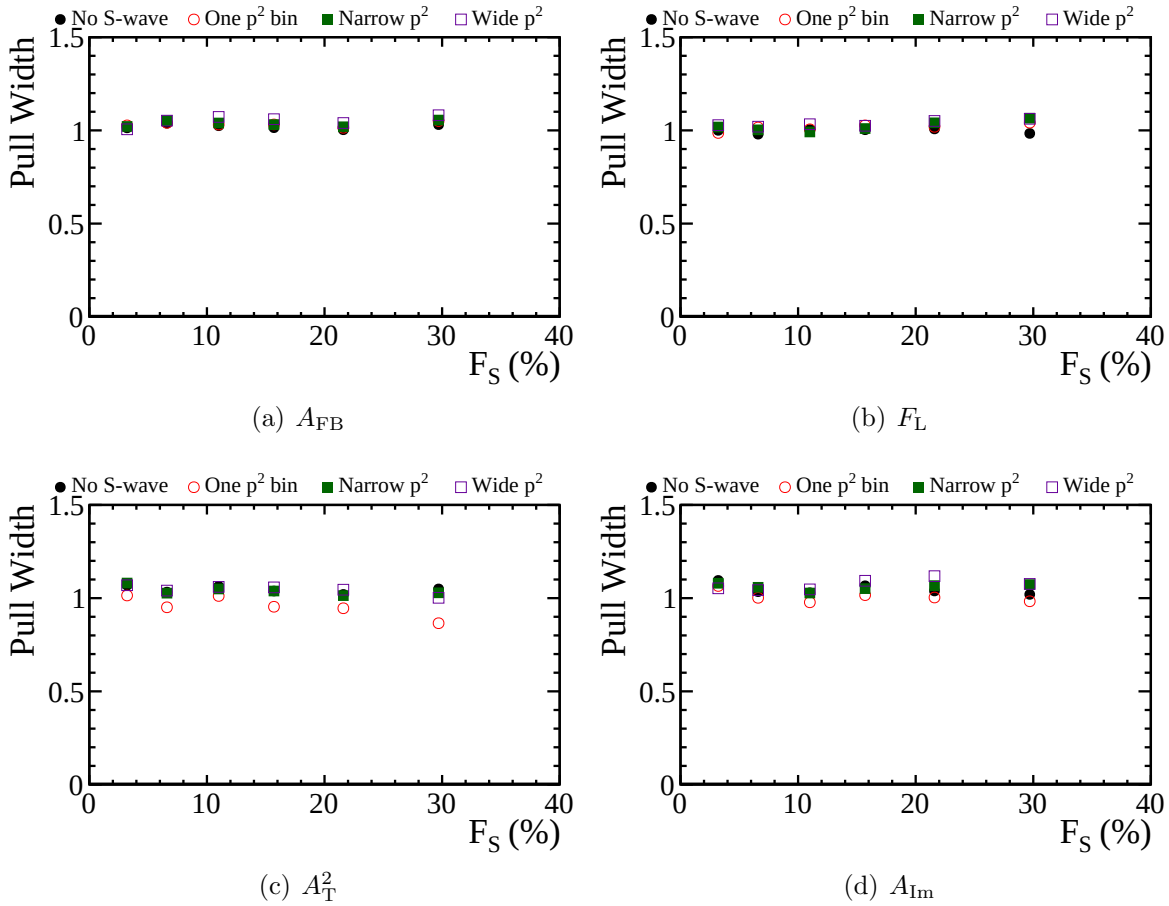

(a) $A_{\rm FB}$ (b) $F_{\rm L}$

(c) $A_{\rm T}^2$ (d) $A_{\rm Im}$

Figure 6.13: Pull width for the three different methods to incorporate the S-wave and when the S-wave is ignored. There is a slight shift when the S-wave is included for datasets of less than 200 events but this is removed from all the observables when the S-wave is included in the fit for datasets of over 500 events.

on the angular observables from fitting a more complicated angular distribution can be minimised by performing the fit in a wide region around the $K^{*0}(892)$ resonance. However, the parameterisation of the $m_{K\pi}$ spectrum also requires consideration of the background component in the wider $m_{K\pi}$ window which may increase the complexity and contribute other biases to measurements of the angular observables.

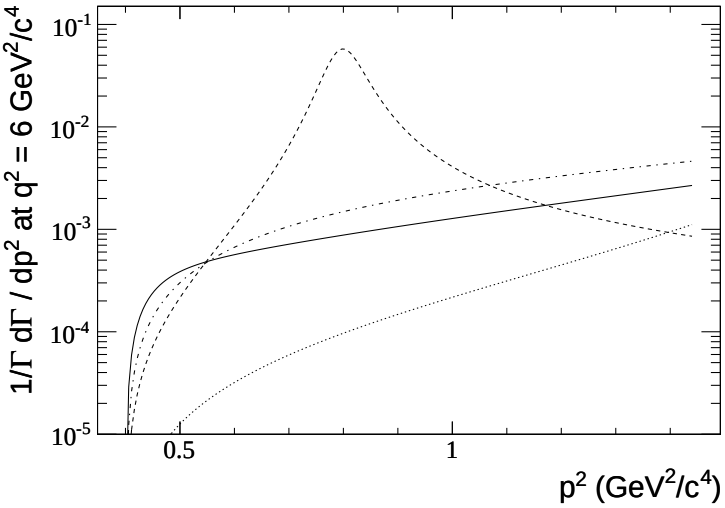

Figure 6.14: An illustration of the p^2 spectrum for the P-wave (solid) and the isobar S-wave (dashed) and the LASS S-wave (dash-dotted) and the D-wave (dotted).

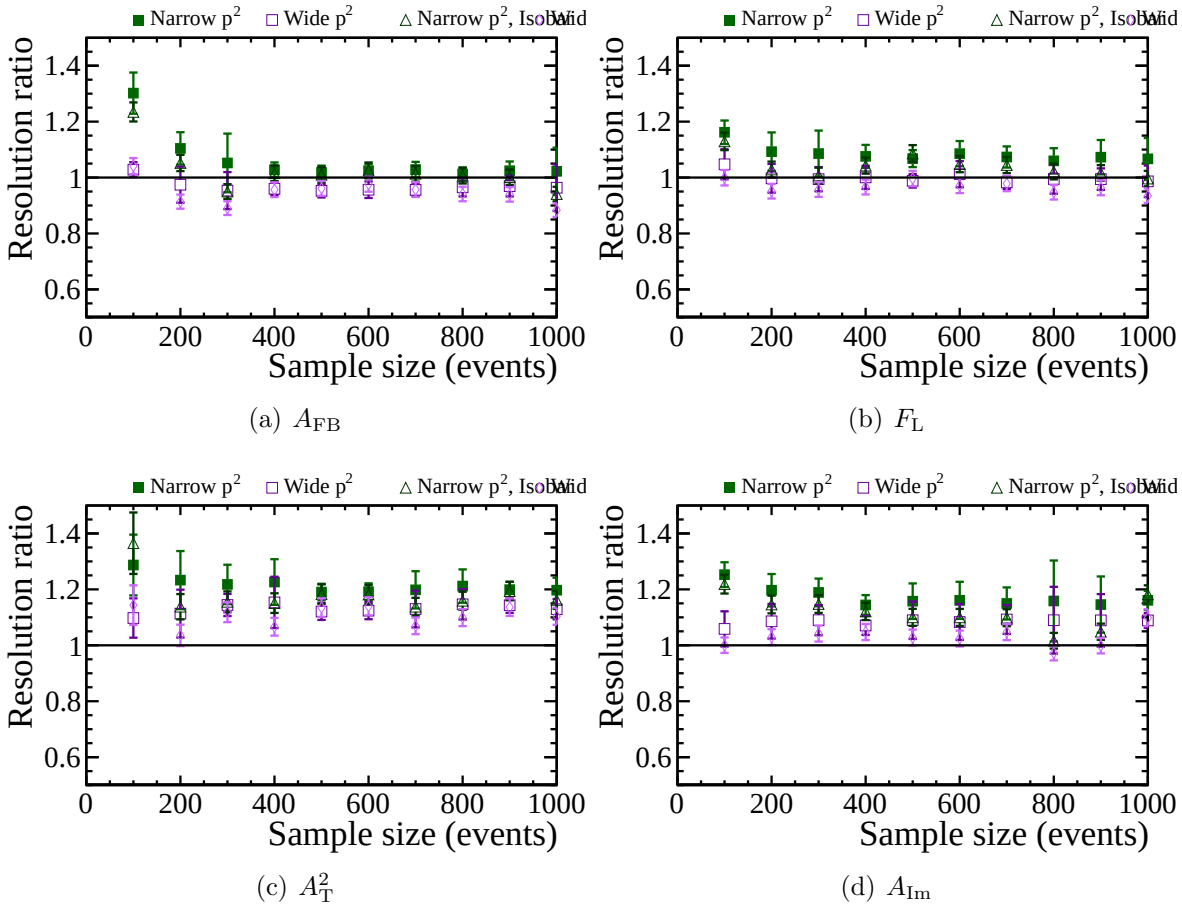

(a) A_{FB} (b) F_{L}

(c) A_{T}^2 (d) A_{Im}

Figure 6.15: Resolutions for three different methods to incorporate the S-wave relative to the resolution obtained when the S-wave is ignored. The S-wave has been generated using an isobar model.

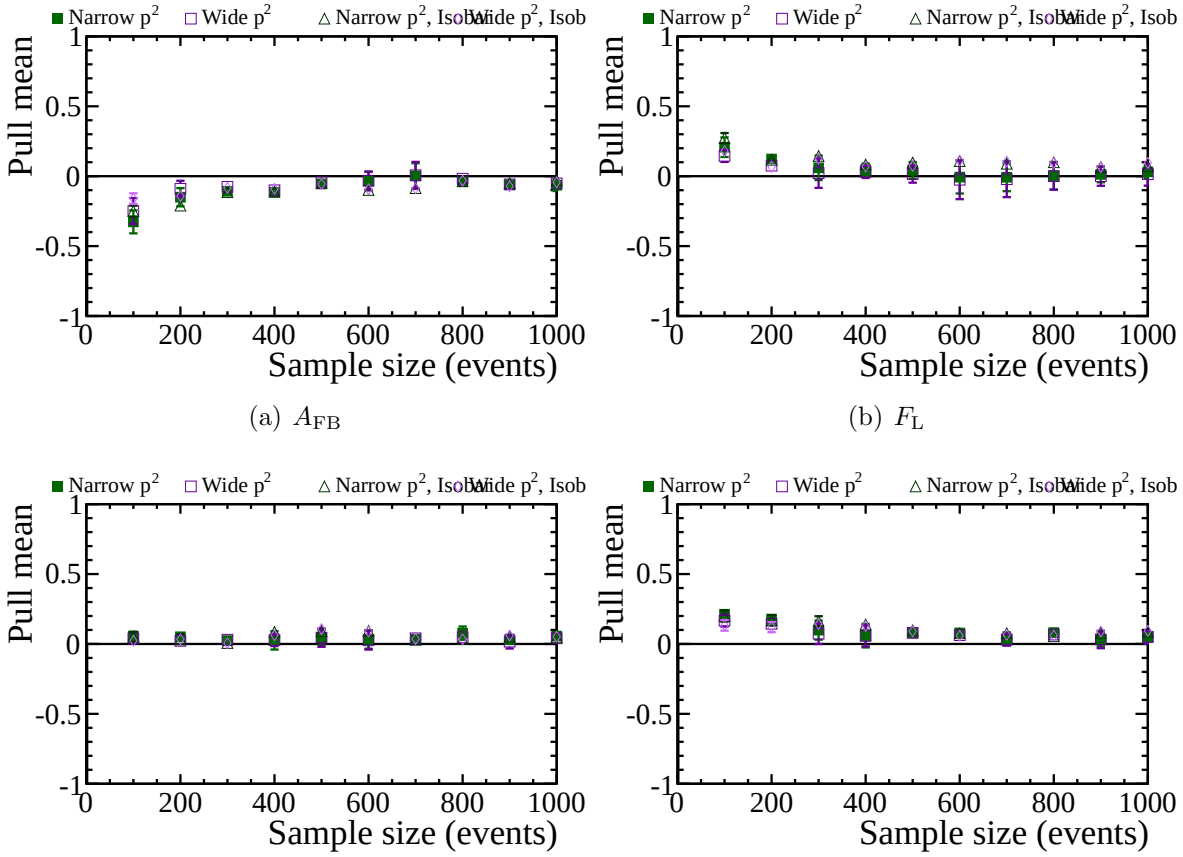

(a) A_{FB} (b) F_{L}

(c) A_{T}^2 (d) A_{Im}

Figure 6.16: Pull mean for the three different methods to incorporate the S-wave and when the S-wave is ignored. The S-wave has been generated using an isobar model. There is a slight shift when the S-wave is included for datasets of less than 200 events but this is removed from all the observables when the S-wave is included in the fit for datasets of over 500 events.

Chapter 7

Measuring the S-wave in $B^0 \to K^+\pi^-\mu^+\mu^-$ at LHCb

This chapter is entirely the work of the author except where referenced.

7.1 Introduction

Measuring the contribution of a $K\pi$ S-wave in $B^0 \to K^+\pi^-\mu^+\mu^-$ is a requirement to understand biases in future measurements of the $B^0 \to K^{*0}\ell^+\ell^-$ angular distribution as shown in the previous chapter. There are no previous measurements of the S-wave in electroweak penguin decays. The closest related measurements of S-wave contributions in decays of B mesons to a $K\pi\mu^+\mu^-$ final state are from $B^0 \to J/\psi\, K^{*0}$ [109, 118] which give a total $K\pi$ S-wave fraction of 7% in the mass window from 800 to 1000 MeV. However, the production of the $K\pi$ state in the electroweak penguins is different from $B^0 \to J/\psi\, K^{*0}$ due to the different form factors.

To measure the $K\pi$ S-wave in $B^0 \to K^+\pi^-\mu^+\mu^-$, the formalism set out in Chapter 6 was combined with the techniques developed in Chapter 5 and applied to the data collected at LHCb in 2011. In this chapter, the measurement proceeds as follows. Firstly, the data and the simulation used to make the measurement are detailed in Section 7.2.1. The selection of $B^0 \to K^+\pi^-\mu^+\mu^-$ candidates in a wider range of $K\pi$ masses is detailed in Section 7.2.2 and the acceptance correction for this wide $K\pi$ mass range is described

in Section 7.3. The model used to parametrise the distribution of $B^0 \to K^+\pi^-\mu^+\mu^-$ candidates is detailed in Section 7.4. The method used to apply the model to the data and extract the S-wave fraction in the P-wave mass window is described in Section 7.4.2. Sources of systematic uncertainty and possible biases to the measurement are given in Sec. 7.5 and the results of the measurement of the $K\pi$ S-wave contribution to $B^0 \to K^+\pi^-\mu^+\mu^-$ are presented in Section 7.6.

7.2 Selection of $B^0 \to K^+\pi^-\mu^+\mu^-$ candidates

7.2.1 Data

The measurement of the S-wave contribution to $B^0 \to K^+\pi^-\mu^+\mu^-$ was performed on the complete dataset collected at LHCb in 2011. This was the identical dataset used in the second angular analysis presented in Chapter 5 and corresponds to an integrated luminosity of $1.0\,\text{fb}^{-1}$ at $\sqrt{s} = 7\,\text{TeV}$. The data are described in more detail in Section 5.2.

The simulation samples that were used in this measurement consist of the samples already described in Section 5.2.2 along with an additional sample of $B^0 \to K^+\pi^-\mu^+\mu^-$ events. This additional simulation sample was generated uniformly in phase space and in the MC11 configuration using the LHCb simulation as described in Sec. 4.4. This simulation was used to understand the efficiency in the wide $K\pi$ mass range.

The data-simulation corrections developed in Sec 4.4.3 were applied to all of the simulation samples in order to ensure that the efficiency calculations were as accurate as possible.

7.2.2 Selection

The selection of signal $B^0 \to K^+\pi^-\mu^+\mu^-$ events was based on the selection presented in Section 5.3 for $B^0 \to K^{*0}\mu^+\mu^-$ candidates. The allowed mass range of $K\pi$ candidates was widened to include the $K\pi$ threshold at 634 MeV up to 1200 MeV. This is because there are regions of almost pure S-wave either side of the $K_1^{*0}(892)$ as described in Sec 6.2 but this range avoids interference from the $K_2^{*0}(1430)$. A cut-based selection was used to

remove peaking background events before a multi-variate algorithm was used to select a pure sample of $B^0 \to K^+\pi^-\mu^+\mu^-$ events.

However, this expansion of the $K\pi$ mass window necessitated a re-examination of parts of the selection for the angular analysis of $B^0 \to K^{*0}\mu^+\mu^-$. The vetoes for possible peaking backgrounds, such as the $K \leftrightarrow \pi$ swaps and other exclusive b decays, must also work in the wider $K\pi$ mass window. In order to select a clean sample of $B^0 \to K^+\pi^-\mu^+\mu^-$ candidates, the same multivariate algorithm was used to separate potential signal candidates and the remaining combinatorial background. The selection of $B^0 \to J/\psi K^+\pi^-$ events was achieved using the same selection but by specifically selecting the q^2 region between 8 and 10 GeV^2/c^4 as described in Section 5.3.

7.2.3 Peaking backgrounds

$K \leftrightarrow \pi$ swaps

Candidates which cannot be separated through hadron identification are called $K \leftrightarrow \pi$ swaps because they pass the selection with reasonable kaon and pion identification when the kaon and pion masses are swapped. These 'swaps' manifest as duplicate candidates and require vetoing to avoid double counting. These $K \leftrightarrow \pi$ swaps were vetoed in Section 5.3 under two conditions. The invariant mass of the $K\pi$ pair with the pion and kaon masses exchanged must have fallen in the $K\pi$ window and the hadron identification values must have satisfied the condition that the difference between the $\Delta(\log\mathcal{L})_{K\pi}$ for the kaon ($K\Delta\log\mathcal{L}_{K\pi}$) and the pion ($\pi\Delta\log\mathcal{L}_{K\pi}$) was greater than minus ten. However, this condition fails to veto sufficient candidates in the wide $K\pi$ window.

The distribution of $K \leftrightarrow \pi$ swaps in terms of $K\Delta\log\mathcal{L}_{K\pi}$ and $\pi\Delta\log\mathcal{L}_{K\pi}$ for selected $B^0 \to K^+\pi^-\mu^+\mu^-$ candidates is given in Fig. 7.1. The overlap of the two distributions can be seen around the zero point motivating the use of the diagonal cut, $K\Delta\log\mathcal{L}_{K\pi} - \pi\Delta\log\mathcal{L}_{K\pi} > 10$. The efficiency of the swap veto is around 92% on signal events which pass the multivariate selection and less than 2.5% of swapped candidates are retained after the veto. There are less than 0.1% of $K \leftrightarrow \pi$ swap candidates in the simulation after selection.

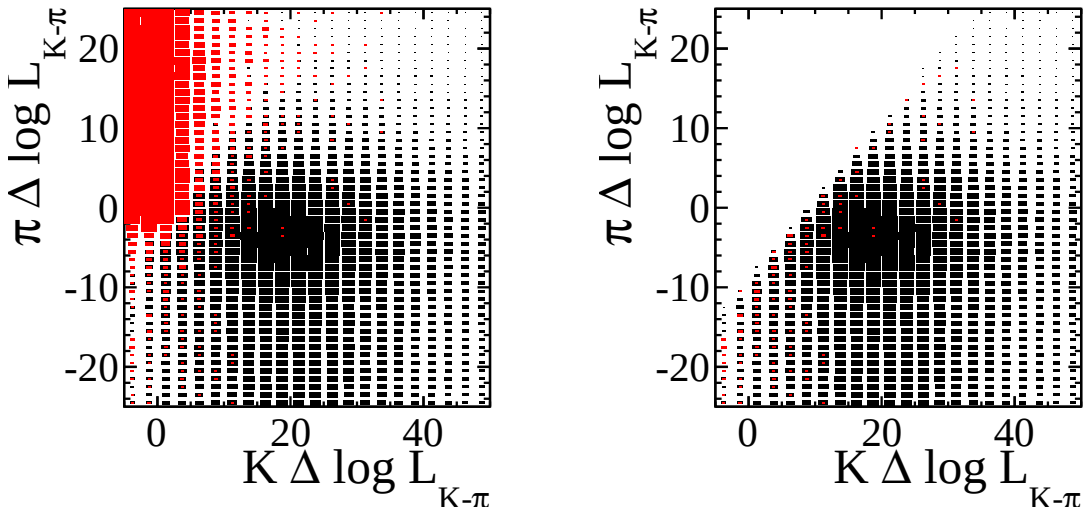

Figure 7.1: The distribution of $B^0 \to K^+\pi^-\mu^+\mu^-$ simulation (a) before and (b) after the $K \leftrightarrow \pi$ swap veto. Candidates with the correction assignment of masses for the kaon and pion are shown in black and candidates with the incorrect assignment of masses are shown in red. There is a clear overlap of candidates around $\Delta(\log \mathcal{L})_{K\pi}$ of 0 for both particles.

Other peaking backgrounds

The possible sources of peaking backgrounds considered have a mass close to the B^0 mass after the misidentification of one or more of the final state particles and could create structure in the $K\pi$ mass spectrum. They are

- $B^0 \to K^{*0}\mu^+\mu^-$ with the pion misidentified as the muon and the muon as the pion.
- $B^0 \to K^{*0}\mu^+\mu^-$ with the kaon misidentified as the muon and the muon as the kaon.
- $B_s^0 \to \phi\mu^+\mu^-$ with one of the kaons misidentified as a pion.
- $B^+ \to K^+\mu^+\mu^-$ with an added soft pion.
- $\Lambda_b^0 \to \Lambda^*(1520)\mu^+\mu^-$ (1) with the proton misidentified as a pion.
- $\Lambda_b^0 \to \Lambda^*(1520)\mu^+\mu^-$ (2) with the proton misidentified as a kaon and the kaon misidentified as a pion.

In order to understand the $K\pi$ mass distribution of these exclusive backgrounds, simulation samples for each decay were used. Each simulation sample was weighted so that the number of events in the sample was equivalent to the expected yield from $1.0\,\text{fb}^{-1}$

Table 7.1: The expected number of peaking background events from selected simulated data in three different mass ranges for an integrated luminosity of $1.0\,\text{fb}^{-1}$. The assumed branching fraction is given in the first column. The first mass range is from $5230 < m_{B^0} < 5330\,\text{MeV}/c^2$ and $800 < m_{K\pi} < 1000\,\text{MeV}/c^2$. The second mass range is from $5230 < m_{B^0} < 5330\,\text{MeV}/c^2$ and $634 < m_{K\pi} < 1200\,\text{MeV}/c^2$ The third range mass range is from $5200 < m_{B^0} < 5700\,\text{MeV}/c^2$, $634 < m_{K\pi} < 1200\,\text{MeV}/c^2$. The errors are statistical.

Background	Γ	Range 1	Range 2	Range 3
$B^0 \to K^{*0}\mu^+\mu^-$ ($K \leftrightarrow \pi$)	1.0×10^7	0.119 ± 0.345	0.158 ± 0.397	0.487 ± 0.698
$B^0 \to K^{*0}\mu^+\mu^-$ ($\pi \leftrightarrow \mu$)	1.0×10^7	0.5 ± 0.707	1.5 ± 1.22	2.33 ± 1.53
$B^0 \to K^{*0}\mu^+\mu^-$ ($K \leftrightarrow \mu$)	1.0×10^7	0 ± 0	0 ± 0	0 ± 0
$B_s^0 \to \phi\mu^+\mu^-$	5.5×10^7	3.1 ± 1.76	5.93 ± 2.44	7.91 ± 2.81
$B^+ \to K^+\mu^+\mu^-$	6.0×10^7	0.0851 ± 0.292	0.17 ± 0.413	1.3 ± 1.14
$\Lambda_b^0 \to \Lambda^*(1520)\mu^+\mu^-$ (1)	1.0×10^7	13.2 ± 4.63	25.1 ± 7.01	79.7 ± 10.93
$\Lambda_b^0 \to \Lambda^*(1520)\mu^+\mu^-$ (2)	1.0×10^7	3.8 ± 2.95	6.82 ± 3.61	13.3 ± 5.64

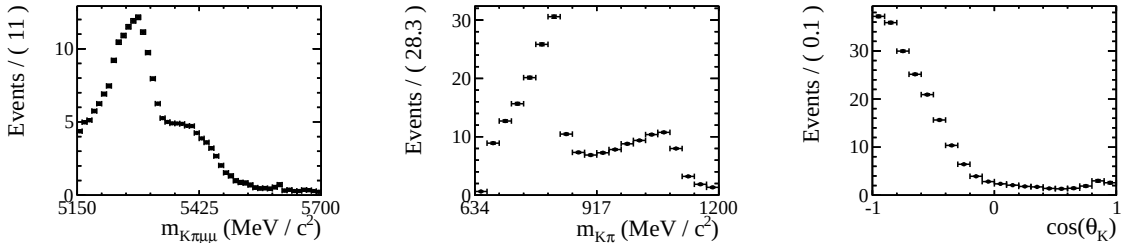

(a) (b) (c)

Figure 7.2: The combined distribution of peaking background events after selection in terms of (a) $m_{K\pi\mu^+\mu^-}$, (b) $m_{K\pi}$ and (c) $\cos\theta_K$. The distribution is composed of simulated $B^0 \to K^{*0}\mu^+\mu^-$, $B_s^0 \to \phi\mu^+\mu^-$, $B^+ \to K^+\mu^+\mu^-$ and $\Lambda_b^0 \to \Lambda^*(1520)\mu^+\mu^-$ normalised to the expected number of events in $1.0\,\text{fb}^{-1}$ of data.

of data. The number of events after selection for the signal B^0 and $K\pi$ mass region, the signal B^0 and the wide $K\pi$ mass region and the wide B^0 and the wide $K\pi$ mass region are shown in Table 7.1. The distribution of peaking background simulation is given in figure 7.2. It is possible to see structure in each of the $m_{K\pi\ell^+\ell^-}$, $m_{K\pi}$ and $\cos\theta_K$ distributions. However, the fraction of peaking background events in the $K\pi\ell^+\ell^-$ mass window is less than $(2.0 \pm 0.2)\%$ after the selection allowing these contributions to be ignored under the P-wave peak.

7.3 Acceptance correction

The distribution of $B^0 \to K^+\pi^-\mu^+\mu^-$ events in terms of p^2, q^2 and $\cos\theta_K$ which pass the selection is not entirely representative of the distribution from all $B^0 \to K^+\pi^-\mu^+\mu^-$ decays. This is because the selection of $B^0 \to K^+\pi^-\mu^+\mu^-$ candidates introduces an acceptance effect in all three of these variables. The mass model used to analyse the distribution of $B^0 \to K^+\pi^-\mu^+\mu^-$ events describes the fundamental distribution of events requiring that any acceptance effect must be corrected for.

The acceptance for $B^0 \to K^+\pi^-\mu^+\mu^-$ is given by the inverse of the efficiency to select $B^0 \to K^+\pi^-\mu^+\mu^-$ events,

$$\epsilon(p^2, q^2, \cos\theta_K) = \frac{S(p^2, q^2, \cos\theta_K)}{G(p^2, q^2, \cos\theta_K)}\,, \tag{7.1}$$

where the efficiency can be calculated by considering the number of simulated events which pass the selection (S) when compared to the number of simulated events at the generator level (G) .

Following the work in Section 5.4, the acceptance is evaluated using simulated $B^0 \to K^+\pi^-\mu^+\mu^-$ events generated uniformly across the phase space. For phase space simulated events, the q^2 region considered is from 0.1 to 19 GeV^2/c^4 and the p^2 region is from the $K\pi$ threshold (0.4) to 1.44 GeV^2/c^4.

The distribution of phase space simulated events at generator level for p^2 and q^2 are given in Fig. 7.3. After the selection has been applied, along with the data-simulation corrections, there are around ten thousand simulated phase space events left, giving a total efficiency for $B^0 \to K^+\pi^-\mu^+\mu^-$ of around 0.1%. In order to make maximum use of the simulation statistics, the efficiency was checked for correlations between the kinematic variables with the aim of factorising the efficiencies into one dimensional functions.

7.3.1 Efficiency in terms of p^2, q^2 and $\cos\theta_K$

The efficiency to select $B^0 \to K^+\pi^-\mu^+\mu^-$ events in terms of p^2, q^2 and $\cos\theta_K$ is shown in Fig. 7.4. It is possible to see the drop at high $\cos\theta_K$ coming from the asymmetric K and

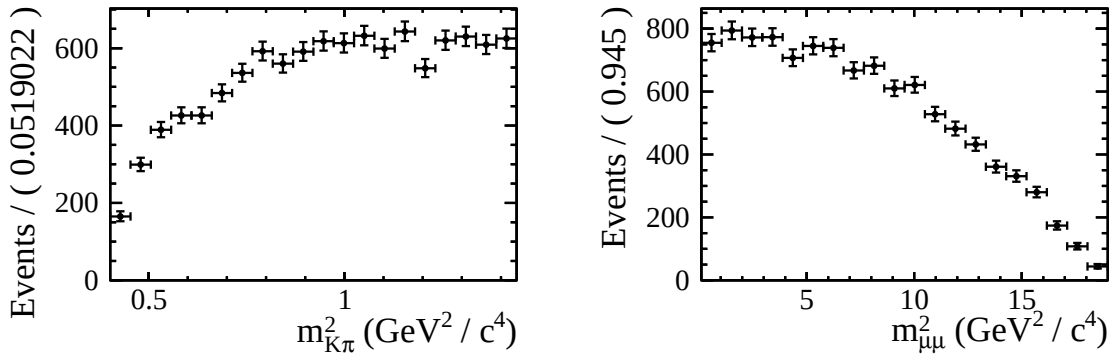

(a) (b)

Figure 7.3: The distribution of phase space $B^0 \to K^+\pi^-\ell^+\ell^-$ simulated events at generator level as a function of (a) p^2 and (b) q^2.

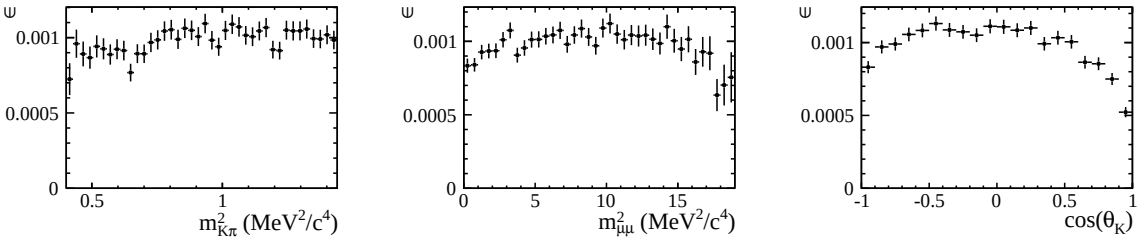

(a) (b) (c)

Figure 7.4: The efficiency as a function of (a) p^2, (b) q^2 and (c) $\cos\theta_K$ for phase space simulated $B^0 \to K^+\pi^-\mu^+\mu^-$ events.

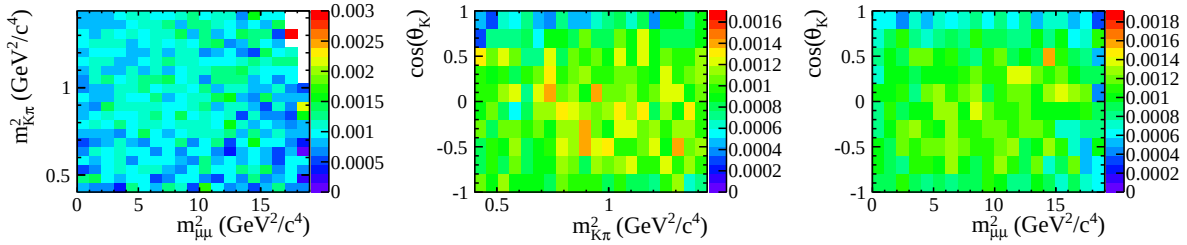

(a) (b) (c)

Figure 7.5: The efficiency as a function of (a) p^2 and q^2, (b) p^2 and $\cos\theta_K$ and (c) q^2 and $\cos\theta_K$ for phase space simulated $B^0 \to K^+\pi^-\mu^+\mu^-$ events. There are between 10 and 100 events which pass the $K\pi\mu^+\mu^-$ candidate selection in each bin.

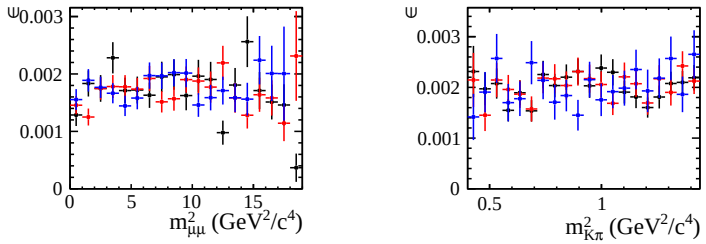

(a) (b)

Figure 7.6: The projected efficiency for (a) p^2 in 1 GeV$^2/c^4$ wide bins around q^2 values of 5, 10 and 15 GeV$^2/c^4$ and (b) q^2 in 0.02 GeV$^2/c^4$ wide bins at p^2 values of 0.49, 0.64 and 0.81 GeV$^2/c^4$. The efficiency projections was tested using the Kolmogorov-Smirnov test and found to be compatible.

π acceptance. There is also a drop in efficiency for low p^2 values and high q^2 values. The efficiency in each of the two dimensional distributions (p^2 v.s. q^2, p^2 v.s. $\cos\theta_K$ and q^2 v.s. $\cos\theta_K$) is shown in Fig. 7.5. There is an asymmetric effect in $\cos\theta_K$ in both the low and high q^2 regions due to the momentum difference between the kaon and pion in the lab frame. There is also a correlation between the efficiency in p^2 and $\cos\theta_K$, changing between low and high values of p^2 at high $\cos\theta_K$ values. The detailed examination of the P-wave efficiency in Section 5.4 shows that there is a correlation between the efficiency in $\cos\theta_K$ and q^2. The projected efficiencies in different regions of p^2 and q^2 are is shown in Figure 7.6. The compatibility of the different efficiency projections was tested using the Kolmogorov-Smirnov test [119]. No extreme p-values were found which implies that the efficiency projections are compatible with coming from the same parent efficiency distribution. This shows that in the limit of the simulation statistics used, there is no

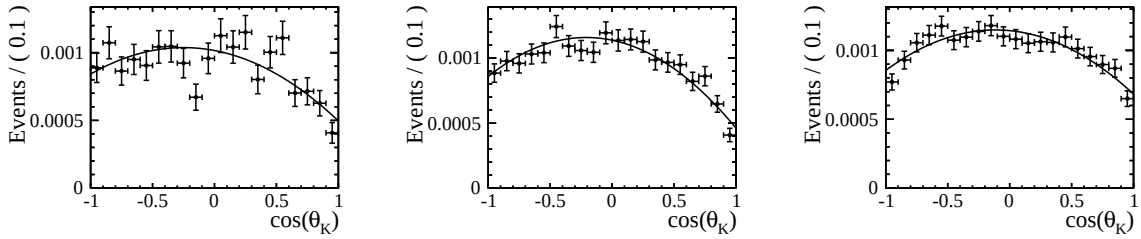

(a) (b) (c)

Figure 7.7: The efficiency as a function of $\cos\theta_K$ for phase space simulated $B^0 \to K^+\pi^-\mu^+\mu^-$ events. The low $m_{K\pi}$ region below $0.64\,\mathrm{GeV}^2/c^4$ is shown in (a), the region around the P-wave resonance in (b) and the high $m_{K\pi}$ region between 1.00 to $1.44\,\mathrm{GeV}^2/c^4$ in (c). The efficiency is fitted with a second order Chebychev polynomial (the black curve) showing the parametrised efficiency in each p^2 bin.

correlation between the efficiency in p^2 and q^2.

In order to examine how the $\cos\theta_K$ efficiency changes in terms of p^2, the efficiency of $B^0 \to K^+\pi^-\mu^+\mu^-$ events was modelled in three bins of p^2. These are the regions from threshold to $0.64\,\mathrm{GeV}^2/c^4$, the P-wave mass window from 0.64 to $1.00\,\mathrm{GeV}^2/c^4$ and above the P-wave from 1.00 to $1.44\,\mathrm{GeV}^2/c^4$. The efficiency as a function of $\cos\theta_K$ for each of these regions is shown in Fig. 7.7. It is possible to see a change in the shape of the efficiency between the different p^2 bins, but there are insufficient simulated statistics to provide an accurate correction in $\cos\theta_K$. Since the statistics of the $B^0 \to K^+\pi^-\mu^+\mu^-$ simulation sample are insufficient to correct in p^2, q^2 and $\cos\theta_K$, $\cos\theta_K$ must be integrated out. However, the integration over $\cos\theta_K$ contributes to a source of systematic uncertainty.

The event-by-event acceptance correction for the $B^0 \to K^+\pi^-\mu^+\mu^-$ events is obtained by the calculating the values for the polynomial models for the p^2 and q^2 efficiencies,

$$\epsilon(p^2, q^2) = P(p^2; p_0, p_1, p_2, p_3) \times P(q^2; q_0, q_1, q_2, q_3)\,, \tag{7.2}$$

and the weight of each event to correct for the acceptance is given by the inverse efficiency,

$$\omega(p^2, q^2) = 1/\epsilon(p^2, q^2)\,. \tag{7.3}$$

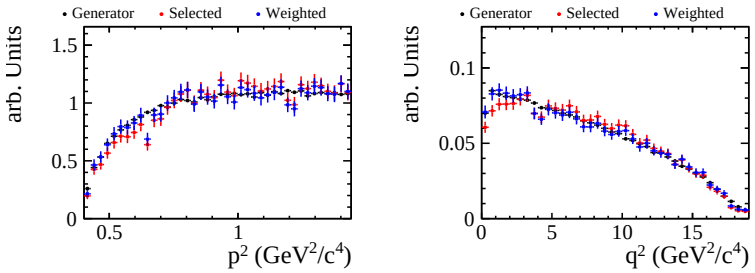

(a) (b)

Figure 7.8: The efficiency as a function of (a) p^2 and (b) q^2 for phase space simulated $B^0 \to K^+\pi^-\mu^+\mu^-$ events. The generator level distribution is shown in black, the distribution of candidates after selection in red and the re-weighted candidates are shown in blue.

7.3.2 Validation

The acceptance correction can be checked to first order by comparing the distribution of re-weighted events to the expected distribution of events at generator level Following Section 5.4, the selected simulation used to calculate $S(p^2, q^2)$ is re-weighted and compared to the distribution of generator level events used to calculate $G(p^2, q^2)$. The distributions of simulation can be seen in Fig. 7.8. It is possible to see that the generator level simulation distributions are correctly recovered after re-weighting.

7.4 Fit for F_S

7.4.1 Fit model

The model used to describe the $K\pi$ and $K\pi\mu^+\mu^-$ mass distribution of $B^0 \to K^+\pi^-\mu^+\mu^-$ candidates is a combination of theoretically derived expressions and empirical functions for the B^0 mass and the $K\pi$ mass. The signal model is factorised into a model for the B^0 mass distribution and a model for the $K\pi$ mass distribution. This is because the difference in phase space available for the $K\pi\mu^+\mu^-$ decay between low and high B mass is only significant at very high q^2, as shown in Fig. 6.1 and thus can be ignored. The background model is factorised into one model for the $m_{K\pi\mu^+\mu^-}$ background and one for

the $m_{K\pi}$ background. The total model for $m_{K\pi\mu^+\mu^-}$ and $m_{K\pi}$ is given by

$$\begin{aligned} f(m_{B^0}, m_{K\pi}) =& f_S \left(S(m_{K\pi\mu^+\mu^-}) \times S(m_{K\pi}; F_{\rm S})\right) \\ &+ (1 - f_S) \left(B(m_{K\pi\mu^+\mu^-}) \times B(m_{K\pi})\right) \end{aligned} \tag{7.4}$$

where S is the signal model, B is the background model and f_S was the fraction of signal $B^0 \to K^+\pi^-\mu^+\mu^-$ candidates in the data.

Model for $m_{K\pi\mu^+\mu^-}$

The distribution of $B^0 \to K^+\pi^-\mu^+\mu^-$ events in terms of the $K\pi\mu^+\mu^-$ invariant mass is described by the same model used in Section 5.5.1. This is a double Crystal Ball function for the signal shape and an exponential function to describe the decreasing combinatorial background,

$$\begin{aligned} S\left(m_{K\pi\mu^+\mu^-}; \sigma_1, \sigma_2, \alpha, n\right) =& \; f \times CB\left(m_{K\pi\mu^+\mu^-}; m_B, \sigma_1, \alpha, n\right) \\ &+ (1 - f) \times CB\left(m_{K\pi\mu^+\mu^-}; m_B, \sigma_2, \alpha, n\right) , \end{aligned} \tag{7.5}$$

$$B\left(m_{K\pi\mu^+\mu^-}; \lambda\right) = N_B \exp\left(-\lambda m_{K\pi\mu^+\mu^-}\right) , \tag{7.6}$$

where α, n and $\sigma_{1,2}$ are the Crystal Ball parameters and λ describes the exponential decay.

Model for $m_{K\pi}$

The distribution of signal events in terms of $m_{K\pi}$ is given by the integral of the angular distribution (see Sec. 6.3) over $\cos\theta_K$,

$$\begin{aligned} S(m_{K\pi}; \mathcal{F}_{\rm S}) &= \int {\rm d}\cos\theta_K \; S(m_{K\pi}, \cos\theta_K; \mathcal{F}_{\rm S}, \mathcal{A}_{\rm S}, F_{\rm L}) \\ &= \int {\rm d}\cos\theta_K \; \left(\frac{1}{2}\mathcal{F}_{\rm S}(m_{K\pi}) + \mathcal{A}_{\rm S}(m_{K\pi})\cos\theta_K\right) \\ &\quad + \int {\rm d}\cos\theta_K \; \mathcal{F}_{\rm P}(m_{K\pi})\left[\frac{3}{2}F_{\rm L}\cos^2\theta_K + \frac{3}{4}(1 - F_{\rm L})(1 - \cos^2\theta_K)\right], \end{aligned} \tag{7.7}$$

where $\mathcal{F}_{\rm S}$ and $\mathcal{F}_{\rm P}$ are functions of $m_{K\pi}$ that describe the S-wave and P-wave respectively, along with the asymmetry $\mathcal{A}_{\rm S}$. The P-wave observable is the fraction of the K_1^{*0} longitudinal polarisation, $F_{\rm L}$. The integrated signal distribution over $\cos\theta_K$ from -1 to 1 is simply given by

$$S(m_{K\pi};\mathcal{F}_{\rm S}) = \mathcal{F}_{\rm S}(m_{K\pi}) + \mathcal{F}_{\rm P}(m_{K\pi})\,. \tag{7.8}$$

The functions describing the S-wave and P-wave are given by

$$\mathcal{F}_{\rm S}(p^2) = \rho(p^2,q^2,J) \times \mathcal{N}_0 \times P_0(p^2)\,, \tag{7.9}$$

$$\mathcal{F}_{\rm P}(p^2) = \rho(p^2,q^2,J) \times \mathcal{N}_1 \times P_1(p^2)\,, \tag{7.10}$$

where N_0 and N_1 are the normalisation of each state and ρ is a phase space factor. The normalisation parameters are directly correlated to the total number of events so the relation $\mathcal{N}_1 = 1 - \mathcal{N}_0$ was used to constrain the signal model further.

The propagator for the P-wave, P_1, is well understood and described by the relativistic Breit-Wigner formula as detailed in Eq. 6.7. The propagator for the S-wave, P_0, can be modelled by either the LASS parametrisation [108] or with an isobar model [117]. The details of each of the models are given in Sec 6.2.

The phase space factor, ρ, is dependent on p^2, q^2 and the spin of the K^{*0} state, J. In order to integrate the angular distribution over q^2, the q^2 dependence of the phase space factor was approximated by using the q^2 value in the centre of the bin in q^2. This approximation contributes a possible source of systematic uncertainty.

The distribution of background events in $m_{K\pi}$ is modelled by

$$B(m_{K\pi}) = f_B \times P_1(m_{K\pi}) + (1-f_B) \times B_1(m_{K\pi};m_0,A,B,C)\,, \tag{7.11}$$

where there are two functions for the $m_{K\pi}$ background model.

The background contribution from $K\pi$ P-wave events is modelled using a relativistic Breit-Wigner function, as detailed in Eq. 6.7, which shares parameters with the signal

model for the $B^0 \to K^+\pi^-\mu^+\mu^-$ P-wave propagator. The contribution from both combinatorial background and S-wave background is accounted for by using a function developed to parametrise the background in fits to the mass difference of D^* and D mesons [120],

$$B_1(m_{K\pi}; m_0, A, B, C) = \left(1 - e^{-(m_{K\pi}-m_0)/C}\right) \times \left(\frac{m_{K\pi}}{m_0}\right)^A + B\left(\frac{m_{K\pi}}{m_0} - 1\right) \qquad (7.12)$$

where m_0 is the $m_{K\pi}$ threshold and A,B and C are arbitrary parameters.

7.4.2 Fit method

The measurement of $F_{\rm S}$ was obtained from a measurement of the $K\pi$ mass spectrum for $B^0 \to K^+\pi^-\mu^+\mu^-$ events. In order to obtain a reasonably accurate fit by minimising the number of free parameters to fit the $m_{K\pi}$ distribution, a multiple stage fit was used to constrain the parameters of the B^0 mass shape before the angular distribution is fitted. The $K\pi\mu^+\mu^-$ mass spectrum, which is independent of the $K\pi$ spectrum for the small p^2 region considered, was used to determine the total fraction of signal and background in each of the q^2 bins. Once the signal fraction was fixed the $K\pi$ line shape was subsequently fitted to obtain the value of $\mathcal{N}_0$. This allows the S-wave fraction, $F_{\rm S}$, to be calculated from the integration of $\mathcal{F}_{\rm S}$ and $\mathcal{F}_{\rm P}$ in the $K\pi$ region from 0.64 to 1.00 GeV^2/c^4.

Constraining the $m_{K\pi\mu^+\mu^-}$ mass

The first part of the fit strategy was to constrain the mass distribution using selected $B^0 \to J/\psi\, K^+\pi^-$ data. This high statistics sample of around 200k events allows the parameters for the double Crystal Ball model to be precisely constrained. There is an additional contribution from $B_s^0 \to J/\psi\, K^+\pi^-$ which is suppressed by several orders of magnitude compared to $B^0 \to J/\psi\, K^+\pi^-$ but still has to be taken into account. The method is the same as was used to constrain the parameters of the two Crystal Ball functions in Section 5.5.3. The result of the fit of the mass model to the $B^0 \to J/\psi\, K^+\pi^-$ data is shown in Fig. 7.9. It can be seen that the double Crystal Ball model results in a good fit to the signal peak and the $B_s^0 \to J/\psi\, K^+\pi^-$ contribution. The values of the signal parameters

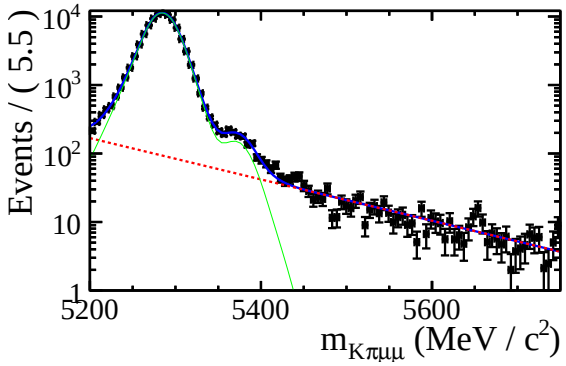

Figure 7.9: The fit to selected $B^0 \to J/\psi K^+\pi^-$ data with the model for the $K\pi\mu^+\mu^-$ distribution. It is possible to see a contribution from $B_s^0 \to J/\psi K^+\pi^-$ to the right of the $B^0 \to J/\psi K^{*0}$ peak. There are 115900 ± 350 $B^0 \to J/\psi K^+\pi^-$ signal events. The total PDF is given in blue, the signal component in green and the background component is the red dashed line.

from this fit are fixed to their values and the value of the background parameter is ignored.

In order to obtain a complete description of the $K\pi\mu^+\mu^-$ mass spectrum for the $B^0 \to K^+\pi^-\mu^+\mu^-$ data, for each q^2 region the data was fitted with the fixed signal model allowing the background parameter and the the total fraction of signal to vary. The results of both these fits allow the fraction of signal, f_S, to be constrained for the fit to the $K\pi$ mass distribution.

Fitting the $K\pi$ mass distribution

The proportion of $K\pi$ S-wave to P-wave, $\mathcal{N}_0$, in each of the q^2 bins was determined by fitting the $K\pi$ mass distribution to the data. In order to constrain the number of remaining parameters, several assumptions were made about both the signal and background model for the $m_{K\pi}$ spectrum. This is a simpler model than the one described in Chapter 6 but the only one possible given the low statistics in data and the reduced accuracy of the acceptance correction.

There are three sets of parameters for the $m_{K\pi}$ signal models: the parameters for the P-wave, the resonant S-wave and the non-resonant S-wave. The parameters describing the K_1^{*0} are well known and can be constrained to the values given in Ref [13]. The parameters for the non-resonant part of the K_0^{*0} model are left free in the fit and their starting values are taken from Table 6.1. The parameters for the resonant $K_0^{*0}(1430)$ are constrained to

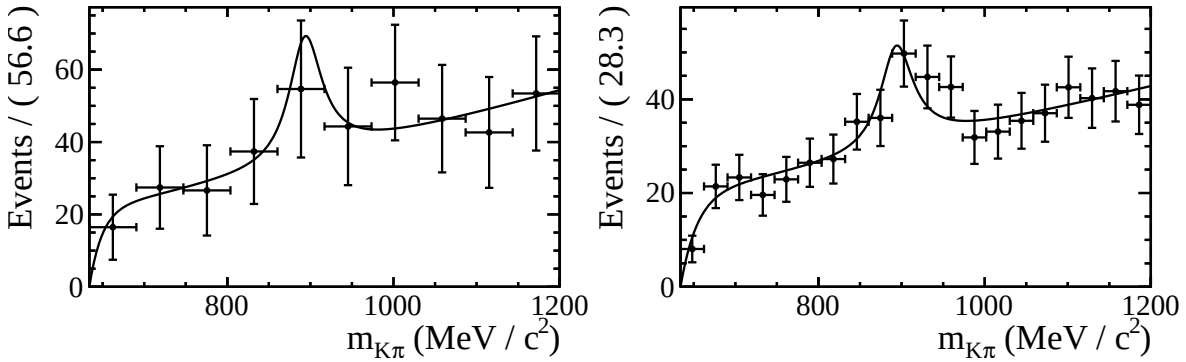

Figure 7.10: The distribution of background events in bins of the $K\pi$ mass in (a) the region from 5200 to 5400 MeV/c^2 and (b) above 5400 MeV/c^2. It is possible to see an increase in the background distribution from threshold for both regions. The background distributions are fitted with the empirical function in Eq 7.12. The background in the B^0 signal region is obtained from extended maximum likelihood fits to the B^0 mass in 10 bins of $m_{K\pi}$.

the values given in Ref [13]. The phase difference between the S-wave and the P-wave is integrated out.

The background distribution in $m_{K\pi}$ is not known a priori but it can be assumed that there is an increase from the $K\pi$ threshold due to the phase space available. Reasonable ranges for the parameters for the empirical $m_{K\pi}$ background function were obtained through fits to the $K\pi$ mass spectrum using events with a $m_{K\pi\mu^+\mu^-}$ of greater than 5400 MeV. This assumes that these events with high $K\pi\mu^+\mu^-$ masses can be used to model the $m_{K\pi}$ background spectrum. This was checked by fitting the background in the B^0 signal window with the same empirical background model. The distribution of $B^0 \to K^+\pi^-\mu^+\mu^-$ background events in the B^0 signal region and above the B^0 signal region are shown in Fig. 7.10. It is possible to see that the background increases from threshold and there is a small contribution from a $K\pi$ P-wave state of around 5%. The final fit model contains the S-wave proportion, $\mathcal{N}_0$, along with the signal and background model parameters for the $K\pi$ mass spectrum as free parameters. In the case of the fit model converging to a limit of zero S-wave contribution, the Feldman-Cousins technique [104] was used to calculate a 95% upper limit on the value of $F_{\rm S}$.

7.4.3 Determination of F_{S}

Once the constrained model has been applied to the data, the proportions of S-wave and P-wave were calculated by integration over $m_{K\pi}$ from 0.64 to 1 GeV^2/c^4. The fraction of the S-wave in the P-wave resonance region was calculated by integrating Equation 7.7, to give the differential branching fraction in terms of p^2 and q^2,

$$\frac{1}{\Gamma''}\frac{\mathrm{d}^3\Gamma}{\mathrm{d}q^2\mathrm{d}p^2} = \mathcal{F}_{\mathrm{S}}(p^2,q^2) + \mathcal{F}_{\mathrm{P}}(p^2,q^2) \tag{7.13}$$

so the S-wave fraction integrated over p^2 and q^2 is given by

$$F_{\mathrm{S}} = \frac{\int \mathcal{F}_{\mathrm{S}}(p^2,q^2)\mathrm{d}p^2\mathrm{d}q^2}{\int \left[\mathcal{F}_{\mathrm{S}}(p^2,q^2) + \mathcal{F}_{\mathrm{P}}(p^2,q^2)\right]\mathrm{d}p^2\mathrm{d}q^2}\,. \tag{7.14}$$

7.5 Systematic uncertainties

There are several distinct sources of systematic uncertainty that are considered to affect the measurement of the $K\pi$ S-wave in $B^0 \to K^+\pi^-\mu^+\mu^-$. The systematic uncertainties affecting the event selection, the corrections to simulation and the model to describe the B mass distribution have previously been considered in Section 5.6. These effects have a possible impact in this analysis and are therefore tested in a similar manner. There are new sources of systematic uncertainty from the model used for the $m_{K\pi}$ distribution. These come from both the background and signal models, along with the phase space integration assumed over q^2. Each of the sources of systematic uncertainty are discussed below along with the method used to estimate a possible bias.

The selection

The possible mis identification of K^* and $\overline{K}^*$ was found in Chapter 5 to be negligible and consequently can be ignored for this measurement. The amount of $K\pi$ swaps should be negligible due to the cut placed on the $K\Delta\log\mathcal{L}_{K\pi}$ and $\pi\Delta\log\mathcal{L}_{K\pi}$ combination and is ignored. The contributions from possible peaking background decays are vetoed to a sufficient degree and similarly ignored.

The data-simulation corrections

The sources of systematic uncertainty that contribute to the corrections applied to the simulation are described in Section 5.6. These come from the relative efficiency between the data and the simulation for the tracking, the trigger and the muon identification. The smearing of the track IP and the regeneration of the hadron $\Delta(\log\mathcal{L})$ distributions are also possible sources of systematic uncertainty. The degree of systematic uncertainty contributed by these corrections is evaluated using the same method as described in Section 5.6.

The acceptance correction

The factorisation of the efficiency between p^2 and $\cos\theta_K$ is tested by reducing the range of $\cos\theta_K$. This removes the contribution from events at high $\cos\theta_K$ which may have an erroneous weight applied from the acceptance correction. The reduction in the range of $\cos\theta_K$ changes the model used for the signal since the integral no longer vanishes. The integral over the angular distribution in terms of p^2, q^2 and $\cos\theta_K$ for a symmetric $\cos\theta_K$ range is given by

$$\begin{aligned}&\int_{-c}^{c} S(m_{K\pi},\cos\theta_K;\mathcal{F}_{\rm S},\mathcal{A}_{\rm S},F_{\rm L})\,{\rm d}\cos\theta_K \\ &\quad=\frac{1}{2}\mathcal{F}_{\rm S}(m_{K\pi})(2c)+\mathcal{F}_{\rm P}(m_{K\pi})\left[c^3F_{\rm L}+\frac{3}{4}(1-F_{\rm L})(2c-\frac{2}{3}c^3)\right],\end{aligned} \tag{7.15}$$

where the term with $\mathcal{A}_{\rm S}$ vanishes for the symmetric $\cos\theta_K$ range. For a $\cos\theta_K$ range of less than -1 to 1, $F_{\rm L}$ does not integrate out and a correction is required.

The change in $F_{\rm S}$ in the q^2 bin from 1 to 6 GeV^2/c^4 when the $\cos\theta_K$ range is changed is shown in Fig. 7.11. To calculate the correction from the integration, the values of $F_{\rm L}$ measured in Chapter 5 are used. It is possible to see that the results with and without fitting $\cos\theta_K$ for different fiducial ranges of $\cos\theta_K$ are compatible. The contribution from this source of systematic uncertainty is chosen to be from the change in $F_{\rm S}$ when the integration range is changed from $|\cos\theta_K|<1$ to $|\cos\theta_K|<0.7$.

The integration over $\cos\theta_K$ is also checked by fitting the angular distribution in terms

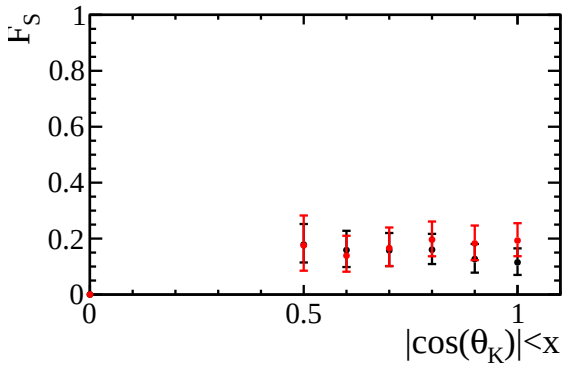

Figure 7.11: The change in $F_{\rm S}$ for different ranges of $\cos\theta_K$. The effect of including events at high $\cos\theta_K$ may contribute to a source of systematic uncertainty. The change in $F_{\rm S}$ when only p^2 and q^2 is fitted is shown in black and the change in $F_{\rm S}$ when $\cos\theta_K$ is included in the angular distribution is shown in red.

of p^2 and $\cos\theta_K$. The acceptance correction from Sec. 5.4 is used as an approximation. The values of $F_{\rm L}$ obtained from these fits are compatible within statistical errors with the results obtained in Section 5.7.

The fit model

There are several possible sources of systematic uncertainty in the choice of model used to describe the $K\pi\mu^+\mu^-$ mass distribution. The degree to which is $F_{\rm S}$ can be affected by the m_{B^0} mass distribution comes from the two-stage fit used to obtain the overall fraction of signal in the data for a given region of q^2. In order to test for any bias in the signal shape, the double Crystal Ball function was replaced by a double Gaussian function. This will change the tails of the signal distribution and change the quality of the background fit. In order to test possible uncertainties from the choice of background model, the exponential function was replaced with a second order Chebychev polynomial as the background model.

Following the work in Section 6.7, an isobar model consisting of a constant non-resonant term, the $K^{*0}(1430)$ and the $\kappa(600)$ was used as an alternative model the $K\pi$ mass spectrum.

The degree to which the approximation of the phase space factor across the q^2 bin effects the final value of $F_{\rm S}$ is evaluated by using the q^2 values at both the low and high

edge of the q^2 bin in the phase space factor,

$$\rho(m_{B^0}, p^2, q^2) = \begin{cases} \rho(m_{B^0}, p^2, q^2_{max}) \\ \rho(m_{B^0}, p^2, q^2_{min}) \end{cases} \tag{7.16}$$

This was found to contribute to a minor source of systematic uncertainty.

7.5.1 Summary of systematic uncertainties

The size of possible contributions from sources of systematic uncertainty on the measurement of F_{S} are given in Table 7.2.

Table 7.2: Table of possible sources of systematic uncertainty on the measurement of F_S. Only the bins with a non-zero S-wave contribution are shown. The bins with no S-wave are unaffected by the possible sources of systematic uncertainty.

q^2 (GeV^2/c^4) bin	$0.1 < q^2 < 2.0$	$2.0 < q^2 < 4.3$	$4.3 < q^2 8.68$	$10.09 < q^2 < 12.9$	$14.18 < q^2 16.0$	$16 < q^2 < 19$	$1 < q^2 < 6$
Central value	0.164	0.000	0.092	0.001	0.000	0.000	0.083
Stat down	0.060	0.000	0.033	0.000	0.000	0.000	0.048
Stat up	0.069	0.135	0.039	0.044	0.007	0.002	0.057
Sys down	0.013	0.000	0.046	0.000	0.000	0.000	0.050
Sys up	0.011	0.001	0.021	0.000	0.000	0.000	0.018
Bkg order 1	0.000	0.000	0.000	0.000	0.000	0.000	-0.026
Bkg order 3	0.000	0.000	0.000	0.000	0.000	0.000	0.000
PID down	0.000	0.000	0.000	0.000	0.000	0.000	0.000
PID up	0.000	0.000	0.000	0.000	0.000	0.000	0.000
fit the B mass	0.000	0.000	-0.001	0.000	0.000	0.000	0.003
isobar model	0.000	0.000	0.000	0.000	0.000	0.000	0.000
Muon ID down	0.000	0.000	-0.029	0.000	0.000	0.000	0.000
Muon ID up	0.000	0.000	0.000	0.000	0.000	0.000	0.000
IP smearing	0.000	0.000	-0.029	0.000	0.000	0.000	0.000
q^2 efficiency down	0.000	0.000	0.000	0.000	0.000	0.000	0.000
q^2 efficiency up	0.000	0.000	0.000	0.000	0.000	0.000	0.000
$\cos\theta_K$ limit	-0.008	0.001	0.001	0.000	0.000	0.000	-0.029
q^2 high edge	-0.010	0.000	-0.020	0.000	0.000	0.000	-0.018
q^2 low edge	0.011	0.000	0.021	0.000	0.000	0.000	0.018
Tracking Down	0.000	0.000	0.000	0.000	0.000	0.000	0.000
Tracking Up	0.000	0.000	0.000	0.000	0.000	0.000	0.000
Trigger Down	0.000	0.000	0.000	0.000	0.000	0.000	-0.026
Trigger Up	0.000	0.000	0.000	0.000	0.000	0.000	0.000

Table 7.3: Table showing the fraction of $K\pi$ S-wave between 0.64¡p^2 ¡1.00 in six bins of q^2 for selected $B^0 \to K^+\pi^-\mu^+\mu^-$ events from $1.0\,\text{fb}^{-1}$ of data collected at $\sqrt{s} = 7\,\text{TeV}$ at LHCb in 2011. For the regions where no S-wave is found, results are quoted at 95% confidence limit.

Bin (GeV^2/c^4)	F_S
$0.10 < q^2 < 2.00$	$0.164^{-0.069\ -0.011}_{-0.060\ +0.013}$
$2.00 < q^2 < 4.30$	< 0.135 (at 95% C.L.)
$4.30 < q^2 < 8.68$	$0.092^{-0.039\ -0.021}_{-0.033\ +0.046}$
$10.09 < q^2 < 12.90$	< 0.044 (at 95% C.L.)
$14.18 < q^2 < 16.00$	< 0.007 (at 95% C.L.)
$16.00 < q^2 < 19.00$	< 0.002 (at 95% C.L.)
$1.00 < q^2 < 6.00$	$0.083^{-0.057\ -0.018}_{-0.048\ +0.050}$

The dominant sources of systematic uncertainty come from the use of the crystal ball function to fit the $K\pi\mu^+\mu^-$ invariant mass and from the mis-modelling of the q^2 and p^2 efficiency.

7.6 Results

The results of the fit to each of the q^2 bins for the B^0 mass spectrum are shown in Fig. 7.12 and for the $K\pi$ mass spectrum are shown in Fig. 7.13. The results of the measurement of the $K\pi$ S-wave in $B^0 \to K^+\pi^-\mu^+\mu^-$ using $1.0\,\text{fb}^{-1}$ of integrated luminosity collected at LHCb are presented in Fig. 7.14. The central values, statistical and systematic errors in 6 bins of q^2 are given in Table 7.3. There is an indication of a non-zero S-wave contribution at low q^2, specifically in the region below $2\,\text{GeV}^2/c^4$, the region from 4.3 to $8.68\,\text{GeV}^2/c^4$ and in the region from 1 to 6 GeV^2/c^4. The p-values of the zero S-wave hypothesis for each of the bins with non-zero S-wave are 0.05, 0.07 and 0.02 respectively. None of these bins are significant enough to provide evidence of a $K\pi$ S-wave and the other bins contain insufficient events to measure any contribution from a $K\pi$ S-wave. The value of F_S in the q^2 bin from 1 to 6 GeV^2/c^4 and in the p^2 bin from 0.64 to 1 GeV^2/c^4 was found to be

$$F_\text{S} = 0.083^{+0.057}_{-0.048}(\text{stat.})^{+0.018}_{-0.050}(\text{syst.}) \tag{7.17}$$

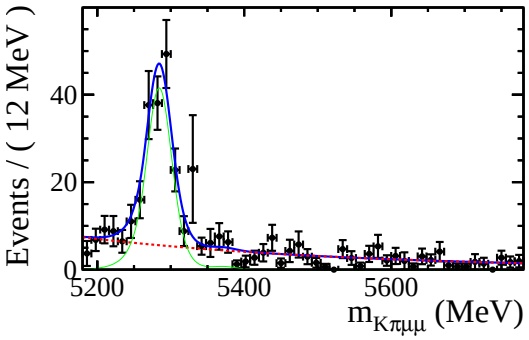

(a) $0.10 < q^2 < 2.00\,\mathrm{GeV}^2/c^4$

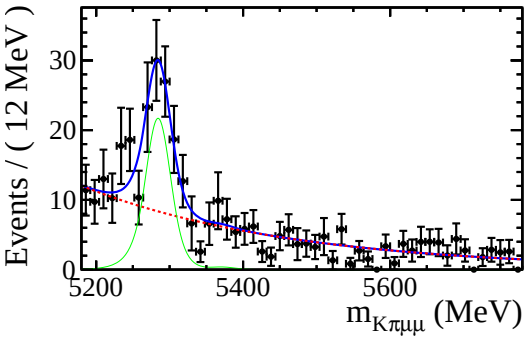

(b) $2.00 < q^2 < 4.30\,\mathrm{GeV}^2/c^4$

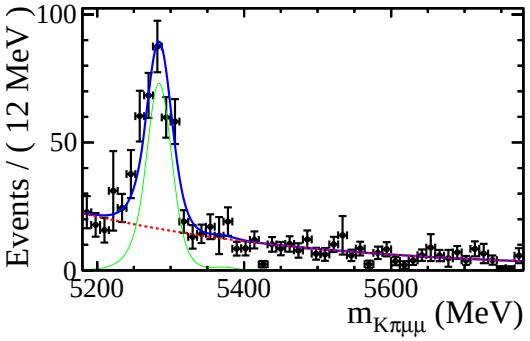

(c) $4.30 < q^2 < 8.68\,\mathrm{GeV}^2/c^4$

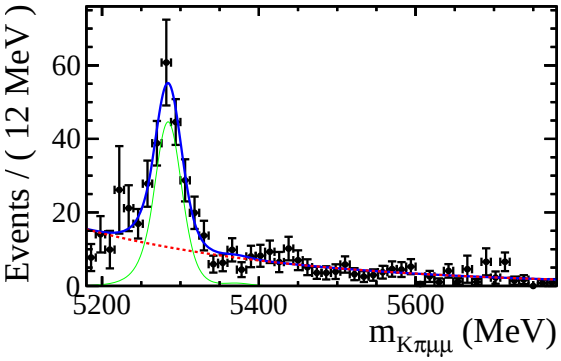

(d) $10.09 < q^2 < 12.9\,\mathrm{GeV}^2/c^4$

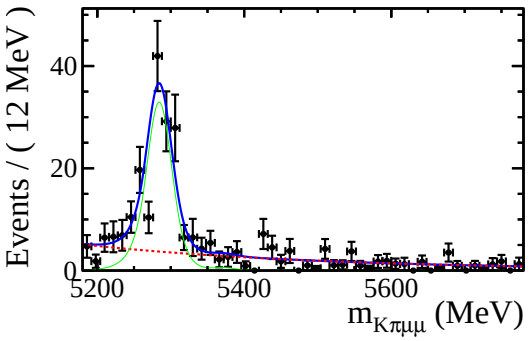

(e) $14.18 < q^2 < 16.0\,\mathrm{GeV}^2/c^4$

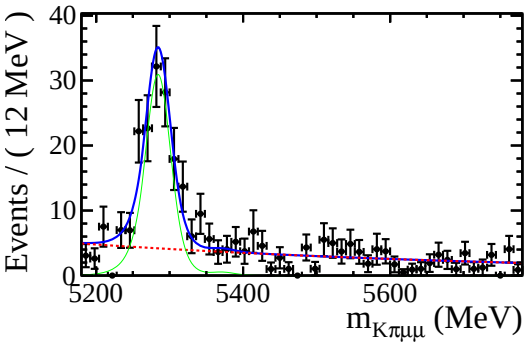

(f) $16.00 < q^2 < 19.0\,\mathrm{GeV}^2/c^4$

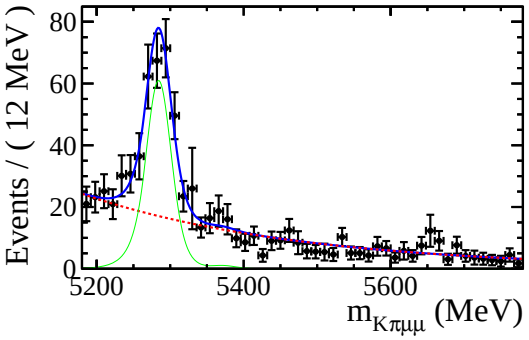

(g) $1.00 < q^2 < 6.00\,\mathrm{GeV}^2/c^4$

Figure 7.12: The result of the fit to the $K\pi\mu^+\mu^-$ mass spectrum in six q^2 bins for selected $B^0 \to K^+\pi^-\mu^+\mu^-$ events from $1.0\,\mathrm{fb}^{-1}$ of data.

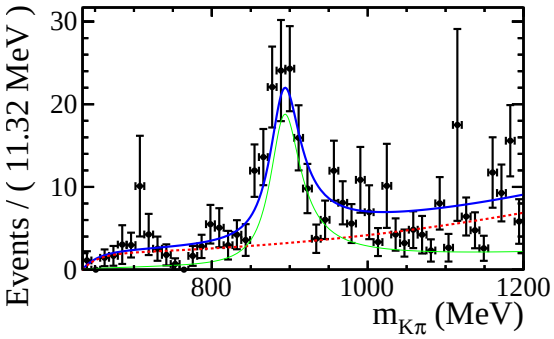

(a) $0.10 < q^2 < 2.00\,\mathrm{GeV}^2/c^4$

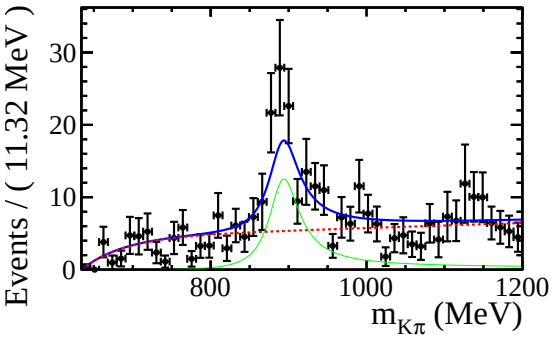

(b) $2.00 < q^2 < 4.30\,\mathrm{GeV}^2/c^4$

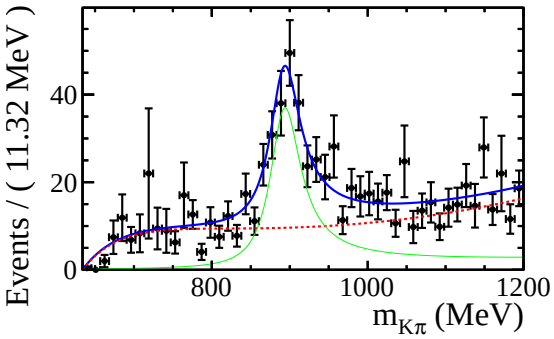

(c) $4.30 < q^2 < 8.68\,\mathrm{GeV}^2/c^4$

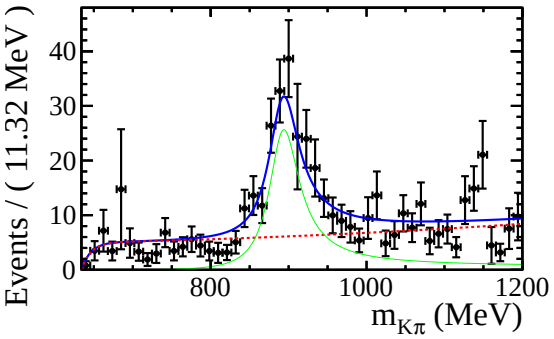

(d) $10.09 < q^2 < 12.9\,\mathrm{GeV}^2/c^4$

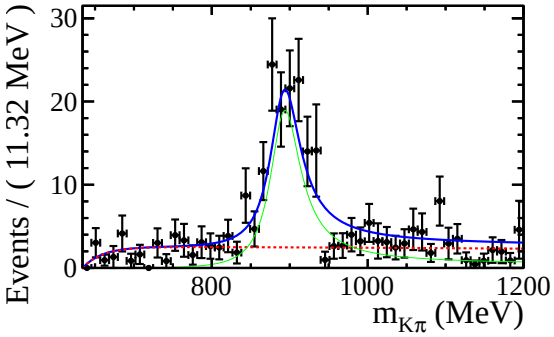

(e) $14.18 < q^2 < 16.0\,\mathrm{GeV}^2/c^4$

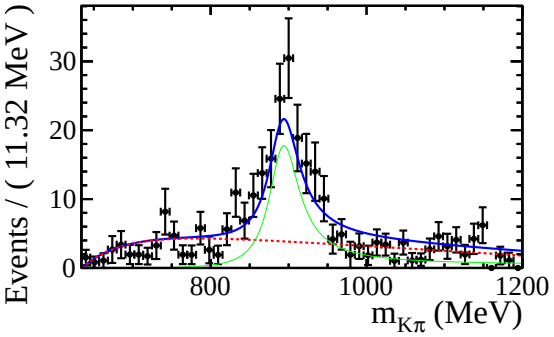

(f) $16.0 < q^2 < 19.0\,\mathrm{GeV}^2/c^4$

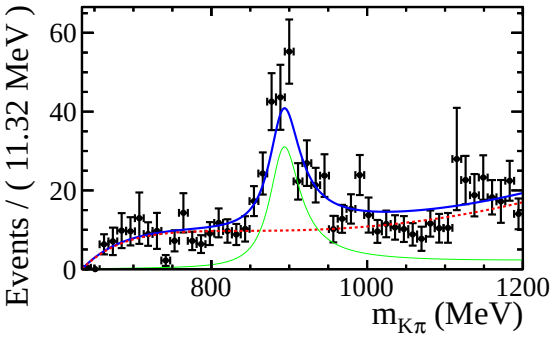

(g) $1.00 < q^2 < 6.00\,\mathrm{GeV}^2/c^4$

Figure 7.13: The results of the fit to the $K\pi$ mass spectrum for selected $B^0 \to K^+\pi^-\mu^+\mu^-$ events from $1.0\,\mathrm{fb}^{-1}$ of data.

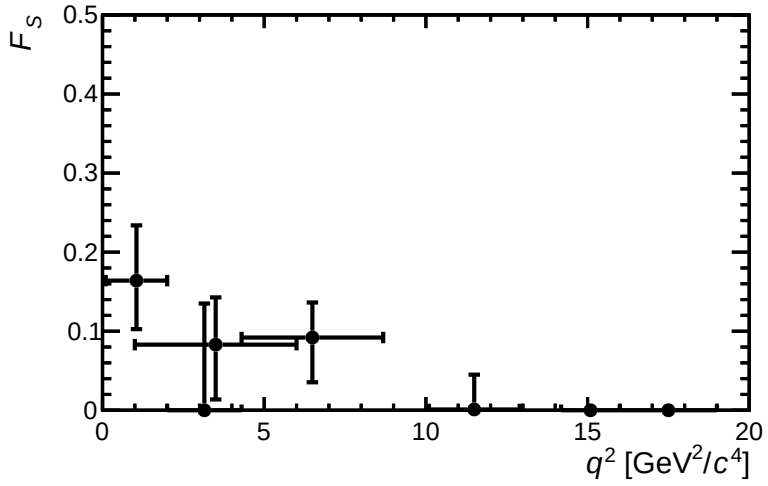

Figure 7.14: The fraction of $K\pi$ S-wave in six bins of q^2 for selected $B^0 \to K^+\pi^-\mu^+\mu^-$ events from $1.0\,\text{fb}^{-1}$ of data collected at $\sqrt{s} = 7\,\text{TeV}$ at LHCb in 2011. For the regions where no S-wave is found, the upper error bar indicates the 95% confidence limit.

7.7 Conclusions

The contribution from a $K\pi$ S-wave to $B^0 \to K^{*0}\mu^+\mu^-$ was analysed using $1.0\,\text{fb}^{-1}$ of data collected at LHCb at $\sqrt{s}$ =7 TeV in 2011. The central value of the S-wave fraction is non-zero in three bins of q^2 but all the measurements are compatible with no S-wave contribution. An S-wave fraction of 0.08 has less than a 5% effect on the measured values of A_{FB} and F_{L} in the range from $1 < q^2(\,\text{GeV}^2/c^4) < 6$ as described in Table 3 of Ref. [2]. Although the values found here do not have a significant effect on the current analysis, any new measurements of $B^0 \to K^{*0}\mu^+\mu^-$ must consider contamination from a $K\pi$ S-wave. This will add additional complications to the model of the angular distribution used to measure the angular observables in the form of additional parameters for both the signal and the background $K\pi$ shape as well as the interference between the S- and the P-wave. This will therefore influence the precision that can be obtained on the angular observables and reduce the improvement gained from the increase in statistics with a larger dataset. The dominant systematic effect in the current analysis comes from making the approximation that the phase space function is at the centre of the q^2 bin. This can be improved by varying the phase space factor in the fit model based on the q^2 and B mass of the $B^0 \to K^+\pi^-\mu^+\mu^-$ candidate.

The accuracy of future measurements of the $K\pi$ S-wave in $B^0 \to K^+\pi^-\mu^+\mu^-$ can be improved by fitting $\cos\theta_K$ to include the interference term between the S- and the P-wave. This requires an improved acceptance correction, possible with either a larger simulation sample or by alternatively including the angular acceptance in the fit model.

Chapter 8

Summary

> *Well, I mean, yes idealism, yes the dignity of pure research, yes the pursuit of truth in all its forms, but there comes a point I'm afraid where you begin to suspect that the entire multidimensional infinity of the Universe is almost certainly being run by a bunch of maniacs.*
>
> - Douglas Adams, *The Hitchhiker's Guide to the Galaxy* (1979)

In this thesis, measurements of the $b \to s$ electroweak penguin decay $B^0 \to K^+\pi^-\mu^+\mu^-$ were made using the LHCb detector at the LHC. The world's best measurements of the dimuon forward-backward asymmetry $A_{\rm FB}$ and the fraction of K^{*0} longitudinal polarisation were presented along with the first measurement of the $K\pi$ S-wave contribution to $B^0 \to K^+\pi^-\mu^+\mu^-$.

This thesis is based on data taken at LHCb in 2011 during run 1 of the LHC. The changing conditions of the data-taking environment from 2010 to 2011 required a re-development of the trigger for $B^0 \to K^{*0}\mu^+\mu^-$. These results provided cross-checks in the first truly multi-variate trigger in LHCb for data-taking during 2011 and beyond.

Two angular analyses of $B^0 \to K^{*0}\mu^+\mu^-$ were presented. The first angular analysis of $B^0 \to K^{*0}\mu^+\mu^-$ using $0.38\,\text{fb}^{-1}$ of data measured $A_{\rm FB}$ and $F_{\rm L}$ in 6 bins of q^2 providing the most precise measurements of these angular observables at the time. The second angular analysis improved on the measurements of the first and also measured the angular observables $S_{3,}$ S_9 and A_9 using $1.0\,\text{fb}^{-1}$ of data.

The results obtained for the $B^0 \to K^{*0}\mu^+\mu^-$ angular observables were combined with other measurements of $b \to s\ell^+\ell^-$ and $b \to s\gamma$ decays to place the most precise constraints to date on the values of the Wilson coefficients $\mathcal{C}_7$, $\mathcal{C}_9$ and $\mathcal{C}_{10}$ [12]. The measurements of the branching fraction of $B_s^0 \to \mu^+\mu^-$ and $B^0 \to K^{*0}\gamma$ were used constrain the magnitudes of $\mathcal{C}_9$ and $\mathcal{C}_{10}$ and the magnitude of $\mathcal{C}_7$ respectively. The measurements of the inclusive branching fraction of $B \to X_s\gamma$ and $B \to X_s\ell^+\ell^-$ [48] along with the branching fraction of $B^+ \to K^+\mu^+\mu^-$ were used to constrain combinations of the Wilson coefficients. The measurements of the differential branching fraction, $A_{\rm FB}$ and $F_{\rm L}$ from $B^0 \to K^{*0}\mu^+\mu^-$ presented in this thesis were used to constrain combinations of $\mathcal{C}_7$, $\mathcal{C}_9$ and $\mathcal{C}_{10}$. The two dimensional contours obtained in Ref [12] for combinations of the real and imaginary parts of the Wilson coefficients are shown in Fig. 8.1. These constraints are compatible with the SM prediction at the 2σ level but it can be seen that the constraints placed on the imaginary parts of the Wilson coefficients are looser than the constraints placed on the real parts.

The measurement of observables in electroweak penguin decays are complementary to direct searches for specific signatures of new particles at ATLAS and CMS at the LHC. For example, the constraints on the Wilson coefficients can be converted into a limit on the mass of any new particle that contributes in $B^0 \to K^{*0}\mu^+\mu^-$ of around 1 TeV [12]. These limits can be compared to the limits on the mass of new particles of several hundred GeV from direct production, such as in Ref. [121]. The constraints obtained from electroweak penguin decays are model-independent to the level that they only assume that any new particles have similar couplings to the CKM elements in the SM. wheras the limits from searches for the direct production of new particles place are dependent on the type of model used to produce the signature that is searched for. A similar comparison can be made to the limits on the mass of dark matter particles from indirect scattering experiments [122].

The inclusion of a $K\pi$ S-wave in the angular distribution of $B^0 \to K^+\pi^-\ell^+\ell^-$ was shown to have an overall dilution effect on measurements of the $B^0 \to K^{*0}\ell^+\ell^-$ angular observables. The toy studies presented here show significant bias on the angular observ-

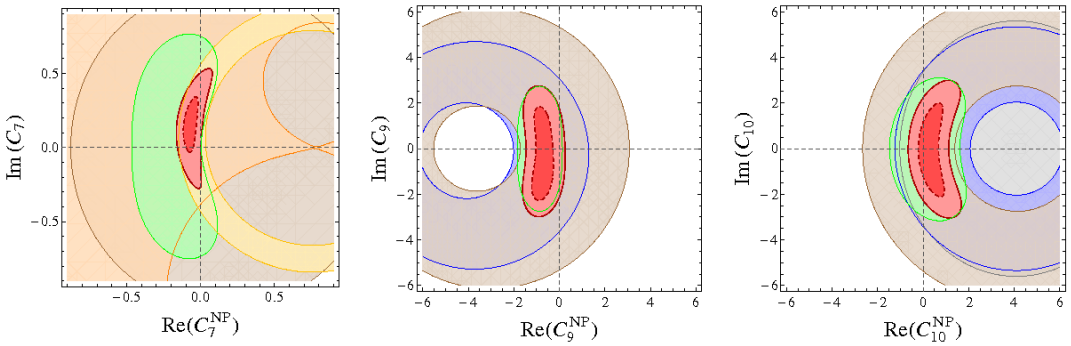

(a) Constraints on the real and imaginary parts of the left-handed Wilson coefficients

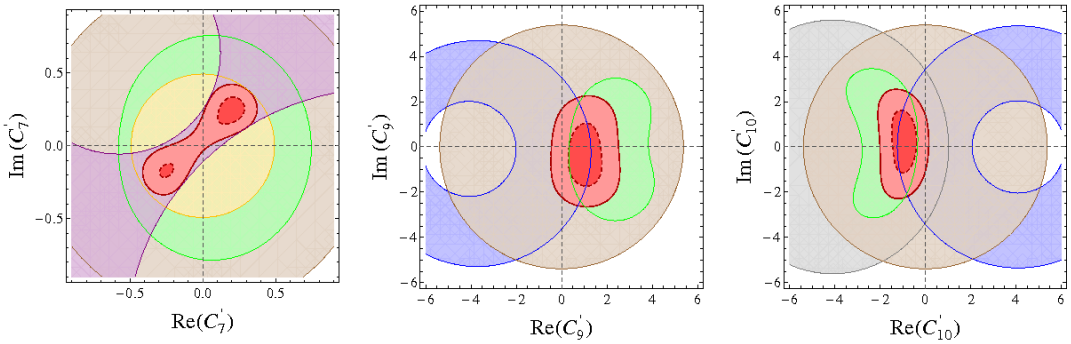

(b) Constraints on the real and imaginary parts of the right-handed Wilson coefficients

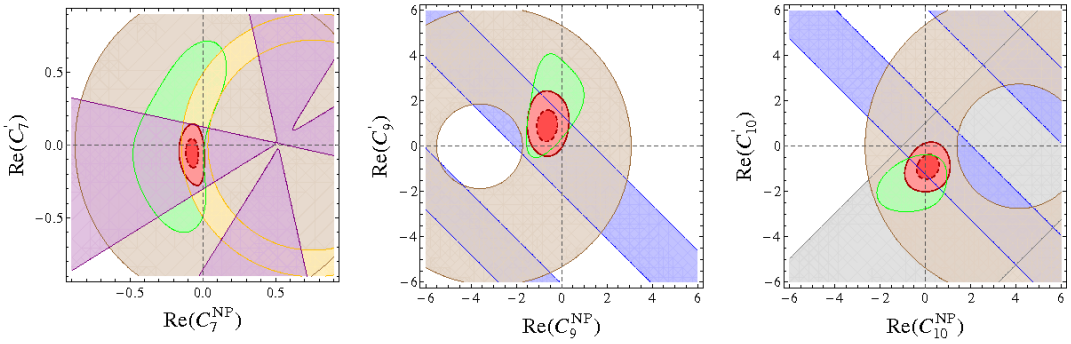

(c) Constraints on the real part of the $(\mathcal{C}_{7,9,10}, \mathcal{C}^{'}_{7,9,10})$ plane

Figure 8.1: Individual 2σ constraints on the unprimed Wilson coefficients from $B \to X_s\ell^+\ell^-$ (brown), $\mathcal{B}(B \to X_s\gamma)$ (yellow), $A_{CP}(b \to s\gamma)$ (orange), $B^0 \to K^{*0}\gamma$ (purple), $B^0 \to K^{*0}\mu^+\mu^-$ (green), $B^+ \to K^+\mu^+\mu^-$ (blue) and $B_s^0 \to \mu^+\mu^-$ (gray) as well as the combined 1 and 2σ constraints (pink and red respectively). Taken with permission from Ref. [12].

ables from an S-wave contribution of 7% in the P-wave mass window for datasets of over 500 events. In order to measure the size of this effect in data, the $K\pi$ S-wave was measured using $1.0\,\text{fb}^{-1}$ of data from LHCb. The integrated S-wave contribution between $0.64 < p^2 < 1.00\,\text{GeV}^2/c^4$ and between $1 < q^2 < 6\,\text{GeV}^2/c^4$ is

$$F_{\text{S}} = 0.083^{+0.057}_{-0.048}(\text{stat.})^{+0.018}_{-0.050}(\text{syst.})\,. \tag{8.1}$$

The measurement shows that further investigation is required for any future angular analysis of $B^0 \to K^{*0}\mu^+\mu^-$. The complete data recorded by LHCb in 2011 and 2012 is expected to total $3.0\,\text{fb}^{-1}$. This gives 600 $B^0 \to K^{*0}\mu^+\mu^-$ candidates between $1 < q^2 < 6\,\text{GeV}^2/c^4$ which will result in a bias of 0.6σ in F_{L} and 0.3σ in A_{FB} if an S-wave of 7% is ignored.

The next measurements of $B^0 \to K^{*0}\mu^+\mu^-$ will be based on datasets of several thousand candidates from LHCb and CMS. This will enable precision measurements of the angular observables in finer bins of q^2 in order to better determine the shape of A_{FB} at both low and high q^2. Measurements of the q^2 value at which A_{FB} crosses zero will allow further tests of the SM predictions as theoretical predictions have reduced uncertainties from the form factors at this point.

At the time of writing, the first run of the LHC has finished and the machine has been shut down for 2 years in order to upgrade the accelerator. Although the first two years of data have resulted in the discovery of the Higgs, there are no obvious hints of physics beyond the Standard Model in the measurements from the LHC. However, as direct searches yield few positive signs of physics beyond the SM, interest turns again to measuring the subtle effects in indirect searches. The electroweak penguin decays of b hadrons are already placing stringent constraints on the size of new physics couplings within the flavour sector. The datasets from the second run of the LHC will enable precision measurements of both the $B^0 \to K^+\pi^-\ell^+\ell^-$ spectrum and full angular analyses of $B^0 \to K^{*0}\mu^+\mu^-$.

Bibliography

[1] LHCb collaboration, R. Aaij *et al.*, *Differential branching fraction and angular analysis of the decay* $B^0 \to K^{*0}\mu^+\mu^-$, Phys. Rev. Lett. **108** (2012) 181806, arXiv:1112.3515.

[2] LHCb Collaboration, R. Aaij *et al.*, *Differential branching fraction and angular analysis of the decay* $B^0 \to K^{*0}\mu^+\mu^-$, JHEP **08** (2013) 131, arXiv:1304.6325.

[3] T. Blake, U. Egede, and A. Shires, *The effect of S-wave interference on the* $B^0 \to K^{*0}\ell^+\ell^-$ *angular observables*, JHEP **03** (2013) 027, arXiv:1210.5279.

[4] F. Alessio, R. Jacobsson, and R. Le Gac, *LHCb Operations Plots Webpage*, Apr, 2013.

[5] LHCb collaboration, A. A. Alves Jr. *et al.*, *The LHCb detector at the LHC*, JINST **3** (2008) S08005.

[6] BaBar collaboration, B. Aubert and others., *Measurement of decay amplitudes of* $B \to J/\psi K^*$, $\psi(2S)K^*$, *and* $\chi_{c1}K^*$ *with an angular analysis*, Phys. Rev. **D76** (2007) 031102, arXiv:0704.0522.

[7] BaBar collaboration, B. Aubert and others., *Angular distributions in the decays* $B^0 \to K^{*0}\ell^+\ell^-$, Phys. Rev. **D79** (2009) 031102, arXiv:0804.4412.

[8] Belle collaboration, J.-T. Wei and others., *Measurement of the differential branching fraction and forward-backward asymmetry for* $B^0 \to K^{*0}\ell^+\ell^-$, Phys. Rev. Lett. **103** (2009) 171801, arXiv:0904.0770.

[9] CDF Collaboration, T. Aaltonen and others., *Measurement of the Forward-Backward Asymmetry in the $B^0 \to K^{*0}\mu^+\mu^-$ Decay and First Observation of the $B_s^0 \to \phi\mu^+\mu^-$ Decay*, Phys. Rev. Lett. **106** (2011) 161801, arXiv:1101.1028.

[10] CDF collaboration, T. Aaltonen and others., *Measurements of the angular distributions in the decays $B^0 \to K^{*0}\mu^+\mu^-$ at CDF*, arXiv:1108.0695].

[11] C. Bobeth, G. Hiller, and D. van Dyk, *More benefits of semileptonic rare B decays at low recoil: CP Violation*, JHEP **07** (2011) 067, arXiv:1105.0376.

[12] W. Altmannshofer and D. M. Straub, *Cornering New Physics in $b \to s$ Transitions*, JHEP **08** (2012) 121, arXiv:1206.0273.

[13] Particle Data Group, J. Beringer *et al.*, *Review of particle physics*, Phys. Rev. **D86** (2012) 010001.

[14] WMAP Collaboration, C. Bennett *et al.*, *Nine-Year Wilkinson Microwave Anisotropy Probe (WMAP) Observations: Final Maps and Results*, arXiv:1212.5225.

[15] S. Dodelson, *Modern cosmology*, Academic Press, 2003.

[16] F. Zwicky, *On the Masses of Nebulae and of Clusters of Nebulae*, APJ **86** (1937) 217.

[17] G. D'Amico, M. Kamionkowski, and K. Sigurdson, *Dark Matter Astrophysics*, arXiv:0907.1912.

[18] B. Famaey and S. McGaugh, *Modified Newtonian Dynamics (MOND): Observational Phenomenology and Relativistic Extensions*, Living Rev. Rel. **15** (2012) 10, arXiv:1112.3960.

[19] J. Martin, *Everything You Always Wanted To Know About The Cosmological Constant Problem (But Were Afraid To Ask)*, Comptes Rendus Physique **13** (2012) 566, arXiv:1205.3365.

[20] S. Glashow, *Partial Symmetries of Weak Interactions*, Nucl. Phys. **22** (1961) 579.

[21] S. Weinberg, *A Model of Leptons*, Phys. Rev. Lett. **19** (1967) 1264.

[22] A. Salam, *Weak and Electromagnetic Interactions*, Conf. Proc. **C680519** (1968) 367.

[23] P. W. Higgs, *Spontaneous Symmetry Breakdown without Massless Bosons*, Phys. Rev. **145** (1966) 1156.

[24] G. Guralnik, C. Hagen, and T. Kibble, *Global Conservation Laws and Massless Particles*, Phys. Rev. Lett. **13** (1964) 585.

[25] T. Kibble, *Symmetry breaking in nonAbelian gauge theories*, Phys. Rev. **155** (1967) 1554.

[26] H. Yukawa, *On the interaction of elementary particles*, Proc. Phys. Math. Soc. Jap. **17** (1935) 48.

[27] N. Cabibbo, *Unitary Symmetry and Leptonic Decays*, Phys. Rev. Lett. **10** (1963) 531.

[28] M. Kobayashi and T. Maskawa, *CP Violation in the Renormalizable Theory of Weak Interaction*, Prog. Theor. Phys. **49** (1973) 652.

[29] C.-N. Yang and R. L. Mills, *Conservation of Isotopic Spin and Isotopic Gauge Invariance*, Phys. Rev. **96** (1954) 191.

[30] E. Abers and B. Lee, *Gauge Theories*, Phys. Rept. **9** (1973) 1.

[31] F. Halzen and A. D. Martin, *Quarks and leptons: an introductory course in modern particle physics*, Wiley, 1984.

[32] A. V. Manohar and M. B. Wise, *Heavy quark physics*, Camb. Monogr. Part. Phys. Nucl. Phys. Cosmol. **10** (2000) 1.

[33] T. Mannel, *Effective Field Theories in Flavor Physics*, Springer Tracts Mod. Phys. **203** (2004) 1.

[34] UA1 collaboration, G. Arnison *et al.*, *Experimental Observation of Isolated Large Transverse Energy Electrons with Associated Missing Energy at* $\sqrt{s} = 540$ *GeV*, Phys. Lett. **B122** (1983) 103.

[35] UA1 collaboration, G. Arnison *et al.*, *Experimental Observation of Lepton Pairs of Invariant Mass Around 95-GeV/c**2 at the CERN SPS Collider*, Phys. Lett. **B126** (1983) 398.

[36] CMS collaboration, S. Chatrchyan *et al.*, *Observation of a new boson at a mass of 125 GeV with the CMS experiment at the LHC*, Phys. Lett. **B716** (2012) 30, arXiv:1207.7235.

[37] ATLAS collaboration, G. Aad *et al.*, *Observation of a new particle in the search for the Standard Model Higgs boson with the ATLAS detector at the LHC*, Phys. Lett. **B716** (2012) 1, arXiv:1207.7214.

[38] D. Melikhov, N. Nikitin, and S. Simula, *Probing right-handed currents in* $B^0 \to K^* \ell^+\ell^-$ *transitions*, Phys. Lett. **B442** (1998) 381, arXiv:hep-ph/9807464.

[39] K. Wilson and W. Zimmermann, *Operator product expansions and composite field operators in the general framework of quantum field theory*, Commun. Math. Phys. **24** (1972) 87.

[40] W. Altmannshofer *et al.*, *Symmetries and Asymmetries of* $B \to K^*\mu^+\mu^-$ *Decays in the Standard Model and Beyond*, JHEP **01** (2009) 019, arXiv:0811.1214.

[41] C. Bobeth, M. Misiak, and J. Urban, *Photonic penguins at two loops and m(t) dependence of BR[*$B \to X_{(s)}\ell^+\ell^-$*]*, Nucl. Phys. **B574** (2000) 291, arXiv:hep-ph/9910220.

[42] CLEO collaboration, *Evidence for penguin-diagram decays: First observation of* $b \to k^*(892)\gamma$, Phys. Rev. Lett. **71** (1993) 674.

[43] BaBar collaboration, B. Aubert *et al.*, *Measurement of branching fractions and CP and isospin asymmetries in $B \to K^*(892)\gamma$ decays*, Phys. Rev. Lett. **103** (2009) 211802, arXiv:0906.2177.

[44] Belle collaboration, A. Limosani *et al.*, *Measurement of Inclusive Radiative B-Meson Decays with a Photon Energy Threshold of 1.7 GeV*, Phys. Rev. Lett. **103** (2009) 241801.

[45] LHCb collaboration, R. Aaij *et al.*, *Measurement of the ratio of branching fractions $\mathcal{B}(B^0 \to K^{*0}\gamma)/\mathcal{B}(B_s^0 \to \phi\gamma)$*, Phys. Rev. **D85** (2012) 112013, arXiv:1202.6267.

[46] LHCb collaboration, R. Aaij *et al.*, *Measurement of the ratio of branching fractions $\mathcal{B}(B^0 \to K^{*0}\gamma)/\mathcal{B}(B_s^0 \to \phi\gamma)$ and direct CP asymmetry in $B^0 \to K^{*0}\gamma$*, Nucl. Phys. **B867** (2013) 1, arXiv:1209.0313.

[47] LHCb collaboration, *Measurement of the direct CP asymmetry in the $B_d^0 \to K^{*0}\gamma$ decay*, LHCb-CONF-2012-004.

[48] Heavy Flavor Averaging Group, Y. Amhis *et al.*, *Averages of b-hadron, c-hadron, and tau-lepton properties as of early 2012*, arXiv:1207.1158.

[49] A. Ali, B. D. Pecjak, and C. Greub, *Towards $B \to V\gamma$ decays at NNLO in SCET*, Eur. Phys. J. **C55** (2008) 577, arXiv:0709.4422.

[50] F. Krüger, L. M. Sehgal, N. Sinha, and R. Sinha, *Angular distribution and CP asymmetries in the decays $\overline{B} \to K^-\pi^+e^-e^+$ and $\overline{B} \to \pi^-\pi^+e^-e^+$*, Phys. Rev. **D61** (2000) 114028.

[51] Z. Ligeti and F. J. Tackmann, *Precise predictions for $\bar{B} \to X_s\ell^+\ell^-$ in the large q^2 region*, Phys. Lett. **B653** (2007) 404, arXiv:0707.1694.

[52] T. Huber, T. Hurth, and E. Lunghi, *Logarithmically Enhanced Corrections to the Decay Rate and Forward Backward Asymmetry in $\bar{B} \to X_s\ell^+\ell^-$*, Nucl. Phys. **B802** (2008) 40, arXiv:0712.3009.

[53] Kruger, F. and others., *Probing new physics via the transverse amplitudes of* $B^0 \to \overline{K}^{*0}(\to K^-\pi^+)\ell^+\ell^-$ *at large recoil*, Phys. Rev. **D71** (2005) 094009, arXiv:hep-ph/0502060.

[54] U. Egede and others., *New observables in the decay mode* $B^0 \to K^{*0}\mu^+\mu^-$, JHEP **11** (2008) 032, arXiv:0807.2589.

[55] U. Egede and others., *New physics reach of the decay mode* $\bar{B} \to \bar{K}^{*0}\ell^+\ell^-$, JHEP **10** (2010) 056, arXiv:1005.0571.

[56] C. Bobeth, G. Hiller, and D. van Dyk, *The Benefits of* $\bar{B} \to \bar{K}^*\ell^+\ell^-$ *Decays at Low Recoil*, JHEP **07** (2010) 098, arXiv:1006.5013.

[57] J. Matias, F. Mescia, M. Ramon, and J. Virto, *Complete Anatomy of* $\bar{B}_d \to \bar{K}^{*0}(\to K\pi)\ell^+\ell^-$ *and its angular distribution*, JHEP **04** (2012) 104, arXiv:1202.4266.

[58] LHCb collaboration, R. Aaij and others., *Differential branching fraction and angular analysis of the decay* $B^0 \to K^{*0}\mu^+\mu^-$, arXiv:1112.3515.

[59] LHCb collaboration, R. Aaij *et al.*, *Measurement of the CP asymmetry in* $B^0 \to K^{*0}\mu^+\mu^-$ *decays*, arXiv:1210.4492.

[60] J. Lefranois and M. Schune, *Measuring the photon polarization in* $b\to s\gamma$ *using the* $B^0 \to K^{*0}e^+e^-$ *decay channel*, .

[61] C.-D. Lu and W. Wang, *Analysis of* $B \to K_J^*(\to K\pi)\mu^+\mu^-$ *in the higher kaon resonance region*, Phys. Rev. **D85** (2012) 034014, arXiv:1111.1513.

[62] B. Grinstein and D. Pirjol, *Factorization in* $B^0 \to K\ \pi\ \ell^+\ell^-$ *decays*, Phys. Rev. **D73** (2006) 094027, arXiv:hep-ph/0505155.

[63] D. Becirevic and A. Tayduganov, *Impact of* $B \to K_0^*\ell^+\ell^-$ *on the New Physics search in* $B \to K^*\ell^+\ell^-$ *decay*, arXiv:1207.4004.

[64] J. Matias, *On the S-wave pollution of* $B^0 \to K^{*0}\ell^+\ell^-$ *observables*, Phys. Rev. **D86** (2012) 094024, arXiv:1209.1525.

[65] D. Becirevic and E. Schneider, *On transverse asymmetries in $B \to K^{*0}\ell^+\ell^-$*, Nucl. Phys. **B854** (2012) 321, arXiv:1106.3283.

[66] Gargamelle Neutrino collaboration, F. Hasert *et al.*, *Observation of Neutrino Like Interactions Without Muon Or Electron in the Gargamelle Neutrino Experiment*, Phys. Lett. **B46** (1973) 138.

[67] Lefevre, C, *LHC: the guide*, cds.cern.ch/record/1092437, Jan, 2008.

[68] LHCb collaboration, R. Aaij *et al.*, *Measurement of $\sigma(pp \to b\bar{b}X)$ at $\sqrt{s} = 7$ TeV in the forward region*, Phys. Lett. **B694** (2010) 209, arXiv:1009.2731.

[69] M. Adinolfi *et al.*, *Performance of the LHCb RICH detector at the LHC*, arXiv:1211.6759.

[70] R. Aaij *et al.*, *The LHCb trigger and its performance*, arXiv:1211.3055.

[71] Brice, M., *Assembling the last module of the vertex locator for LHCb. Assemblage en salle propre de l'exprience LHCb du 42e et dernier module du VELO (Localisateur du vertex)*, cds.cern.ch/record/1024838, Mar, 2007.

[72] LHCb collaboration, R. Aaij *et al.*, *Measurement of charged particle multiplicities in pp collisions at $\sqrt{s} = 7$ TeV in the forward region*, Eur. Phys. J. **C72** (2012) 1947, arXiv:1112.4592.

[73] A. Jaeger *et al.*, *Measurement of the track finding efficiency*, LHCb-PUB-2011-025.

[74] C. G. Blanks, *V^0 production ratios at LHCb and the alignment of its RICH detectors*, PhD thesis, London, Imperial College, 2011, CERN-THESIS-2011-212.

[75] G. Lanfranchi *et al.*, *The Muon Identification Procedure of the LHCb Experiment for the First Data*, LHCb-PUB-2009-013.

[76] A. A. Alves Jr *et al.*, *Performance of the LHCb muon system.*, LHCb-DP-2012-002.

[77] M. de Cian, *Track Reconstruction Efficiency and Analysis of $B^0 \to K^{*0}\mu^+\mu^-$ at the LHCb Experiment*, PhD thesis, Universitat Zurich, 2013, Presented 2013.

[78] LHCb collaboration, R. Aaij *et al.*, *Measurement of J/ψ production in pp collisions at $\sqrt{s} = 7$ TeV*, Eur. Phys. J. **C71** (2011) 1645, arXiv:1103.0423.

[79] G. Corti *et al.*, *Software for the LHCb experiment*, IEEE Trans. Nucl. Sci. **53** (2006) 1323.

[80] R. Antunes-Nobrega, A. Frana-Barbosa *et al.*, *LHCb reoptimized detector design and performance: Technical Design Report*, Technical Design Report LHCb, CERN, Geneva, 2003.

[81] M. Clemencic *et al.*, *The LHCb simulation application,* GAUSS*: design, evolution and experience*, J. of Phys. : Conf. Ser. **331** (2011) 032023.

[82] T. Sjöstrand, S. Mrenna, and P. Skands, *PYTHIA 6.4 physics and manual*, JHEP **05** (2006) 026, arXiv:hep-ph/0603175.

[83] I. Belyaev *et al.*, *Handling of the generation of primary events in* GAUSS*, the LHCb simulation framework*, Nuclear Science Symposium Conference Record (NSS/MIC) **IEEE** (2010) 1155.

[84] D. J. Lange, *The EvtGen particle decay simulation package*, Nucl. Instrum. Meth. **A462** (2001) 152.

[85] GEANT4 collaboration, S. Agostinelli *et al.*, *GEANT4: A simulation toolkit*, Nucl. Instrum. Meth. **A506** (2003) 250.

[86] GEANT4 collaboration, J. Allison *et al.*, *Geant4 developments and applications*, IEEE Trans. Nucl. Sci. **53** (2006) 270.

[87] A. Jaeger *et al.*, *Measurement of the track finding efficiency*, LHCb-PUB-2011-02.

[88] LHCb collaboration, B. Adeva *et al.*, *Roadmap for selected key measurements of LHCb*, arXiv:0912.4179.

[89] M. Williams *et al.*, *The HLT2 Topological Lines*, LHCb-PUB-2011-002.

[90] V. V. Gligorov, C. Thomas, and M. Williams, *The HLT inclusive B triggers*, LHCb-PUB-2011-016. LHCb-INT-2011-030.

[91] L. Breiman, J. H. Friedman, R. A. Olshen, and C. J. Stone, *Classification and regression trees*, Wadsworth international group, Belmont, California, USA, 1984.

[92] B. P. Roe *et al.*, *Boosted decision trees as an alternative to artificial neural networks for particle identification*, Nucl. Instrum. Meth. **A543** (2005) 577, arXiv:physics/0408124.

[93] R. E. Schapire and Y. Freund, *A decision-theoretic generalization of on-line learning and an application to boosting*, Jour. Comp. and Syst. Sc. **55** (1997) 119.

[94] T. Blake, *Ring Imaging Cherenkov Detectors and the Rare Decay $B^0 \to K^{*0}\mu^+\mu^-$ at LHCb*, PhD thesis, Imperial College London, London, 2008.

[95] N. Serra, *A study of rare B-meson decay with muons in the final state with the LHCb detector*, PhD thesis, Universit degli Studi di Cagliari, Cagliari, 2008, CERN-THESIS-2010-022.

[96] SLD collaboration, K. Abe *et al.*, *A Measurement of R(b) using a vertex mass tag*, Phys. Rev. Lett. **80** (1998) 660, arXiv:hep-ex/9708015.

[97] A. Ali, P. Ball, L. T. Handoko, and G. Hiller, *Comparative study of the decays $B \to (K,K^*)\ell^+\ell^-$ in the standard model and supersymmetric theories*, Phys. Rev. **D61** (2000) 074024.

[98] M. Needham, *Clone Track Identification using the Kullback-Liebler Distance*, LHCb-2008-002.

[99] CDF collaboration, T. Aaltonen *et al.*, *Measurement of the CP-Violating Phase $\beta_s^{J/\Psi\phi}$ in $B_s^0 \to J/\Psi\phi$ Decays with the CDF II Detector*, Phys. Rev. **D85** (2012) 072002, arXiv:1112.1726.

[100] LHCb collaboration, R. Aaij *et al.*, *Measurement of the CP-violating phase ϕ_s in the decay $B_s^0 \to J/\psi\phi$*, Phys. Rev. Lett. **108** (2011) 101803. 9 p.

[101] P. Tchebychev, *Théorie des mécanismes connus sous le nom de parallélogrammes, par M. P. Tchébychev,... 1re partie...*, Eggers, 1854.

[102] T. Skwarnicki, *A study of the radiative cascade transitions between the Upsilon-prime and Upsilon resonances*, PhD thesis, Institute of Nuclear Physics, Krakow, 1986, DESY-F31-86-02.

[103] M. Williams, *How good are your fits? Unbinned multivariate goodness-of-fit tests in high energy physics*, JINST **5** (2010) P09004, arXiv:1006.3019.

[104] G. J. Feldman and R. D. Cousins, *Unified approach to the classical statistical analysis of small signals*, Phys. Rev. D **57** (1998) 3873.

[105] C. Bobeth, G. Hiller, D. van Dyk, and C. Wacker, *The Decay $B^0 \to K^{*0}\ell^+\ell^-$ at Low Hadronic Recoil and Model-Independent Delta B = 1 Constraints*, JHEP **01** (2012) 107, arXiv:1111.2558.

[106] W. Altmannshofer, P. Paradisi, and D. M. Straub, *Model-Independent Constraints on New Physics in $b \to s$ Transitions*, JHEP **1204** (2012) 008, arXiv:1111.1257.

[107] LHCb collaboration, *Differential branching fraction and angular analysis of the $B^0 \to K^{*0}\mu^+\mu^-$ decay*, LHCb-CONF-2012-008.

[108] LASS collaboration, D. Aston *et al.*, *A study of $K^-\ \pi^+$ scattering in the reaction $K^-\ p \to K^-\ \pi^+\ n$ at 11* GeV/ c, Nucl. Phys. B **296** (1987) 493. 58 p.

[109] BaBar collaboration, B. Aubert and others., *Ambiguity-free measurement of* $\cos 2\beta$*: Time-integrated and time-dependent angular analyses of $B \to J/\psi\, K\pi$*, Phys. Rev. **D71** (2005) 032005, arXiv:hep-ex/0411016.

[110] LHCb collaboration, R. Aaij and others., *Determination of the sign of the decay width difference in the B_s system*, arXiv:1202.4717.

[111] Y. Xie, P. Clarke, G. Cowan, and F. Muheim, *Determination of 2β(s) in $B_{0(s)}$ -¿ J/psi K+ K- Decays in the Presence of a K+ K- S-Wave Contribution*, JHEP **09** (2009) 074, arXiv:0908.3627.

[112] D0 collaboration, V. M. Abazov *et al.*, *Measurement of the CP-violating phase $\phi_s^{J/\psi\phi}$ using the flavor-tagged decay $B_s^0 \to J/\psi\phi$ in 8 fb^{-1} of $p\bar{p}$ collisions*, Phys. Rev. **D85** (2012) 032006, arXiv:1109.3166.

[113] LHCb collaboration, R. Aaij *et al.*, *Measurement of the CP-violating phase ϕ_s in the decay $B_s^0 \to J/\psi\phi$*, Phys. Rev. Lett. **108** (2012) 101803, arXiv:1112.3183.

[114] J. M. Blatt and V. F. Weisskopf, *Theoretical nuclear physics*, Springer, New York, NY, 1979.

[115] BaBar collaboration, B. Aubert and others., *Search for the Z(4430)- at BaBar*, Phys. Rev. **D79** (2009) 112001.

[116] LHCb collaboration, R. Aaij *et al.*, *Measurement of CP violation and the B_s^0 meson decay width difference with $B_s^0 \to J/\psi K^+K^-$ and $B_s^0 \to J/\psi\pi^+\pi^-$ decays*, Phys. Rev. **D87** (2013) 112010, arXiv:1304.2600.

[117] Fermilab E791 collaboration, E. M. Aitala *et al.*, *Dalitz plot analysis of the decay $D^+ \to K^-\pi^+\pi^+$ and indication of a low-mass scalar $k\pi$ resonance*, Phys. Rev. Lett. **89** (2002) 121801.

[118] LHCb collaboration, R. Aaij *et al.*, *Measurement of $B_s \to J/\psi\bar{K}^{*0}$ branching fraction and angular amplitudes*, Phys. Rev. **D86** (2012) 071102(R), arXiv:1208.0738.

[119] K. A, *Sulla determinazione empirica di una legge di distribuzione*, G. Ist. Ital. Attuari **83** (1933).

[120] LHCb collaboration, R. Aaij *et al.*, *Measurement of mixing and CP violation parameters in two-body charm decays*, JHEP **04** (2012) 129, arXiv:1112.4698.

[121] CMS Collaboration, S. Chatrchyan *et al.*, *Search for supersymmetry in hadronic final states with missing transverse energy using the variables α_T and b-quark multiplicity in pp collisions at $\sqrt{s}$ = 8 TeV*, arXiv:1303.2985.

[122] A. Geringer-Sameth and S. M. Koushiappas, *Exclusion of canonical WIMPs by the joint analysis of Milky Way dwarfs with Fermi*, Phys. Rev. Lett. **107** (2011) 241303, arXiv:1108.2914.

Appendix A

Tables of systematic contributions

A.1 The angular analysis of $B^0 \to K^{*0}\mu^+\mu^-$ of $0.38\,\text{fb}^{-1}$

The estimated value for the sources of systematic uncertainty for the differential branching fraction, A_{FB} and F_{L}. The effects included for the data-simulation corrections are the relative tracking efficiency, the relative trigger efficiency, the PID correction and the relative muon identification efficiency. The additional variations in the signal mass model and the background mass model along are included. The dominant effect is from the error on the weights from the acceptance correction.

A.2 The angular analysis of $B^0 \to K^{*0}\mu^+\mu^-$ of $1.0\,\text{fb}^{-1}$

The values of the contributions from possible sources of systematic uncertainty for the angular analysis of $B^0 \to K^{*0}\mu^+\mu^-$ based on $1.0\,\text{fb}^{-1}$ of data are given below. A glossary of the contributions described in Sec. 5.6 are given in Table A.4. The contributions to A_{FB}. F_{L}, S_3 and S_9 are given in Tables A.5, A.6, A.7 and A.8. The contributions to A_{T}^{Re}, A_{T}^{Im}, A_{T}^{2} and A_9 are given in Tables A.11, A.9, A.10 and A.12. The contributions to the measurement of the differential branching fraction are given in Table A.13

Table A.1: Systematic uncertainty on the estimate of A_{FB} in each of the q^2 bins.

$q^2(\,\mathrm{GeV}^2/c^4)$	Relative tracking efficiency	Relative trigger efficiency	PID. correction	μ-ID	Bkg. Model	Sig. Mass Model	Bkg. Mass Model	Weights	Tot.
$0.10 < q^2 < 2.00$	0.01	<0.01	<0.01	<0.01	0.04	<0.01	0.01	0.03	0.06
$2.00 < q^2 < 4.30$	<0.01	<0.01	<0.01	<0.01	0.03	<0.01	0.01	0.03	0.04
$4.30 < q^2 < 8.68$	<0.01	<0.01	<0.01	<0.01	0.02	<0.01	<0.01	0.01	0.02
$10.09 < q^2 < 12.86$	0.01	0.01	<0.01	0.01	<0.01	<0.01	<0.01	0.02	0.02
$14.18 < q^2 < 16.00$	<0.01	<0.01	<0.01	<0.01	0.01	0.01	<0.01	0.02	0.03
$16.00 < q^2 < 19.00$	0.02	0.02	<0.01	0.02	0.01	<0.01	<0.01	0.04	0.06
$1.00 < q^2 < 6.00$	0.01	<0.01	<0.01	<0.01	0.02	<0.01	0.01	0.03	0.04

Table A.2: Systematic uncertainty on the estimate of F_L in each of the q^2 bins.

$q^2(\,\mathrm{GeV}^2/c^4)$	Relative tracking efficiency	Relative trigger efficiency	PID. correction	μ-ID	Bkg. Model	Sig. Mass Model	Bkg. Mass Model	Weights	Tot.
$0.10 < q^2 < 2.00$	<0.01	<0.01	<0.01	<0.01	0.02	<0.01	<0.01	<0.01	0.02
$2.00 < q^2 < 4.30$	0.01	0.01	<0.01	0.01	0.02	<0.01	0.01	0.01	0.03
$4.30 < q^2 < 8.68$	<0.01	<0.01	<0.01	<0.01	<0.01	<0.01	<0.01	0.01	0.01
$10.09 < q^2 < 12.86$	0.01	0.01	<0.01	0.01	0.01	<0.01	<0.01	0.02	0.03
$14.18 < q^2 < 16.00$	0.02	0.01	<0.01	0.01	0.02	0.01	<0.01	0.03	0.05
$16.00 < q^2 < 19.00$	0.01	0.01	<0.01	0.01	<0.01	<0.01	<0.01	0.03	0.03
$1.00 < q^2 < 6.00$	0.01	0.01	<0.01	0.01	0.02	<0.01	<0.01	0.02	0.03

Table A.3: Systematic uncertainty on the estimate of dBF/dq^2 in each of the q^2 bins.

$q^2(\,\mathrm{GeV}^2/c^4)$	Relative tracking efficiency	Relative trigger efficiency	PID. correction	μ-ID	Bkg. Model	Sig. Mass Model	Bkg. Mass Model	Weights	Tot.
$0.10 < q^2 < 2.00$	0.03	0.02	<0.01	0.04	0.02	0.02	0.01	0.06	
$2.00 < q^2 < 4.30$	0.01	0.01	<0.01	0.01	<0.01	0.01	<0.01	0.02	
$4.30 < q^2 < 8.68$	0.02	0.02	<0.01	0.03	0.01	0.02	0.01	0.05	
$10.09 < q^2 < 12.86$	0.01	0.03	<0.01	0.04	0.04	0.03	0.01	0.07	
$14.18 < q^2 < 16.00$	0.02	0.02	<0.01	0.03	0.02	0.02	0.01	0.05	
$16.00 < q^2 < 19.00$	0.03	0.01	<0.01	0.02	0.02	0.01	0.01	0.05	
$1.00 < q^2 < 6.00$	0.01	0.01	<0.01	0.02	<0.01	0.01	<0.01	0.03	

Table A.4: A glossary of the possible sources of systematic uncertainty

Systematic	Description
CTK[...]	Variation of the acceptance in $\cos\theta_K$ by $\pm 10\%$
CTL[...]	Variation of the acceptance in $\cos\theta_l$ by $\pm 10\%$
CTL,CTK[...]	Variation of the acceptance in $\cos\theta_l$ and $\cos\theta_K$ by $\pm 10\%$ in a factorisable way
Nonfac	Variation of the acceptance in $\cos\theta_l$ and $\cos\theta_K$ by 10% in a non-factorisable way
HadronP	Removal of tracks with $p < 5\,\mathrm{GeV}/c$ in the analysis and acceptance correction
Muon ID	Variation of `IsMuon` relative efficiency within its measured uncertainty
KPI[...]	Variation of the $K^{*0} \to \overline{K}^{*0}$ mis-ID
NoMultCan	Removal of events containing multiple candidates
Sigma[...]	Variation of the mass resolution of $B^0 \to K^{*0}\mu^+\mu^-$ with respect to $B^0 \to K^{*0}J/\psi$ by 5%
Tracking	Variation of the relative tracking efficiency between data and MC within in the measured uncertainty
Trigger	Simulation of trigger efficiency with a 3% efficiency loss for soft-muons
S-wave	See text
PID Correction [Up,Down]	Assignment of DLL value for neighbouring bin for events close to bin edge
Bin [Up, Down]	Change q^2 binning scheme take acceptance for bin above or bin below.

Systematic	$0.1 < q^2 < 2.0$	$2.0 < q^2 < 4.3$	$4.3 < q^2 < 8.68$	$10.09 < q^2 < 12.86$	$14.18 < q^2 < 16.0$	$16.0 < q^2 < 19.0$	$0.1 < q^2 < 6.0$
fileNominal	-0.020 +/- 0.001	-0.185 +/- 0.001	0.171 +/- 0.000	0.277 +/- 0.001	0.486 +/- 0.001	0.291 +/- 0.001	-0.151 +/- 0.001
AC CTL Up	-0.002	-0.003	0.002	0.004	0.006	0.002	-0.002
AC CTL Down	0.001	0.004	-0.002	-0.004	-0.005	-0.004	0.004
AC CTK Up	0.001	0.006	-0.005	-0.007	-0.010	-0.006	0.006
AC CTK Down	0.000	-0.007	0.005	0.008	0.012	0.007	-0.005
AC CTL Up CTK Down	0.001	0.003	-0.004	-0.003	-0.004	-0.004	0.002
AC CTL Down CTK Up	-0.000	0.010	-0.008	-0.011	-0.013	-0.012	0.010
AC CTL Up CTK Down	-0.003	-0.010	0.009	0.014	0.016	0.011	-0.008
AC CTL Down CTK Down	-0.002	-0.002	0.003	0.004	0.006	0.002	-0.002
AC Non-factorisable Up	0.001	0.001	-0.000	0.001	0.000	-0.000	0.002
AC Non-factorisable Down	0.002	-0.000	0.001	-0.000	-0.000	0.001	0.000
AC q^2 binning +1	0.001	-0.002	0.002	0.002	-0.003	-0.007	-0.001
AC q^2 binning -1	-0.001	0.004	-0.002	0.005	0.007	0.005	0.001
1st Order Background Model	-0.001	0.002	0.000	0.001	0.002	-0.000	0.000
3rd Order Background Model	-0.000	-0.001	-0.000	0.000	-0.001	0.000	0.002
K^{*0} mis-ID Down	-0.000	0.002	-0.001	-0.000	0.000	0.000	0.001
K^{*0} mis-ID Up	-0.001	-0.001	0.001	0.001	0.002	0.000	0.000
Signal mass width Down	-0.002	-0.000	0.001	0.002	-0.000	-0.000	0.001
Signal mass width Up	-0.001	0.001	0.001	0.001	0.001	0.000	0.001
S-wave component	-0.000	0.007	-0.008	-0.011	-0.014	-0.012	0.007
IP Smearing	0.002	0.002	-0.001	0.001	0.005	0.001	-0.002
B^0 p_T re-weighting	-0.001	-0.000	0.002	0.003	0.002	0.001	-0.001
B^0 p re-weighting	-0.000	-0.002	0.002	0.006	0.005	0.003	-0.001
IsMuon efficiency Up	0.001	0.002	-0.001	0.000	0.001	0.000	0.002
IsMuon efficiency Down	-0.001	-0.006	0.002	0.001	0.002	-0.001	-0.002
Removal of soft tracks	0.001	-0.003	0.003	0.007	0.007	0.004	-0.002
PID performance +5%	0.001	0.001	-0.000	0.001	0.000	-0.003	0.001
PID performance -5%	-0.001	0.000	0.000	-0.002	0.000	-0.003	0.002
PID performance +10%	-0.001	0.002	-0.001	-0.001	0.000	-0.002	0.003
PID performance -10%	-0.000	-0.002	-0.001	0.001	-0.003	-0.002	0.002
PID performance +30%	-0.001	-0.000	-0.001	0.000	0.001	-0.000	0.004
PID performance -30%	-0.000	-0.001	-0.000	0.001	-0.003	-0.003	0.003
Tracking efficiency Up	0.002	-0.000	0.001	-0.000	0.001	0.001	0.001
Tracking efficiency Down	0.000	-0.001	0.001	0.000	-0.000	-0.000	0.001
Trigger efficiency Up	0.001	-0.002	0.001	0.003	0.004	-0.000	-0.001
Trigger efficiency Down	0.000	0.000	0.002	0.002	0.002	0.001	0.000

Table A.5: Variation of $A_{\rm FB}$ when systematically varying fit parameters or the weights applied to the data.

Systematic	$0.1 < q^2 < 2.0$	$2.0 < q^2 < 4.3$	$4.3 < q^2 < 8.68$	$10.09 < q^2 < 12.86$	$14.18 < q^2 < 16.0$	$16.0 < q^2 < 19.0$	$0.1 < q^2 < 6.0$
fileNominal	0.362 +/- 0.001	0.669 +/- 0.001	0.551 +/- 0.001	0.462 +/- 0.001	0.330 +/- 0.001	0.374 +/- 0.001	0.633 +/- 0.001
AC CTL Up	-0.010	-0.008	-0.008	-0.007	-0.010	-0.007	-0.006
AC CTL Down	0.012	0.004	0.010	0.008	0.007	0.008	0.012
AC CTK Up	0.017	0.010	0.018	0.018	0.014	0.015	0.018
AC CTK Down	-0.019	-0.014	-0.021	-0.017	-0.018	-0.019	-0.016
AC CTL Up CTK Down	0.008	0.005	0.012	0.011	0.006	0.010	0.009
AC CTL Down CTK Up	0.028	0.017	0.027	0.025	0.019	0.025	0.027
AC CTL Up CTK Down	-0.030	-0.022	-0.029	-0.028	-0.025	-0.027	-0.025
AC CTL Down CTK Down	-0.011	-0.008	-0.010	-0.010	-0.010	-0.008	-0.007
AC Non-factorisable Up	-0.001	-0.001	-0.000	0.000	-0.001	0.000	0.002
AC Non-factorisable Down	0.001	-0.001	-0.001	0.000	-0.000	-0.002	0.001
AC q^2 binning +1	0.004	-0.003	-0.007	-0.001	0.004	0.014	-0.001
AC q^2 binning -1	-0.005	0.004	0.008	-0.012	-0.013	-0.011	0.007
1st Order Background Model	0.001	0.005	-0.001	0.002	-0.002	-0.001	0.002
3rd Order Background Model	-0.001	-0.005	-0.000	-0.001	-0.000	-0.002	0.001
K^{*0} mis-ID Down	-0.000	-0.000	-0.000	-0.001	-0.003	-0.001	0.002
K^{*0} mis-ID Up	-0.001	-0.001	0.000	-0.000	-0.002	0.000	0.001
Signal mass width Down	0.001	-0.003	-0.000	-0.003	0.000	-0.000	0.001
Signal mass width Up	-0.000	-0.002	-0.001	-0.001	-0.002	0.000	0.001
S-wave component	0.004	-0.009	-0.008	-0.001	0.003	0.003	-0.009
IP Smearing	0.017	-0.000	0.003	0.000	-0.007	-0.007	-0.007
B^0 p_T re-weighting	-0.002	-0.003	-0.004	-0.004	-0.004	-0.002	-0.002
B^0 p re-weighting	0.003	-0.005	-0.010	-0.011	-0.008	-0.005	-0.004
IsMuon efficiency Up	0.007	0.002	0.002	0.000	-0.001	-0.002	0.007
IsMuon efficiency Down	-0.013	-0.011	-0.005	-0.000	-0.002	0.002	-0.005
Removal of soft tracks	0.004	-0.006	-0.012	-0.015	-0.012	-0.015	-0.003
PID performance +5%	0.005	0.001	0.003	-0.000	0.001	0.007	0.006
PID performance -5%	0.003	-0.000	0.002	0.005	-0.001	0.006	0.007
PID performance +10%	0.011	-0.000	0.004	0.001	-0.001	0.005	0.010
PID performance -10%	-0.004	-0.006	0.002	-0.000	0.004	0.004	0.006
PID performance +30%	0.011	-0.001	0.004	0.002	-0.002	0.003	0.010
PID performance -30%	-0.002	-0.004	0.002	0.000	0.004	0.004	0.006
Tracking efficiency Up	-0.001	-0.002	-0.002	-0.001	-0.002	-0.001	0.002
Tracking efficiency Down	-0.001	-0.002	0.001	0.002	-0.000	-0.000	0.002
Trigger efficiency Up	-0.002	-0.003	-0.005	-0.005	-0.006	-0.003	-0.003
Trigger efficiency Down	0.003	-0.002	-0.005	-0.006	-0.004	-0.004	-0.000

Table A.6: Variation of F_{L} when systematically varying fit parameters or the weights applied to the data.

Systematic	$0.1 < q^2 < 2.0$	$2.0 < q^2 < 4.3$	$4.3 < q^2 < 8.68$	$10.09 < q^2 < 12.86$	$14.18 < q^2 < 16.0$	$16.0 < q^2 < 19.0$	$0.1 < q^2 < 6.0$
fileNominal	-0.050 +/- 0.001	-0.027 +/- 0.001	0.072 +/- 0.001	-0.142 +/- 0.001	0.029 +/- 0.001	-0.203 +/- 0.001	0.023 +/- 0.001
AC CTL Up	-0.002	-0.001	0.001	-0.001	-0.003	-0.002	0.003
AC CTL Down	-0.001	-0.002	0.000	0.000	-0.001	-0.001	0.001
AC CTK Up	0.000	-0.000	-0.001	0.003	-0.004	0.003	0.001
AC CTK Down	-0.002	0.000	0.002	-0.003	-0.002	-0.005	0.003
AC CTL Up CTK Down	0.000	-0.000	-0.001	0.001	-0.002	-0.001	-0.000
AC CTL Down CTK Up	0.000	0.000	-0.002	0.004	-0.003	0.004	0.002
AC CTL Up CTK Down	-0.002	-0.002	0.003	-0.005	-0.000	-0.005	0.002
AC CTL Down CTK Down	-0.001	-0.002	0.001	-0.004	-0.001	-0.005	0.003
AC Non-factorisable Up	-0.001	-0.003	0.002	-0.001	-0.001	-0.002	0.002
AC Non-factorisable Down	-0.000	-0.002	0.001	-0.001	-0.000	-0.001	0.000
AC q^2 binning +1	-0.002	0.000	-0.001	-0.001	0.004	0.002	0.001
AC q^2 binning -1	0.004	-0.002	-0.003	-0.008	0.006	0.000	0.001
1st Order Background Model	-0.001	0.000	0.000	-0.001	-0.003	-0.001	0.002
3rd Order Background Model	-0.001	-0.001	0.001	-0.001	-0.002	-0.001	0.001
K^{*0} mis-ID Down	0.000	-0.000	0.001	-0.001	-0.001	-0.001	0.001
K^{*0} mis-ID Up	-0.000	-0.001	0.001	-0.002	-0.001	-0.001	0.002
Signal mass width Down	-0.000	-0.001	0.001	-0.002	-0.002	-0.001	0.003
Signal mass width Up	-0.001	-0.002	0.001	-0.001	-0.002	0.000	0.002
S-wave component	0.005	0.002	-0.006	0.011	-0.005	0.016	-0.001
IP Smearing	0.003	-0.002	0.000	0.003	0.003	-0.010	0.005
B^0 p_T re-weighting	0.001	0.000	0.001	-0.003	-0.000	-0.000	0.002
B^0 p re-weighting	-0.002	0.000	0.004	-0.002	-0.001	0.001	0.002
IsMuon efficiency Up	0.000	-0.000	0.001	-0.001	-0.001	-0.000	0.002
IsMuon efficiency Down	-0.003	-0.002	0.001	-0.001	-0.004	-0.001	-0.000
Removal of soft tracks	-0.003	0.000	0.001	-0.003	-0.001	-0.006	-0.002
PID performance +5%	0.001	-0.000	-0.002	-0.001	-0.004	0.000	0.001
PID performance -5%	0.000	-0.000	-0.001	0.000	-0.001	0.001	0.001
PID performance +10%	0.004	0.001	-0.002	-0.001	-0.003	0.002	-0.001
PID performance -10%	0.000	0.001	-0.001	-0.000	-0.006	-0.003	0.002
PID performance +30%	0.005	0.000	-0.002	0.000	-0.004	0.002	0.001
PID performance -30%	-0.001	0.000	-0.002	-0.001	-0.006	-0.003	0.001
Tracking efficiency Up	-0.001	-0.001	0.001	-0.001	-0.002	-0.001	0.002
Tracking efficiency Down	-0.001	-0.001	0.000	0.000	-0.001	-0.001	0.001
Trigger efficiency Up	-0.003	0.001	0.003	0.000	-0.002	-0.002	0.000
Trigger efficiency Down	-0.003	-0.001	0.002	-0.001	-0.001	-0.000	0.002

Table A.7: Variation of S_3 when systematically varying fit parameters or the weights applied to the data.

Systematic	$0.1 < q^2 < 2.0$	$2.0 < q^2 < 4.3$	$4.3 < q^2 < 8.68$	$10.09 < q^2 < 12.86$	$14.18 < q^2 < 16.0$	$16.0 < q^2 < 19.0$	$0.1 < q^2 < 6.0$
fileNominal	0.056 +/- 0.001	-0.018 +/- 0.001	0.010 +/- 0.001	-0.019 +/- 0.001	0.002 +/- 0.001	0.057 +/- 0.001	0.065 +/- 0.001
AC CTL Up	0.002	0.000	-0.000	-0.000	0.000	0.000	0.000
AC CTL Down	0.000	0.001	-0.000	-0.000	-0.000	0.002	-0.002
AC CTK Up	-0.003	0.001	0.000	-0.000	0.000	-0.001	-0.002
AC CTK Down	0.000	0.000	0.001	-0.002	0.002	0.001	0.001
AC CTL Up CTK Down	-0.002	0.001	-0.001	0.000	-0.000	-0.002	-0.002
AC CTL Down CTK Up	-0.002	-0.000	-0.001	0.001	0.001	-0.002	-0.003
AC CTL Up CTK Down	0.000	0.000	-0.001	-0.000	-0.001	0.001	0.003
AC CTL Down CTK Down	0.000	0.002	-0.000	-0.001	-0.000	0.001	0.003
AC Non-factorisable Up	0.001	-0.001	0.000	0.000	-0.001	-0.000	-0.001
AC Non-factorisable Down	-0.002	0.000	0.000	-0.000	-0.002	-0.000	0.000
AC q^2 binning +1	-0.001	0.000	0.000	-0.000	-0.001	-0.002	-0.000
AC q^2 binning -1	0.002	0.001	-0.001	0.001	-0.002	-0.000	-0.000
1st Order Background Model	-0.001	0.001	-0.001	0.000	0.001	-0.000	-0.001
3rd Order Background Model	-0.001	0.001	-0.001	-0.001	-0.001	-0.002	-0.000
K^{*0} mis-ID Down	-0.000	-0.000	-0.000	-0.002	-0.001	-0.001	-0.000
K^{*0} mis-ID Up	-0.001	0.000	-0.001	-0.001	-0.002	0.001	-0.001
Signal mass width Down	0.002	-0.001	-0.001	-0.001	-0.001	-0.001	-0.001
Signal mass width Up	-0.000	0.000	-0.001	-0.000	0.001	-0.001	-0.002
S-wave component	-0.006	-0.001	-0.002	0.000	-0.001	-0.005	-0.006
IP Smearing	-0.001	0.001	-0.001	-0.000	-0.001	0.000	0.000
B^0 p_T re-weighting	-0.000	-0.001	-0.000	0.001	-0.000	-0.002	-0.001
B^0 p re-weighting	-0.001	-0.001	-0.001	0.000	-0.000	0.001	0.002
IsMuon efficiency Up	-0.000	0.001	0.001	0.001	-0.000	0.001	-0.000
IsMuon efficiency Down	-0.000	-0.000	-0.001	-0.001	-0.001	-0.001	0.000
Removal of soft tracks	-0.001	0.000	0.000	-0.001	-0.001	-0.000	-0.001
PID performance +5%	-0.001	0.002	-0.000	0.000	-0.002	-0.001	-0.002
PID performance -5%	-0.001	0.000	0.001	0.000	-0.000	-0.001	-0.002
PID performance +10%	-0.000	-0.001	-0.001	-0.001	0.001	-0.001	-0.000
PID performance -10%	0.000	-0.002	0.000	-0.000	-0.000	-0.002	0.001
PID performance +30%	-0.000	0.001	-0.000	-0.001	-0.001	-0.000	-0.001
PID performance -30%	0.000	-0.001	0.000	0.001	0.000	-0.002	-0.001
Tracking efficiency Up	-0.001	-0.000	-0.001	0.000	-0.001	0.000	-0.001
Tracking efficiency Down	-0.002	-0.000	-0.001	-0.000	-0.000	-0.001	-0.001
Trigger efficiency Up	-0.001	-0.000	-0.001	0.000	-0.000	0.000	0.001
Trigger efficiency Down	-0.000	-0.000	-0.001	0.002	0.000	0.001	0.000

Table A.8: Variation of S_9 when systematically varying fit parameters or the weights applied to the data.

Systematic	$0.1 < q^2 < 2.0$	$2.0 < q^2 < 4.3$	$4.3 < q^2 < 8.68$	$10.09 < q^2 < 12.86$	$14.18 < q^2 < 16.0$	$16.0 < q^2 < 19.0$	$0.1 < q^2 < 6.0$
fileNominal	-0.045 +/- 0.002	-0.745 +/- 0.003	0.511 +/- 0.001	0.697 +/- 0.001	0.960 +/- 0.001	0.626 +/- 0.001	-0.556 +/- 0.002
AC CTL Up	0.005	-0.002	0.002	-0.000	0.001	0.002	-0.001
AC CTL Down	0.005	0.002	0.001	-0.001	0.001	0.000	-0.002
AC CTK Up	0.008	0.004	0.005	0.004	0.003	0.004	-0.006
AC CTK Down	0.007	0.003	-0.005	-0.004	-0.001	-0.002	0.003
AC CTL Up CTK Down	0.008	-0.003	0.006	0.003	0.003	0.005	-0.006
AC CTL Down CTK Up	-0.000	-0.001	0.006	0.003	0.001	0.007	-0.006
AC CTL Up CTK Down	0.004	-0.002	-0.005	-0.005	-0.001	-0.004	0.009
AC CTL Down CTK Down	0.003	0.002	-0.004	-0.004	-0.001	-0.001	0.004
AC Non-factorisable Up	0.001	0.007	0.002	0.001	0.001	0.003	-0.005
AC Non-factorisable Down	0.000	-0.001	0.001	-0.002	0.000	-0.001	-0.001
AC q^2 binning +1	0.006	-0.002	-0.001	0.003	0.001	0.005	-0.003
AC q^2 binning -1	0.003	-0.001	0.003	-0.005	0.000	0.002	-0.001
1st Order Background Model	0.010	0.002	0.001	0.001	0.002	-0.001	-0.001
3rd Order Background Model	0.003	0.002	0.003	-0.001	-0.001	-0.000	-0.003
K^{*0} mis-ID Down	0.003	0.001	-0.001	-0.002	-0.001	-0.003	-0.000
K^{*0} mis-ID Up	0.003	-0.003	0.003	0.002	0.003	0.004	-0.000
Signal mass width Down	0.001	-0.003	-0.000	0.001	0.001	0.000	-0.001
Signal mass width Up	-0.001	-0.001	-0.000	0.000	0.001	0.002	-0.001
S-wave component	0.005	0.039	-0.032	-0.032	-0.021	-0.022	0.042
IP Smearing	0.004	0.004	0.001	0.002	0.001	-0.003	0.001
B^0 p_T re-weighting	0.006	-0.003	0.000	-0.002	0.000	0.002	-0.001
B^0 p re-weighting	0.007	-0.001	0.002	0.000	0.001	-0.001	-0.002
IsMuon efficiency Up	0.000	0.001	-0.001	0.000	0.002	0.002	-0.001
IsMuon efficiency Down	0.007	-0.005	-0.001	-0.000	0.001	0.001	-0.001
Removal of soft tracks	0.003	-0.000	-0.005	-0.001	0.000	-0.001	-0.001
PID performance +5%	0.001	0.005	0.004	0.003	0.001	0.002	-0.003
PID performance -5%	0.003	-0.005	0.001	0.000	0.002	0.003	-0.005
PID performance +10%	-0.000	0.000	0.004	0.002	0.001	0.004	-0.001
PID performance -10%	0.004	-0.001	0.002	0.002	0.002	0.001	-0.003
PID performance +30%	0.004	0.001	-0.000	0.000	0.000	0.003	-0.006
PID performance -30%	0.001	-0.001	0.001	0.001	0.001	0.002	-0.005
Tracking efficiency Up	0.003	-0.001	-0.002	-0.001	0.002	0.001	-0.000
Tracking efficiency Down	0.001	-0.003	0.001	-0.002	0.003	0.001	0.000
Trigger efficiency Up	0.002	-0.005	-0.000	-0.003	0.001	0.000	0.002
Trigger efficiency Down	0.002	-0.001	-0.001	-0.002	0.001	0.002	-0.002

Table A.9: Variation of $A_{\mathrm{T}}^{\mathrm{Re}}$ when systematically varying fit parameters or the weights applied to the data.

Systematic	$0.1 < q^2 < 2.0$	$2.0 < q^2 < 4.3$	$4.3 < q^2 < 8.68$	$10.09 < q^2 < 12.86$	$14.18 < q^2 < 16.0$	$16.0 < q^2 < 19.0$	$0.1 < q^2 < 6.0$
fileNominal	-0.158 +/- 0.003	-0.151 +/- 0.005	0.318 +/- 0.003	-0.527 +/- 0.003	0.082 +/- 0.003	-0.649 +/- 0.003	0.135 +/- 0.004
AC CTL Up	-0.001	0.006	0.007	0.010	0.003	0.009	-0.002
AC CTL Down	-0.008	-0.004	0.010	-0.009	0.000	-0.008	0.004
AC CTK Up	-0.004	0.000	0.012	-0.006	-0.001	-0.005	-0.001
AC CTK Down	-0.007	-0.001	0.006	0.001	-0.008	0.007	-0.004
AC CTL Up CTK Down	-0.007	-0.007	0.013	-0.004	-0.000	-0.000	-0.007
AC CTL Down CTK Up	-0.002	0.001	0.015	-0.005	0.003	-0.005	0.007
AC CTL Up CTK Down	0.004	0.007	0.002	0.010	-0.002	0.011	-0.004
AC CTL Down CTK Down	-0.004	-0.010	0.010	-0.000	-0.003	-0.000	0.010
AC Non-factorisable Up	-0.003	0.001	0.009	-0.003	0.002	0.000	-0.002
AC Non-factorisable Down	-0.004	-0.000	0.008	0.004	0.001	-0.000	-0.000
AC q^2 binning +1	-0.012	0.002	-0.004	0.007	0.015	-0.005	-0.002
AC q^2 binning -1	0.011	-0.022	-0.007	-0.014	0.011	0.015	0.013
1st Order Background Model	-0.007	-0.006	0.013	-0.006	0.006	-0.009	0.005
3rd Order Background Model	-0.002	0.008	0.008	0.003	-0.001	0.002	-0.001
K^{*0} mis-ID Down	-0.008	0.006	0.007	0.003	0.001	0.004	-0.014
K^{*0} mis-ID Up	-0.004	0.008	0.009	0.003	-0.003	0.006	-0.007
Signal mass width Down	0.003	-0.002	0.005	0.010	0.003	0.003	0.000
Signal mass width Up	-0.005	-0.001	0.010	-0.002	0.002	-0.002	0.008
S-wave component	0.009	0.011	-0.032	0.049	-0.006	0.051	-0.023
IP Smearing	0.002	-0.005	0.004	0.008	0.013	-0.031	0.024
B^0 p_T re-weighting	-0.009	-0.006	0.004	0.005	0.000	0.002	-0.002
B^0 p re-weighting	-0.009	-0.002	0.010	0.009	0.004	0.013	-0.004
IsMuon efficiency Up	-0.004	0.002	0.019	0.001	0.003	-0.004	0.002
IsMuon efficiency Down	-0.006	0.007	0.000	-0.006	-0.010	-0.003	-0.006
Removal of soft tracks	-0.013	0.007	-0.001	0.012	0.005	-0.000	-0.015
PID performance +5%	0.003	0.007	-0.001	0.004	-0.006	-0.005	-0.007
PID performance -5%	-0.006	0.005	0.001	0.002	0.002	0.000	-0.009
PID performance +10%	0.010	0.003	-0.005	-0.001	-0.003	0.007	-0.009
PID performance -10%	0.003	-0.010	0.003	0.002	-0.017	-0.013	-0.008
PID performance +30%	0.009	0.001	-0.006	0.001	-0.006	0.009	-0.011
PID performance -30%	0.003	0.006	-0.002	0.001	-0.018	-0.007	-0.004
Tracking efficiency Up	-0.004	-0.022	0.005	-0.001	0.003	0.001	-0.006
Tracking efficiency Down	-0.008	0.003	0.007	-0.005	0.001	-0.008	-0.002
Trigger efficiency Up	-0.003	0.012	0.005	0.003	-0.001	0.006	0.003
Trigger efficiency Down	-0.009	-0.003	0.011	-0.000	0.000	0.003	0.009

Table A.10: Variation of A_{T}^2 when systematically varying fit parameters or the weights applied to the data.

Systematic	$0.1 < q^2 < 2.0$	$2.0 < q^2 < 4.3$	$4.3 < q^2 < 8.68$	$10.09 < q^2 < 12.86$	$14.18 < q^2 < 16.0$	$16.0 < q^2 < 19.0$	$0.1 < q^2 < 6.0$
fileNominal	0.176 +/- 0.003	-0.094 +/- 0.006	0.044 +/- 0.003	-0.076 +/- 0.003	-0.001 +/- 0.003	0.184 +/- 0.003	0.349 +/- 0.004
AC CTL Up	0.001	0.001	-0.000	0.009	0.008	-0.001	-0.001
AC CTL Down	0.009	-0.004	-0.002	0.005	0.004	-0.001	0.013
AC CTK Up	0.004	0.007	0.003	0.001	0.008	-0.001	0.004
AC CTK Down	-0.000	-0.002	-0.000	0.008	0.006	-0.000	0.004
AC CTL Up CTK Down	0.002	0.004	0.002	0.010	0.008	-0.002	0.000
AC CTL Down CTK Up	0.006	-0.004	0.004	0.003	0.005	0.004	0.015
AC CTL Up CTK Down	-0.005	0.003	-0.000	0.001	0.006	0.002	-0.009
AC CTL Down CTK Down	-0.002	0.006	0.005	0.004	0.004	0.003	0.009
AC Non-factorisable Up	0.000	-0.006	0.001	0.005	0.004	0.003	0.007
AC Non-factorisable Down	0.002	0.003	0.002	0.004	0.005	-0.001	0.000
AC q^2 binning +1	0.002	0.002	-0.001	0.011	0.008	0.002	0.007
AC q^2 binning -1	-0.003	-0.011	-0.003	0.004	0.003	-0.006	0.011
1st Order Background Model	-0.002	-0.001	0.007	0.001	0.006	-0.005	0.006
3rd Order Background Model	0.005	0.012	-0.002	0.002	0.004	-0.002	0.000
K^{*0} mis-ID Down	0.003	-0.005	-0.000	0.007	0.002	0.001	0.003
K^{*0} mis-ID Up	0.005	-0.006	0.005	0.008	0.005	-0.001	0.004
Signal mass width Down	0.004	0.015	-0.004	0.009	0.008	0.002	0.003
Signal mass width Up	0.003	-0.001	0.001	0.000	0.007	-0.003	0.009
S-wave component	-0.016	0.000	-0.001	0.012	0.007	-0.014	-0.038
IP Smearing	0.007	0.001	-0.002	0.004	0.004	-0.001	0.002
B^0 p_T re-weighting	0.001	0.004	0.002	0.009	0.007	-0.006	0.013
B^0 p re-weighting	0.006	0.005	0.003	0.001	0.008	0.001	0.001
IsMuon efficiency Up	0.005	-0.001	0.002	0.005	0.004	-0.003	0.003
IsMuon efficiency Down	-0.005	0.002	-0.001	0.006	0.003	-0.008	0.006
Removal of soft tracks	0.008	0.001	-0.007	0.006	0.005	-0.001	0.003
PID performance +5%	-0.001	-0.007	0.006	-0.001	0.005	0.005	0.005
PID performance -5%	0.006	0.006	0.004	0.007	0.013	0.002	0.007
PID performance +10%	0.004	0.003	-0.006	0.006	0.007	0.002	0.005
PID performance -10%	0.004	0.002	0.000	-0.001	0.006	-0.002	0.007
PID performance +30%	0.001	-0.008	-0.004	0.006	0.012	-0.002	0.003
PID performance -30%	0.001	0.003	-0.003	0.002	0.005	0.001	-0.003
Tracking efficiency Up	-0.000	-0.012	-0.005	0.005	0.002	-0.002	0.001
Tracking efficiency Down	0.007	-0.001	-0.002	-0.003	0.006	-0.003	0.013
Trigger efficiency Up	0.003	0.004	0.001	0.008	0.006	-0.000	0.010
Trigger efficiency Down	0.006	-0.002	0.005	0.003	0.008	-0.004	0.007

Table A.11: Variation of $A_{\mathrm{T}}^{\mathrm{Im}}$ when systematically varying fit parameters or the weights applied to the data.

Systematic	$0.1 < q^2 < 2.0$	$2.0 < q^2 < 4.3$	$4.3 < q^2 < 8.68$	$10.09 < q^2 < 12.86$	$14.18 < q^2 < 16.0$	$16.0 < q^2 < 19.0$	$0.1 < q^2 < 6.0$
fileNominal	0.119 +/- 0.001	0.048 +/- 0.001	-0.133 +/- 0.001	0.002 +/- 0.001	-0.061 +/- 0.001	0.001 +/- 0.001	0.021 +/- 0.001
AC CTL Up	0.002	-0.001	-0.001	-0.002	-0.001	-0.000	0.001
AC CTL Down	0.001	-0.001	0.000	-0.001	0.000	-0.000	-0.001
AC CTK Up	-0.001	-0.001	0.003	-0.001	0.001	0.002	0.001
AC CTK Down	0.004	0.003	-0.005	-0.000	0.000	0.002	0.002
AC CTL Up CTK Down	0.000	-0.000	0.003	0.000	0.000	-0.001	-0.000
AC CTL Down CTK Up	0.000	-0.002	0.005	-0.000	0.001	0.000	-0.000
AC CTL Up CTK Down	0.003	0.002	-0.005	-0.001	-0.002	-0.001	0.002
AC CTL Down CTK Down	0.004	0.002	-0.004	0.001	-0.000	0.001	0.001
AC Non-factorisable Up	0.002	0.000	-0.001	0.001	0.000	0.003	0.000
AC Non-factorisable Down	0.001	0.001	-0.001	-0.001	0.000	0.002	0.001
AC q^2 binning +1	-0.002	-0.001	-0.003	-0.000	0.001	0.001	0.001
AC q^2 binning -1	0.003	0.000	0.001	0.000	0.000	0.001	0.001
1st Order Background Model	0.003	-0.001	-0.000	-0.000	0.000	0.001	-0.001
3rd Order Background Model	0.002	-0.001	0.000	-0.001	0.002	-0.001	0.001
K^{*0} mis-ID Down	0.001	-0.001	-0.000	-0.001	0.001	0.000	0.001
K^{*0} mis-ID Up	0.001	-0.000	-0.001	0.000	0.001	0.001	0.000
Signal mass width Down	0.001	0.002	-0.001	0.003	-0.000	0.003	0.001
Signal mass width Up	0.001	0.000	-0.001	-0.000	0.001	0.000	0.001
S-wave component	-0.008	-0.001	0.013	-0.001	0.007	0.002	-0.003
IP Smearing	-0.001	0.001	-0.001	-0.000	-0.001	0.001	0.000
B^0 p_T re-weighting	0.000	0.000	-0.002	-0.001	0.000	0.002	0.000
B^0 p re-weighting	0.003	0.001	-0.003	-0.002	-0.001	-0.000	-0.000
IsMuon efficiency Up	0.002	-0.001	0.001	-0.001	-0.001	0.000	0.000
IsMuon efficiency Down	0.002	0.002	-0.001	-0.002	0.001	0.001	0.002
Removal of soft tracks	0.003	-0.000	-0.002	0.000	-0.000	0.002	0.000
PID performance +5%	0.001	0.000	0.000	-0.001	0.002	0.001	0.000
PID performance -5%	-0.000	-0.001	0.001	-0.001	0.001	0.001	0.001
PID performance +10%	0.002	-0.000	0.000	-0.002	-0.001	0.002	0.001
PID performance -10%	0.003	0.000	0.001	-0.002	0.001	0.001	-0.000
PID performance +30%	0.001	0.001	-0.000	0.000	-0.000	0.002	0.000
PID performance -30%	0.001	0.001	0.001	0.001	0.001	0.000	0.000
Tracking efficiency Up	0.000	0.002	-0.001	0.000	0.001	0.001	0.001
Tracking efficiency Down	0.001	-0.000	-0.000	-0.001	0.001	0.002	0.000
Trigger efficiency Up	0.003	-0.000	-0.001	-0.002	-0.001	0.000	0.001
Trigger efficiency Down	0.004	0.001	-0.001	-0.000	-0.002	-0.000	0.002

Table A.12: Variation of A_9 when systematically varying fit parameters or the weights applied to the data.

Systematic	$0.1 < q^2 < 2.0$	$2.0 < q^2 < 4.3$	$4.3 < q^2 < 8.68$	$10.09 < q^2 < 12.86$	$14.18 < q^2 < 16.0$	$16.0 < q^2 < 19.0$	$0.1 < q^2 < 6.0$
Nominal	0.61	0.30	0.49	0.42	0.54	0.37	0.34
B^0 p_T re-weighting	0.61	0.30	0.49	0.42	0.54	0.38	0.34
PID performance -5%	0.62	0.30	0.49	0.42	0.53	0.37	0.35
PID performance -10%	0.62	0.29	0.49	0.42	0.53	0.38	0.35
PID performance -30%	0.62	0.29	0.49	0.42	0.53	0.38	0.35
PID performance +5%	0.62	0.30	0.49	0.42	0.53	0.37	0.35
PID performance +10%	0.63	0.30	0.50	0.42	0.53	0.36	0.35
PID performance +30%	0.63	0.30	0.50	0.42	0.53	0.36	0.35
Removal of soft tracks	0.60	0.30	0.49	0.43	0.55	0.39	0.34
IsMuon efficiency Down	0.61	0.29	0.49	0.43	0.54	0.38	0.34
IsMuon efficiency Up	0.61	0.30	0.50	0.42	0.53	0.37	0.35
B^0 p re-weighting	0.61	0.30	0.49	0.42	0.54	0.38	0.35
IP Smearing	0.61	0.29	0.49	0.43	0.54	0.38	0.34
AC CTK Down	0.63	0.31	0.51	0.44	0.56	0.39	0.36
AC CTK Up	0.60	0.28	0.47	0.41	0.52	0.36	0.33
AC CTL Down	0.63	0.30	0.51	0.44	0.56	0.39	0.35
AC CTL Up	0.60	0.29	0.48	0.41	0.52	0.36	0.33
AC CTL Down CTK Down	0.65	0.32	0.53	0.46	0.58	0.40	0.37
AC CTL Up CTK Up	0.58	0.28	0.46	0.40	0.51	0.35	0.32
AC Non-factorisable Up	0.61	0.29	0.49	0.42	0.54	0.38	0.34
AC Non-factorisable Down	0.61	0.30	0.49	0.43	0.54	0.37	0.35
Tracking efficiency Down	0.62	0.30	0.49	0.42	0.54	0.37	0.35
Tracking efficiency Up	0.61	0.29	0.49	0.42	0.54	0.38	0.34
Trigger efficiency Down	0.61	0.30	0.49	0.42	0.54	0.38	0.35
Trigger efficiency Up	0.61	0.30	0.49	0.42	0.54	0.38	0.35
Signal mass width Up	0.62	0.30	0.50	0.43	0.55	0.38	0.35
Signal mass width Down	0.60	0.29	0.48	0.42	0.53	0.37	0.34
Peaking Bkg	0.62	0.30	0.50	0.43	0.55	0.38	0.35

Table A.13: Variation of the differential branching fraction measurement when systematically varying fit parameters or the weights applied to the data.

Appendix B

Licence

SPRINGER LICENSE
TERMS AND CONDITIONS

Sep 11, 2013

This is a License Agreement between Alexander Shires ("You") and Springer ("Springer") provided by Copyright Clearance Center ("CCC"). The license consists of your order details, the terms and conditions provided by Springer, and the payment terms and conditions.

All payments must be made in full to CCC. For payment instructions, please see information listed at the bottom of this form.

License Number	3225840073935
License date	Sep 11, 2013
Licensed content publisher	Springer
Licensed content publication	Journal of High Energy Physics
Licensed content title	Cornering new physics in b → s transitions
Licensed content author	Wolfgang Altmannshofer
Licensed content date	Jan 1, 2012
Volume number	2012
Issue number	8
Type of Use	Thesis/Dissertation
Portion	Figures
Author of this Springer article	No
Order reference number	
Title of your thesis / dissertation	Exploring b to s electroweak penguin decays at LHCb
Expected completion date	Sep 2013
Estimated size(pages)	200
Total	0.00 GBP
Terms and Conditions	

Introduction

The publisher for this copyrighted material is Springer Science + Business Media. By clicking "accept" in connection with completing this licensing transaction, you agree that the following terms and conditions apply to this transaction (along with the Billing and Payment terms and conditions established by Copyright Clearance Center, Inc. ("CCC"), at the time that you opened your Rightslink account and that are available at any time at http://myaccount.copyright.com).

Limited License

With reference to your request to reprint in your thesis material on which Springer Science and Business Media control the copyright, permission is granted, free of charge, for the use indicated in your enquiry.